Universidad de Sevilla

Grupo de Elasticidad y Resistencia de Materiales

PhD. academic degree in Engineering

Analytical and numerical predictions by LEBIM and FFM for interface cracks in composites and their joints

Author:

María del Mar Muñoz-Reja Moreno

Advisors:

Assoc. Prof. Luis Távara Mendoza

Prof. Vladislav Mantič Leščišin

2021

"...Keep Ithaka always in your mind.
Arriving there is what you're destined for.
But don't hurry the journey at all.
Better if it lasts for years,
so you're old by the time you reach the island,
wealthy with all you've gained on the way,
not expecting Ithaka to make you rich..."

Ithaka-C.P.Cavafy

Acknowledgements

In the following lines I would like to express my gratitude to all the people that took part, directly or indirectly, in the present PhD thesis during the last years.

First of all, I would like to express my sincere esteem to my PhD advisors Dr. Vladislav Mantič and Dr. Luis Távara, not only for their continuous support, guidance and endless motivation, but also for all the opportunities they gave me along this period, which have enabled my growth as a person and a researcher. I am particularly grateful to Dr. Mantič for teaching me the importance of rigorous and meticulous scientific practice and for teaching me not to stop asking myself questions. Also specifically, I am grateful to Dr. Távara because I have learnt from him not to lose patience in the face of the adversity of unsatisfactory results and to see them as a new opportunity for scientific advancement.

I also would like to express my gratitude to the director of the group of Elasticity and Strength of Materials (GERM) Dr. Federico París for trusting me and providing me with the opportunity to get to know the world of scientific research. I wish to extend my thanks to each and every one of my colleagues at GERM. It would be unfair to highlight some colleagues more than others because without one of them (professors, technical experts, PhD students and administration staff) the research group would not have achieved the resources, knowledge and recognition which I have benefited for the realization of this thesis. From a more personal point of view, I would also like to thank my colleagues at GERM for promoting an inspiring working environment and a comfortable atmosphere which helped me to develop the work reflected herein.

Next, I would like to thank my friends and colleagues from *Departamento de Mecánica de Medios Continuos* at *Escuela Politécnica Superior* for their help in those things that, in spite of being not visible in this thesis, have been essential for the adequate development of my doctoral studies. I am particularly indebted to Dr. Enrique Nieto and Dr. Fernando Fernandez because without their help this work that motivates me so much could not be done.

During these years I had the opportunity of collaborating with Dr. Pietro Cornetti from the *Politecnico di Torino* (Italy). I would like to express my gratitude to him for the interesting discussions and his knowledge shared with me. I am greatly indebted to him for introducing me to the world of reinforced concrete using composite materials. I would also like to express my gratitude to all my colleges and friends within the *Polito*, I appreciate their kindness and nice treatment.

In addition, I had the opportunity to collaborate with Dr. Ferri Aliabadi, from Imperial College London (United Kingdom). The excellent treatment, his attention

Contents

List of Figures

List of Tables

CHAPTER 1

Introduction

1.1 Failure in composites and their joints. Motivation.

The use of composite materials in different industrial sectors is gaining a particular relevance over the last two decades as a consequence of their superior specific stiffness and strength ratios in comparison to metals.

Stemming from their complex nature (heterogeneous materials, typically with several characteristic length scales), damage in composites is inevitably dependent upon their internal structure that determines the characteristics failure modes (inter-fiber failure, fiber failure, delamination events, fiber-kinking, matrix-fiber decohesion, among others). The optimized use of composites has motivated the development of a wide set of engineering modelling tools. Notice that the advantage of the high strength-to-weight ratio of composites can be partially reduced or even totally missed if higher safety factors have to be employed as a consequence of a certain lack of knowledge on their failure mechanisms. This fact has motivated a huge effort of studying the failure in composites during the last decades. Despite the large number of studies carried out in this regard, the failure mechanisms in composites still lack a way to be fully defined. The main reason is the coexistence of failure mechanisms that are associated with the microstructure at different scales, as well as the interaction between them, adds a high complexity to the failure mechanisms from a macro scale point of view.

These failure mechanisms are particularly complex in laminates including plies with different orientations. Recalling that in long fibre reinforced composites the fibres are oriented in the direction where a greater stiffness and strength is needed. Moreover, these materials are being gradually incorporated in the manufacturing lines of components of first level of responsibility, in terms of structural integrity, among other engineering applications in the strategic aeronautical industry. Historically, a large number of failure criteria have been proposed based on a variety of assumptions. According to París (2001), a deep knowledge of the failure process in composite

materials is necessary in order to improve the failure criteria currently proposed. Since these criteria should be consistent with the interaction between the different scales of the damage existing in composites and the behaviour of the interfaces between the different components of the composite, among other things (Davila et al., 2005; París et al., 2007; Melro et al., 2013a,b).

In this sense, the integrity of composite structures is determined by, among other conditions, the durability and strength of their adhesive joints and interfaces in general. The adhesion must be guaranteed at several levels of the structure, namely at fibre-matrix interfaces, interfaces between unidirectional plies in laminates, joints between laminates and pieces, etc. Thus, one of the main concerns to design this kind of structures is the adequate characterization of the interfaces between solids on micro-, meso- and macro-scale. In this thesis, problem including interfaces on composite materials at two scales will be studied (micro-scale and meso-scale):

- When composite unidirectional laminates are subjected to transverse loads they usually exhibit a matrix failure, called also interfibre failure, typically initiated in the form of debonds at fibre-matrix interfaces. That is why, the modelling of these interfaces is so important and it has intensively been studied in the past. An extensive review of works studying the problem of debond propagation along the fibre-matrix interface can be found in Davila et al. (2005), París et al. (2007), Melro et al. (2013a,b), Távara et al. (2011) and references therein.

- Bonding of fibre-reinforced polymer (FRP) sheets is one of the most common ways to repair and strengthen civil engineering structures (Hollaway, 2010). An adequate interface characterization of this kind of joints is quite relevant because the joint failure usually occurs due to loss of adhesion between the adherents (J.G.Teng, 2001; Mazzotti et al., 2016).

Despite all the failure criteria proposed to date and all the work that has made great progress in the knowledge regarding the failure of composite materials, the study of crack initiation is still a pending subject for the scientific and engineering community. This is mainly due to the inadequacy of the Linear Elastic Fracture Mechanics (LEFM) to predict the crack onset in an undamaged material or interface since LEFM always assumes the presence of a crack. Although the crack initiation at micro and meso scales is still an open matter, some works have been developed in order to study the initiation by computational methods such as Cohesive Zones Models (CZMs) (Barenblatt, 1959; Hilleborg et al., 1976; Needleman, 1987; Carpinteri, 1989a,b; Camacho and Ortiz, 1996; Maier and Frangi, 1998; Camanho et al., 2003; Ortiz and Pandolfi, 1999; Vodička, 2016). However, one of the problems with the CZM is that they require large computational resources. The CZMs assume different hypotheses to those adopted in LEFM avoiding the presence of stress singularity at the crack tip. Specifically, the CZMs assume a stress softening in front of the crack tip. This softening zone is the so-called fracture process zone. Although, at the beginning, the CZMs were used to study the behaviour of materials similar to concrete, their use in composite materials opened up several areas of research at different scales.

Another way to describe the behaviour of a thin interface between solids can be to model a layer of linear-elastic springs which allows studying the interface failure by

different fracture criteria and by appropriate stiffness parameters. The above mentioned interface models, originally proposed by Prandtl (1933), Volkersen (1938) and Goland and Reissner (1944), are usually referred to in the literature as (linear-)elastic interfaces, weak interfaces or imperfect interfaces. Klarbring (1991) and Geymonat et al. (1999), proposed a simplified model in which the elastic layer is treated as a material surface, disappearing from a geometrical point of view but being represented by its energy of adhesion. A comprehensive review for this kind of interface model can be found in Geymonat et al. (1999).

Although the weak interface model has been known for a long time, recently several authors coupled this model with suitable fracture criteria to obtain analytical solutions for structural joints under different geometrical, material and loading parameters, e.g. Lenci (2001); Carpinteri et al. (2009); Bennati et al. (2009); Távara et al. (2010, 2011); Cornetti et al. (2012); Weißgraeber and Becker (2013); Mantič et al. (2015); Dimitri et al. (2018); Muñoz Reja et al. (2018); Rosendahl and Weißgraeber (2019) and Bennati et al. (2019). Based on the same idea, 2D and 3D computational implementation of the Linear Elastic-Brittle Interface Model (LEBIM) were proposed (Mantič et al., 2015; Távara et al., 2010, 2011, 2019a). In these papers, the numerical implementations were based on the Boundary Element Method (BEM) or the Finite Element Method (FEM) and achieved by exploiting a Sequentially Linear Analysis (SLA) solving scheme to predict the interface crack onset and propagation. The developed codes have proven to be efficient and robust tools to study the interface failure for several problems at different scales (micro, meso and macro).

In the LEBIM, due its simplicity, three mechanical properties are directly related to each other: the interface fracture energy, strength and stiffness. Therefore if two of them are defined (usually the fracture toughness and strength), then the third one is actually also given, which usually leads to an interface compliance higher than the actual one. Thus, obtaining an inadequate characterization for stiff interfaces. Another disadvantage of the LEBIM is that its damage propagation always has an infinitesimal growth, similarly to the LEFM. However, in some fracture processes, the failure occurs instantaneously, leading to a crack growth with a finite length.

A way to overcome these drawbacks is to apply the Coupled Criterion of Finite Fracture Mechanics (CCFFM) approach to LEBIM, which makes the stiffness become an independent variable. The FFM theory assumes that cracks are formed instantaneously with a finite length (Hashin, 1996). Therefore, in the energy balance the finite crack length Δa is used instead of an infinitesimal crack. Moreover, Leguillon (2002), Cornetti et al. (2006) and Mantič (2009), proposed a coupled stress and energy criterion to obtain the critical load needed to produce a crack of finite length. Accordingly, the two conditions are able to provide the unknown critical load and critical (finite) crack length (see Weißgraeber et al. (2016) for a review). This approach is usually referred to as Coupled Criterion of the Finite Fracture Mechanics (CCFFM).

1.2   Objectives of the thesis.

This thesis is part of research line that has been carried out by the Group of Elasticity and Strength of Materials of the University of Seville (GESM) since the beginning of 1990, and which has produced many advances in the knowledge of the failure mechanisms in composites from the physical, mathematical and experimental point of view. Thus, at the beginning of this thesis, the research group had already established a deep physical and mathematical knowledge of several failure problems in composite materials, as well as different theories that constitute the fracture mechanics behaviour. Throughout all these years, the research group has developed different computer tools that have helped to advance in the mentioned fields of knowledge. Some of these tools have been fundamental in achieving the objectives of this thesis, particularly those related to the Linear Elastic Brittle Interface Model (LEBIM) and the numerical methods of calculation which allow solving the partial differential equations of continuum mechanics. Specifically in this thesis, the Boundary Elements Method (BEM) and Finite Elements Method (FEM) have been used.

The objective, in the long term, of this research is to contribute to the generation of failure criteria that allow the prediction of damage at the macro-, meso- and micro-scale interfaces for composite materials and their applications. The specific objective of this thesis is the study of a failure criterion based on the Couple Criterion of the Finite Fracture Mechanics (CCFFM) applied to LEBIM (CCFFM + LEBIM), and the production of analytical and numerical tools based on this new criterion. In addition, these tools will be used to study specific problems in which composite materials and their joints are present.

The tasks carried out to fulfill these general objectives are described in the following.

(i) Development of the analytical formulation of the coupled criterion applied to the LEBIM. This development is divided into the two existing approaches, at the present time:

- The first approach is based on the definition of the curves that produce the formulation of the coupled criterion of Leguillon (2002). With this approach, the coupled criterion applied to the LEBIM would imply the integration of the Energy Relay Rate (ERR) along the path of the interface failure.

- On the other hand, the second approach is based on Principle of Minimum Total Energy subject to a Stress Condition (PMTE-SC) presented by Mantič (2014). This approach is based on the energetic minimization of the possible damaged configurations of the problem under study.

(ii) Suitable numerical implementations of two previous approaches in three codes:

- An algorithm based on the definition of the curves of the CCFFM is implemented in a Boundary Element Method (BEM) code. This BEM code was

developed by GESM and had IT already implemented the LEBIM before starting this thesis.

- A Python script is developed to implement the same algorithm as above. This code uses the commercial code ABAQUS based on the Finite Element Method (FEM) to solve the displacement field of each problem. In this code a user subroutine UMAT is used to model the interface by LEBIM. This UMAT has been developed in the GESM.

- Another algorithm is developed in Python to implement the PMTE-SC applied to the LEBIM. This code also uses the commercial code ABAQUS and the same UMAT subroutine mentioned above.

(iii) Study of relevant particular cases of damage mechanisms, in form of cracks onset and growth at macro and micro scale by CCFFM + LEBIM. The objective of this point is to analyse the scope of the methodology developed in this thesis, both numerically and analytically.

- Analysis of a crack in a thin adhesive layer for an isotropic DCB specimen (macro scale). This simple and well-known example allows analysing in detail the difference between the two approaches of the CCFFM + LEBIM.

- The evaluation of the shear strength in adhesive joints between concrete and carbon fiber reinforced polymer (CFRP) laminates by CCFFM + LEBIM (macro scale). Pull-push shear tests are studied in detail and the predictions by the methodology presented in this thesis are compared with two experimental test campaigns found in literature.

- Micro-mechanical behavior of interface cracks between matrix and fibre under transversal loads (micro scale).

1.3 Outlines of the thesis.

The present thesis is organized in seven Chapters. Leaving aside the present introduction and the last chapter of conclusions and future developments, it can be divided in three parts:

Part 1: State of art.
In chapter two, a brief bibliographical review regarding fracture mechanics is presented. The failure mechanisms along the interface between two solids are briefly described and the formulation used in the LEBIM is also reviewed for its use in the following sections.

Part 2: Development of the couple criteria applied to LEBIM and numerical tools:
A general formulation of the coupled criterion applied to the LEBIM (CCFFM + LEBIM) is developed at the beginning of Chapter 3. The mechanical characteristics of the interface necessary to apply the couple criterion are described. Subsequently, the two approaches of the CCFFM + LEBIM developed in this thesis are explained

separately and the two pseudo-codes that have been used to implement them are described.

Part 3: Study cases of damage and failure in composite materials at macro and micro scale:
This part includes Chapters 4, 5 and 6. Each of them is a case study analysed using the CCFFM + LEBIM.

- The first of the three cases, described in Chapter 4, includes an isotropic Double Cantilever Beam test (DCB). It is studied under displacement control and under load control separately. Although this test is included among the problems solved by the CCFFM + LEBIM, it could actually be part of the development of the coupled criteria applied to LEBIM. Since this test is used to study the new criterion by means of the two approaches described above. In other words, the objective of this case study is to analyse the behaviour of the new criterion rather than the study of the test. Two analytical studies based on an Euler-Bernoulli beam model and joined by an elastic interface are developed. The analytical results are compared with the results of the two numerical tools implemented and described in Chapter 4.

- Chapter 5 studies in detail the double pull-push shear tests (DPPS) which are used to characterize the concrete reinforcement joints with composite materials. The analytical development of this problem is similar to the DCB. However, this study is a little more complicated, since a Timoshenko beam is used and the interface is capable of transmitting normal and tangential stresses. Then, the CCFFM + LEBIM based on curves is applied to the beam analytical model and the prediction is compared with experimental tests from the literature. Another experimental-analytical-numerical comparison is presented using an inverse analysis to characterize the mechanical properties of the interface.

- Finally, the micro-mechanical behavior of interface cracks between matrix and fibres under transversal loads is studied in Chapter 6. First, an isolated fibre embedded in a matrix under transversal uni-axial tension loads or biaxial transverse loads model (either tension-tension or tension-compression) is studied. Furthermore, the influence between two fibres is studied and the non-symmetrical response of a symmetrical isolated fibre problem is analysed.

CHAPTER 2

Interface crack onset and propagation

The work developed in this thesis is based on two main bases. On the one hand, a novel fracture mechanics theory is used. This theory couple the two main criteria of fracture mechanics: the maximum stress criterion and the energy criterion. On the other hand, the damage model developed in this work is applied to the failure of interfaces between two solids, at macro and micro scale. For this reason, some fundamental milestones that will frame the theory and formulation developed in the rest of this manuscript are briefly described in this chapter.

2.1 Classical fracture mechanics.

Although the study fracture mechanics dates back to the 16th century with the first research by Leonardo Da Vinci, the main developments in this area have taken place in the last century. This area of research remains to this day the source of numerous studies and novel theories that attempt to explain the process of creating a new surface on a solid. In addition to scientific studies to understand fracture mechanics in different materials, numerous contributions from an engineering point of view must be highlighted. These engineering contributions allow modelling complex problems in a simple way and with an adequate precision.

Although the basis of the Linear Elastic Fracture Mechanics (LEFM) theory is still essential today in order to explain the most advanced concepts of Fracture Mechanics, this theory was not the first field of study within Fracture Mechanics. At the beginning of the 20th century, several authors tried to explain the fracture process from the point of view of the deformable solid and applying a criterion of maximum stress. Among all the contributions of the time, it is noticeable the work of Wieghardt (1907). In that work, Wieghardt studied in detail the first elastic solution at the vertex of a corner and deduced the existence of a stress singularity proportional to r^λ, with $0 < \lambda < 1$ and r being the distance to the mentioned vertex. This solution could be

the first elastic solution with a recognised stress singularity (Erdogan, 2000). Other important works that contributed in the solution of the crack stress field were: the research of Inglis (1913) which solved the stress field in a thin plate with an elliptical hole, the research of Westergaard (1939) which obtained the power of singularity of the stresses around the crack tip:

$$\sigma \propto (1/\sqrt{r}); \tag{2.1}$$

and the work of the Sneddon (1946) which studied plane cracks in three dimensions.

However, the study of fracture mechanics from a maximum stress point of view left many unsolved questions. For example, how can a maximum stress criterion be applied to an infinite stress? Or, why the size of the solid do not affect the crack propagation? (a fact already observed in Da Vinci studies). In order to solve these issues, Griffith (1921) established a theory based on the First Principle of Thermodynamics: the energy of a system decrease when the system change from a state of non-equilibrium to a state of equilibrium. Based on this principle, Griffith established his theory on which Fracture Mechanics is currently based: *according to the well-known " theorem of minimum energy" the equilibrium state of anelastic body, deformed by specified surface forces, is such that the potential energy of the whole system is a minimum.* Griffith applied the energy balance at a flat homogeneous isotropic plate of uniform thickness, containing a straight crack (of area A and length a) and being subjected to stresses (σ) applied in its plane at its outer edge. Griffith used the solution of Inglis (1913) to develop his theory and concluded that the crack in a solid propagates if the stress exceeds the critical stress of the cracked solid.

$$\sigma_f = \frac{2E\gamma_s}{\pi a}, \tag{2.2}$$

where E is the Young modulus of the material and γ_s is the surface energy of the solid, which is interpreted as the energy needed to break the intermolecular bond and to generate a new surface. With this expression, Griffith answered the question of the "size effect" observed previously, since the energy used to generate the new surface in the solid must be proportional to the atomic bonds to be broken, that is, proportional to the area of the new surface generated.

Griffith obtained good results concerning experimental tests on brittle materials (e.g. ceramics and glass). However, the theory of Griffith did not work for materials whose fracture involves other damage mechanisms that include the dissipation of energy by irreversible processes, such as the plastic deformation at the crack tip. For this reason, for some materials, the theory of Griffith was not able to predict either the energy needed to generate a new crack or the stress field at the crack tip.

Years later and independently, Irwin (1948) and Orowan (1949) added a term to the expression of Griffith to include plastic behaviour in the fracture. And Irwin (1957) proposed a redefinition of the theory of Griffith which established the relationship between the energy approach and the elastic solution of the crack, being today the basis of the LEFM. In this work, Irwin defined the concept of Energy Relase Rate (ERR), as the elastic potential energy released per unit area of the new crack, G. He also defined the energy needed to generate this new crack per unit area and called it "fracture critical energy" (G_c). The fracture critical energy can be found in the

literature as $G_c = R = 2\gamma_s$. Besides, he proposed the following necessary condition for the propagation of the crack:

$$G_c \leq G \tag{2.3}$$

This theory indicated that the elastic analysis of a fracture problem gives good results with a small crack front process zone, even with unrealistic stresses in the same area. It is possible because the energy needed to propagate the crack is taken from the elastic mass of the solid and therefore crack propagation do not depend so much on the stresses at the crack tip. Also, Irwin, from the works of Wieghardt (1907), Westergaard (1939) and Sneddon (1946) formulated the asymptotic solutions for the problems of cracks at small distance r from the crack tip. These asymptotic solutions are defined by three stress intensity factors (SIF) K_I, K_{II} and K_{III} (and three sets of related angular functions). K_I is the SIF for mode I and it is associated with the crack opening mode. K_{II} is the SIF for mode II and it is associated with the crack sliding mode. Finally, K_{III} is the SIF for mode III and it is associated with the tearing mode. And he established a simple relationship between the energy release rate and the stress intensity factor for an infinite cracked plate under tension:

$$K_I^2 = GE \quad \text{for plane stress, and} \quad K_I^2(1 - \nu^2) = GE \quad \text{for plane strain} \tag{2.4}$$

This fact is important due to G represents a global magnitude associated to the strain energy of the whole solid and K_I is a local magnitude. The critical intensity factor K_{Ic} is usually referred to as "fracture toughness" but, in the literature, this denomination is used for a variety of terms. In this thesis, the designations of the terms are those that appear in Fig. 2.1. This figure also shows the relationship between the material properties and the driving force that leads to the fracture of the solid under study.
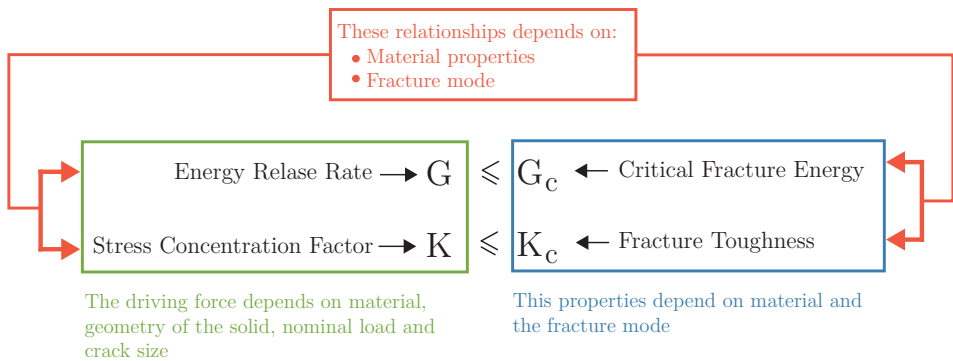
Figure 2.1: The relationship between the material properties and the driving force that leads to the fracture.

From the works of Irwin, there has been a significant increase in contributions to fracture mechanics from various points of view. One of the main focuses of research over the years has been to design tests that are capable of reliably determining

the fracture toughness (for the three individual modes or mixed mode) in different materials. There has also been a significant contribution to the development of non-linear fracture mechanics. These contributions, together with the development of new computer tools, has provided answers to complex problems.

This century has been very productive in the field of fracture mechanics. The next sections of this thesis will focus on the contributions concerning the development of this thesis.

2.2 Interfacial fracture mechanics.

The increasing use of composite materials in different fields of engineering has led to the study of the behaviour of these materials and their joints with other materials, such as concrete or metals. This means that in structures where there is composite there is also a large presence of very thin regions between two different domains. These areas are defined as interfaces and the mechanical properties of the composite depend on them, including fracture toughness. Therefore, the interface behaviour has been a prosperous field of study in the recent years. This area of research has addressed a variety of problems in order to understand the role of interfaces at different scales (micro, meso and macro).

Within the field of composites, the study of the different interfaces is an important issue to design a structural system adjusted to the actual behaviour of these composites. In this way, the development of more efficient structures, from an engineering point of view, would be possible. Therefore, the Fracture Mechanics study applied to the failure of these interfaces arises from the need to characterise interfacial cracks in different engineering applications. For example, joints between metals or concrete and a composite material, delamination in composites and, at micro-mechanical level, the failure between the fibres and the matrix.

Therefore, the fracture mechanics applied to interfaces has produced a lot of research in recent years. The first works of Williams (1959); England (1965); Erdogan (1965); Rice and Sih (1965) and Malyshev and Salganik (1965) studied the interface failure assuming an open crack model. In these models, the displacements coincide on both sides of the undamaged part of the interface, while in the damaged interface, both materials are separated while remaining free of traction. However, this model suffered from some inconsistencies in the stress and displacement fields close to the crack tip, for some specific cases. When England (1965) and Erdogan (1965) studied these inconsistencies became aware of the existence of regions where crack faces physically interpenetrate on a very small scale (atomic or subatomic). For this reason Comninou (1977) developed the contact model of interface cracks.

Rice (1988) analysed the behaviour of these contact areas and deduced that the Williams open model was suitable for the study of interface failure if the non-linear response size close the crack tip (plastic strain, contact, etc.) is small enough compared to the smaller characteristic length of the model (layer thickness, crack length, etc.). However, if the area where this non-linear behaviour exists are larger than the characteristic length of the problem, then linear elastic contact models (Comninou, 1977), elastoplastic models (Shih and Asaro, 1988, 1989) or non-linear elastic models (Knowles and Sternberg, 1983; Geubelle and Knauss, 1995) should be considered.

Although the contact model solution could be a suitable solution to model any failure along interfaces, this model is not always suitable to characterize the fracture, because the non-linear behavior can be very complicated to predict, in some cases. Depending on the non-linear behaviour of the contact zone, these problems can be easily solved with simple algorithms or can take time to converge with more complicated algorithms. In any case, the computing time is considerably extended with these models.

Mantič et al. (2006) deduced a new relationship between the mixity measures of Fracture Modes I and II based on the SIF approach and the ERR approach, if the contact zone is less than the shortest characteristic length of the problem. As Rice deduced, in this situation, the open model contains all the relevant information. However, if the contact area is significant, only a contact model is suitable to predict the failure propagation at the interface. Therefore, Hills and Barber (1993) and Hills et al. (1996) propose to use a numerical method that takes into account both models and that this algorithm itself decides which model to use in each case. This model was implemented by Liu and Feng-Chen (1996). Furthermore, these numerical procedures are also important in the cases where the two crack tips have different behaviours (Bank-Sills and Ashkenazi, 2000) or for those cases where the contact behaviour is changed with the failure propagation at the interface (fibre-matrix interface).

Another characteristic of the interface fracture is that the failure tends to grow along the interface, rather than to kink out of the interface, because it is a weak plane. In a homogeneous material, this weak plane is locally associated with the I-mode of fracture. However, because the interface failure may remain within the interface or may kink into one of the adjacent materials, the fracture mode will depend on the ERR and the G_c in each possible option. According to He and Hutchinson (1989) and Mantič et al. (2006), the conditions to propagate inside or outside the interface are as follows:

$$
\begin{aligned}
\frac{G^{\text{int}}}{G_c^{\text{int}}} > \frac{G^{\text{kink}}}{G_c^{\text{kink}}} &\rightarrow \text{ to propagate into interface} \\
\frac{G^{\text{int}}}{G_c^{\text{int}}} < \frac{G^{\text{kink}}}{G_c^{\text{kink}}} &\rightarrow \text{ to kink into one of the adjacent material}
\end{aligned}
\tag{2.5}
$$

where "int" refers to the propagation along the interface and "kink" refers to the propagation outside the interface.

According to Rice (1988) and He and Hutchinson (1989), G_c^{int} can be measured according to the mixity at crack tip (phase angle ψ_K). Therefore the fracture toughness of an interface can be expressed as: $G_c^{\text{int}}(\psi_K)$, and it is an interface property independent of the geometry and applied load. This behavior complicates the characterization of the fracture at the interface when compared to the fracture of homogeneous materials, where the crack path propagation is defined by fracture toughness K_I. Many experimental tests have demonstrated this high dependence on the critical energy of the interface and therefore on the mixity of the fracture mode, for example: Wang and Suo (1990); Hutchinson and Suo (1992); Liechti and Chai (1992); Wang (1997) and Bank-Sills and Ashkenazi (2000).

Several phenomenological laws have been developed to define $G_c^{\text{int}}(\psi_K)$. Three that have fitted well with the experimental test have been those of Hutchinson and Suo (1992), Charalambides and A.J.Kinloch (1992) and Benzeggagh and Kenane (1996).

Most of the cases studied in this thesis will use the law proposed in Hutchinson and Suo (1992), adapted to the Linear Elastic Brittle Interface Model (LEBIM).

A complete and exhaustive development of the contents included in this section can be found at Mantič et al. (2006). Besides, a basic reference work on interfacial fracture mechanics is Hutchinson and Suo (1992), and an introduction to interfacial crack modelling can be found at Hills et al. (1996).

2.3 The Coupled Criterion of Finite Fracture Mechanics (CCFFM).

LEFM works well for cracked structures and sufficiently large cracks, but Griffith's criterion is not able to predict the crack onset and the propagation for small cracks. However, many engineers assert that the study of the onset crack initiation has not any sense because microcrack and other defects exist within any material system prior to be loaded. In fact, most materials contain microcracks or voids due to their manufacture. However, if these defects are assumed to be present at a small scale, the crack initiation can be studied at a larger scale, for which the material can be modelled like continuum and homogeneous material. The study of the crack initiation in a continuum and homogeneous material can be developed if the microcracks and other defects are small enough to affect the hypothesis of continuity and homogeneity.

García (2014) illustrated this scale effect on the damage. Before loading, the material can have a distribution of defects that are not visible at a certain scale. When the material is loaded the initial defects and other new defects start to grow stably or generate other irreversible processes. This process leads to the appearance of a crack on a higher scale, in which the damage variable was defined.

The Finite fracture mechanics (FFM) is based on this damage mechanims, where the crack is produced instantly with a finite length, after the abruptly coalescence of defects for a critical value of the tension. Therefore, the FFM does not maintain the Griffth hypothesis which to assume that crack growth is infinitesimal. And this is why, it is able to predict the fracture onset with a finite segment of the crack.

Hashin (1996) proposed the term "Finite fracture mechanics" to develop an energy-based criterion which assumes a crack onset of a finite length. However, the term has been also employed since then to refer to the common framework of the method named "Theory of critical distances", which have been proposed throughout the last half-century (e.g. Neuber (1958); Tszeng (1993); Hashin (1996); Taylor et al. (2005) and Cornetti et al. (2006)).

In the framework of the FFM, Leguillon (2002) proposed the coupled criterion of the FFM (CCFFM), which is the base of this thesis. This criterion combines two criteria traditionally used separately in brittle and quasi-brittle materials: the stress criterion and the energy criterion. Since the first one is commonly used to predict failure without stress singularities, and the energy criterion is employed in the

presence of cracks. However, Leguillon postulated that the necessary and sufficient condition for a finite-crack onset is the simultaneous fulfilment of both stress and incremental energy criteria.

Leguillon (2002) presented this coupled criterion with a simple and well known example. Leguillon showed that by using only the energy criterion to predict the failure of a bar of a homogeneous and isotropic material submitted to an increasing applied strain, the critical failure stress decreases while increasing the bar length. This is because the elastic energy stored in the bar is proportional to its length, while the energy dissipated in the formation of the new surface is only proportional to the cross-section of the bar. Therefore, an erroneous deduction would be that for sufficiently long bars the critical failure stress tends to zero. However, Leguillon solves this problem by applying the energy criterion and the stress criterion, he took as the critical failure stress the minimum stress that fulfils both criteria.

This coupled criterion remains within the framework of continuous mechanics as opposed to atomistic models, allowing for much shorter computing times without losing rigour. In addition, the coupled approach also needs less computational time compared to other approaches within the continuous medium (cohesive zone models or damage mechanics).

Leguillon (2002); Taylor et al. (2005); Cornetti et al. (2006); Camanho et al. (2012); Sapora et al. (2015) and Doitrand and Sapora (2020), among others, have demonstrated experimental evidence supporting the hypothesis of Leguillon. Taylor et al. (2005) shows the prediction of the coupled criterion by several experiments with short cracks that cannot be studied by the LEFM. Another classical problem studied using this coupled criterion has been the crack onset at V-notches since the LEFM can not predict the crack onset in this case either (Carpinteri et al., 2008; Sapora et al., 2013, 2014, 2015). However, the coupled criterion can indeed predict this case, as Leguillon (2002) proved.

2.3.1 Stress criterion.

The stress criteria are normally based on phenomenological laws because these criteria depend heavily on the material microstructure and the failure of the material on a smaller scale than the study where the stress criterion is applied. These criteria are defined by a critical stress value of the material $\sigma_{c,ch}$, normally associated with the tensile strength, and applied to a specific combination of the components of the stress tensor, σ_{ij}, at a specific point x.

Under the framework of finite fracture mechanics, the stress criterion must be evaluated before the crack onset, and this criterion must be satisfied at every point x of the new surface ΔS_c originated into the material. Following the formulation of Mantič (2009, 2014) and García (2014), a quite general expression could be written by functional $f(\sigma_{ij}, \Delta S_c)$:

$$f(\sigma_{ij}(x), \Delta S_c) \geq \sigma_{c,ch}, \quad \text{with} \quad x \in \Delta S_c \qquad (2.6)$$

In the present manuscript, the stress criterion have been used in two different ways within the context of the CCFFM:

- Originally, Leguillon (2002) introduced the pointwise stress criterion, where the normal traction at every point x along the future new surface ΔS_{c} is compared with $\sigma_{\text{c,ch}}$.

- Alternatively to the pointwise criterion, Cornetti et al. (2006) proposed to compare $\bar{\sigma}$ with $\sigma_{\text{c,ch}}$, where $\bar{\sigma}$ is the averaged value of σ of all the points into ΔS_{c}.

Both described stress criteria have been applied to several problems by some authors. For example, Cornetti et al. (2012) and l'Armée and Becker (2019) compared the predictions of both criteria and obtained, for both methods, results in agreement with experimental values. Often, the difference between the critical loads predicted by both criteria is so small that the typical dispersion of the experiments is longer than this difference. In this manuscript both methods will be described in the context of the CCFFM applied to LEBIM and their formulations will be developed in Section 3.1.1.

A usual expression for the stress criterion in the context of the CCFFM and introduced by Mantič (2009) is:

$$\frac{\sigma_{\text{nom}}}{\sigma_{\text{c,ch}}} \geq s(x) \stackrel{\text{def}}{=} \frac{1}{f(\sigma_{ij}(x), \Delta S_{\text{c}})}, \tag{2.7}$$

where σ_{nom} is the applied nominal stress which depends on the problem and represents the external loads.

2.3.2   Incremental energy criterion.

The energy criterion of the CCFFM is the same energy balance used by Griffith between the pre- and post-crack states:

$$\Delta\Pi + \Delta E_{\text{k}} + \Delta R = 0, \tag{2.8}$$

where $\Delta\Pi$ is the potential energy variation between the two states, ΔE_{k} is the variation of kinetic energy between the two states and ΔR is the energy dissipated at this abrupt formation of a new crack surface (ΔS_{c}). Following Leguillon (2002), in the development of this thesis the heat exchange will be neglected and the initial state is considered quasistatic. Therefore, $\Delta E_{\text{k}} \geq 0$ can be established. And the energy criterion can be expressed as Leguillon proposed:

$$-\Delta\Pi \geq \Delta R \tag{2.9}$$

This equation indicates that the crack onset and propagation can be produced if the solid release enough elastic energy. Another way of rewriting this energy balance is the one proposed by Mantič (2014). In this case, $\Pi + R$ should keep constant or decrease at a crack onset. Note that the potential elastic energy (Π) is conservative, therefore, it should only depend on the state before and after of the crack formation. Remember that, as explained above, Π depends on the external loads and the geometrical and elastic properties of the solids of the problem.

In order to calculate the released energy, $\Delta\Pi$, Mantič (2014) indicated different ways to do it, and García (2014) explained each one in detail with its advantages and disadvantages:

- The first method is based on the definition of the ERR. If G is integrated over the new generated surface (ΔS_c), the released energy in the fracture process is obtained: $-\Delta\Pi = \int_{\Delta S_c} G$. One of the advantages of this procedure is that many G solutions can be simply integrated. However, due to this procedure depends on crack path, for cases where this path is not a priori known it is not very efficient.

- The second method is a variant of the well-known Virtual Crack Closure Technique (VCCT). VCCT is used under the assumption that the virtual infinitesimal extension of the crack does not significantly influence the elastic solution close to the crack tip. An advantage of this method is that it only depends on the initial and the final state of the crack so it is not necessary to study the path followed by the crack. However, if the displacements of the crack faces are very small, this method lead to some computational errors.

- Maybe, the most general method is to calculate the deformation energy of the system, before and after the crack formation, and to obtain their difference (ΔU). The variation in the work of external forces must also be calculated (ΔW). Since, $\Delta\Pi = \Delta U - \Delta W$, the energy balance of Eq. (2.9) can be directly applied. One of the advantages of this method is that only the beginning and the end of the crack path must be studied. Another advantage is that the information regarding the internal energies of the solids and the work done by the external loads is usually available in most FEM codes.

Another important term in the energy balance is the energy dissipated in the fracture process (ΔR). This concept is based on Griffith (1921, 1924), where he proposed that a certain amount of energy is needed to break the atomic bonds in the fracture of the materials. In Section 2.1, it was already explained that Griffith developed his theory for brittle materials, where this definition of dissipated energy was quite close to the actual fracture mechanism. However, for other type of materials, the processes associated with the energy dissipation during crack growth are more complex and this energy dissipation does not include other irreversible processes in the material failure. A simple way to evaluate the energy dissipated in the new surface ΔS_c, is:

$$\Delta R = G_c \Delta S_c, \qquad (2.10)$$

where G_c is the constant fracture energy dissipated per unit of a new crack area, and it can vary with the fracture mode mixity ψ depending on the type of material. For example, in isotropic and homogeneous materials the onset and propagation of the crack is normally produced in mode I. However, the variations of the $G_c(\psi)$ depends on the irreversible process close to the crack tip, for this reason, the critical energy of the fracture depends strongly on the material and on its micro-structure. This dependency on the fracture mode mixity is under discussion in CCFFM formulations currently, since the definition of ψ is associated with a continuous propagation of the crack, a fact that the FFM does not contemplate (see discussion in García (2014)).

Following Mantič (2009) and García et al. (2014), a general and non-dimensional form for linear elastic materials and proportional loading with nominal stress σ_{nom} of the energy balance (based on 2.9) can be expressed as:

$$\frac{\sigma_{\text{nom}}^2 l_{\text{ch}}^3}{E_{\text{ch}}} \Delta\hat{\Pi}(\Delta S_{\text{c}}) \geq G_{\text{c,ch}} l_{\text{ch}}^2 \Delta\hat{R}(\Delta S_{\text{c}}), \tag{2.11}$$

where l_{ch} and E_{ch} are two characteristic variables of the problem that are associated with the geometry and elastic properties of the problem itself. These variables are used to apply the energy balance in a dimensionless form, due to the rest of the variables, on which the energy balance depends, can be reduced by these two (Mantič, 2009; García et al., 2014). Additionally, $G_{\text{c,ch}}$ is the characteristic critical fracture energy of the problem and $G_{\text{c}}(\psi)$ depend on it.

2.3.3   CCFFM General formulation.

As explained above, in general terms, the coupled criterion of finite fracture mechanics applies the stress criterion and the energy criterion to a specific problem and set the lowest failure stress that satisfies both criteria as the critical one. This stress is called $\sigma_{\text{nom,c}}$ and it is the result of minimizing the σ_{nom} in both criteria. For this reason, both criteria must be expressed with respect to the same fracture characteristic $\sigma_{\text{c,ch}}$, which was taken in the stress criterion associated with the strength. Therefore, if the energy criterion takes the same form as the stress criterion, as introduced by Mantič (2009) and García et al. (2014), it can be expressed as:

$$\frac{\sigma_{\text{nom}}}{\sigma_{\text{c,ch}}} \geq \gamma\sqrt{g(\Delta S_{\text{c}})} \quad \text{with} \quad g(\Delta S_{\text{c}}) = \frac{\Delta\hat{R}(\Delta S_{\text{c}})}{-\Delta\hat{\Pi}(\Delta S_{\text{c}})} \tag{2.12}$$

where $g(\Delta S_{\text{c}})$ represents the ratio of the dimensionless dissipated energy to the dimensionless released energy and γ is a dimensionless brittleness number defined in the context of the CCFFM by Mantič (2009) as:

$$\gamma = \frac{1}{\sigma_{\text{c,ch}}} \sqrt{\frac{G_{\text{c,ch}} E_{\text{ch}}}{l_{\text{ch}}}} \tag{2.13}$$

Mantič (2014) described the dimensionless function $\gamma\sqrt{g(\Delta S_{\text{c}})}$ as a (hyper)surface of dimension n (or curve with $n = 1$) of the incremental energy criterion defined for ΔS_{c}. Where ΔS_{c} is the possible failure surface set by the stress criterion, and n is the set of parameters describing the generation of that new surface ΔS_{c} (e.g. onset point, orientation, path followed, etc). Each n value defines the possible crack paths from its onset to the complete generation of the surfaces.

The formulation of the CCFFM can be written as in Eq. (2.14) by joining the expressions of each criterion.

$$\frac{\sigma_{\text{nom,c}}}{\sigma_{\text{c,ch}}} = \min_{\Delta S_{\text{c}}} \max \left\{ s(\Delta S_{\text{c}}), \gamma\sqrt{g(\Delta S_{\text{c}})} \right\}, \tag{2.14}$$

The dimensional functions $s(\Delta S_{\text{c}})$ and $\gamma\sqrt{g(\Delta S_{\text{c}})}$ are defined in the possible fracture region ΔS_{c} and the minimum nominal load that satisfies both criteria must be determined. It can also be said that the criterion look for the minimum damaged

area ΔS_c that satisfies both criteria. The minimization of this expression refers to the surface of the crack and sets the maximum of the two criteria, i.e. the value that fulfils the criteria and produces a minimum crack surface should be taken.

However, the minimization of this surface is quite complex since the possible paths of the crack are infinite. For this reason, the works applying the coupled criterion assume additional hypotheses about the geometry of the crack on which the minimization is performed, reducing the possible crack paths to a finite and sufficiently low number to obtain analytical or semi-analytical results.

2.4 2D Linear Elastic Brittle Interface Model

Interface conditions ahead of an interface crack front play a critical role when defining a crack growth model. The Linear Elastic-(perfectly) Brittle Interface Model (LEBIM) was proposed and studied by Prandtl (1933); Entov and Salganik (1968); Lenci (2001) and Carpinteri et al. (2009), among many others, to model cracks propagating along a weak surface/interface (which may represent, e.g., an adhesive layer). It is characterized by a continuous spring-distribution with a linear elastic-(perfectly) brittle law, which relates the displacement jump across this surface (material separation, in Mode I) and tractions acting there.

An improved constitutive law including a failure criterion of the LEBIM was introduced by Távara et al. (2010, 2011) and Mantič et al. (2015). This model covers also interfaces fracture due to shear under compression, by extending the range of variation of the interface fracture toughness with the fracture mode mixity, and considering the possibility of frictionless elastic contact at broken portions of the interface. LEBIM can also be considered as a non-smooth limit case of the intrinsic CZM, see Bialas and Mróz (2005); Valoroso and Champaney (2006); Jiménez et al. (2007); Cornetti et al. (2012) and Dimitri et al. (2017). Moreover, Jiménez et al. (2007) and Távara et al. (2019a) showed that in some specimens LEBIM predictions can better fit experimental test results than the predictions obtained by a classical CZM.

Although initially, this interface model represented an adhesive layer of a small thickness $h > 0$, it can characterize debonding mechanisms between two solids of different materials, strictly speaking, there is no additional third material between bonded materials, as may occur in the case of fibre-matrix interface in an actual composite.

In LEBIM the interface is modelled by a continuous distribution of springs with a linear elastic behaviour up to its breakage (Távara et al., 2011, 2010; Mantič et al., 2015). Although 3D LEBIM is giving good results (Távara et al., 2019a) in this thesis a 2D LEBIM in plane strain is used. Thus, the normal and shear tractions at an undamaged interface point x, $\sigma(x)$ and $\tau(x)$, respectively, are proportional to the normal and tangential relative displacements at this point, $\delta_n(x)$ and $\delta_t(x)$,

$$\sigma(x) = k_n \delta_n(x), \quad \text{and} \quad \tau(x) = k_t \delta_t(x), \tag{2.15}$$

with k_n and k_t giving the normal and tangential stiffness of the spring located at x.

It can be shown that the ERR $G(x)$ is given by the energy (per unit area) stored in the unbroken spring at x and not necessarily located at the crack tip and at

a infinitesimal interface segment (see Mantič et al. (2015) and further references therein), leading to

$$G(x) = G_I(x) + G_{II}(x), \tag{2.16}$$

where,

$$G_I(x) = \frac{\langle\sigma(x)\rangle_+ \langle\delta_n(x)\rangle_+}{2} = \frac{\langle\sigma(x)\rangle_+^2}{2k_n} = \frac{k_n\langle\delta_n(x)\rangle_+^2}{2} \tag{2.17a}$$

$$G_{II}(x) = \frac{\tau(x)\delta_t(x)}{2} = \frac{\tau^2(x)}{2k_t} = \frac{k_t\delta_t^2(x)}{2}, \tag{2.17b}$$

$\langle\cdot\rangle_+ = \frac{(\cdot)+|\cdot|}{2}$ denoting the positive part of a number.

The fracture mode mixity is characterized by the energy based angle defined as $\tan^2\psi_G = G_{II}(x)/G_I(x)$ for $\sigma(x) > 0$. Nevertheless, a generalization of this angle covering any value of σ is necessary. In the present thesis the angle ψ defined as,

$$\tan\psi = \sqrt{\kappa^{-1}}\tan\psi_\sigma = \sqrt{\kappa}\tan\psi_u, \quad \text{for} \quad -\pi \le \psi, \psi_\sigma, \psi_u \le \pi, \tag{2.18}$$

is used (cf. Mantič et al. (2015)), where

$$\kappa = \frac{k_t}{k_n}, \quad \tan\psi_\sigma = \frac{\tau}{\sigma} \quad \text{and} \quad \tan\psi_u = \frac{\delta_t}{\delta_n}. \tag{2.19}$$

The interface failure criterion adopted in LEBIM is defined in terms of the ERR, G and the interface fracture energy G_c (fracture toughness). Therefore, an interface point breaks when the ERR, $G(x)$ (defined in (2.16)) reaches the fracture energy, $G_c(\psi(x))$, which depends on the fracture mode mixity of the point x.

$$G_c(\psi(x)) = G_{Ic}(\psi(x)) + G_{IIc}(\psi(x)), \tag{2.20}$$

where, in view of (2.16),

$$G_{Ic}(\psi(x)) = \frac{\langle\sigma_c(\psi(x))\rangle_+ \langle\delta_{nc}(\psi(x))\rangle_+}{2} = \frac{\langle\sigma_c(\psi)\rangle_+^2}{2k_n}, \tag{2.21a}$$

$$G_{IIc}(\psi(x)) = \frac{\tau_c(\psi(x))\delta_{tc}(\psi(x))}{2} = \frac{\tau_c^2(\psi(x))}{2k_t}, \tag{2.21b}$$

where $\sigma_c(\psi(x))$ and $\tau_c(\psi(x))$ are the maximum allowed traction components at the point x, and $\delta_{nc}(\psi(x))$ and $\delta_{tc}(\psi(x))$ the corresponding maximum relative displacements at the same point, as Figure 2.2 represents. The fracture toughness in pure mode I, i.e. for $\psi(x) = 0$, is denoted as $G_c(0) = G_{Ic}(0) = \bar{G}_{Ic}$, and similarly in mode II for $\psi = \frac{\pi}{2}$, $G_c\left(\frac{\pi}{2}\right) = G_{IIc}\left(\frac{\pi}{2}\right) = \bar{G}_{IIc}$. Then, defining $\bar{\sigma}_c = \sigma_c(0)$ and $\bar{\tau}_c = \tau_c\left(\frac{\pi}{2}\right)$, and dimensionless functions $\hat{\sigma}_c(\psi(x))$ and $\hat{\tau}_c(\psi(x))$, with $\hat{\sigma}_c(0) = 1$, $\hat{\sigma}_c\left(\frac{\pi}{2}\right) = 0$ and $\hat{\tau}_c(0) = 0$, by

$$\sigma_c(\psi(x)) = \bar{\sigma}_c\hat{\sigma}_c(\psi(x)) \quad \text{and} \quad \tau_c(\psi(x)) = \bar{\sigma}_c\hat{\tau}_c(\psi(x)). \tag{2.22}$$

The pure modes I and II fracture toughness are expressed as

$$\bar{G}_{Ic} = \frac{\bar{\sigma}_c^2}{2k_n}, \quad \text{and} \quad \bar{G}_{IIc} = \frac{\bar{\tau}_c^2}{2k_t}. \tag{2.23}$$
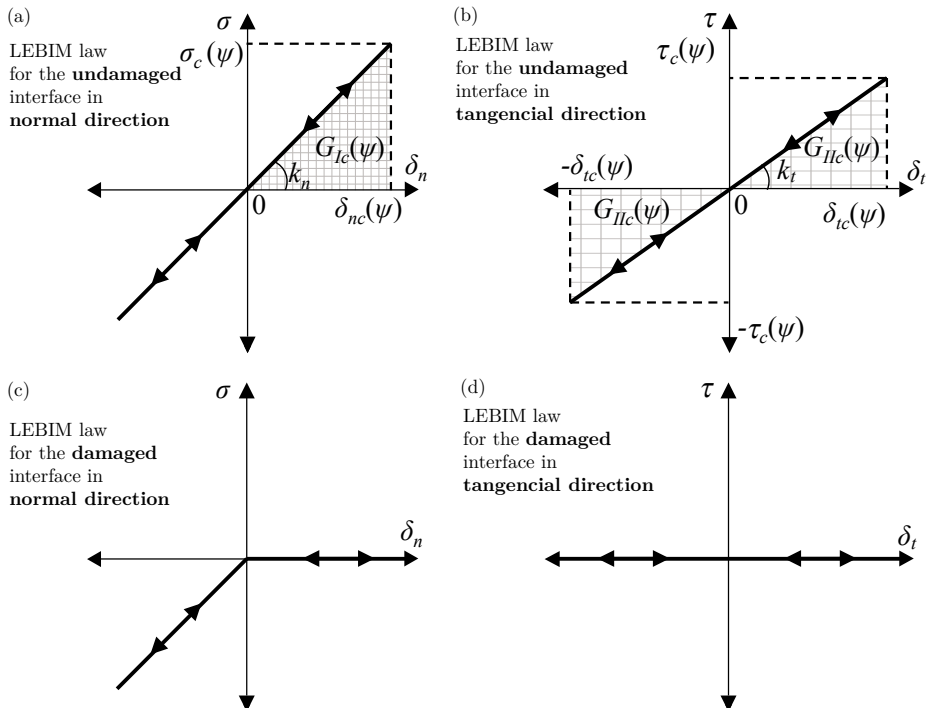
Figure 2.2: LEBIM constitutive law.

Similarly, a dimensionless function for critical energy $\hat{G}_c(\psi(x))$, verifying $\hat{G}_c(0) = 1$, can be defined by

$$G_c(\psi(x)) = \bar{G}_{\mathrm{Ic}}\hat{G}_c(\psi(x)). \tag{2.24}$$

In Mantič et al. (2015), the relation between the dimensionless functions $\hat{\sigma}_c(\psi)$ and $\hat{\tau}_c(\psi)$, and the critical energy $\hat{G}_c(\psi(x))$ was established as:

$$\hat{\sigma}_c(\psi(x)) = \sqrt{\hat{G}_c(\psi(x))} \cdot \left\{ \begin{array}{ll} \cos\psi(x), & |\psi(x)| \leq \frac{\pi}{2}, \\ -|\cot\psi(x)|, & |\psi(x)| \geq \frac{\pi}{2}, \end{array} \right. \tag{2.25a}$$

$$\hat{\tau}_c(\psi(x)) = \sqrt{\kappa}\sqrt{\hat{G}_c(\psi(x))} \cdot \left\{ \begin{array}{ll} \sin\psi(x), & |\psi(x)| \leq \frac{\pi}{2}, \\ \mathrm{sign}\,\psi(x), & |\psi(x)| \geq \frac{\pi}{2}, \end{array} \right. \tag{2.25b}$$

It is important to note that Mantič et al. (2015) evaluated the ERR in LEBIM by means of the VCCT, and show that the ERR of a small portion of the linear elastic brittle interface is determined by the tractions at the point where the breakage initiates and just at the moment before the breakage occurs (Lenci, 2001). For this reason, LEBIM can be applied using an energy failure criterion, but it can also be defined in terms of tractions or even relative displacements at the interface point under study.

Note that in Figure 2.2, in the normal law once a portion of interface is broken, a negative normal displacement, $\delta_n < 0$, can be allowed leading to an interface overlapping due to the penalty contact condition. It is possible because an elastic frictionless

contact is considered there, and it is based on the idea that once the assumed interface layer is broken some portions of this layer remains on the interface surfaces. Thus, when these surfaces enter in contact, it seems reasonable that the portions of the layer could compress with the same stiffness in normal direction as it had before breaking.

2.4.1 Interface failure criteria

Two different failure criteria are used in the present thesis according to the revision of several failure criteria applied in LEBIM presented in Mantič et al. (2015). Both criteria were originally physically motivated, and fitted well results of several experimental campaigns in the past. They are written in a suitable form to match the formulation introduced above. The dimensionless function $\hat{G}_c(\psi(x))$, which in the present formulation governs, according to (2.25), both the energy and stress based criteria, is defined for each failure criterion.

2.4.1.1 Hutchinson and Suo criterion

This criterion, originally proposed by Hutchinson and Suo (1992) for interface cracks at perfect interfaces, and referred hereinafter as HS-criterion, is adapted here to define the fracture toughness in mixed mode as (cf. Mantič et al. (2015)):

$$\hat{G}_c(\psi(x)) = 1 + \tan^2(1 - \lambda_{\mathrm{HS}})\psi(x), \tag{2.26}$$
$$\text{with}\quad |\psi(x)| < \bar{\psi}_a(\lambda_{\mathrm{HS}}), \quad 0 \le \lambda_{\mathrm{HS}} \le 1,$$

where

$$\bar{\psi}_a(\lambda_{\mathrm{HS}}) = \min\{\psi_a(\lambda_{\mathrm{HS}}), \pi\} \quad \text{and}\quad \psi_a(\lambda_{\mathrm{HS}}) = \frac{\pi}{2(1 - \lambda_{\mathrm{HS}})}, \tag{2.27}$$

$\bar{\psi}_a$ is the angle of the failure curve asymptotes, λ_{HS} is the fracture mode-sensitivity parameter of Hutchinson and Suo, $0.2 \le \lambda_{\mathrm{HS}} \le 0.3$ is a typical range for interfaces with moderately strong fracture mode dependence.

2.4.1.2 Quadratic criterion

The quadratic criterion, originally proposed as a stress criterion (see Brewer and Lagace (1988) and Hashin (1980)) is represented here by the implicit equation for the failure curve in the plane of dimensionless tractions:

$$\mathrm{sign}(\hat{\sigma}_c(\psi(x)))\hat{\sigma}_c^2(\psi(x)) + \frac{\bar{\sigma}_c^2}{\bar{\tau}_c^2}\,\hat{\tau}_c^2(\psi(x)) = 1, \tag{2.28}$$

where the fracture mode sensitivity is defined by the ratio $\frac{\bar{\sigma}_c}{\bar{\tau}_c}$. Then, the dimensionless fracture toughness function can be expressed as, cf. Muñoz Reja et al. (2016),

$$\hat{G}_c(\psi(x)) = \frac{\langle \cos\psi(x)\rangle_+^2 + \sin^2\psi(x)}{\mathrm{sign}(\cos\psi(x))\cos^2\psi(x) + \frac{\bar{\sigma}_c^2}{\bar{\tau}_c^2}\,\kappa\,\sin^2\psi(x)}, \tag{2.29}$$

with $|\psi| < \psi_a$, where $\psi_a = \arctan(\bar{\sigma}_c, \bar{\tau}_c\,\kappa)$ is the angle of the failure curve asymptotes.

2.4.2 LEBIM implementation in BEM and FEM.

The 2D LEBIM was successfully implemented in a Boundary Elements Method (BEM) code and in a Finite Element Method (FEM) code by Távara et al. (2010) and Távara et al. (2018), respectively.

Távara et al. (2010) and Távara et al. (2011) implement LEBIM in a 2D BEM code (París and Cañas, 1997; Graciani et al., 2005), whose original version allowed to model isotropic axisymmetric and anisotropic plane problems, with multiple solids perfectly bonded or with contact zones between them. Távara incorporated into this code the possibility of defining weak interfaces between elastic solids since the BEM is a suitable tool for modelling a crack that grows along the weak interface. This is due to the non-linearity introduced is associated only with the boundary of the interface. This code has been used in this thesis to incorporate the CCFFM with one of the implementations developed in the following chapter. It should also be noted that, in this code, the conditions of balance and compatibility along the contact areas are imposed in a weak form, allowing non-conforming discretizations.

Also Távara et al. (2018) and Távara et al. (2019) implement the LEBIM in the commercial code ABAQUS based on FEM. For this implementation, a user subroutine UMAT was used. The interface model developed is based on the continuum-based approach, assuming an interface layer with a finite (small) thickness, which is denoted by h. Therefore, the interface is meshed like the rest of the solids and these elements transmit the stress from one solid to another solid assuming a spring behaviour. Additionally, when one of these elements is damaged it is not capable of transmitting tension but it can still transmit compression if it is in contact with another solid. This behaviour is obtained by manipulating the constitutive operator of each element of the interface (see Távara et al. (2018) for a more exhaustive description).

CHAPTER 3

CCFFM applied to LEBIM

The main aim of this chapter is to present a new way of solving problems of crack onset and propagation along interfaces by a combination of the Coupled Criterion of Finite Fracture Mechanics (CCFFM) (Leguillon, 2002; Cornetti et al., 2006; Mantič, 2009) described in Section 2.3 with the Linear Elastic Brittle Interface Model (LEBIM) (Távara et al., 2010, 2011; Mantič et al., 2015) described in Section 2.4

The computational implementations and engineering applications of non-classical models of Fracture Mechanics, such as Cohesive Zone Models (CZMs) and LEBIM (for a comparison, see Dimitri et al. (2017); Távara et al. (2019) and Cornetti et al. (2019), have increased considerably especially in the last decade. This fact justifies that this topic is of great interest regarding the crack onset and propagation predictions.

Traditionally, LEBIM has been applied to characterize interfaces with a relatively low stiffness. This is because the fracture toughness and critical tractions of an interface modelled by LEBIM are coupled by an equation involving the interface stiffness. However, such an interface model may be far from reality, because thin adhesive layers are sometimes characterized by a large stiffness. Due to this fact, the CCFFM approach has been incorporated into LEBIM (Cornetti et al., 2012; Muñoz Reja et al., 2016, 2018, 2020b,a). Using this new approach, it was possible to uncouple the fracture toughness, critical traction and stiffness of an adhesive interface.

As Section 2.3 describes, the present coupled criterion of FFM is used to predict the crack onset and/or growth by finite increments of its length along a linear-elastic-interface. It is based on the interface strength and fracture toughness criteria, each of them representing a necessary but not sufficient condition for such a crack onset and/or growth. Following the theoretical concepts explained at Section 2.3, this criterion can be formulated by two different ways:

- CCFFM applied to LEBIM based on stress and energy criteria curves, where the energy criterion is evaluated by the integral of the energy release rate.

- CCFFM applied to LEBIM based on Principle of Minimum Total Energy subjected to a Stress Condition (PMTE-SC), where the energy criterion is evaluated by the potential energy before and after crack onset.

Each of these ways has a different formulation and implementation in the used numerical codes BEM and FEM based, that will be developed in the following sections of this chapter.

3.1 General framework of the CCFFM applied to 2D LEBIM

As described previously, the present coupled criterion of FFM is based on the interface strength and fracture toughness criteria, each of them representing a necessary but not sufficient condition for such a crack onset and/or growth according to CCFFM exposed in 2.3.

3.1.1 Stress based (strength) criterion

In the context of the CCFFM (2.3.1), the stress criterion is evaluated before the crack onset at the entire surface ΔS_c where the crack will initiate. However, as the coupled criterion is applied to interfaces, the stress criterion is imposed at every undamaged point x along every interface of the problem. The aim is to obtain one or more finite segments of the crack from $x = 0$ to $x = \Delta a$ satisfying the stress criterion. This condition is usually applied in one of the two following ways:

- As a pointwise criterion (Leguillon, 2002):

$$\min_{0 \leq x \leq \Delta a} \frac{t(x)}{t_c(\psi(x))} \geq 1 \tag{3.1}$$

- As an average criterion (Cornetti et al., 2006):

$$\frac{1}{\Delta a} \int_0^{\Delta a} \frac{t(x)}{t_c(\psi(x))} \, \mathrm{d}x \geq 1 \tag{3.2}$$

where the traction vector modulus at an undamaged interface point x and its critical value, respectively, are defined as

$$t(x) = \sqrt{\sigma^2(x) + \tau^2(x)}, \tag{3.3a}$$
$$t_c(\psi(x)) = \sqrt{\sigma_c^2(\psi(x)) + \tau_c^2(\psi(x))}. \tag{3.3b}$$

$\sigma(x)$ and $\tau(x)$ are proportional to the normal and tangential relative displacements at the point x and are defined in Eq. (2.15). Let the critical normal and shear stress components for pure mode I and II, respectively, be defined as $\sigma_c(0) = \bar{\sigma}_\mathrm{c} > 0$ and $\tau_c\left(\frac{\pi}{2}\right) = \bar{\tau}_\mathrm{c} > 0$. Then, the critical normal and shear stress, $\sigma_c(\psi)$ and $\tau_c(\psi)$, can be defined by some dimensionless functions in the same way as the original LEBIM (2.22), i.e. similarly as in (2.22):

$$\sigma_c(\psi) = \sigma_{\mathrm{c,ch}} \hat{\sigma}_c(\psi) \quad \text{and} \quad \tau_c(\psi) = \sigma_{\mathrm{c,ch}} \hat{\tau}_c(\psi), \tag{3.4}$$

Note that $\hat{\sigma}_c(\psi)$ is the dimensionless expression associated to the tensile strength of the interface. It should be noticed that sometimes it is interesting to obtain a

dimensionless function of the critical stress with respect to the shear strength of the interface studied. For that reason, as in the Section 2.3.1, it seems reasonable to denominate this characteristic variable of the material in general terms as $\sigma_{\mathrm{c,ch}}$, as it is shown in Eq. (3.4).

Following the dimensionless and general formulation introduced in Mantič (2014) (2.3.1), the stress criterion can be written in general form, as:

Pointwise criterion: $\dfrac{\sigma_{\mathrm{nom}}}{\sigma_{\mathrm{c,ch}}} \geq s(x) = \dfrac{\hat{t}_c(\psi(x))}{\hat{t}(x)} \quad \forall\, x \in [0, \Delta a],$ (3.5a)

Average criterion: $\dfrac{\sigma_{\mathrm{nom}}}{\sigma_{\mathrm{c,ch}}} \geq s(x) = \dfrac{1}{\frac{1}{\Delta a}\int_0^{\Delta a} \frac{\hat{t}(x)}{\hat{t}_c(\psi(x))}\,\mathrm{d}x} \quad \forall\, x \in [0, \Delta a],$ (3.5b)

with $\quad \hat{t}(x) = \dfrac{t(x)}{\sigma_{\mathrm{nom}}} \quad$ and $\quad \hat{t}_c(\psi(x)) = \dfrac{t_c(\psi(x))}{\sigma_{\mathrm{c,ch}}},$

where σ_{nom} is the applied nominal stress which depends on the problem; $\sigma_{\mathrm{c,ch}}$ is a characteristic interface strength parameter previously defined. Note that, $t_c(\psi(x))$ can be expressed by considering several stress criteria like in LEBIM (see Section 2.4.1). Specifically, in this thesis a stress criterion based on the Hutchinson and Suo (1992) phenomenological law is used, see Mantič et al. (2015); Muñoz Reja et al. (2016) and Muñoz Reja et al. (2020b) for further details.

3.1.2 Energy based (fracture toughness) criterion

To initiate or propagate an interface crack by a finite increment of its length $\Delta a > 0$ the following energy balance condition must be fulfilled:

$$-\Delta\Pi(\Delta a) \geq \Delta R(\Delta a),$$ (3.6)

where the left and right hand side are defined as the decrement of the potential energy $(-\Delta\Pi)$ and the dissipated energy (ΔR) at this (typically instantaneous) finite crack-advance Δa, respectively. As outlined in the Section 2.9, the energy released in the fracture process can be obtained with different methods. Two methods are used in this thesis:

- Calculating the integral of the ERR over the surface generated by the broken interface, Δa;

- Calculating the potential energy of the system, before and after the failure of the interface. If the increment of potential energy and work is obtained, the energy balance of Eq. (3.6) can be directly applied.

The use of each approach to the coupled criterion leads to a different implementation of the CCFFM+LEBIM: CCFFM+LEBIM by the curve method or by the Principle of Minimum Total Energy subjected to a Stress Condition (PMTE-SC). In the following sections, both implementations will be discussed.

The energy condition can also be written in terms of dimensionless functions by denoting a characteristic fracture energy of the interface $G_{\mathrm{c,ch}}$ and a characteristic

stiffness of the interface k_{ch}.

$$\frac{\sigma_{\text{nom}}^2}{2k_{\text{ch}}}\Delta\hat{\Pi}(\Delta a) \geq G_{\text{c,ch}}\Delta\hat{R}(\Delta a) \tag{3.7}$$

Note that Eq. (3.7) is similar to that proposed by Mantič (2009) and García et al. (2014) at Eq. (2.11). However, the most notable differences between them are: the length of the broken interface Δa instead of the new surface generated in the solid, and the characteristic interface stiffness k_{ch} instead of the characteristic elastic property of the problem. These differences arise due to the problems under study with this new method are 2D interface problems. For this reason, the term $\frac{E_{\text{ch}}}{l_{\text{ch}}}$ in Eq. (2.11) could be compared with the k_{ch}, since the interface stiffness is always defined by an interface elastic property divided by the its thickness (Távara et al., 2008).

The energy dissipated in the debonding process, $\hat{R}(\Delta a)$, depends on the fracture mode mixity $\psi(\xi)$ associated to every point of the finite segment of the crack, Δa. However, there are two conceptually different ways to obtain the fracture mode mixity used in literature:

- $\psi(\xi) = \psi_1(x)$ for $x = \xi$, defined by the stress state at each point x of the potential crack surface before the crack onset, as García and Leguillon (2012) and Leguillon and Murer (2012) proposed.

- $\psi(\xi) = \psi_2(a)$ for $a = \xi$, defined by the ratio of ERR components ($G_I(a)$ and $G_{II}(a)$) of a virtual crack growing between the initial configuration and the finite crack produced by the crack onset, as Mantič (2009) proposed.

Although the fracture mode mixity is usually evaluated just ahead of the crack tip supposing a quasistatic crack growth (second option), it may present difficulties for interface cracks between dissimilar materials due to the oscillatory character of crack tip fields, as highlighted in Mantič (2009). For this reason, the alternative is based on employing the stress field along the potential crack path prior to the crack onset (first option). Furthermore, the second option could be unreachable for CCFFM applied to LEBIM based on Principle of Minimum Total Energy subjected to a Stress Condition, since the intermediate cases between the onset and the end of the crack are not analysed. Also, this approach is consistent with the hypothesis of abrupt crack onset as it does not need an assumption of quasistatic crack growth.

3.1.3   General formulation of the CCFFM applied to LEBIM

Following the previous formulation of the CCFFM at Eq. (2.11), the dimensionless function $g(\Delta a)$ can be defined as, see also Mantič (2009):

$$g(\Delta a) = \frac{\Delta\hat{R}(\Delta a)}{-\Delta\hat{\Pi}(\Delta a)} \tag{3.8}$$

Thus, following Cornetti et al. (2012), the parameter μ can be defined as:

$$\mu = \frac{2G_{\text{c,ch}}\,k_{\text{ch}}}{\sigma_{\text{c,ch}}{}^2}, \tag{3.9}$$

and the energy criterion can be rewritten as:

$$\frac{\sigma_{\text{nom}}}{\sigma_{\text{c,ch}}} \geq \sqrt{\mu\, g(\Delta a)} \tag{3.10}$$

It should be noted that the fundamental difference between this dimensionless expression for CCFFM+LEBIM and that proposed by Mantič (2009) and García et al. (2014) at Eq. (2.12), are the dimensionless brittleness number γ and the parameter μ. Both terms represent the fracture fragility of the problem under study. However, due to the method presented in this thesis considers the interface failure between two solids, the parameter μ is associated with the interface fragility while γ is associated with the fragility of all the materials involved in the problem (Mantič, 2009). The relationship between γ and μ can be obtained if, in Eq. (2.13), E_{ch} and l_{ch} are substituted by k_{ch}:

$$\gamma = \frac{1}{\sigma_{\text{c,ch}}} \sqrt{G_{\text{c,ch}} k_{\text{ch}}} \quad \text{and} \quad \mu = \frac{2 G_{\text{c,ch}}\, k_{\text{ch}}}{\sigma_{\text{c,ch}}^2}$$

$$\text{then} \quad \mu = 2\gamma^2 \tag{3.11}$$

The possible dimensionless parameters which characterizes the interface brittleness in pure mode I and II can be expressed as:

$$\mu_I = \frac{2 k_n \bar{G}_{\text{Ic}}}{\bar{\sigma}_{\text{c}}^2} \quad \text{and} \quad \mu_{II} = \frac{2 k_t \bar{G}_{\text{IIc}}}{\bar{\tau}_{\text{c}}^2}. \tag{3.12}$$
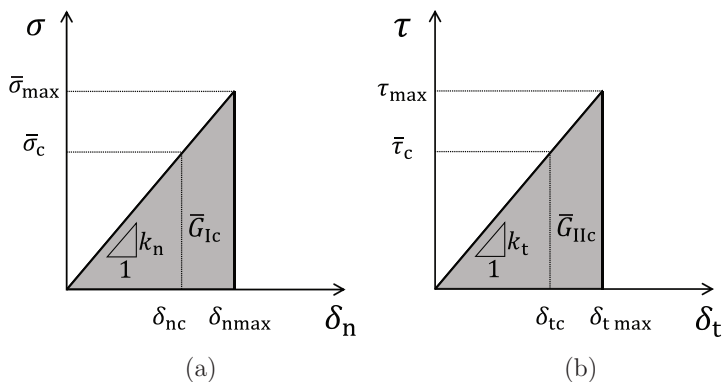
Figure 3.1: CCFFM+LEBIM constitutive law in pure fracture (a)mode I and (b)mode II.

Following the original LEBIM, in Fig. 3.1 the constitutive law for CCFFM applied to LEBIM in mode I and mode II are represented. These figures show that that μ can also be defined, in general term, as: $\mu = \sigma_{\text{max,ch}}^2 / \sigma_{\text{c,ch}}^2$, where $\sigma_{\text{max,ch}}$ and $\sigma_{\text{c,ch}}$, are associated to the energy and stress based criterion, respectively. Thus, for $\mu = 1$ the present model becomes equivalent to the original LEBIM. When μ value increases the interface becomes stiffer, and for $\mu \to \infty$ the perfect interface (with vanishing relative displacements along undamaged parts) is recovered.

As can be seen from the above the fracture toughness, strength and stiffness of the interface, characterized herein by the values of $G_{c,ch}$, $\sigma_{c,ch}$ and k_{ch}, are independent in the present FFM+LEBIM approach. Recall that in the original LEBIM, these interface parameters were related by the equations $\bar{G}_{Ic} = \bar{\sigma}_c^2/2k_n$ and $\bar{G}_{IIc} = \bar{\tau}_c^2/2k_t$ ($G_{c,ch} = \sigma_{c,ch}^2/2k_{ch}$, in its general form).

Unlike perfect interfaces, where stress and energy based failure criteria are of a different nature, here they are closely linked according to the relation between tractions and the ERR associated to a point at a linear elastic interface. Hence, for the sake of simplicity of the present coupled criterion formulation, both the energy and stress conditions will be based on the same particular failure criterion giving the shape to the dimensionless functions defined above in 2.25a and 2.25b. Therefore, in this whole work:

$$\hat{\sigma}_{max}(\psi) = \hat{\sigma}_c(\psi) \quad \text{and} \quad \hat{\tau}_{max}(\psi) = \hat{\tau}_c(\psi) \tag{3.13}$$

A consequence of this choice is that the failure curves of the stress and energy criterion in the (σ, τ) plane are given by scaled curves. Moreover typically the predictions by the FFM+LEBIM will be governed either by both criteria or by the energy criterion only, as will be seen later on.

The interface failure envelopes are presented in the plane of the dimensionless interface tractions in Fig. 3.2, for both HS and quadratic criteria defined above, having the same ratio $\bar{\tau}_c/\bar{\sigma}_c$. The relations between the maximum and critical normal and shear stress can be observed, and also how these relations vary with parameter μ (3.12). It is noticeable that the curve associated to the stress based criterion does not vary with μ, while the curves associated to the energy based criterion scale with the value of μ. According to the parameterized expressions in (2.25), a failure under interface compressions may occur. In such cases an interface crack may appear or propagate in presence of high values of shear stresses. It is also interesting to see in Fig. 3.2, that the failure curves in the compressive zone tends to a constant slope defined by the asymptote angle ψ_a in each criterion.
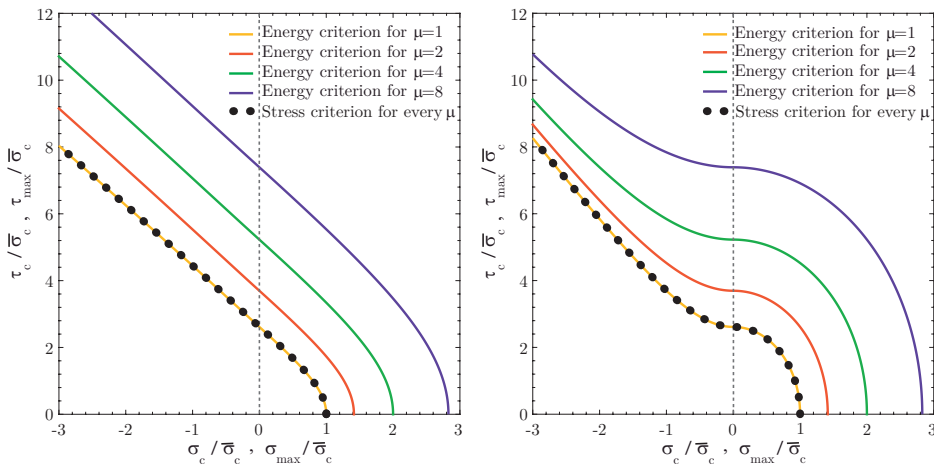
Figure 3.2: Maximum and critical normal and shear stress given by (a) HS-criterion and (b) quadratic criterion.

Fig. 3.3 presents plots of the corresponding dimensionless fracture toughness functions $\hat{G}_c(\psi)$ for both HS and quadratic criteria. Although there is some similarity in their overall tendencies, $\hat{G}_c(\psi)$ for HS-criterion is a convex function whereas $\hat{G}_c(\psi)$ for the quadratic criterion has a plateau for ψ close to $\frac{\pi}{2}$ where tension switch to compression.
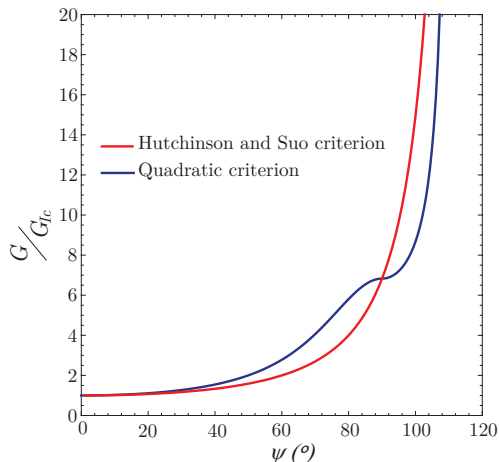
Figure 3.3: Dimensionless fracture toughness functions $\hat{G}_c(\psi) = \frac{G_c(\psi)}{\hat{G}_{Ic}}$ for both HS and quadratic criteria.

At last, both criteria in Eqs. (3.5) and (3.10) are joined to express the new method of the CCFFM applied to LEBIM as:

$$\frac{\sigma_{\mathrm{nom,c}}}{\sigma_{\mathrm{c,ch}}} = \min_{\Delta a} \max \left\{ s(\Delta a), \sqrt{\mu\, g(\Delta a)} \right\}, \qquad (3.14)$$

where $\sigma_{\mathrm{nom,c}}$ is the minimum load that satisfies both criteria and produces a crack with length $a_{\mathrm{crit}} = \Delta a$. $G_{\mathrm{c,ch}}$, $\sigma_{\mathrm{c,ch}}$ and k_{ch} are usually chosen according to the predominant fracture mode of the studied problem in order to obtain a better understanding of the results.

Note that, for $\Delta a \rightarrow 0$ the functions $s(\Delta a)$ and $g(\Delta a)$ represent the original LEBIM if the same particular failure criterion to the dimensionless functions of the Eq. (3.13) is used. It is due on one hand to the equivalence between the ERR and the tractions, and on the other hand to the equivalence between the fracture energy and critical tractions, at a particular unbroken interface-point, as Mantič et al. (2015) showed by Eq. (2.17) and Eqs. (2.21,2.25), respectively. This equivalence implies that for $\Delta a \rightarrow 0$ and $\mu = 1$ the CCFFM+LEBIM reverts into the original LEBIM, due to the characterization of the interface failure (represented by $\mu = 1$) and by the infinitesimal propagation of the LEBIM ($\Delta a \rightarrow 0$). These two features of the original LEBIM highlight the two main reasons for the application of the CCFFM to the LEBIM:

- On one hand, it is possible to uncouple the fracture toughness, critical traction and stiffness of an adhesive interface with $\mu > 1$.

- On other hand, the LEBIM is released from the imposition of an infinitesimal propagation of the failure, because CCFFM+LEBIM is able to predict the fracture onset with a finite segment of the crack Δa at a given moment. In this way, the abrupt failure of the interface due to adhesive defects can be modelled.

Following this same idea, it can be concluded that $s(\Delta a \to 0) = \sqrt{g(\Delta a \to 0)}$. And it can also be said that for $\mu > 1$, $s(\Delta a \to 0) < \sqrt{\mu \, g(\Delta a \to 0)}$. This means that in cases where the interface failure propagation is infinitesimal, this model of CCFFM+LEBIM refers to the energy criterion only. This statement is further developed in the following section where the curves $s(\Delta a)$ and $\sqrt{\mu \, g(\Delta a)}$ are studied. Therefore, in any case where $\sqrt{\mu \, g(\Delta a)}$ keeps a positive growth with respect to Δa (i.e. $\frac{\delta \sqrt{\mu \, g(\Delta a)}}{\delta \Delta a} > 0$) the CCFFM+LEBIM will be defined by the energy criterion only and the interface failure propagation would be infinitesimal.

3.2   CCFFM applied to LEBIM based on the stress and energy criteria curves.

The approach of the CCFFM applied to LEBIM based on the stress and energy criteria curves is the most direct method based on the formulation presented in the previous section. Because it is based on the study of the behaviour of the functions $s(\Delta a)$ and $\sqrt{\mu \, g(\Delta a)}$, defined in Eqs. (3.5) and (3.8) respectively. This approach is very useful for the comprehension of the CCFFM applied to LEBIM in simple cases of interface damage. However, it is not the most versatile method for its application in problems including multiple interface failures or with unknown damage path behaviour. This is due to a fundamental characteristic of this approach is that the energy criterion must be evaluated in intermediate states produced between the initial and final failure length, Δa.

The stress criterion directly uses the definition of the function $s(x)$ in Eq. (3.5), which is continuously evaluated for an interval of x from crack onset x_{o}, to the finite segment of the crack Δa. Even if $s(x)$ is defined along the possible crack path, the evaluation of any stress criteria should always be done before the propagation of the crack, i.e. including only undamaged points along this finite segment. According to this approach, the interface crack onset location corresponds to the undamaged point of maximum stress. Note that, this statement is based on the above reasoning, since in the crack onset location x_{o}, where $(\Delta a \to 0)$, the stress criterion and the energetic criterion must coincide. However, from the general point of view of the coupled criterion in Eq. (3.14), the result of $a_{\mathrm{crit}} = \Delta a$ may predict a different crack onset location than x_{o}. Nevertheless, exploring around the point of maximum stress of the problem seems appropriate. Also, it should be noted that this approach is normally used to solve cases where the damage onset location is known, with one or two possible crack paths, i.e. $n = 1$ or $n = 2$ (see Section 2.3.3).

Based on the previous description, the first step to apply this method is to evaluate the stress criterion for the whole undamaged interface of the problem and to determine the position of x_{o} using the minimum value of the curve $s(x)$. Once the crack onset location is defined, the propagation of the interface crack is studied, starting from

this point only. This means that when the failure starts at x_o, this method of curves cannot explore beyond x_o, even if the stress criterion was also fulfilled in another zone of the interface.

After the evaluation of the stress criterion, the energy criterion must be satisfied. Therefore, to initiate or propagate an interface crack by a finite increment of its length $\Delta a > 0$ the following energy balance condition must be fulfilled

$$ -\Delta\Pi(\Delta a) = \int_0^{\Delta a} G(a)\, \mathrm{d}a \geq \int_0^{\Delta a} G_c(\psi(\xi))\, \mathrm{d}a \simeq \Delta R(\Delta a), \qquad (3.15) $$

where the left and right hand side, respectively, represent the energy released (the decrement of the potential energy $-\Delta\Pi$) and an estimation of the required (dissipated) energy (ΔR) at this (typically instantaneous) finite crack-advance.

The ERR $G(a)$, defined by (2.16), is associated to a crack tip moving from the position $a = 0_+$ to $a = \Delta a$ (Lenci, 2001; Carpinteri et al., 2009) as defined in (3.16); although strictly speaking, in the case of a crack onset the ERR $G(a = 0)$ is associated to an undamaged interface point at the position $a = 0$ (Mantič et al., 2015). This observation may be useful in the numerical evaluation of the integral of $G(a)$.

$$ G(a) = G_I(a) + G_{II}(a) = \frac{\langle\sigma(a)\rangle_+\langle\delta_n(a)\rangle_+}{2} + \frac{\tau(a)\delta_t(a)}{2} = \frac{\langle\sigma(a)\rangle_+^2}{2k_n} + \frac{\tau^2(a)}{2k_t}, \ (3.16) $$

As described in Section 3.1.2, the estimation of the dissipated energy ΔR under fracture mixed-mode is currently under discussion in the literature on FFM and several approaches have recently been proposed (Mantič, 2009; Carraro and Quaresimin, 2014; García et al., 2015; Carrere et al., 2015). In the present work, $G_c(\psi(\xi))$ defines the fracture energy (fracture toughness) required to break the spring at the crack tip moving from the position $\xi = 0_+$ to $\xi = \Delta a$. The definition of ξ depends on the path chosen for the calculation of the fracture mode mixity, as in Section 3.1.2, where $\psi = \psi_1$ and $\xi = x$, or $\psi = \psi_2$ and $\xi = a$. Specifically, in this approach based on the curves, the evaluation of $\psi(\xi)$ in both ways are possible. Also, in the case of a crack onset, $G_c(\psi(\xi = 0))$, strictly speaking, is associated to an unbroken spring at $a = 0$. A generalization of the formulation proposed for pure fracture modes to a general fracture mixed-mode leads to the following expressions:

$$ G_c(\psi(a)) = G_{Ic}(\psi(a)) + G_{IIc}(\psi(a)), \qquad (3.17) $$

where, in view of (2.21),

$$ G_{Ic}(\psi(\xi)) = \frac{\langle\sigma_{\max}(\psi(\xi))\rangle_+\langle\delta_{n\max}(\psi(\xi))\rangle_+}{2} = \frac{\langle\sigma_{\max}(\psi(\xi))\rangle_+^2}{2k_n}, \qquad (3.18a) $$

$$ G_{IIc}(\psi(\xi)) = \frac{\tau_{\max}(\psi(\xi))\delta_{t\max}(\psi(\xi))}{2} = \frac{\tau_{\max}^2(\psi(\xi))}{2k_t}, \qquad (3.18b) $$

where $\sigma_{\max}(\psi(\xi))$ and $\tau_{\max}(\psi(\xi))$ are the maximum allowed traction components associated to the energy criterion, and $\delta_{n\max}(\psi(\xi))$ and $\delta_{t\max}(\psi(\xi))$ the corresponding maximum relative displacements, and following the original LEBIM in (2.22):

$$ \sigma_{\max}(\psi) = \bar{\sigma}_{\max}\hat{\sigma}_{\max}(\psi) \quad \text{and} \quad \tau_{\max}(\psi) = \bar{\sigma}_{\max}\hat{\tau}_{\max}(\psi), \quad \text{or} \qquad (3.19a) $$

$$ \sigma_{\max}(\psi) = \bar{\tau}_{\max}\hat{\sigma}_{\max}(\psi) \quad \text{and} \quad \tau_{\max}(\psi) = \bar{\tau}_{\max}\hat{\tau}_{\max}(\psi), \qquad (3.19b) $$

and the pure fracture toughness mode I and II are expressed as

$$\bar{G}_{\mathrm{Ic}} = \frac{\bar{\sigma}_{\mathrm{max}}^2}{2k_n}, \quad \text{and} \quad \bar{G}_{\mathrm{IIc}} = \frac{\bar{\tau}_{\mathrm{max}}^2}{2k_t}. \tag{3.20}$$

Similarly to (2.24), a dimensionless function for fracture toughness $\hat{G}_c(\psi(\xi))$ can be defined by:

$$G_c(\psi(\xi)) = \bar{G}_{\mathrm{Ic}}\hat{G}_c(\psi(\xi)) \quad \text{or} \quad G_c(\psi(\xi)) = \bar{G}_{\mathrm{IIc}}\hat{G}_c(\psi(\xi)), \tag{3.21}$$

obviously verifying $\hat{G}_c(0) = 1$ for every case of the previous equation.

The interface fracture and stiffness parameters ($G_{\mathrm{c,ch}}$, $\sigma_{\mathrm{c,ch}}$ and k_{ch}) are usually chosen according to the predominant fracture mode to obtain a better understanding of the studied problem and because these parameters should be determined by suitable experiments, possibly by applying some inverse procedures.

Following the general formulation of Section 3.1.3, the dimensionless function $g(\Delta a)$ can be defined by (3.8):

$$g(\Delta a) = \frac{\int_0^{\Delta a} \hat{G}_c(\psi(\xi))\,\mathrm{d}\xi}{\int_0^{\Delta a} \hat{G}(a)\,\mathrm{d}a}, \tag{3.22}$$

Once the two dimensionless curves $s(\Delta a)$ and $g(\Delta a)$ have been defined, the CCFFM can be established by Eq. (3.14). Then, the envelopes of both curves are analysed to obtain the minimum Δa that fulfils the two imposed criteria, as expressed in Eq. (3.14). Three different situations that can be reached using the CCFFM + LEBIM by the curves approach are shown in Fig. 3.4. In this figures the $s(\Delta a)$ and $\sqrt{\mu\ g(\Delta a)}$ curves present a different behaviour.

As mentioned previously, this approach is appropriate for interface failure where the possible crack path is parameterized by 1 or 2 variables (all those in the figure depend on one variable). Therefore, Fig. 3.4 shows the optimization of the two functions in Eq. (3.14) by a representation of the function envelope for three representative cases (the Figs. (c) y (d) are equivalent).

In all the plots included in Fig. 3.4, the blue zone represents the safe zone obtained by the energy criteria and the pink zone represents the safe zone obtained by the stress criteria. The CCFFM + LEBIM criterion predicts the minimum value of the nominal stress ($\frac{\sigma_{\mathrm{nom,c}}}{\sigma_{\mathrm{c,ch}}}$) that satisfies both criteria producing a finite segment of crack (a_{crit}). In each plot, this minimum is highlighted by an orange dot.

Firstly, the similarities of the three cases in Fig. 3.4 will be described. It should be noted that every plot is generated for $\mu > 1$, and the function $\sqrt{\mu\ g(\Delta a)}$ (which represents the energy criterion) always starts with a value higher than $s(\Delta a)$ (which represents the stress criterion). This is because the crack onset location in both criteria is associated with the same point x_{o} and because $s(\Delta a \to 0) < \sqrt{\mu\ g(\Delta a \to 0)}$, as mentioned above. Also, the stress criterion is always represented by an increasing function, because the failure onset location has been taken at the point with lowest value of the stress criterion.

The differences between the three cases in the figure are determined by the behaviour of the energy criterion. In case (a), the function $\sqrt{\mu\ g(\Delta a)}$ advances with a negative slope, fast enough to produce an intersection with the function $s(\Delta a)$ at a
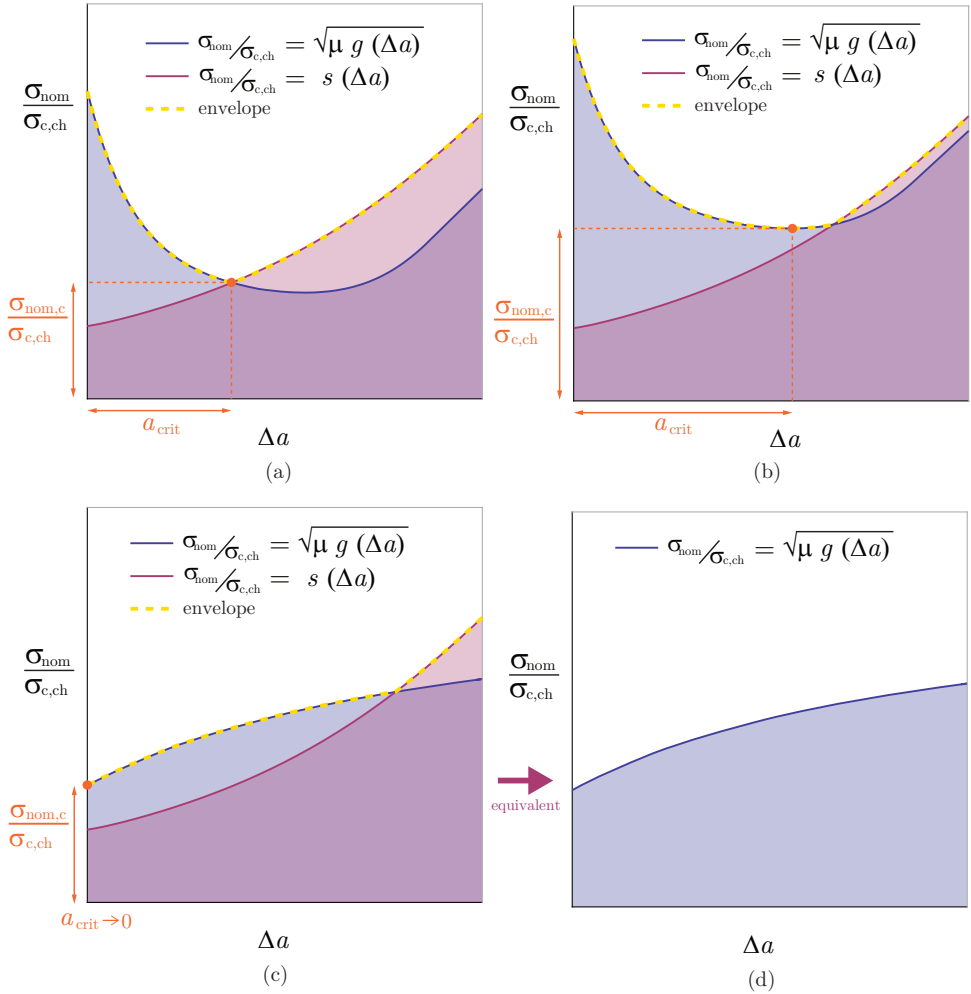
Figure 3.4: Some examples of the CCFFM+LEBIM by the curves approach.

smaller value of Δa than that produced by the minimum point in the energy crite-
rion. However, in case (b), the lowest nominal load is determined by the minimum of
the energy criterion curve. These two cases are named by Mantič (2008) as scenario
C (coupled scenario) and scenario E (energy scenario), correspondingly. Although
the shape of the curves are characteristic of the case under study, the parameter μ
governs the scale of the curve of the energy criterion, since higher values of μ higher
values of $\frac{\sigma_{nom}}{\sigma_{c,ch}}$ are obtained. This can determine the difference between scenario C or
E for the same problem but with different μ, and therefore different characteristics
of the interface. On the other hand, figure (c), represents a case where the energy
criterion has a positive growth with respect to Δa. In this case the crack growth at
the interface is infinitesimal for any μ value. This case would be the same as applying
the original LEBIM with the fracture characteristics of the energy criterion interface,
i.e. with $G_{c,ch}$ and $\sigma_{max,ch}$ instead of $\sigma_{c,ch}$, as shown in figure (d).

3.2.1 Implementation of the CCFFM applied to LEBIM by the curves method

An extended version of the computer code used in Muñoz Reja et al. (2016) is described and tested in the following. It is based on the stress and energy criteria functions ($s(\Delta a)$ and $g(\Delta a)$) defined in the previous section. The pseudocode is shown in Algorithm 3.1 and the variables used therein are described in Table 3.1. It should be noticed that the algorithm can be implemented in a BEM or FEM code.

As mentioned in Section 2.4.2, specifically, two implementations of this code are developed for 2D BEM and FEM. BEM implementation used the in-house code developed in Graciani et al. (2005). This code was extended in Távara et al. (2011) including LEBIM at interfaces. FEM implementation uses a python script that calls ABAQUS to solve the linear elastic solutions when necessary. The interface behaviour in ABAQUS is included by means of a user subroutine UMAT presented in Távara et al. (2018).

Other implementations of CCFFM in FEM have recently published, e.g., Li et al. (2019) and Doitrand et al. (2020) developed general purpose numerical procedures, whereas l'Armée and Becker (2019) developed a numerical procedure suitable to study failure modes of single lap adhesive joints.

The input data of the code are the geometrical and mechanical characteristics of the solids and the interfaces among them, and the boundary conditions of the analysed case.

The index of the main loop in the pseudocode is k, representing a finite crack advance. For each step k, the code calculates the critical load that generates the new finite interface crack growth, Δa_{FFM}^k. The critical load, $\sigma_{\text{nom,c}}$, is provided by the load factor f_{FFM}^k which multiplies (proportionally) the loads imposed to the model (introduced as boundary condition). Following the notation of the previous section: $\sigma_{\text{nom,c}} = f_{\text{FFM}}^k \cdot \sigma_{\text{nom}}$.

In the first part of the k loop, the load factors needed to break each individual interface node n ("spring") using the stress criterion are calculated (f_s^n). The obtained load factors define the discrete form of function $s(\Delta a)$ along the interfaces. The minimum value obtained for these factors defines the position where crack onset occurs (initiates) for each step k. Then, three possible crack paths are proposed (starting from the node where crack onset occurs) for crack growth: clockwise, anticlockwise or symmetrical growth. Subsequently, the code propagates, according to the three possible paths with finite increments (virtual cracks) Δa_{vir}^j, to obtain the discrete form of curve $\sqrt{\mu\, g(\Delta a)}$ using the load factor $f_e^j(\Delta a_{\text{vir}}^j)$ by means of the energy criterion. For every virtual crack path, the load factor f_{FFM}^d, giving the minimum load that satisfies both the stress and the energy criteria, is obtained using the discrete envelope function of $s(\Delta a)$ and $\sqrt{\mu\, g(\Delta a)}$. Finally, the load factor in every step k (f_{FFM}^k) is set as the lowest f_{FFM}^d value.

In the particular cases where an a priory knowledge about the behaviour of stress and energy criteria functions, $s(\Delta a)$ and $g(\Delta a)$, is available, the presented algorithm can be easily modified to save computing time to exit the optimization loops once the foreseen situation representing the global minimum of the discrete envelope function is achieved. For example, if the algorithm finds the first local minimum which

presumably coincides with the global minimum in some situations.

Table 3.1: Variables used in the pseudocode

N_i	Interface node number, from N_1 to N_{total}
	(sequential numbering of interface nodes is assumed)
EC	Energy Criterion
SC	Stress Criterion
ECLF	Energy Criterion Load Factor
SCLF	Stress Criterion Load Factor
N_O	Node where the damage Onset initiates in each step k
d	Number of the three possible damage directions starting from
	N_O ($d = 1, 2, 3$) for every step k
N_{LNI}	Last Node of the Interface for a direction d
Δa_{vir}^j	Finite segment of the crack.
	If $d=1$ its length is obtained by deactivating nodes
	from N_O to j ($j > N_O$)
	If $d=2$ its length is obtained by deactivating nodes
	from j to N_O ($j < N_O$)
	If $d=3$ deactivated nodes are from $2N_O - j$ to j ($j > N_O$)
f_{FFM}^d	Load factor obtained by CCFFM+LEBIM for each d direction
Δa_{FFM}^d	Finite segment of the crack by CCFFM+LEBIM for each d direction
f_{FFM}^k	Final load factor by CCFFM+LEBIM for each step k.
Δa_{FFM}^k	Final segment of the crack by CCFFM+LEBIM for each step k

---

Algorithm 3.1: General pseudocode of CCFFM applied to LEBIM by curves method for a numerical code based on BEM or FEM. The data used in this code are defined in Table 3.1

---

for k step **do**

    Solve the system of equations by BEM or FEM;

    for $n=N_1,...,N_{\text{total}}$ **do**

        $f_s^n = t_c^n/t^n$ // f_s^n is the SCLF at the node n by (3.5a)

    Obtain $f_s^{\min}=\min\limits_{n}(f_s^n)=f_s^{N_O}$ at the node N_O;

    Define three possible damage directions starting from N_O, d:

        1. Clockwise

        2. Anticlockwise

        3. Symmetrical growth

    for $d=1,...,3$ **do**

        for $j=N_O,...,N_{\text{LNI}}(d)$ **do**

            if $d=1$ or 2 **then**

                Deactivate/break interface nodes from N_O to j. Then, the virtual crack Δa_{vir}^j, is set

            else   // d=3

                Deactivate/break nodes from $2N_O - j$ to N_O ($j > N_O$) and deactivate/break nodes from N_O to j. Then, the virtual crack, Δa_{vir}^j, is set;

            Solve the system of equations by BEM or FEM for Δa_{vir}^j;

            Obtain f_e^j // f_e^j is the ECLF for the virtual crack Δa_{vir}^j by (3.10)

            if $f_e^j \geq f_s^j$ **then**

                $f_{\text{env}}^j = f_e^j$ // f_{env}^j is the discrete envelope representation of f_e^j and f_s^n

            else

                $f_{\text{env}}^j = f_s^j$

        Set f_{FFM}^d and Δa_{FFM}^d using the lowest value of f_{env}^j;

    Set f_{FFM}^k and Δa_{FFM}^k using the lowest value of f_{FFM}^d;

3.3 CCFFM applied to LEBIM based on the Principle of Minimum Total Energy subjected to a Stress Condition (PMTE-SC).

In a similar way as the previous CCFFM approach applied to LEBIM, the present approach is also used to predict the crack onset and/or growth by finite increments of the crack length along a linear elastic interface and it is based on the formulation exposed in Section 3.1. The main difference with the previous methodology is that this approach, based on the Principle of Minimum Total Energy subjected to a Stress Condition (PMTE-SC), is more versatile for solving complex fracture problems. This is mainly because it is more suitable for a general computational implementation of a time stepping procedure covering problems for initiation and propagation of several cracks. Moreover the total energy can be formulated as a separately convex functional in terms of the displacements and damage variable fields, allowing to apply efficient

and stable optimization algorithms to minimize the total energy.

This new formulation of the coupled criterion was introduced by Mantič (2014), where several aspects and applications of the principle of minimum total energy to the crack onset and propagation in composites were analysed, assuming a quasistatic problem evolution (i.e. inertial forces are neglected). Following the formulation of the coupled criterion proposed by Mantič (2014) and the analysis given in Section 2.3 in this thesis, the coupled criterion can be redefined as:

$$\min_{\Delta a \subset A_\sigma} \quad \Pi(\Delta a) + R(\Delta a), \tag{3.23}$$

where $\Pi(\Delta a)$ is the potential energy of the system and $R(\Delta a)$ is the energy dissipated after an interface damage advance (new interface crack surface) Δa. $A_\sigma \subset \Gamma_C$ is the set of all (still) undamaged interface points on the interface (Γ_C) where the stress pointwise criterion defined in (3.5a) is satisfied before the considered crack advance happens. $\Delta a \subset \Gamma_C$ defines a possible crack advance, i.e. it represents the set of points going to be damaged in this crack advance.

The key idea behind this formulation is that a new crack surface can only appear in those regions where sufficiently high stresses are applied before the fracture process occurs. The stress criterion would work as a filter for the PMTE since in some cases this criterion, without considering a stress condition, could erroneously predict a crack propagation for too low applied loads, e.g., in the test of a bar subjected to tensile load, discussed by Leguillon (2002) and mentioned in Section 2.3.
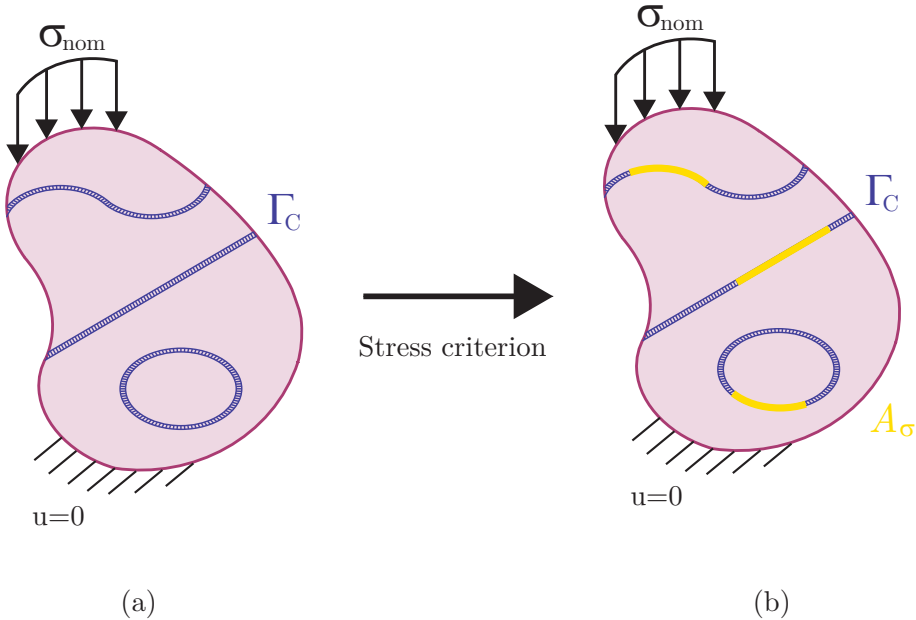
Figure 3.5: (a) Undamaged points of the interface Γ_C, and (b) A_σ representation (the set of points that satisfy the pointwise stress criterion)

In Fig. 3.5 the set A_σ obtained after the application of the stress criterion is schematically represented, for a plane elastostatic problem including several interfaces

(Γ_{C}) shown in blue. For a given external load σ_{nom}, the undamaged points along Γ_{C} whose traction vector is greater than their critical traction vector are obtained by computing a stress criterion (3.5a). Note that the set A_σ depends on the load applied in each case and could be empty ($A_\sigma = \emptyset$) for sufficiently small applied loads. However, A_σ will not be an empty set when the external load is large enough.

Once the set of points which can be damaged is known, i.e. which points will be active when applying the principle of minimum total energy, the possible new crack surfaces leading to the solution of the above minimization problem a_{crit} must be explored. As indicated by Mantič (2014), the PMTE-SC leads to searching of a minimum by evaluating the total energy after the appearance of new crack surfaces. However, in complex problems, in addition to a global minimum, several local minima may appear which, especially those close to the initial configuration, can make difficult to reach the global minimum. For this reason, special care should be taken when exploring possible damaged areas within A_σ. Thus, suitable starting subsets $D_n \subset A_\sigma$ for $n \in [1, N]$ should be proposed. The number N can be given, e.g., by the number of locations where damage could initiate, or the number of their possible combinations, which will be explored for the search of the total-energy minimum.

It is suitable to define a damage variable, denoted here as ζ, which describes the damage at each interface point, being 0 for a fully damaged point and 1 for an undamaged one. This means that for a point $x \in D_n$, the damage variable associated to this starting subset D_n vanishes at x, i.e. $\zeta_n(x) = 0$, whereas for a point y in the complementary subset $A_\sigma \setminus D_n$, $\zeta_n(y) = 1$. Typically, at least the empty set $\emptyset$ and the full set A_σ are among the possible subsets D_n. A heuristic procedure, e.g., based on the level sets given by the stress criterion and/or the components of Γ_{C} with nodes in A_σ, can be used to define the starting subsets D_n leading to an approximation of the minimum of the total energy computed at acceptable computational costs. It can be expected, for simple cases, that all the D_n will result in the same global minimum.
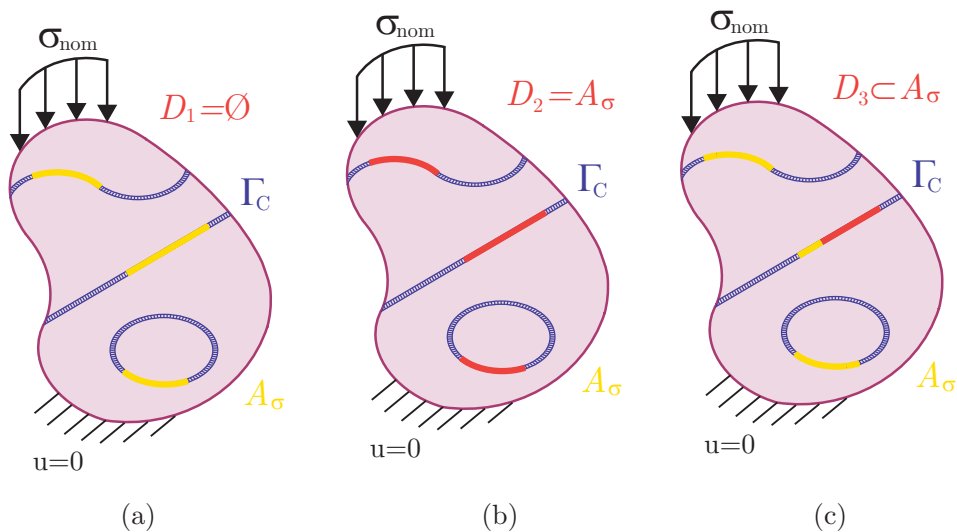
Figure 3.6: Examples of suitable subsets $D_n \subset A_\sigma$.

An example of three possible D_n configurations are represented in Fig. 3.6. Recall that these D_n are subsets of A_σ shown in Fig. 3.5. Figs. 3.6 (a) and (b) correspond to the empty set (all points within A_σ are undamaged) and the full set (all points in A_σ are damaged), respectively. At least these two subsets should always be used in a minimization of the total-energy. In Fig. 3.6 (c) the minimization of the total energy starts considering all points in the red zone (D_3) as damaged. The rest of the points included in $A_\sigma \setminus D_3$ (yellow zone) are considered as undamaged.

Once the N starting damage configurations are defined, each of them is used in a minimization procedure to obtain the a_{crit} associated to the configuration with the lowest total energy. Note that a_{crit} can be continuous or discontinuous along the interface components. It can also be possible that the minimum energy is associated to a no crack advance, i.e. $a_{\mathrm{crit}} = \emptyset$, or viceversa to a maximum crack advance, i.e. $a_{\mathrm{crit}} = A_\sigma$. Therefore, the interpretation that the damage can abruptly coalescence from several defects seems to be in line with the present approach of the FFM.

The minimization problem described in Eq. (3.23) can also be rewritten in terms of the energy variation from an initial state a_0 (even if it is previously cracked or not) to a final state (i.e. after the failure) a_{crit}. It should be noticed that starting from an initial configuration a_0 (either with or without a previous damage), a new damage can only appear along the interface if $\Pi(\Delta a_0) + R(\Delta a_0) \geq \Pi(\Delta a_{\mathrm{crit}}) + R(\Delta a_{\mathrm{crit}})$. Therefore,

$$\min_{\Delta a \in A_\sigma} \quad \Delta\Pi(\Delta a) + \Delta R(\Delta a) \tag{3.24}$$

is equivalent to Eq. (3.23), and it is referred to in Mantič (2014) as the (incremental) principle of maximum decrease of the total energy.

Obviously, in Eq. (3.24), the original condition of the coupled criterion in Eq. (3.1.2) is fulfilled, since in the initial configuration $\Delta\Pi(\Delta a_0) + \Delta R(\Delta a_0) = 0$. It can also be seen that by minimizing $\Delta\Pi(\Delta a) + \Delta R(\Delta a)$ not only the energy condition is fulfilled (which can be satisfied by many failure configurations) but the minimum energy state of the system is being looked for. Therefore, the novel formulation presented by Mantič (2014) is able to predict the damage along the interface in those cases where the prediction by the original formulation (Eq. (2.14)) of the coupled criterion is not unique. However, the critical load predicted by both formulations is be the same.

A new theoretical formulation of the CCFFM+LEBIM introduced by Mantič (2014) is the basis for the first computational implementation of PMTE-SC described in the following. Fig. 3.7, extracted from Mantič (2014), represents four typical scenarios when applying the PMTE-SC:

(a) The possible crack advances along the interface part where the stress criterion is satisfied (A_σ) do not fulfill the energy criterion. This is due to the fact that $\Delta\Pi(\Delta a) + \Delta R(\Delta a) > 0$ in A_σ zone, and therefore the interface failure remains the same as in the initial state $a_0 = a_{\mathrm{crit}}$.

(b) The maximum crack advance along the interface part where the stress criterion is satisfied (A_σ) fulfills the energy criterion. This allows a crack onset by tunneling through the total energy barrier $\Delta\Pi(\Delta a_{\mathrm{crit}}) + \Delta R(\Delta a_{\mathrm{crit}}) = 0$.

(c) The stress values are high enough to satisfy the stress criterion in a long part of the interface (A_σ). Several of the possible crack advances fulfill the en-
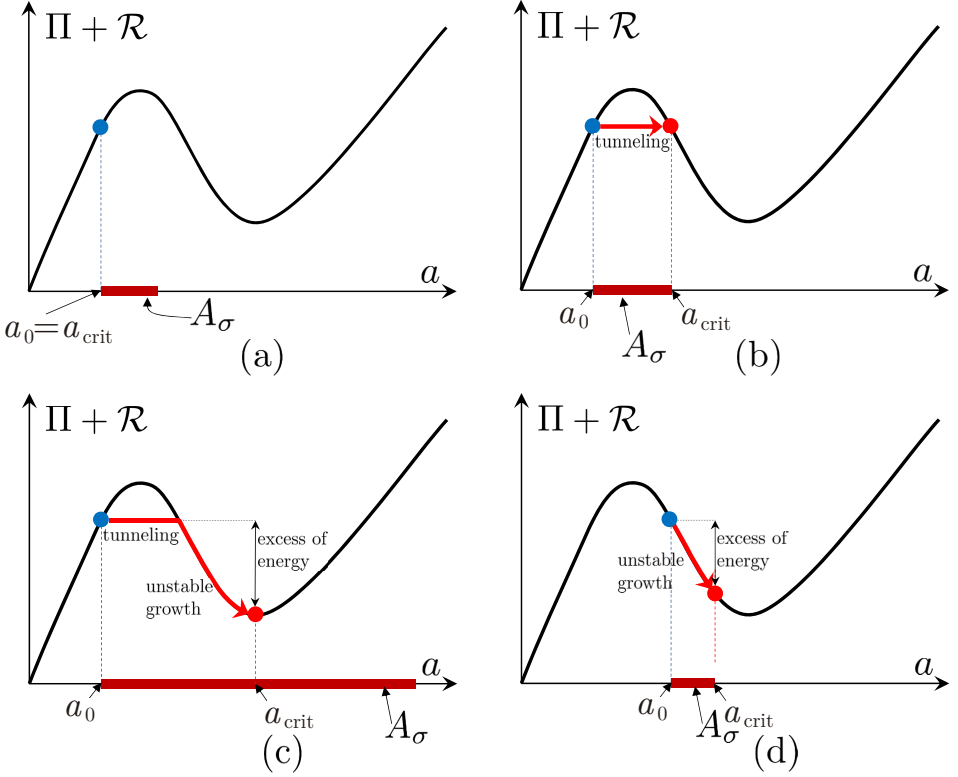
Figure 3.7: Typical scenarios of the application of the principle of minimum total energy subjected to the stress condition (from Mantič (2014)).

ergy criterion. This situation allows damage to occur by tunneling through the total energy barrier and the subsequent unstable growth of the crack with $\Delta\Pi(\Delta a_{\text{crit}}) + \Delta R(\Delta a_{\text{crit}}) < 0$.

(d) The stress values are high enough only in a small region, without covering the whole decreasing part of potential energy graph shown in the figure, $\Delta\Pi(\Delta a_{\text{crit}}) + \Delta R(\Delta a_{\text{crit}}) < 0$.

3.3.1 Implementation of the Alternating Minimization Algorithm for PMTE-SC.

This section presents the algorithm based on the PMTE-SC introduced in the previous section and implemented in a FEM code. Although, this algorithm can also be implemented in a BEM code, this implementation is not included in the present thesis. A Python script is developed to be used together with the commercial code ABAQUS and the UMAT described in Section 2.4.2 and developed in Távara et al. (2018).

It should be noticed that the algorithm introduced herein, unlike the previous one (Algorithm 3.1), does not provide the minimum load that satisfies both the stress and the energy criteria, but predicts the finite interface segment that fails for a determined

load. Therefore, the definition of steps in these pseudocodes is very different. While in Algorithm 3.1, the load and the damage in each step is predicted by the algorithm itself, in the present Algorithm 3.2, the load is imposed by the user and the produced damage is provided by the algorithm. Then, in this pseudocode, each load step k is defined by a specific imposed load and the results are the variable ζ^k describing the damage configuration and the displacement field u^k. It should be noted, that for a specific load the damage may occur after several iterations m, since the initial configuration of each step m (i.e. $u^{k,m}$ and $\zeta^{k,m}$) may change even if the load remains constant.

In the first part of the code, the k-th load provides the zone of the interface that satisfies the stress criterion $A_\sigma^{k,m}$. From $A_\sigma^{k,m}$, the suitable subsets $D_n^{k,m}$ are set for the iteration k, m. In particular, only two subsets are considered in this code: $D_1^{k,m} = \emptyset$ and $D_2^{k,m} = A_\sigma^{k,m}$, leaving for future developments the exploration of other suitable subsets.

The main novelty of the pseudocode is included in its second part, since it deals with the minimization of the total energy in Eq. (3.23) for each suitable starting subset $D_n^{k,m}$, defining the first damage configuration $\zeta_n^{k,m}$ for each n. Following Roubíček et al. (2013); Vodička et al. (2014) and Roubíček (2015), in the present implementation, an Alternating Minimization Algorithm (AMA) is designed to split the minimization procedure shown in Eq. (3.23) into the separate minimization with respect to the displacement field of the system $u_n^{k,m}$ and then with respect to the damage variable $\zeta_n^{k,m}$. Thus, each j-th AMA iteration is divided in two:

i) Firstly, the displacement field $u_{n,j}^{k,m}$ is obtained by minimizing the total energy in Eq. (3.23) for a starting damage configuration defined by $D_n^{k,m}$. Notice that, this is the direct solution obtained by FEM, since this method provides the displacements in all nodes of a FEM mesh for a stable equilibrium configuration when the potential energy is minimal (Zienkiewicz et al., 2005). Obviously the dissipated energy does not change here.

ii) Secondly, for the displacement field obtained in (i), the damage configuration $\zeta_{n,j}^{k,m}$ in Eq. (3.23) is minimized from the same first damage configuration $D_n^{k,m}$. Then, the damage configuration $\zeta_{n,j}^{k,m}$ is defined by the damage variable at each element along $A_\sigma^{k,m}$. The minimization with respect to the damage configuration ($\zeta_{n,j}^{k,m}$) can be carried out by the simplex algorithm or by a loop over every element in $A_\sigma^{k,m}$ comparing the change of the elastic strain energy in the element and the change of the dissipated energy for either *element breaking or healing*. It should be noticed that during element breaking, the elastic energy in the element vanishes and the dissipated energy associated with the element increases (it is given by the associated fracture energy). However, during element healing the elastic energy in the element increases (it is given by the relative displacements of the end-points of the broken element) and the dissipated energy associated to the element decreases (vanishes).

The AMA is repeated until a difference of the damage variable between two steps less than ϵ is obtained, for all $D_n^{k,m}$. Then, comparing solutions for all n, the configuration $u_n^{k,m}$ and $\zeta_n^{k,m}$ that provides the lowest $\Pi + \Delta R$ values is chosen. Iterations

loop on m continues if the damage keep propagating for the same applied load (related to a step k). Note that $\Delta\Pi = \Pi^m - \Pi^{m-1}$, but Π^{m-1} does not vary at each step m. Therefore it is similar to minimize $\Delta\Pi$ than minimize Π^m. However, from a computational point of view in FEM, the second option is more direct.

It may also happen, that for an imposed load (step k) the interface is completely damaged after several m steps, not being able to properly capture a possible snap-through behaviour. To solve this issue, the load at k-th step could start from zero each time a damage occurs and allowing only one iteration in m.

Table 3.2: Data used in the pseudocode.

Variables used in the pseudocode:	
f	Imposed load or displacement in the study case.
Δf	Load increment between two steps.
ζ(element)	Damage variable for each element along the interface.
	0 value means damaged interface element
	(with zero stiffness in tension and shear).
	1 value means undamaged interface element
	(with full initial stiffness).
ζ	Damage configuration of Γ_C given by all values ζ(element).
u	Displacement field
ψ	Fracture mode mixity associated to $\psi_2(a)$ described in Section 3.1.2,
$t_c(\psi)$	Critical traction modulus for the stress based criterion.
$G_c(\psi)$	Critical fracture energy for the energy based criterion.
A_σ	Set including all undamaged elements that satisfy the stress criterion
D	Proposed subset of A_σ that contains damaged elements assumed
	before the minimization. Note that $A_\sigma \setminus D$ is composed for the rest of the
	undamaged elements of A_σ.
N	Number of considered starting damage configurations.
ϵ	Difference of the damage variable between two AMA iterations.
Each variable defined above may be affected by the following subscripts and superscripts:	
k	Load step.
m	Iteration within a load step.
n	First damage configuration within an iteration. $n \in [1, N(k,m)]$, with $N(k,m) \geq 2$
j	AMA iteration

Algorithm 3.2: General pseudocode for an Alternating Minimization Algorithm for PMTE-SC [a]. The data used in this code are defined in Table 3.2

---

for k step **do**

    The iteration m is initialized with $m = 1$;

    if $k=1$ **then**

        The variables are set: $\begin{cases} f^k \text{ selected based on original LEBIM} \\ \zeta^k = \emptyset \text{ and } \zeta^{k,m} = \emptyset \\ u^k = \emptyset \text{ and } u^{k,m} = \emptyset \end{cases}$

    else

        The variables are set: $\begin{cases} f^k = f^{k-1} + \Delta f \\ \zeta^k = \emptyset \text{ and } \zeta^{k,m} = \zeta^{k-1} \\ u^k = \emptyset \text{ and } u^{k,m} = \emptyset \end{cases}$

    while $\zeta^k = \emptyset$ **do**

        m=m+1 ;

        Minimize $u^{k,m-1} \mapsto \Pi(f^k, u^{k,m-1}, \zeta^{k,m-1})$;   // FEM calculation

        Update $u^{k,m} = u^{k,m-1}$;

        From $u^{k,m}$ compute $\psi^{k,m}$ and then: $t_c(\psi^{k,m})$ and $G_c(\psi^{k,m})$ on Γ_C ;

        Set $A_\sigma^{k,m}$ on Γ_C by stress criterion ;

        if $A_\sigma^{k,m} = \emptyset$ **then**

            Set solution $u^{k,m}$ and $\zeta^{k,m} = \zeta^{k,m-1}$

        else

            Define $D_n^{k,m} \subset A_\sigma^{k,m}$ for $n \in [1, N(k,m)]$, with $N(k,m) \geq 2$;

            Define the first $\zeta_n^{k,m}$ for every N;

            for $n = 1$ **to** $N(k,m)$ **do**

                $j = 1$;

                $\zeta_{n,j}^{k,m} = \zeta_n^{k,m}$;

                while $\|\zeta_{n,j}^{k,m} - \zeta_{n,j-1}^{k,m}\| \leq \epsilon$ **do**

                    $j = j + 1$;

                    minimize $u_{n,j}^{k,m} \mapsto$ // FEM calculation
                    $\mapsto \Pi(f^k, u_{n,j}^{k,m}, \zeta_{n,j-1}^{k,m}) + R(G_c(\psi^{k,m}), \zeta_{n,j-1}^{k,m} - \zeta^{k,m-1})$;

                    minimize $\zeta_{n,j}^{k,m} \mapsto \Pi(f^k, u_{n,j}^{k,m}, \zeta_{n,j}^{k,m}) + R(G_c(\psi^{k,m}), \zeta_{n,j}^{k,m} - \zeta^{k,m-1})$
                      subject to $0 \leq \zeta_{n,j}^{k,m}(\text{elem}) \leq \zeta^{k,m-1}(\text{elem}) \,\forall$ elements $\in A_\sigma^{k,m}$
                      and $\zeta_{n,j}^{k,m}(\text{elem}) = \zeta^{k,m-1}(\text{elem}) \,\forall$ elements $\notin A_\sigma^{k,m}$;

                Set solution $u_n^{k,m} = u_{n,j}^{k,m}$ and $\zeta_n^{k,m} = \zeta_{n,j}^{k,m}$;

                Store configuration
                $[u_n^{k,m}, \zeta_n^{k,m}, \Pi(f^k, u_n^{k,m}, \zeta_n^{k,m}) + R(G_c(\psi^{k,m}); \zeta_n^{k,m} - \zeta^{k,m-1})]$;

            Set solution $u^{k,m} = u_n^{k,m}$ and $\zeta^{k,m} = \zeta_n^{k,m}$ for the n with the lowest value
            of $\Pi(t^k, u_n^{k,m}, \zeta_n^{k,m}) + R(u^{k,m-1}; \zeta_n^{k,m} - \zeta^{k,m-1})$;

        Set solution $u^k = u^{k,m}$ and $\zeta^k = \zeta^{k,m}$;

CHAPTER 4

Double cantilever beam: A comparison between the two approaches of the CCFFM applied to LEBIM.

4.1 Introduction

The main objective of this chapter is to compare the predictions of the interface failure for a specific case by the two approaches of the coupled criterion applied to the LEBIM which are exposed in Section 3.2 and Section 3.3. For this purpose, two analytical studies, based on the curve method and the PMTE-SC, have been developed and applied to the Double Cantilever Beam (DCB) test. For this study an Euler-Bernoulli beam model has been used as well as an elastic interface to model the joint.

The DCB is a well-known test used to determine the fracture toughness in pure fracture mode I of adhesively bonded joints. This test allows a good understanding and characterization of the adhesive layer which is very important in the quality evaluation of adhesively bonded joints. In particular it allows determining the parameters that characterize their resistance to fracture and failure. The DCB test is also used as a prediction method for delamination growth and to compare the performance of different composite laminates. A review of several applications of this test can be found in Garg (1988) and Tay (2003).

In Section 4.2, an analytical model is developed to obtain the stress and the displacement fields along the interface between the two beams of the test. Similar models were developed by Volkersen (1938), Goland and Reissner (1944), Kanninen (1973), Erdogan (1997), Benveniste and Miloh (2001), Lenci (2001) and Dimitri et al. (2017), among other authors. With this model, the CCFFM+LEBIM is applied using

the curves methodology and the PMTE-SC methodology, developed in Section 4.3 and Section 4.4. This investigation studies the effect of applying a displacement control or a load control, for each of the two approaches of the CCFFM + LEBIM. The interface is characterised by the μ parameter expressed in mode I. Both studies will be carried out separately and with different parametrization.

One of the most important result of this chapter is the detailed study of the PMTE-SC applied to the DCB test. Since it allows the analysis of the behaviour of this failure methodology applied to the delamination of an interface. In section Section 3.3, the interpretation of the energy balance introduced by Mantič (2014) was developed. Where the increment of the potential energy plus the increment of the energy dissipated at the abrupt formation of a new delamination must be equal or smaller than zero:

$$\Delta\Pi(\Delta a) + \Delta R(\Delta a) \leq 0, \tag{4.1}$$

i.e., $\Pi(a) + R(a)$ should keep constant or decrease for a crack onset, being $R(a)$ the total dissipated energy during the failure of the interface of size a and $\Pi(a)$ the stored elastic energy $U(a)$ plus the potential energy of the external load $\Pi_{ext} = -W$. Therefore, the study of the minimization of the function $\Pi(a) + R(a)$ provides a crack onset (Δa) with the least possible damage and with the minimum possible energy, in a zone (Δa) of the undamaged interface that verifies the stress criterion.

Specifically, in the case studied in this chapter, the whole interface between the two beams of the DCB is a potential failure zone, starting from a pre-crack $a = 0$ to the end of the interface. However, the crack will only grow in those zones where the stress criterion is satisfied and which will depend on the applied load. In these zones, where the stress criterion is verified, the function $\Pi(a) + R(a)$ must be minimized for both the displacement control and the load control tests.

As can be seen in Section 4.2.3 of this chapter, there are no differences in the stress field between the two types of test, but there is a difference in the energy behaviour of the DCB test when the load control or the displacement control are imposed.

It is important to highlight that in both tests a crack growth in mode I is predominated and therefore the shear stresses are omitted. Hence, the function $\psi(\xi)$ is always zero, even if it is defined by the stress state at each point x of the potential crack surface before the crack onset or by the ratio of ERR components of a virtual crack growing between the initial configuration and the finite crack produced by the crack onset (see Section 3.2).

4.2 Analytical model for the Double Cantilever Beam

Referring to the free-body diagram of an element of length $\mathrm{d}x$ represented in Fig. 4.1, the following equilibrium equations can be written for the upper beam:

$$\frac{\mathrm{d}V(x)}{\mathrm{d}x} + b\,\sigma(x) = 0 \tag{4.2}$$

$$\frac{\mathrm{d}M(x)}{\mathrm{d}x} - V(x) = 0, \tag{4.3}$$

where, $V(x)$ and $M(x)$ are the shear force and the bending moment per unit width, respectively; and $\sigma(x)$ is the normal stress component along the adhesive.
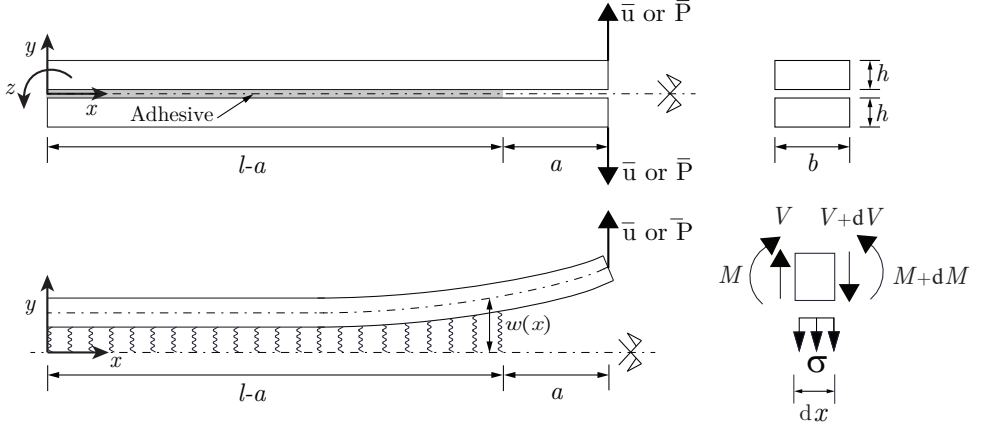
Figure 4.1: Double Cantilever Beam test configuration and equilibrium of an infinitesimal element of a beam. The bar over u and P means the imposed limit conditions.

The kinematic equations for each of the beams are:

$$\chi(x) = \frac{\mathrm{d}\varphi(x)}{\mathrm{d}x} \tag{4.4}$$

$$\varphi(x) = \frac{\mathrm{d}w(x)}{\mathrm{d}x}, \tag{4.5}$$

where $\varphi(x)$, $\chi(x)$ and $w(x)$ are the rotation, curvature and transverse displacement respectively.

Also, the constitutive equation for each beams is

$$\chi(x) = \frac{12M(x)}{E'h^3b}, \tag{4.6}$$

where, $E' = \frac{E}{(1-\nu_b^2)}$ is the elastic modulus for plane strain conditions for an isotropic material.

As the adhesive layer is modelled by a spring distribution, then the normal stress component is directly related to its respective relative displacement, δ_n, between the adherents. Then, the Euler-Bernoulli beam kinematical assumption yields

$$\sigma(x) = k_n\delta_n(x) = 2k_nw(x), \tag{4.7}$$

where k_n represent the normal stiffness of the adhesive layer or in a broader view the stiffness of the bonded joint.

Differentiating Eq. (4.5) and accounting for the Eqs. (4.4) and (4.6) we obtain

$$\frac{\mathrm{d}^2w(x)}{\mathrm{d}x^2} = \frac{12M(x)}{E'h^3b} \tag{4.8}$$

Differentiating Eq. (4.8) and accounting for the Eq. (4.3) we get

$$\frac{\mathrm{d}^3w(x)}{\mathrm{d}x^3} = \frac{12V(x)}{E'h^3b} \tag{4.9}$$

Differentiating Eq. (4.9) and accounting for the Eqs. (4.2) and (4.7) we get

$$\frac{\mathrm{d}^4 w(x)}{\mathrm{d}x^4} + \frac{24 k_n w(x)}{E'h^3} = 0 \tag{4.10}$$

Note that, considering Eq. (4.7) and the previous Eq (4.10), a similar differential equation for the normal stress component is obtained:

$$\frac{\mathrm{d}^4 \sigma(x)}{\mathrm{d}x^4} + \frac{24 k_n \sigma(x)}{E'h^3} = 0 \tag{4.11}$$

In order to get dimensionless expressions, the characteristic length parameter l_{ch}, relating the stiffness of the beam to that of the interface, is defined in a similar way as in Dimitri et al. (2017) and Kanninen (1973):

$$l_{ch} = \sqrt[4]{\frac{E'h^3}{6 k_n}}. \tag{4.12}$$

Table 4.1: Dimensionless variables and parameters.

$\xi = \frac{x}{l_{ch}}$	$\lambda = \frac{l}{l_{ch}}$	$\eta = \frac{h}{l_{ch}}$	$\alpha = \frac{a}{l_{ch}}$
$\hat{w} = \frac{w}{\bar{u}}$	$\hat{\sigma} = \frac{\sigma}{P/b\, l_{ch}}$		

Then, Eqs. (4.10) and Eqs. (4.11) can be rewritten in terms of the dimensionless parameters defined in Table 4.1 as:

$$\hat{w}^{\mathrm{iv}}(\xi) + 4\hat{w}(\xi) = 0 \tag{4.13}$$
$$\hat{\sigma}^{\mathrm{iv}}(\xi) + 4\hat{\sigma}(\xi) = 0 \tag{4.14}$$

where the derivatives are now taken with respect to ξ. To solve (4.14), first its characteristic (fourth-order) equation is written as

$$q^4 + 4 = 0 \tag{4.15}$$

and the four roots of Eq. (4.15) can be expressed as:

$$q_{1,2} = 1 \pm i, \quad q_{3,4} = -1 \pm i, \tag{4.16}$$

Finally, the dimensionless displacement $\hat{w}(\xi)$ and stress $\hat{\sigma}(\xi)$ can be expressed in a similar way as in Dimitri et al. (2017):

$$\hat{w}(\xi) = e^{\xi}(C_1 \sin\xi + C_2 \cos\xi) + e^{-\xi}(C_3 \sin\xi + C_4 \cos\xi) \tag{4.17}$$
$$\hat{\sigma}(\xi) = e^{\xi}(C_1 \sin\xi + C_2 \cos\xi) + e^{-\xi}(C_3 \sin\xi + C_4 \cos\xi) \tag{4.18}$$

where $C_1, \ldots, C_4$ are integration constants to be determined from the boundary conditions.

(a)

(b)
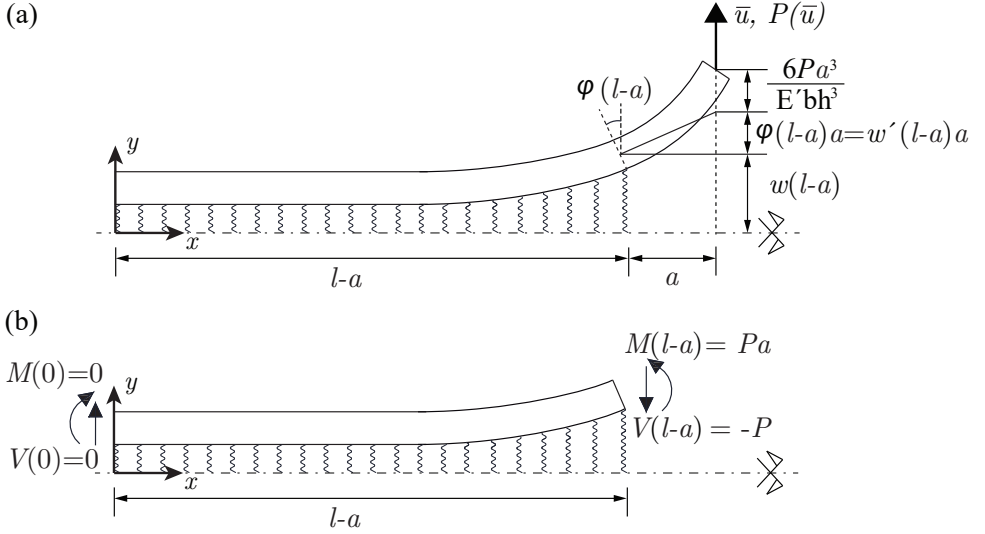
Figure 4.2: Boundary conditions used to model the DCB test under displacement control.

4.2.1   Displacement field solution along the interface under displacement control.

The four boundary conditions are obtained by substituting the values of the shear force, bending moment and the displacement at the extreme of the beams into the previous equations.

As Fig. 4.2(b) represented, the first two boundary conditions are given by evaluating Eqs. (4.8) and (4.9) at $x = 0$:

$$\hat{w}''(0) = 0 \tag{4.19}$$

$$\hat{w}'''(0) = 0 \tag{4.20}$$

For the third and fourth boundary conditions application is necessary to write the reaction $P(\bar{u})$ as a function of $w(x)$. According to Fig. 4.2(b) and Eq. (4.9) this relation can be obtained as:

$$w'''(l - a) = \frac{-12P(\bar{u})}{E'h^3b} \tag{4.21}$$

The third boundary condition can be seen in Fig. 4.2(a) where the displacement applied at the extreme of the beams is $\bar{u}$. With the relation between $P(\bar{u})$ and $w'''(l - a)$ the third boundary condition can be written in terms of the dimensionless parameters:

$$\hat{w}(\lambda - \alpha) + \hat{w}'(\lambda - \alpha)\alpha - \hat{w}'''(\lambda - \alpha)\frac{\alpha^3}{3} = 1 \tag{4.22}$$

Finally, the last boundary condition must satisfy that $M(l - a) = Pa$. Therefore from Eq. (4.8) and Eq. (4.21) the following boundary condition can be obtained:

$$\hat{w}''(\lambda - \alpha) - \hat{w}'''(\lambda - \alpha)\alpha = 0 \tag{4.23}$$

The system of equations is solved using the software Wolfram Mathematica. The displacement field obtained depends on three of the dimensional parameters defined in the Table 4.1 (ξ, α and λ). However, only ξ and α, will change in the rest of the problem formulation. Since ξ refers to any point along the interface between the beams and α refers to the crack tip location. Therefore, in the rest of the formulation, the displacement field is written according to these two variables only. Thus, Eq. (4.24) represents the solution of the displacement field along the interface for an undamaged point ξ and an initial crack length α :

$$
\hat{w}(\xi, \alpha) = \Bigg[-3 \big(e^{3\alpha + \zeta + \lambda} + e^{\alpha - \zeta + 3\lambda} \big) \alpha \cos(\alpha - \zeta - \lambda) +
$$

$$
+ 3\, e^{3\alpha - \zeta + \lambda} \bigg(\big(-1 - e^{2\zeta} + \alpha \big) \cos(\alpha + \zeta - \lambda) - e^{2\zeta} \big(-1 + \alpha \big) \sin(\alpha - \zeta - \lambda) \bigg) -
$$

$$
- 3\, e^{3\alpha - \zeta + \lambda} \bigg(\big(\alpha + e^{2\zeta}(-1 + 2\alpha) \big) \sin(\alpha + \zeta - \lambda) \bigg) +
$$

$$
+ 3\, e^{\alpha - \zeta + 3\lambda} \bigg(\big(1 + e^{2\zeta}(1 + \alpha) \big) \cos(\alpha + \zeta - \lambda) + 2 \cos(\zeta) \sin(\alpha - \lambda) \bigg) +
$$

$$
+ 3\, e^{\alpha - \zeta + 3\lambda} \alpha \bigg(\sin(\alpha - \zeta - \lambda) + (2 + e^{2\zeta}) \sin(\alpha + \zeta - \lambda) \bigg) \Bigg] \Bigg/
$$

$$
\Bigg[e^{4\alpha} \bigg(-3 + 2\alpha \big(3 + (-3 + \alpha)\alpha \big) \bigg) + e^{4\lambda} \bigg(3 + 2\alpha \big(3 + \alpha(3 + \alpha) \big) \bigg) +
$$

$$
2\, e^{2(\alpha + \lambda)} \bigg(-4\alpha^3 + 2\alpha \big(-3 + \alpha^2 \big) \cos\big(2(\alpha - \lambda) \big) + \big(3 - 6\alpha^2 \big) \sin\big(2(\alpha - \lambda) \big) \bigg) \Bigg]
$$

$$
(4.24)
$$

The displacement at the crack tip will also be necessary, for the rest of the problem development, which is obtained by evaluating $\xi = \lambda - \alpha$:

$$
\hat{w}(\lambda - \alpha, \alpha) = \Bigg[3\, e^{4\alpha} \big(-1 + \alpha \big) + 3\, e^{4\lambda} \big(1 + \alpha \big) -
$$

$$
- 6\, e^{2(\alpha + \lambda)} \bigg(\alpha \cos\big(2(\alpha - \lambda) \big) - \sin\big(2(\alpha - \lambda) \big) \bigg) \Bigg] \Bigg/
$$

$$
\Bigg[e^{4\alpha} \bigg(-3 + 2\alpha \big(3 + (-3 + \alpha)\alpha \big) \bigg) + e^{4\lambda} \bigg(3 + 2\alpha \big(3 + \alpha(3 + \alpha) \big) \bigg) +
$$

$$
2\, e^{2(\alpha + \lambda)} \bigg(-4\alpha^3 + 2\alpha \big(-3 + \alpha^2 \big) \cos\big(2(\alpha - \lambda) \big) + \big(3 - 6\alpha^2 \big) \sin\big(2(\alpha - \lambda) \big) \bigg) \Bigg]
$$

$$
(4.25)
$$

4.2.2 Stress field solution along the interface under load control.

The four boundary conditions are obtained by substituting the values of the shear force and the bending moment at $x = 0$ and $x = l - a$ as shown in Fig. 4.3(b).

Thus, the first two boundary conditions are given by evaluating Eqs. (4.8) and (4.9) at $x = 0$. These boundary conditions can be expressed in terms of the normal

(a)

(b)
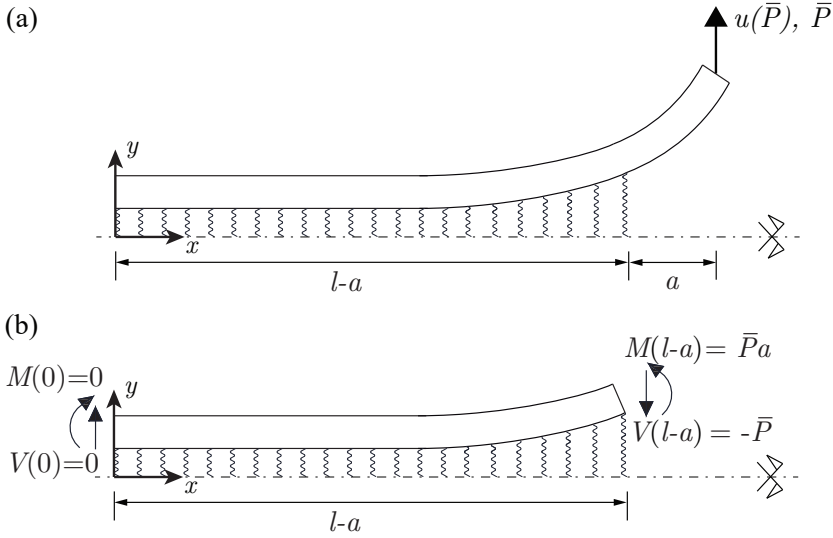
Figure 4.3: Boundary conditions used to model the DCB test with load control.

stress component, see Eq. (4.7):

$$\hat{\sigma}''(0) = 0 \qquad (4.26)$$

$$\hat{\sigma}'''(0) = 0 \qquad (4.27)$$

In the third boundary condition $V(l-a) = -\bar{P}$ must be fulfilled and from Eqs. (4.9) the following expression can be obtained:

$$\hat{\sigma}'''(\lambda - \alpha) = -4 \qquad (4.28)$$

And the last boundary condition is obtained from Eq. (4.8) to satisfy $M(l-a) = \bar{P}a$.

$$\hat{\sigma}''(\lambda - \alpha) = 4\alpha \qquad (4.29)$$

In a similar way as done for the analysis under displacement control, this system is solved using Wolfram Mathematica. Then, the stress distribution along the interface is obtained which depends on the same parameters and variables as the solution defined in Section 4.2.2. Thus, the following function defines the normal stress component at an undamaged point ξ within an undamaged zone of the interface and an initial crack length α:

$$
\begin{aligned}
\hat{\sigma}(\xi, \alpha) = \Big[& -2\big(e^{3\alpha+\zeta+\lambda}+e^{\alpha-\zeta+3\lambda}\big)\alpha\cos(\alpha-\zeta-\lambda)+ \\
& +2\,e^{3\alpha-\zeta+\lambda}\left(\big(-1-e^{2\zeta}+\alpha\big)\cos(\alpha+\zeta-\lambda)-e^{2\zeta}\big(-1+\alpha\big)\sin(\alpha-\zeta-\lambda)\right)- \\
& -2\,e^{3\alpha-\zeta+\lambda}\left(\big(\alpha+e^{2\zeta}(-1+2\alpha)\big)\sin(\alpha+\zeta-\lambda)\right)+ \\
& +2\,e^{\alpha-\zeta+3\lambda}\left(\big(1+e^{2\zeta}(1+\alpha)\big)\cos(\alpha+\zeta-\lambda)+2\cos(\zeta)\sin(\alpha-\lambda)\right)+ \\
& +2\,e^{\alpha-\zeta+3\lambda}\,\alpha\left(\sin(\alpha-\zeta-\lambda)+(2+e^{2\zeta})\sin(\alpha+\zeta-\lambda)\right)\Big] \Big/ \\
& \left[e^{4\alpha}+e^{4\lambda}+2\,e^{2(\alpha+\lambda)}\left(-2+\cos\big(2(\alpha-\lambda)\big)\right)\right]
\end{aligned}
$$

(4.30)

Note that, although the numerator of Eq. (4.30) is proportional to the numerator of Eq. (4.24), the solutions of the test under displacement control and under load control are different.

For the rest of the problem formulation, normal stresses at the crack tip are obtained by evaluating $\xi = \lambda - \alpha$:

$$
\begin{aligned}
\hat{\sigma}(\lambda-\alpha, \alpha) = \Big[& 2\,e^{4\alpha}\big(-1+\alpha\big)+2\,e^{4\lambda}\big(1+\alpha\big)- \\
& -4\,e^{2(\alpha+\lambda)}\left(\alpha\cos\big(2(\alpha-\lambda)\big)-\sin\big(2(\alpha-\lambda)\big)\right)\Big] \Big/ \\
& \left[e^{4\alpha}+e^{4\lambda}+2\,e^{2(\alpha+\lambda)}\left(-2+\cos\big(2(\alpha-\lambda)\big)\right)\right]
\end{aligned}
$$

(4.31)

4.2.3 Stresses distribution and displacement field along the interface for a specific case.

In order to analyze the behaviour of the solutions for the stress and displacement fields obtained in the previous sections, the data included in Table 4.2 are used to graphically represent the normal stress component and the displacement for a specific interface. The obtained values of the dimensionless parameters defined in Table 4.1 are also presented in Table 4.2.

Fig. 4.4 (a) show the obtained stress and displacements distribution for load control and displacement control respectively. The distribution are presented in their dimensionless form, for an initial crack length $\alpha = 0$. It should be noticed that the nondimensionalization is obtained using the boundary conditions at the end of the beam for each configuration. Results in Fig. 4.4 (b) indicates that the solution of the dimensionless displacement field under displacement control is just twice the dimensionless stress distribution under load control.

Fig. 4.5 represents the dimensionless stress and displacement at the crack tip as it moves from 0 to λ. It can be seen that the good agreement between the displacement

Table 4.2: Default mechanical and geometrical characteristics used for the debond analysis of the DCB test.

	l(mm)	h(mm)	b(mm)	a(mm)	E(GPa)	ν
Beams	237	1.5	1	0	135	0.3
	k_n(MPa/μm)					
Adhesive	0.30					
Characteristic length: l_{ch}=4.08388mm						
Dimensionless parameters	λ=58.033		α=0.000	η=0.367		

(a) $\hat{w}(\xi,0)$ and $\hat{\sigma}(\xi,0)$ (b) $2\hat{w}(\xi,0)$ and $\hat{\sigma}(\xi,0)$
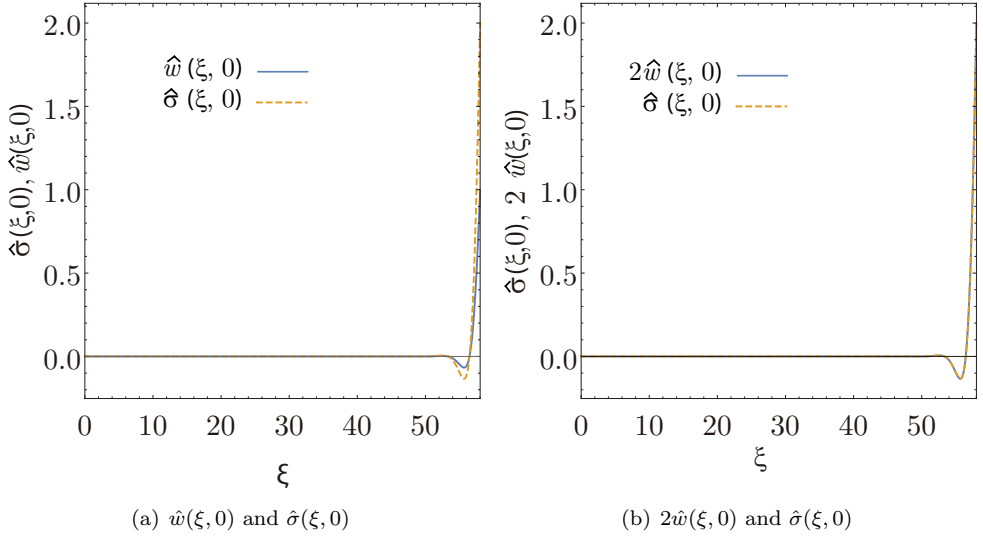
Figure 4.4: $\hat{w}(\xi,0)$ under displacement control and $\hat{\sigma}(\xi,0)$ under load control for $\alpha = 0$.

and stress distribution in Fig.4.4 is lost as the crack length α increases. This due to the evolution of both solutions is very different for each boundary condition at the end of the beam. While the displacement at the crack tip under the displacement control, $\bar{u}$, gradually decreases, the stress at the same point and under load control, $\bar{P}$, significantly increases. These different behaviours of both solutions will lead to a great difference in the failure evolution along the interface for each test.

(a) $\hat{w}(\lambda - \alpha, \alpha)$

(b) $\hat{\sigma}(\lambda - \alpha, \alpha)$
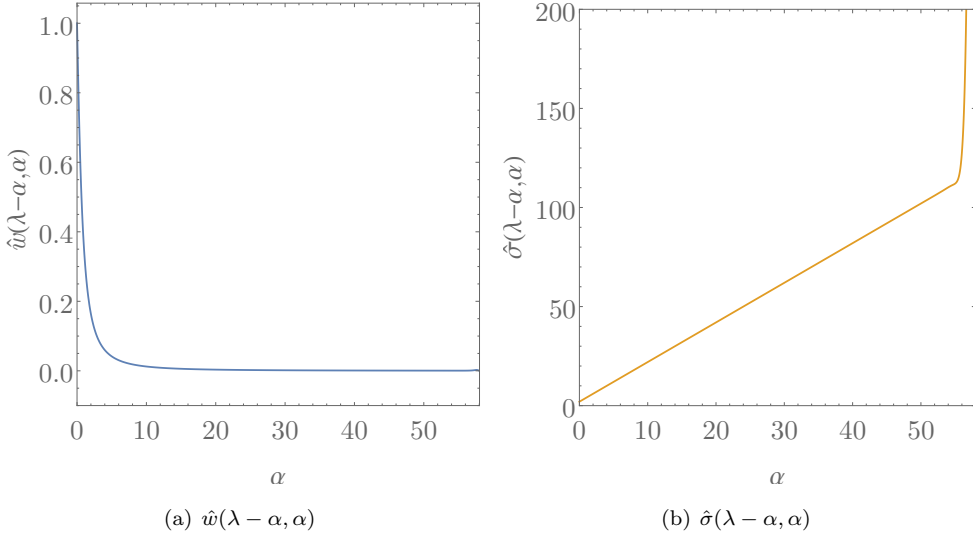
Figure 4.5: $\hat{w}(\lambda - \alpha, \alpha)$ under displacement control and $\hat{\sigma}(\lambda - \alpha, \alpha)$ under load control at the crack tip.

4.3 CCFFM applied to linear-elastic interfaces for the DCB under displacement control.

4.3.1 Solution obtained by the stress and energy criteria curves.

Following the theoretical concepts exposed in Section 3.2, for the specific case of the DCB test under displacement control, the ERR can be defined for a point associated with the crack tip whose position in this system is $(\lambda - \alpha)$, as:

$$G(\lambda - \alpha) = 2k_n\bar{u}^2\hat{w}^2(\lambda - \alpha, \alpha) = 2k_n\bar{u}^2\hat{G}(\lambda - \alpha) \quad \text{with} \quad \hat{G}(\lambda - \alpha) = \hat{w}^2(\lambda - \alpha, \alpha) \tag{4.32}$$

where α can be interpreted as the "virtual advance" of the crack tip in the energy criterion framework. On the other hand, in the stress criterion framework, α has a "fixed position" representing the initial position of the crack tip.

Therefore, the energy criterion can be defined as:

$$\frac{2k_n\bar{u}^2}{G_{\text{Ic}}} \geq g(\Delta\alpha) \quad \text{con} \quad g(\Delta\alpha) = \frac{\Delta\alpha}{\int_\alpha^{\alpha+\Delta\alpha} \hat{G}(\lambda - \alpha)\,\mathrm{d}\alpha} \tag{4.33}$$

depending on a finite crack increase $\Delta\alpha$.

To be consistent with the nondimensionalization used in the previous sections and to be able to subsequently compare the results of the test under displacement control and load control, the definition of critical displacement as $w_{\text{c}} = \frac{\sigma_{\text{c}}}{2k_n}$ will be used, where σ_{c} is the critical normal stress for pure mode I. Note that, the stress criterion is evaluated on the whole undamaged interface $(\lambda - \alpha - \Delta\alpha \leq \xi \leq \lambda - \alpha)$, and it must be satisfied in the same $\Delta\alpha$ zone that the energy criterion:

if $\quad s(\xi) = \dfrac{1}{\hat{w}(\xi, \alpha)} \quad$ then $\quad \dfrac{\bar{u}}{w_c} \geq s(\Delta\alpha) \quad$ for all $\quad \xi, \; \lambda - \Delta\alpha \leq \xi \leq \lambda$

$$(4.34)$$

and for a specific value of $\quad \alpha$

Finally, if the parameter μ defined in Section 3.1.3 is rewritten according to the critical displacement ($\mu = \frac{G_{\mathrm{Ic}}}{2k_n w_c^2}$) the CCFFM by curves can be expressed as:

$$\frac{\bar{u}}{w_c} \geq \frac{\bar{u}_{\mathrm{f}}}{w_c} = \min_{\Delta\alpha} \max \left\{ s(\Delta\alpha), \sqrt{\mu \, g(\Delta\alpha)} \right\} \tag{4.35}$$

where $\bar{u}_{\mathrm{f}}$ is the minimum displacement applied to the beam end that satisfies both criteria and produces a crack with length $\Delta\alpha_{\mathrm{c}} = \Delta\alpha$.

In order to interpret the behaviour of the failure criterion included in Eq. (4.35) for this specific test, both curves have been represented using the geometrical and mechanical characteristics described in the Table 4.2 and for $\mu = 8$.
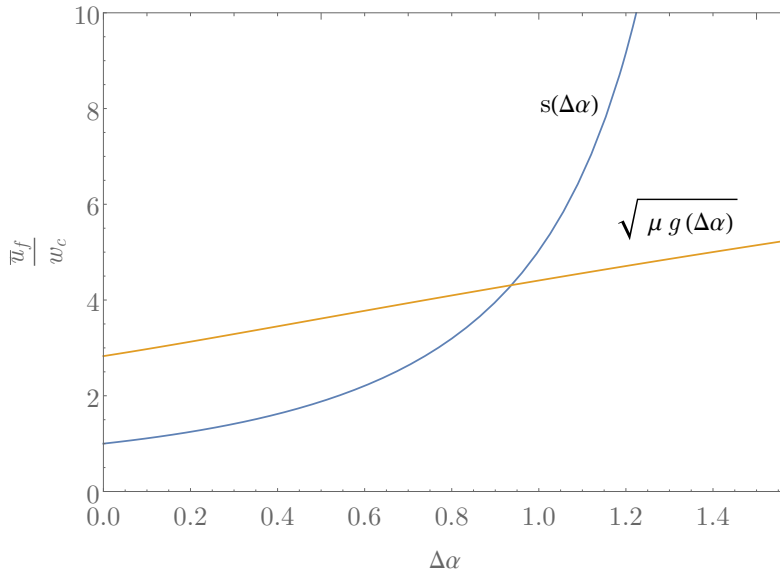
Figure 4.6: $s(\Delta\alpha)$ and $\sqrt{\mu g(\Delta\alpha)}$ functions for the DCB under displacement control with $\mu = 8$.

Fig. 4.6 shows that for small values of $\Delta\alpha$, the energy criterion starts above the stress criterion and with a positive slope. As already justified in Section 3.2, the initial part of the energy criterion function ($\Delta\alpha \to 0$) will always be larger than the initial part of the stress criterion function, due to $\mu > 1$. However, the shape of the increasing function $\sqrt{\mu g(\Delta\alpha)}$ depends on the type of problem. If the slope of the energy criterion curve increases continuously until the intersection with the stress criterion curve, it can be deduced that the growth of the interface crack will be infinitesimal with $\Delta\alpha_{\mathrm{c}} \to 0$. Thus, leading to a stable crack propagation, i.e. if the displacement at the ends of the beams is continuously increased, the interface debond is also produced in a continuous way. Consequently, as in the original LEBIM, the

interface failure is only ruled by the ERR, and the failure criterion can be expressed as:

$$\frac{\bar{u}}{w_{\mathrm{c}}} \geq \frac{\bar{u}_{\mathrm{f}}}{w_{\mathrm{c}}} = \sqrt{\frac{\mu}{\hat{G}(\lambda - \alpha')}} \tag{4.36}$$

Fig. 4.7 shows the characteristic behaviour associated to the failure criterion of the original LEBIM against the energy failure criterion of the CCFFM+LEBIM. While the energy based criterion of the coupled criterion is function of a finite increase of the crack length, $\Delta\alpha$, the criterion on which the infinitesimal failure is based uses a function of a crack growth α'. For a better understanding of the problem, results in Fig. 4.7 do not considered a pre-crack, i.e. $\alpha = 0$.
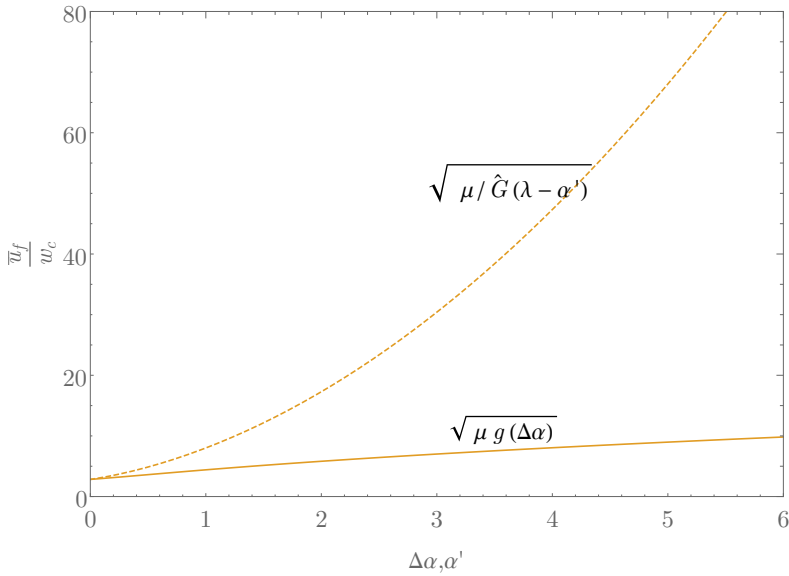
Figure 4.7: $\sqrt{\mu g(\Delta\alpha)}$ and $\sqrt{\frac{\mu}{\hat{G}(\lambda - \alpha')}}$ functions, representing the energy criterion of LEBIM and CCFFM+LEBIM with $\mu = 8$, respectively.

4.3.2   Solution obtained by PMTE-SC.

In Section 3.3, the relation between the change in the potential energy of a system and its deformation was defined as $\Delta\Pi = \Delta U - \Delta W$, but ΔW vanishes under displacement control. Therefore, the incremental energy balance for this test under displacement control can be expressed as:

$$\Delta U(\Delta a) + \Delta R(\Delta a) \leq 0 \tag{4.37}$$

So, in this subsection $U(a) + R(a)$ will be minimized subjected to a stress condition. The first section explains the energy formulation used within this approach to obtain the function $U(a) + R(a)$, which must be minimized. That section also provides the calculation of the minimum by the definition of the ERR, for this specific case. Later,

the CCFFM+LEBIM by PMTE-SC is applied to the same test which was evaluated by the CCFFM+LEBIM in the Section 4.3.1.

4.3.2.1   Energy based formulation

For an easier comprehension of the formulation, the zone of the beams including an undamaged interface is denominated AB, and the zone of the beams where the interface is damaged is named BC, as shown in Fig. 4.8.
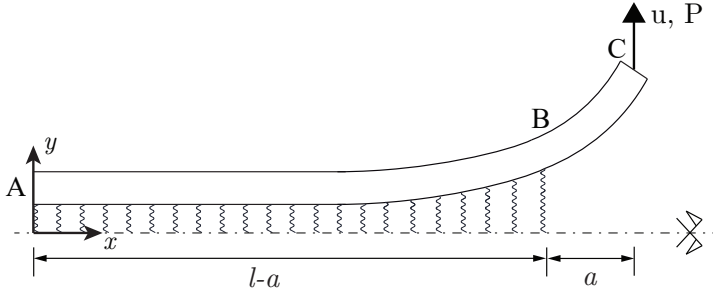
Figure 4.8: DCB test configuration.

In general, the deformation energy of both zones according to Euler-Bernoulli's theory can be expressed as:

$$\begin{aligned} U_{\mathrm{AB}} &= 2U_{\mathrm{AB\ beam}} + U_{\mathrm{AB\ interfaces}} \\ U_{\mathrm{BC}} &= 2U_{\mathrm{BC\ beam}} \end{aligned} \tag{4.38}$$

where,

$$\begin{aligned} U_{\mathrm{AB\ beam}} &= 2\int_{\mathrm{AB}} \frac{1}{2}\left(\frac{12M(x)^2}{E'h^3 b}\right)\mathrm{d}x \\ U_{\mathrm{AB\ interfaces}} &= \int_{\mathrm{AB}} b\ \sigma(x)w(x)\mathrm{d}x \\ U_{\mathrm{BC\ beam}} &= 2\int_{\mathrm{BC}} \frac{1}{2}\left(\frac{12M(x)^2}{E'h^3 b}\right)\mathrm{d}x \end{aligned} \tag{4.39}$$

Eqs. (4.39) show that the deformation energy of a beam is the sum of the deformation energies corresponding to the internal work within the beam and that corresponding to the springs along the interface. Notice that, as this model is based on the Euler-Bernoulli beam theory, the shear deformation energy has not been taken into account, because the shear strain is neglected. It should also be noticed that the displacements along the interface $w(x)$ is half of $\delta_n(x)$, the relative normal displacement between the two beams. The solution for $w(x)$ is defined in Eq.(4.24) and it depends on two problem variables: α and ξ. The dependence on these two variables must be taken into account in order to calculate the definite integrals of Eqs. (4.39).

Accounting for the Eqs. (4.39) and substituting the equations of the beam moment (4.8) and the stress field along the interface (4.7), the elastic energy at AB zone can be written as:

$$U_{\text{AB}}(\alpha) = \frac{E'h^3b}{12}\frac{\bar{u}^2}{l_{ch}^3}\int_0^{\lambda-\alpha}\left(\frac{\delta^2\hat{w}(\xi,\alpha)}{\delta\xi^2}\right)^2 + 4\hat{w}(\xi,\alpha)^2\mathrm{d}\xi \tag{4.40}$$

where the first term of the integral is associated with the deformation of the two beams and the second term is associated with the deformation of the interface.

For the determination of the elastic energy of the BC zone, the equations of the free-body diagram developed in Section 4.2 can not be used, because these are only formulated for the zone where an elastic interface exists. However, the bending moment equation in BC zone can be easily deduced, as:

$$M(x) = P(l-x) \quad \text{for all} \quad x, \ l-a \le x \le l \tag{4.41}$$

Taking into account the relationship between the load of the beam ends and the vertical displacement of the crack tip by Eq. (4.21), the elastic energy of BC zone can be expressed as:

$$U_{\text{BC}}(\alpha) = \frac{E'h^3b}{12}\frac{\bar{u}^2}{l_{ch}^3}\int_{\lambda-\alpha}^{\lambda}\left((\lambda-\xi)\frac{\delta^3\hat{w}(\lambda-\alpha,\alpha)}{\delta\xi^3}\right)^2\mathrm{d}\xi \tag{4.42}$$

The strain energies in both zones can also be expressed in their dimensionless form:

$$\hat{U}_{\text{AB}}(\alpha) = \frac{12l_{ch}^3}{E'h^3b\bar{u}^2}U_{\text{AB}}(\alpha) \quad \text{and} \quad \hat{U}_{\text{BC}}(\alpha) = \frac{12l_{ch}^3}{E'h^3b\bar{u}^2}U_{\text{BC}}(\alpha) \tag{4.43}$$

Thus, the energy dissipated at the abrupt formation of a new crack and the total dissipated energy including the formation of the new debond along the interface are:

$$R(\Delta a) = G_{\text{Ic}}\Delta a\ b \quad \text{and} \quad R(a) = G_{\text{Ic}}a\ b \tag{4.44}$$

Finally, the function to be minimized is:

$$\begin{aligned} U(\alpha) + R(\alpha) &= \frac{E'h^3b\bar{u}^2}{12l_{ch}^3}\left(\hat{U}_{\text{AB}}(\alpha) + \hat{U}_{\text{BC}}(\alpha)\right) + b\ l_{ch}G_{\text{Ic}}\alpha \\ &= b\ l_{ch}G_{\text{Ic}}\left(\frac{\bar{u}^2}{4\mu w_{\text{c}}^2}\left(\hat{U}_{\text{AB}}(\alpha) + \hat{U}_{\text{BC}}(\alpha)\right) + \alpha\right) \end{aligned} \tag{4.45}$$

And its dimensionless form:

$$\hat{U}(\alpha) + \hat{R}(\alpha) = (U(a) + R(a))\frac{1}{b\ l_{ch}G_{\text{Ic}}} = \left(\frac{\bar{u}^2}{4\mu w_{\text{c}}^2}\left(\hat{U}_{\text{AB}}(\alpha) + \hat{U}_{\text{BC}}(\alpha)\right) + \alpha\right) \tag{4.46}$$

The above expression (4.46) is independent of the initial pre-crack (α_0), since it is only affected by the term α which is evaluated in the interval $\alpha_0 < \alpha < \lambda$.

The curves of the energy criterion shown in Fig. 4.9 are obtained using Eq. (4.46) and the parameters included in Table 4.1 for different imposed displacement values at the ends of the beams.

Results in Fig. 4.9 show that for small values of the imposed displacement ($\frac{\bar{u}}{w_{\text{c}}}$), the minimum of the function is obtained at $\alpha = 0$, i.e. no damage growth. However,
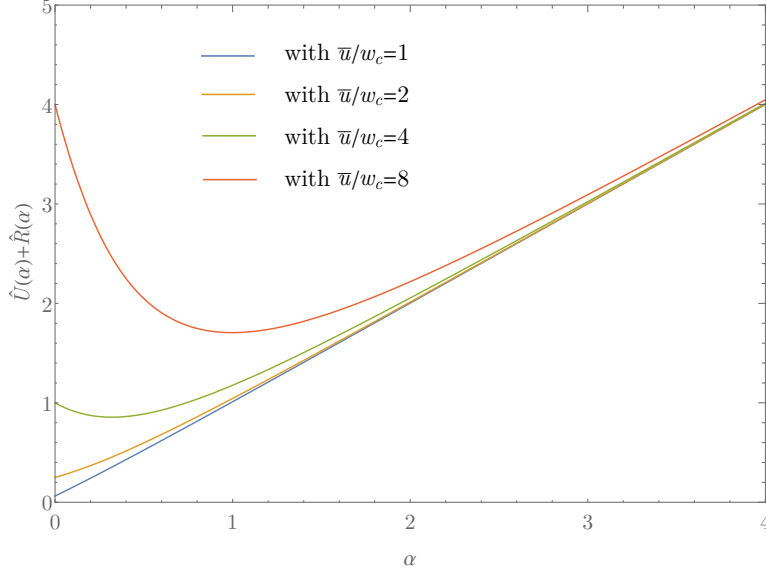
Figure 4.9: Function $\hat{U}(\alpha) + \hat{R}(\alpha)$ for several values of the dimensionless boundary condition in displacement $\frac{\bar{u}}{w_c}$.

when the imposed displacement increases, the energy function curves become convex producing a minimum for values of $\alpha > 0$. It should be noted that if the problem had an initial pre-crack $\alpha_0 = 2$, none of the four imposed displacements represented in the Fig. 4.9 would cause an interface failure. This is because none of the curves have their minimum for α values greater than 2.

A way to find the local minimum of the curves obtained by Eq. (4.46), the first-derivative test can be used within the area where the stress criterion is fulfilled.

$$\frac{d\hat{U}(\alpha)}{d\alpha} + \frac{d\hat{R}(\alpha)}{d\alpha} = 0 \tag{4.47}$$

The definition of the ERR presented in Eq.(4.32) is used to calculate the first term of the derivative. Based on LEFM framework, the ERR $(G(a))$ for crack growth can be calculated as the variation of the potential energy per unit area of the crack $\left(-\frac{d\Pi}{dA}\right)$. However, as this is a displacement control test, in this case, the work developed by the boundary load is null when the crack along the interface growths. For this reason, the energy required for the crack growth is exclusively obtained from the elastic energy of the system:

$$G(a) = -\frac{d\Pi(a)}{dA} = -\frac{dU(a)}{dA} \tag{4.48}$$

Using Eq. (4.32) the ERR can be obtained at the crack tip with $\xi = \lambda - \alpha$.

$$G(a(\lambda - \alpha)) = 2k_n\bar{u}^2\hat{G}(\lambda - \alpha) = 2k_n\bar{u}^2(\hat{w}\,(\lambda - \alpha, \alpha))^2 \tag{4.49}$$

Also, the derivative of the elastic energy of the whole system with respect to crack growth α can be obtained using Eq. (4.43):

$$\frac{\mathrm{d}U(a(\alpha))}{\mathrm{d}A} = \frac{E'h^3b\bar{u}^2}{12l_{ch}^3\,b}\left(\frac{\mathrm{d}\hat{U}_{AB}(a)}{\mathrm{d}a} + \frac{\mathrm{d}\hat{U}_{BC}(a)}{\mathrm{d}a}\right) = \frac{\bar{u}^2k_n}{2}\left(\frac{\mathrm{d}\hat{U}_{AB}(\alpha)}{\mathrm{d}\alpha} + \frac{\mathrm{d}\hat{U}_{BC}(\alpha)}{\mathrm{d}\alpha}\right)$$

$$(4.50)$$

Therefore, the relationship between the expressions of the ERR and the one derived from the elastic energy, in dimensionless form, becomes:

$$4(\hat{w}\left(\lambda - \alpha, \alpha\right))^2 = -\left(\frac{\mathrm{d}\hat{U}_{AB}(\alpha)}{\mathrm{d}\alpha} + \frac{\mathrm{d}\hat{U}_{BC}(\alpha)}{\mathrm{d}\alpha}\right) \tag{4.51}$$

$$4\hat{G}(\lambda - \alpha) = -\left(\frac{\mathrm{d}\hat{U}_{AB}(\alpha)}{\mathrm{d}\alpha} + \frac{\mathrm{d}\hat{U}_{BC}(\alpha)}{\mathrm{d}\alpha}\right) \tag{4.52}$$

Fig. 4.10 shows the relationship between the elastic energy and the ERR of the DCB test under displacement control. Noticed that both curves are perfectly overlapping.
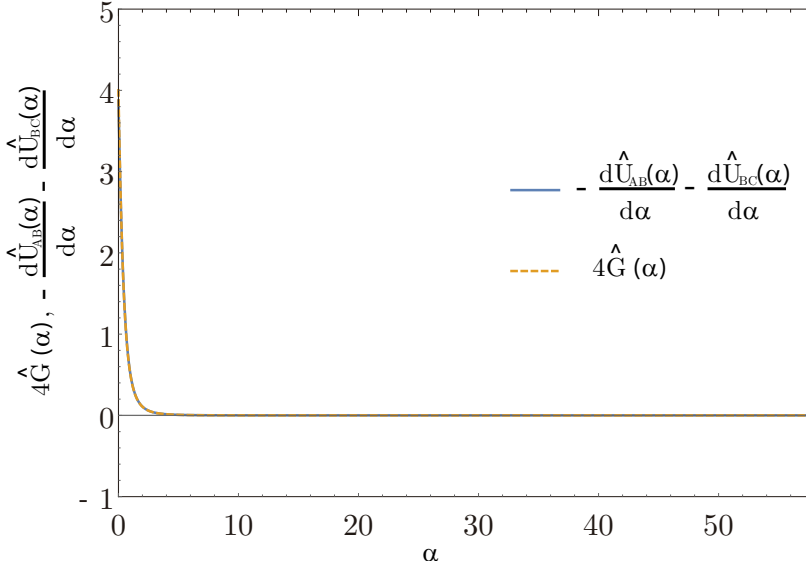
Figure 4.10: Relationship between the elastic energy and the ERR of the DCB test under displacement control.

Hence, the local inflection point of the function is produced for an α value which satisfies:

$$\frac{\mathrm{d}U(a)}{\mathrm{d}A} + \frac{\mathrm{d}R(a)}{\mathrm{d}A} = -2k_n\bar{u}^2(\hat{w}(\lambda - \alpha, \alpha))^2 + G_{Ic} = 0 \tag{4.53}$$

And in dimensionless form:

$$\frac{\bar{u}^2}{\mu w_c^2}\left(\hat{w}(\lambda - \alpha, \alpha)\right)^2 = 1 \tag{4.54}$$

Figure 4.11 represents the results of Eq. (4.46) for the data included in Table 4.1 for several values of the two input variables: the displacement imposed at the ends of the beams ($\frac{\bar{u}}{\mu w_c}$) and the damaged interface area (α). The sum of the strain energy and the dissipated energy forms a convex surface where the "warm" colours represent the areas of the surface with the lowest energy, and "cool" colours the areas with the highest energy. The red dots located in the surface valley are the minimum values for each load ($\frac{\bar{u}}{\mu w_c}$) obtained using Eq. (4.54).
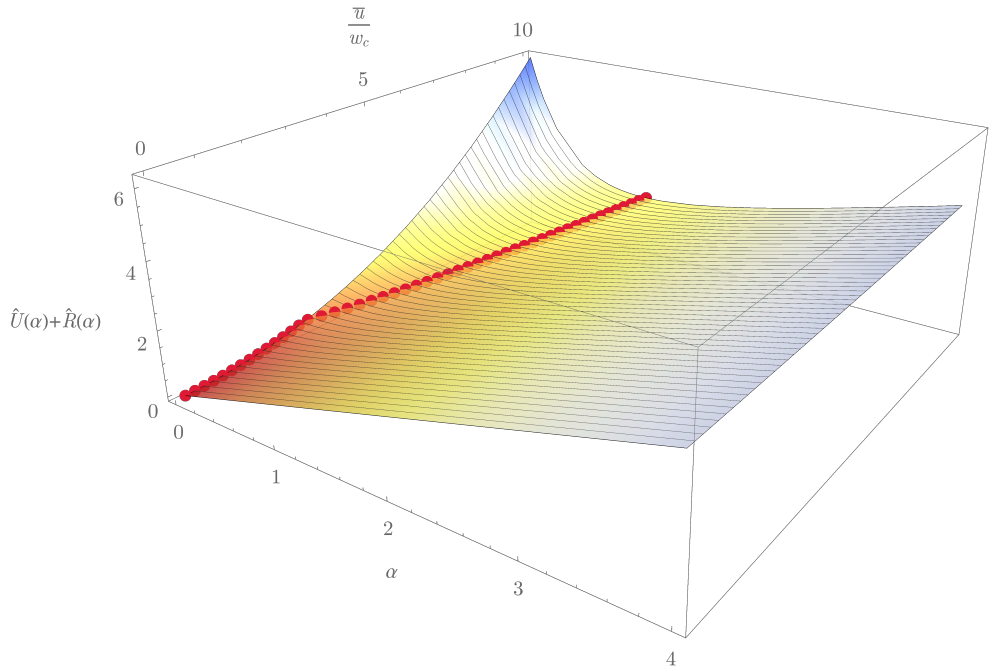
Figure 4.11: Surface which represents Eq. (4.46).

4.3.2.2 Application of the PMTE-SC to a specific case and comparison between methods.

Fig.4.55 shows the function $\hat{U}(\alpha) + \hat{R}(\alpha)$ for the geometrical and mechanical characteristics described in the Table 4.2 and with $\mu = 8$.

As an example and in order to describe the energy behaviour of the system, eleven different $\frac{\bar{u}}{w_c}$ values have been used, which represent the displacement imposed at beam ends for the same w_c. These displacements are increased from 1 to 3.03, in intervals of 0.203 (this value is chosen so the initial part of one the curves coincides with the initial part of the energy criterion curve, see Fig. 4.7, and to get a reasonable size of the displacement increment). Fig. 4.12 shows that for increasing values of $\frac{\bar{u}}{w_c}$ the initial values of the different curves and their curvatures also increase.

Before looking for the minimum of each represented function, the interface zone that verifies the stress criterion must be analysed in each curve, because it is only within this zone that the minimum of the function may occur.

The interface zone that fulfills the stress criterion can be obtained by verifying the following expression, for each ξ point along the undamaged interface:

$$\frac{\bar{u}}{w_{\mathrm{c}}} \geq \frac{1}{\hat{w}(\xi, \alpha)} \quad \text{then} \quad 1 \geq \frac{w_{\mathrm{c}}}{w(\xi, \alpha)}, \tag{4.55}$$

This expression is similar to Eq. 4.34 applied in the curves methodology.
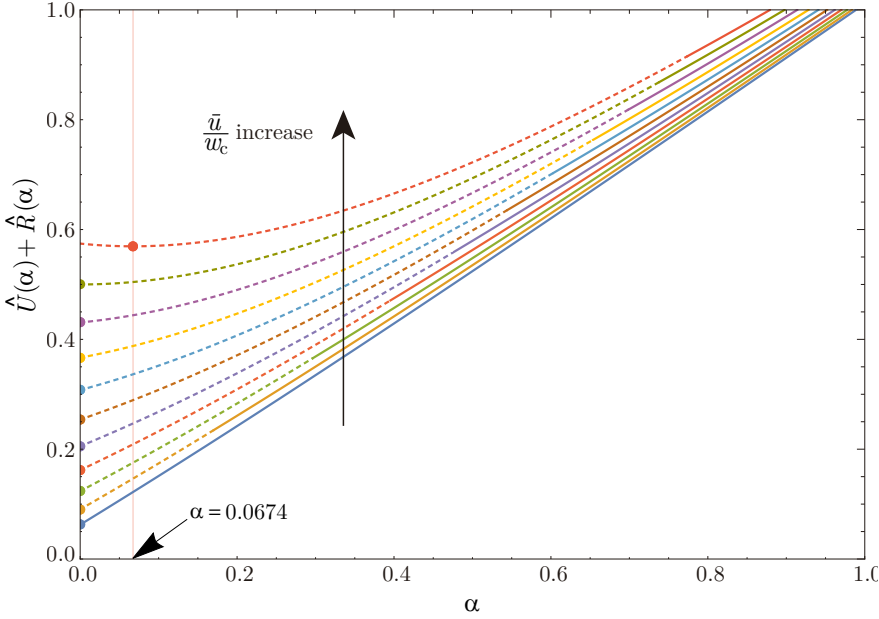
Figure 4.12: Function $\hat{U}(\alpha) + \hat{R}(\alpha)$ for several values of the dimensionless boundary condition in displacement $\frac{\bar{u}}{w_{\mathrm{c}}}$ (ranging from 1 to 3.03 in intervals of 0.203). The discontinuous lines are the zone including α values that satisfy the stress criteria. The dots represent the minimum at each curve.

Eq. (4.55) provides the zone (α values) including points which are prone to fail by the imposed displacement $\bar{u}$. This zone is represented in the Fig. 4.12 by a discontinuous line in each curve. It should be noted that as $\frac{\bar{u}}{w_{\mathrm{c}}}$ increases the zone that satisfies the stress criteria also increases. Starting from the first curve, where not a single point verifies Eq. (4.55), to the last curve, which has the largest zone where failure is possible. After determining the zone where interface failure is possible due to stress criteria, the minimum of each curve $\hat{U}(\alpha) + \hat{R}(\alpha)$ is calculated by the ERR, shown in the previous section. However, the minimum of each curve, with the exception of the last one, is located at the beginning. This means that the failure only occurs in the last (red) curve, even though the stress criterion may allow the failure in the other cases. According to Fig. 4.12, for the $\frac{\bar{u}}{w_{\mathrm{c}}} = 3.03$ the crack growth is produced for $\alpha = 0.0674$.

For a deeper understanding of the PMTE-SC methodology, the results in Fig. 4.12 are compared with the results obtained by the CCFFM+LEBIM by the curves methodology, developed in Section 4.3.1. Fig. 4.13 shows the curves $s(\Delta\alpha)$, $\sqrt{\mu g(\Delta\alpha)}$ and $\sqrt{\frac{\mu}{\hat{G}(\lambda - \alpha')}}$ for $\mu = 8$, as done in Section 4.3.1. For comparison purposes, horizontal lines are included to the plot, these lines coincide with $\frac{\bar{u}}{w_{\mathrm{c}}}$ values and colours used in
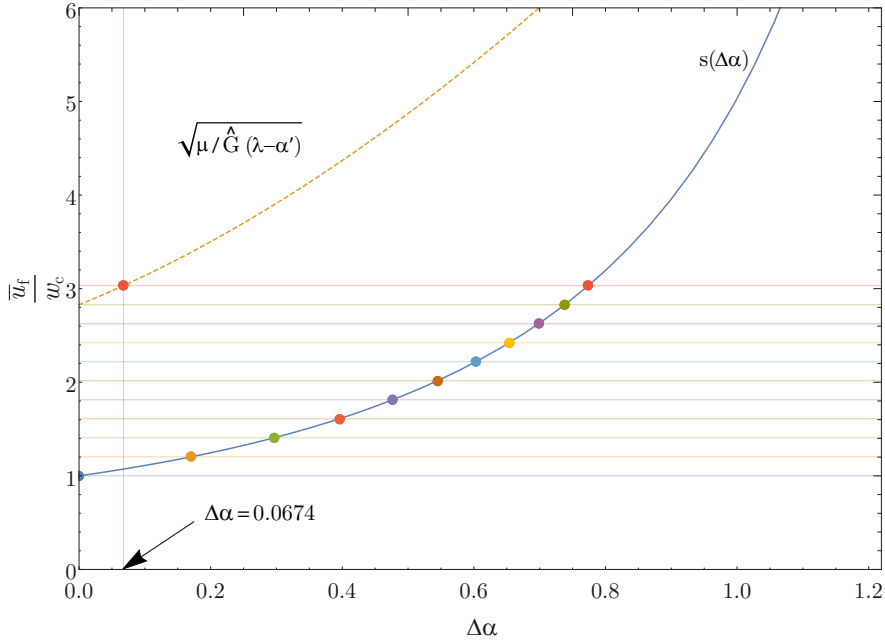
Figure 4.13: Comparison of the $\Delta\alpha$ value predicted using PMTE-SC and the curves methodology. Each horizontal line represents the same aplied dimensionless displacement $\frac{\bar{u}}{w_{\mathrm{c}}}$ included in Fig. 4.12.

Fig. 4.12. The intersection of the horizontal lines with the $s(\Delta\alpha)$ curve is indicated with points of the same colour as the horizontal lines. The dots define, for each $\frac{\bar{u}}{w_{\mathrm{c}}}$, the length of the zone $\Delta\alpha$ that may allow the damage due to the stress criteria. Notice that this zone coincides with the end of the dotted lines in the Fig. 4.12. Moreover, according to the curves methodology, $\frac{\bar{u}}{w_{\mathrm{c}}} = 3.03$ is the only applied displacement that propagates the interface crack (notice that the crack growth predicted is infinitesimal) with a $\Delta\alpha = 0.0674$, exactly as the prediction by the PMTE-SC approach.

4.3.3 Numerical simulation

This section presents a comparison of the numerical results obtained using both CCFFM+LEBIM methodologies described in Section 3.1 for the DCB test under displacement control.

Lets recall that for this specific test, the growth of the interface failure is infinitesimal as the imposed displacement at the ends of the beams increases. Therefore, instead of using the algorithm developed in Section 3.2.1 based on the definition of the curves of the energy and tension criteria, an algorithm based on the LEBIM and developed by Távara et al. (2019) is used, including the interface characteristics affected by the parameter μ, as explained in Section 3.1.3.

Both the algorithm based on LEBIM and the algorithm based on the PMTE-SC (Section 3.3.1), have been developed to be used together with the FEM-based commercial code ABAQUS. Thus, the mesh and the imposed boundary conditions for both cases are exactly the same, see Fig. 4.14. The mechanical and geometrical

characteristics of the model indicated in the Table 4.2 are used, in order to be also able to compare the analytical and numerical results.
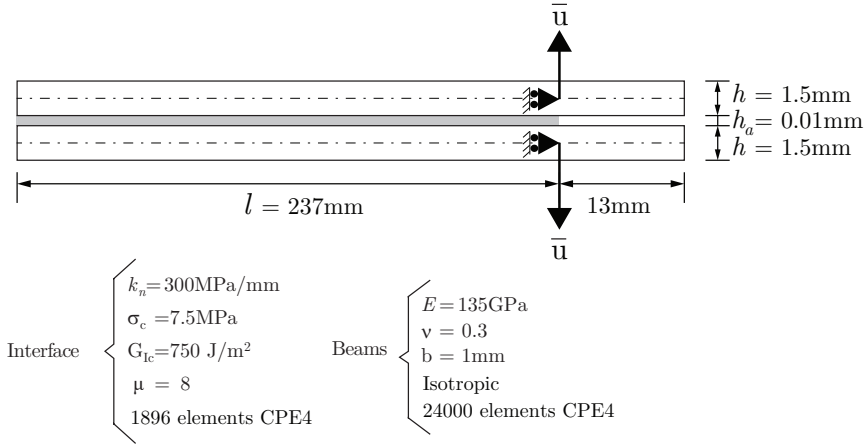
Figure 4.14: DCB boundary conditions used in the numerical model under displacement control.

The numerical code of the original LEBIM uses as input the mechanical parameters in Fig. 4.14, and gives as result the imposed displacement $\bar{u}$ at the ends of the beams that provokes the failure of the interface. Each numerical step produces the failure of a single element. Although the code also allows to use the number of elements to be broken as an input parameter (as a different solving option), in this case where the damage is infinitesimal, it is more appropriate that each numerical step "breaks" a single element only.

It is also interesting the comparison of the numerical and analytical results for the PMTE-SC included in this section. For this purpose, an imposed displacement $\bar{u}$ close to the value that breaks the first element using the original LEBIM is imposed. Resulting in an imposed displacement that do not produce damage in any element. Then, the code automatically looks for the displacement that produces the damage in an element. Subsequently, in each k step, the imposed displacement is increased (in the present example the increment is set to 0.005mm) and each step may cause a finite fracture along the interface or not.

Fig. 4.15 shows ten curves, associated to the first ten steps, representing the sum of $U(a) + R(a)$ in the system. As in the previous section, the discontinuous part within a line corresponds to the interface zone that fulfills the stress criterion and the continuous line corresponds to the interface zone that does not.

These curves are calculated by the Eq. (4.46) and (4.55), and the analytical minimum provided by (4.54) is indicated by an asterisk. The numerical minimum provided by the code implemented in Python is shown as a solid dot. The difference, in terms of a, between the asterisks and the dots are always smaller than the element size, so this difference can be attributed to the discretization of the interface.

Fig. 4.16 presents the numerical load-displacement curve for the DCB test under displacements control by both the original LEBIM code and the PMTE-SC code. Both curves are plotted in the form of a sawtooth wave because the system is loaded
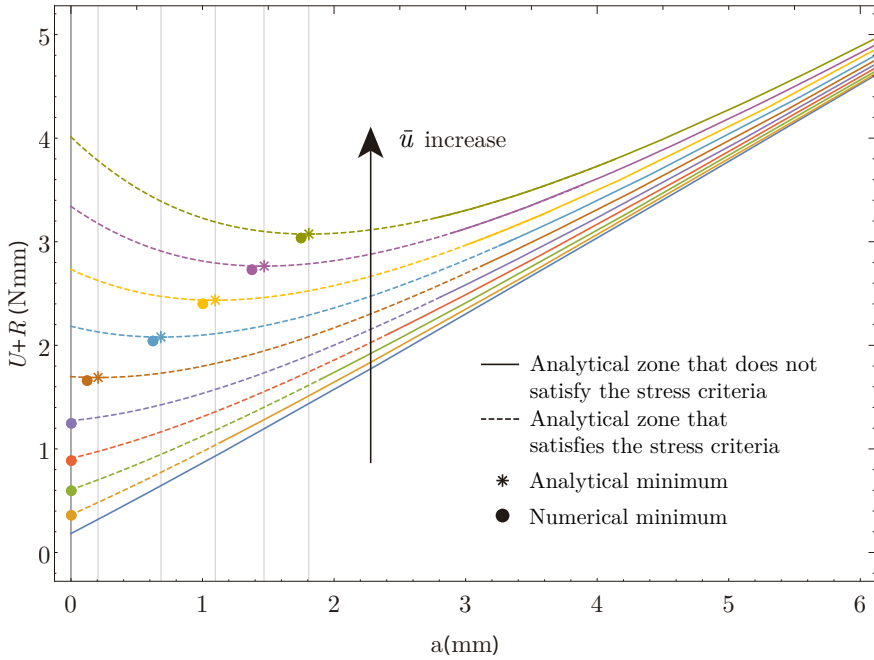
Figure 4.15: Functions $U(a) + R(a)$ for a specific dimensionless boundary condition in displacement $\bar{u}$. The discontinuous part of the lines are the zone which satisfies the stress criteria. The dots are the minimum of every curve obtained by the numerical code. The asterisks are the minimum of every curve obtained by Eq. (4.55).

in displacement. However, the sawtooth size of the LEBIM results is smaller than those provided by the PMTE-SC. This is because the LEBIM code breaks element by element, while in the PMTE-SC code the number of elements damaged along the interface depends on the applied load. At the initial part, jumps in both curves coincide, i.e. element by element. This is due to the slope of the curve is steep. However, due to the load (imposed displacement) increment is constant for each step, in the PMTE-SC method, when the curve decreases its slope damage may be produced along more elements. It should be noticed that damage could be reduced with a routine that controls the size of the load increments, depending on the control variable chosen. Even so, the PMTE-SC represents very well the behaviour of a real test, where a crack is produced for a given imposed displacement.
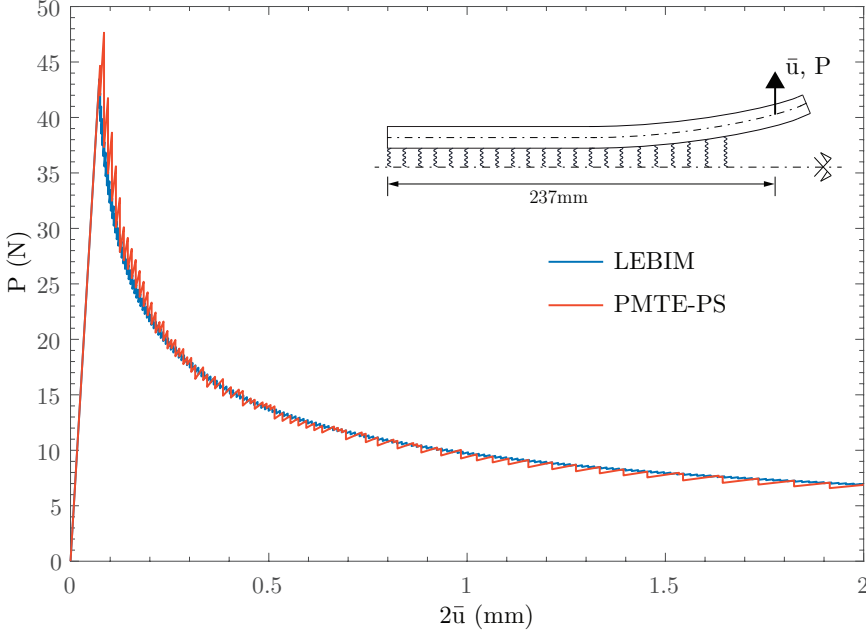
Figure 4.16: Load-Displacement curve for the DCB test under displacement control.

4.4 CCFFM applied to linear-elastic interfaces for the DCB under load control.

4.4.1 Solution obtained by the stress and energy criteria curves.

For the specific case of the BCD test under load control, the ERR can be expressed as:

$$G(\lambda-\alpha) = \frac{\bar{P}^2}{b^2 l_{ch}^2 2k_n}\hat{\sigma}^2(\lambda-\alpha,\alpha) = \frac{\bar{P}^2}{b^2 l_{ch}^2 2k_n}\hat{G}(\lambda-\alpha) \quad \text{with} \quad \hat{G}(\lambda-\alpha) = \hat{\sigma}^2(\lambda-\alpha,\alpha)$$

(4.56)

Following the above relations, the energy criterion can be rewritten as:

$$\frac{\bar{P}^2}{b^2 l_{ch}^2 2k_n G_{\text{Ic}}} \geq g(\Delta\alpha) \quad \text{with} \quad g(\Delta\alpha) = \frac{\Delta\alpha}{\int_{\Delta\alpha} \hat{G}(\lambda-\alpha)\,d\alpha}$$

(4.57)

As in the previous section, the stress criterion can be written as a function of σ_c:

$$\text{if} \quad s(\xi) = \frac{1}{\hat{\sigma}(\xi,\alpha)} \quad \text{then} \quad \frac{\bar{P}}{b\,l_{ch}\sigma_c} \geq s(\Delta\alpha) \quad \text{for all} \quad \xi,\ \lambda-\Delta\alpha \leq \xi \leq \lambda$$

(4.58)

and for a specific value of α.

Finally, if the parameter μ, defined in Section 3.1.3, is rewritten as function of the critical normal tension for pure mode I ($\mu = \frac{2k_n G_{\text{Ic}}}{\sigma_c^2}$), the CCFFM by can be defined as:

$$\frac{\bar{P}}{b\,l_{ch}\sigma_{\rm c}} \geq \frac{\bar{P}_{\rm f}}{b\,l_{ch}\sigma_{\rm c}} = \min_{\Delta\alpha}\max\left\{s(\Delta\alpha), \sqrt{\mu\ g(\Delta\alpha)}\right\} \tag{4.59}$$

where $\bar{P}_{\rm f}$ is the minimum load applied to the beam end that satisfies both criteria and produces a crack with length $\alpha_{\rm c} = \Delta\alpha$.

Following Section 4.3.1, for a deeper understanding of the behaviour of the failure criterion, included in Eq. (4.59), for this specific test, both curves are represented with the geometrical and mechanical characteristics described in Table 4.2 and for $\mu = 8$.
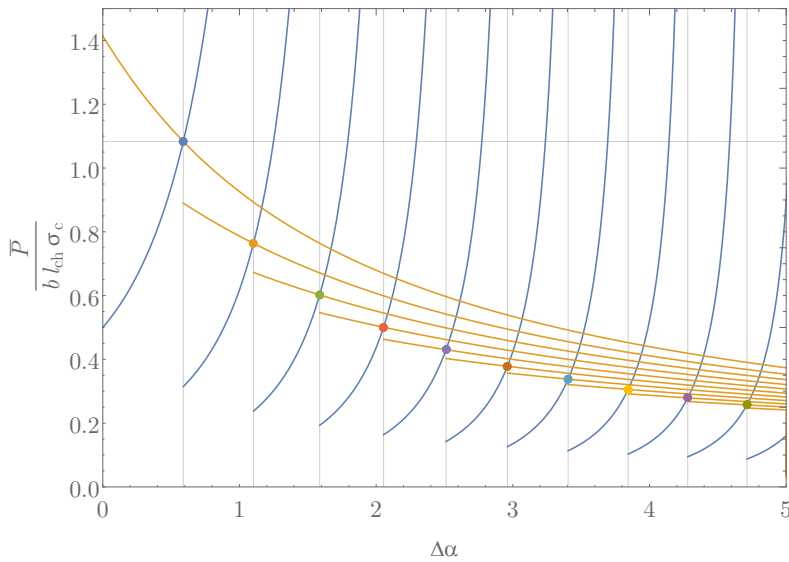
Figure 4.17: $s(\Delta\alpha)$ (blue lines) and $\sqrt{\mu\ g(\Delta\alpha)}$ (yellow lines) functions for the DCB in load control with $\mu = 8$ and several load steps.

In Fig.4.17, yellow lines represent the energy based criterion, while the blue lines represent the stress based criterion. Unlike the previous test, the energy criterion starts with a negative slope, above the stress criterion. Therefore, the minimum that satisfies both criteria is the intersection of the curves. This produces an instantaneous finite segment of the crack $\alpha_{\rm c}$ for a specific load $\frac{\bar{P}_{\rm f}}{b\,l_{ch}\sigma_{\rm c}}$. Both the finite damage and the load are defined by the intersection of both curves. In Fig.4.17, the coordinates of the intersection points $(\alpha_{\rm c}, \frac{\bar{P}_{\rm f}}{b\,l_{ch}\sigma_{\rm c}})$ for each step of the CCFFM+LEBIM is depicted with different colours. Note that if a crack grows up to $\alpha_{\rm c}^{\rm i}$ in an i step, the evaluation of the next crack growth starts at this point.

In Fig.4.18 each point is defined by $\alpha_{\rm c}$ and $\frac{\bar{P}_{\rm f}}{b\,l_{ch}\sigma_{\rm c}}$ for each load step, until the end of the interface. In the DCB test under displacement control, the crack propagation is stable. However, Fig.4.18 shows an unstable crack propagation, because the load $\frac{\bar{P}_{\rm f}}{b\,l_{ch}\sigma_{\rm c}}$ in the first step is the highest load of all the steps.
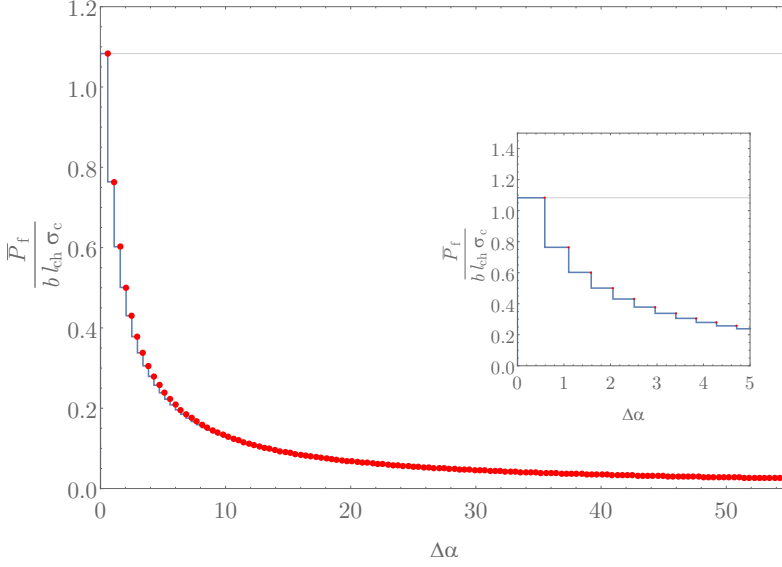
Figure 4.18: Load - Crack propagation curve for the DCB test under load control.

4.4.2   Solution obtained by PMTE-SC

This section is developed in a similar way as the displacement control test in Section 4.3.2 but with some important differences when calculating the system energy. For this reason, the procedure to be followed will not be so detailed, but the differences concerning the previous test studied will be highlighted. An important difference is that the potential energy variation of the system is $\Delta\Pi = \Delta U - \Delta W$, without neglecting the term of work, because it does not disappear under load control. Therefore, the incremental energy balance for the test under load control can be expressed as:

$$\Delta U(\Delta a) - \Delta W(\Delta a) + \Delta R(\Delta a) \leq 0 \qquad (4.60)$$

Thus, in this subsection $U(a) - W(a) + R(a)$ will be minimized subjected to a stress condition.

The outline of this section will follow the same structure as the one in Section 4.3.2.

4.4.2.1   Energy based formulation.

Although the energy based formulation in this section is similar to the one in Section 4.3.2, this has been adapted to the stress field along the interface defined in Eq. (4.7).

Therefore, accounting for Eqs. (4.39) and substituting the equations of the beam moment (4.8) and the stress field along he interface (4.7), the elastic energy at AB zone can be written as:

$$U_{AB}(\alpha) = \frac{\bar{P}^2}{b\,l_{ch}2k_n}\int_0^{\lambda-\alpha}\frac{1}{4}\left(\frac{\delta^2\hat{\sigma}(\xi,\alpha)}{\delta\xi^2}\right)^2 + (\hat{\sigma}(\xi,\alpha))^2\,\mathrm{d}\xi \qquad (4.61)$$

Where the first term of the integral is associated with the deformation of the two beams and the second term with the deformation of the interface. To calculate the elastic energy of the BC section, the equation of bending moment in BC zone is used (Eq. (4.41)), being expressed as:

$$U_{\text{BC}}(\alpha) = \frac{\bar{P}2}{b\ l_{ch}2k_n} \int_{\lambda-\alpha}^{\lambda} 4(\lambda - \xi)^2 \mathrm{d}\xi \tag{4.62}$$

Thus, the dimensionless form of the elastic energies of Eqs. 4.61 and 4.62 are:

$$\hat{U}_{\text{AB}}(\alpha) = \frac{b\ l_{ch}2k_n}{\bar{P}2} U_{\text{AB}}(\alpha) \quad \text{and} \quad \hat{U}_{\text{BC}}(\alpha) = \frac{b\ l_{ch}2k_n}{\bar{P}2} U_{\text{BC}}(\alpha) \tag{4.63}$$

The energy dissipated at this abrupt formation of a new crack and the total dissipated energy including the formation of the new crack along the interface is the same than under displacement control Eq. (4.44).

In order to calculate the work produced by the loads in the system ($W = 2\bar{P}u(\bar{P})$), the load applied at the end of the beams ($\bar{P}$) and the displacement produced by these loads at the same point ($u(\bar{P})$) are needed. To get the displacement, the procedure represented in Fig. 4.2 is used, substituting adequately Eq. 4.7 in each definition of $w(x)$. Therefore the system work can be expressed as:

$$W(\alpha) = 2\bar{P}u(\bar{P}) = \frac{2\bar{P}2}{b\ l_{ch}2k_n} \left(\hat{\sigma}(\lambda - \alpha, \alpha) + \alpha \frac{\delta\hat{\sigma}(\xi, \alpha)}{\delta\xi} \bigg|_{\lambda-\alpha} + \frac{4}{3}\alpha^3 \right)$$

$$\text{with} \quad \hat{W}(\alpha) = \frac{b\ l_{ch}2k_n}{\bar{P}2} W(\alpha) \tag{4.64}$$
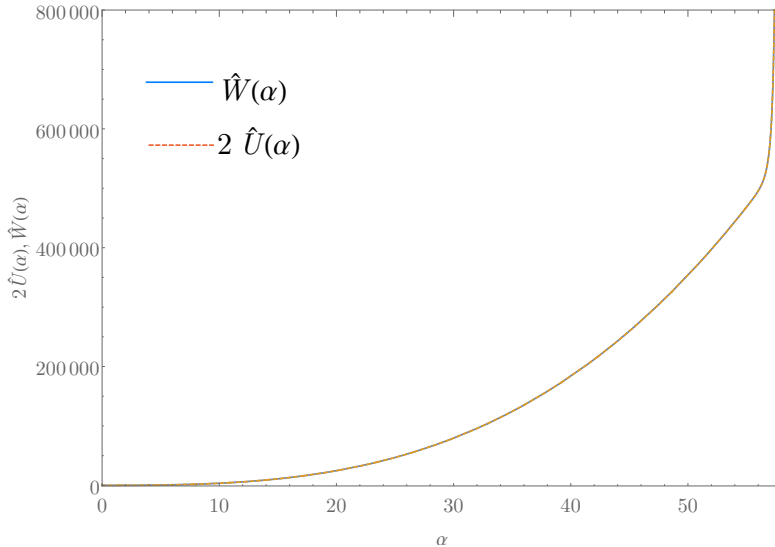
Figure 4.19: Relationshio between W and $2U$.

Note that according to Clapeyron's Theorem (Lamé, 1852; Fosdick and Truski-novsky, 2003), as the system of study has a linear elastic behaviour, it can be stated

that the total elastic energy of the system is equal to half of the work of the external loads that have originated the deformation process, i.e. $W = 2U$.

Fig. 4.19 shows the non-dimensional functions of work ($\hat{W}(\alpha)$) and twice the elastic energy ($\hat{U}(\alpha) = \hat{U}_{\mathrm{AB}}(\alpha) + \hat{U}_{\mathrm{BC}}(\alpha)$). It can be seen that both curves overlap perfectly.

Clayperon's theorem allows in this test a simpler formulation to express the energy function to be minimized:

$$
\begin{aligned}
U(\alpha) - W(\alpha) + R(\alpha) &= \frac{\bar{P}^2}{b\, l_{ch} 2k_n} \left(\hat{U}_{\mathrm{AB}}(\alpha) + \hat{U}_{\mathrm{BC}}(\alpha) - \hat{W}(\alpha) \right) + b\, l_{ch} G_{\mathrm{Ic}} \alpha \\
&= b\, l_{ch} G_{\mathrm{Ic}} \left(\frac{\bar{P}^2}{b^2\, l_{ch}^2 \mu \sigma_c^2} \left(\hat{U}_{\mathrm{AB}}(\alpha) + \hat{U}_{\mathrm{BC}}(\alpha) - \hat{W}(\alpha) \right) + \alpha \right) \\
&= b\, l_{ch} G_{\mathrm{Ic}} \left(-\frac{\bar{P}^2}{2\, b^2\, l_{ch}^2 \mu \sigma_c^2} \hat{W}(\alpha) + \alpha \right)
\end{aligned}
$$

$$(4.65)$$

Therefore, the dimensionless form of this function becomes:

$$
-\hat{U}(\alpha) + \hat{R}(\alpha) = (-U(a) + R(a)) \frac{1}{b\, l_{ch} G_{\mathrm{Ic}}} = \left(-\frac{\bar{P}^2}{2\, b^2\, l_{ch}^2 \mu \sigma_c^2} \hat{W}(\alpha) + \alpha \right) \quad (4.66)
$$

Equation (4.66) is independent of the initial pre-crack (α_0). Because the pre-crack would only affect the term α, which only causes a change of the evaluation interval of the function $\alpha_0 < \alpha < \lambda$.

If Eq. (4.66) is applied to the parameters defined in Table 4.1 for different imposed loads at the ends of the beams, the curves plotted in Fig. 4.20 are obtained. This
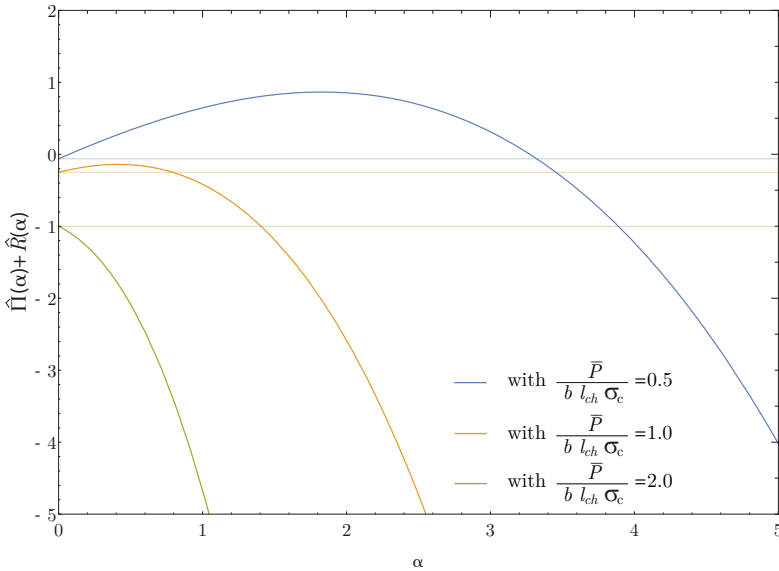
Figure 4.20: Functions $\hat{U}(\alpha) + \hat{R}(\alpha)$ for a specific dimensionless boundary condition in load $\frac{\bar{P}}{b\, l_{ch} \sigma_c}$.

figure shows that the different curves provided by the energy balance are concave and $U + R \to -\infty$. Therefore the global minimum will coincide with the upper endpoint of the function, i.e. the greatest lower bound. Therefore, the interface failure is only possible if the stresses are high enough to satisfy the stress criterion. At least, in the zone where a crack onset by tunneling through the total energy barrier is allowed, that is, in the zone from $\alpha = 0$ to the intersection point with the horizontal lines. This situation is possible because $\Delta U(a) + \Delta R(a) \leq 0$ is consistent. Notice that, in this scenario, it is not necessary to calculate the minimum energy function. Moreover, when the applied load increases, the zone needed to satisfy the stress criterion for tunneling decreases, making easier the failure.

4.4.2.2 Application of the PMTE-SC to a specific case and comparison between methods.

In order to explain the procedure of the CCFFM+LEBIM by PMTE-SC for this test, Fig. 4.67 shows the function $\hat{\Pi}(\alpha) + \hat{R}(\alpha)$ for the geometrical and mechanical characteristics described in the Table 4.2 and with a $\mu = 8$. As in the DCB under displacement control, eleven different $\frac{\bar{P}}{b\, l_{ch}\sigma_c}$ values are used, ranging from 0.5 to 1.47, in intervals of 0.097. The ratio $\frac{\bar{P}}{b\, l_{ch}\sigma_c}$ represents the load imposed at the ends of the beam for the same σ_c along the interface. Results show that when $\frac{\bar{P}}{b\, l_{ch}\sigma_c}$ values increases, the beginning of the curves and their maximums decrease.

In this test, the possible interface failure is determined by the zone that satisfies the stress criterion. Since tunneling is possible for a given α only if every points between 0 and α fulfill the stress criterion. The interface zone that satisfies the stress criterion can be obtained by checking the following expression, for each ξ point of the undamaged interface:

$$\frac{\bar{P}}{b\, l_{ch}\sigma_c} \geq \frac{1}{\hat{\sigma}(\xi,\alpha)} \quad \text{then} \quad 1 \geq \frac{\sigma_c}{\sigma(\xi,\alpha)}, \tag{4.67}$$

This expression is similar to Eq. 4.58 in the curve methodology.

The interface zone that satisfies Eq. (4.67) is represented in Fig. 4.21 by dashed lines. It should be noticed that,as $\frac{\bar{P}}{b\, l_{ch}\sigma_c}$ increases, the zone that fulfills the stress criterion also increases, from the first curve, where no point verifies Eq. (4.67), to the last curve, which has the largest zone where failure is possible. Although this zone increases with the applied load, it can be seen that in the first six curves the interface failure can not occur, since $\Delta\Pi(a) + \Delta R(a) > 0$. However, the load of the seventh curve (light blue) allows a crack onset by tunneling through the total energy barrier because $\Delta\Pi(\Delta a_{\text{crit}}) + \Delta R(\Delta a_{\text{crit}}) = 0$. In the last four curves, the applied loads allow the damage due to tunneling through the total energy barrier and subsequent unstable crack growth, because $\Delta\Pi(\Delta a_{\text{crit}}) + \Delta R(\Delta a_{\text{crit}}) < 0$. It is interesting to notice that this figure includes most of the possible cases described by Mantič (2014) and revisited in Section 3.3.

For a better understanding of the obtained results by the PMTE-SC methodology included Fig. 4.21, a comparison with the CCFFM+LEBIM by the curves methodology developed in Section 4.4.1 is carried out. Fig. 4.22 plots the curves $s(\Delta\alpha)$ and $\sqrt{\mu}\, g(\Delta\alpha)$ for $\mu = 8$, exactly as in the Section 4.4.1. Also, eleven horizontal lines have
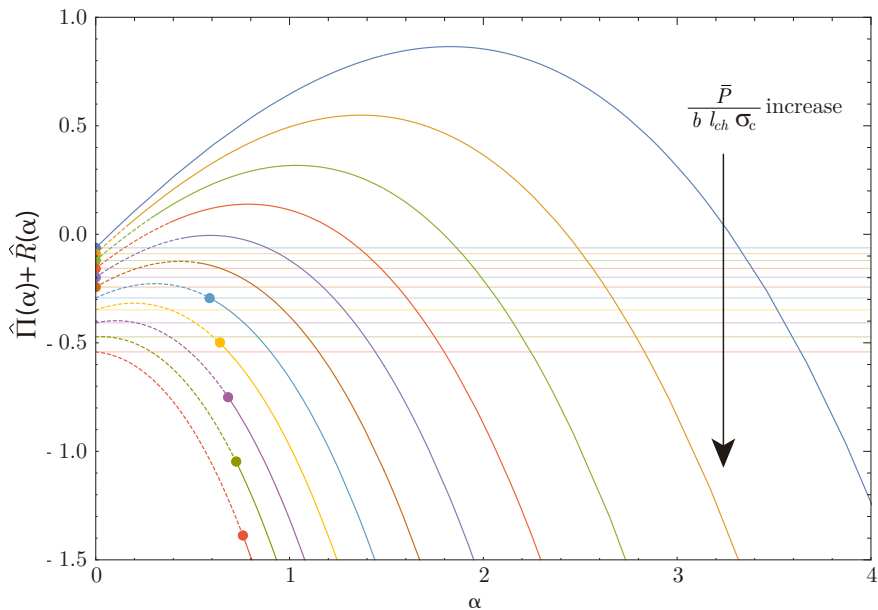
Figure 4.21: Functions $\hat{\Pi}(\alpha) + \hat{R}(\alpha)$ for a specific dimensionless boundary condition in load $\frac{\bar{P}}{b\,l_{ch}\,\sigma_c}$. The discontinuous part within a line represent the region of length α that satisfies the stress criteria.
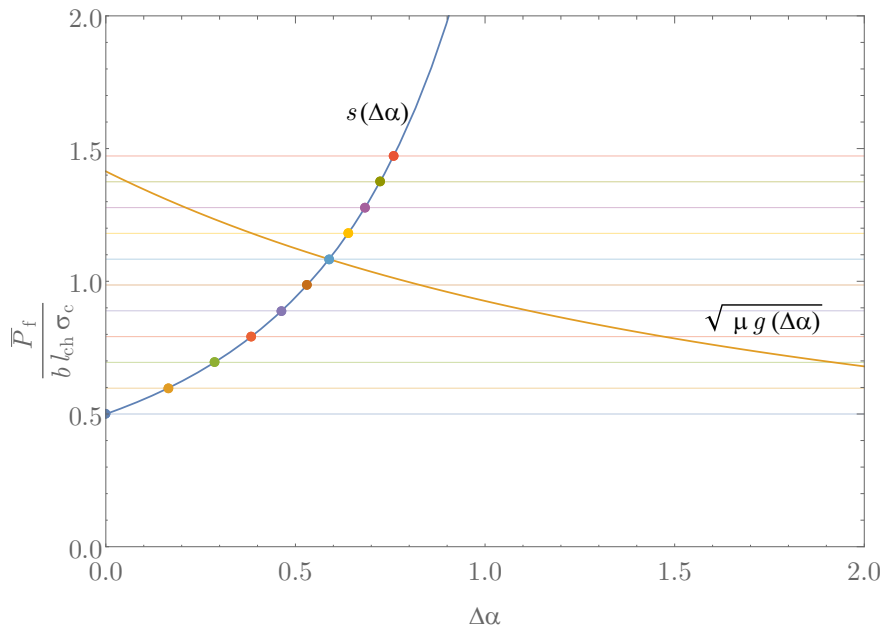
Figure 4.22: Comparison of the $\Delta\alpha$ value predicted using PMTE-SC and the curves methodology. Each horizontal line represents the same applied dimensionless load $\frac{\bar{P}}{b\,l_{ch}\sigma_c}$ included in Fig. 4.21.

been added which coincide with the $\frac{\bar{P}}{b\,l_{ch}\sigma_c}$ values and colours used in Fig. 4.21. The intersection of the horizontal lines with the curve $s(\Delta\alpha)$ is represented with points of the same colour as the horizontal lines. These points define, for each $\frac{\bar{P}}{b\,l_{ch}\sigma_c}$ value, the length of the region $\Delta\alpha$ that satisfies the stress criterion. These points coincide perfectly with the end of the dashed lines in Fig. 4.21. It is interesting to note, that from the seventh point (light blue) the horizontal lines also intercept the curve of the energy criterion. This light blue point defines the minimum load that satisfies both criteria. However, the rest of the loads, greater than this, produce an excess of energy that provoke an unstable growth of the interface crack.

4.4.3 Numerical simulation.

This section presents a comparison of the numerical results obtained with both CCFFM+LEBIM methodologies described in Section 3.1 for the DCB test under load control.

For this test, the algorithms developed in Section 3.2.1 (based on the definition of the curves of the energy and stress criteria) and the one developed in Section 3.3.1 (based on the PMTE-SC) are used. Both algorithms have been developed to be used together with the FEM-based commercial code ABAQUS. This fact allows that the mesh and the boundary conditions used in both cases to be exactly the same. These are described in Fig. 4.23. Unlike the displacement control test, in this test a new condition has been added at the non-loaded end of the upper beam in order to eliminate rigid body motions. The mechanical and geometrical characteristics of the model described in Table 4.2 are used, in order to be able to compare the analytical and numerical results.

$$\bar{P}$$

$$h = 1.5\text{mm}$$
$$h_a = 0.01\text{mm}$$
$$h = 1.5\text{mm}$$

$$l = 237\text{mm} \qquad 13\text{mm}$$

Interface $\begin{cases} k_n = 300\text{MPa/mm} \\ \sigma_c = 7.5\text{MPa} \\ G_{Ic} = 750 \text{ J/m}^2 \\ \mu = 8 \\ 1896 \text{ elements CPE4} \end{cases}$ Beams $\begin{cases} E = 135\text{GPa} \\ \nu = 0.3 \\ b = 1\text{mm} \\ \text{Isotropic} \\ 24000 \text{ elements CPE4} \end{cases}$
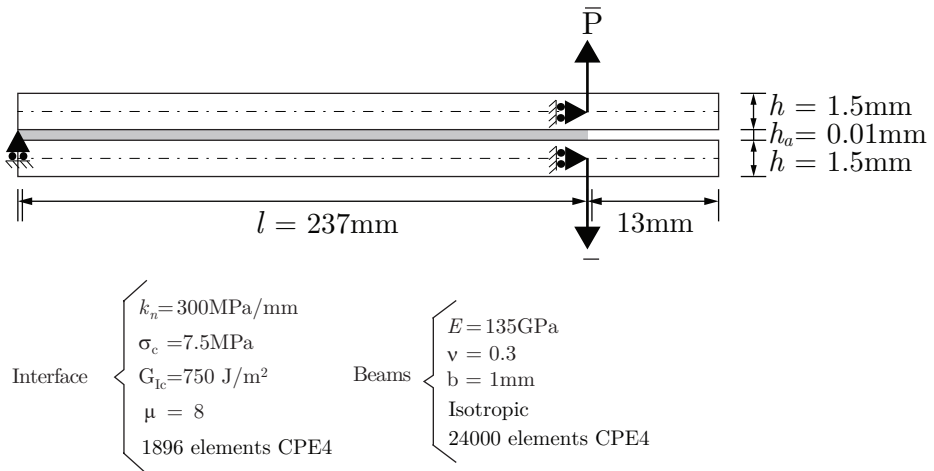
Figure 4.23: DCB boundary conditions used in the numerical model under load control.

The numerical code of the CCFFM+LEBIM by curves uses as input parameters the mechanical model in Fig. 4.23, and gets as output parameter the load $\bar{P}$ that must be imposed at the ends of the beam to obtain a finite segment of interface crack growth

at each step. This implementation calculates each crack growth independently, so it is able to capture possible instabilities of the system.

As in the previous section, a numerical and analytical comparison of the PMTE-SC is done. For this test a load $\bar{P} = $ close to the value that "breaks" the first element using the original LEBIM is imposed but without reaching the breakage of any element. The search for the load that produces the failure of an element is conducted automatically by the code. Subsequently, in each k step, the imposed load is increased (0.5N is used in this example) until a finite fracture along the interface is produced. In order to capture the snap-through instability of the problem, only one iteration of the m step is allowed. Therefore, at each finite fracture jump, the applied load is reset again, taking a load value close to the one that will cause damage in the next element using the original LEBIM. Consequently, after each k step in which the interface damage is produced, the potential energy variation plus the energy dissipation, between one step and the subsequent must be minimized.
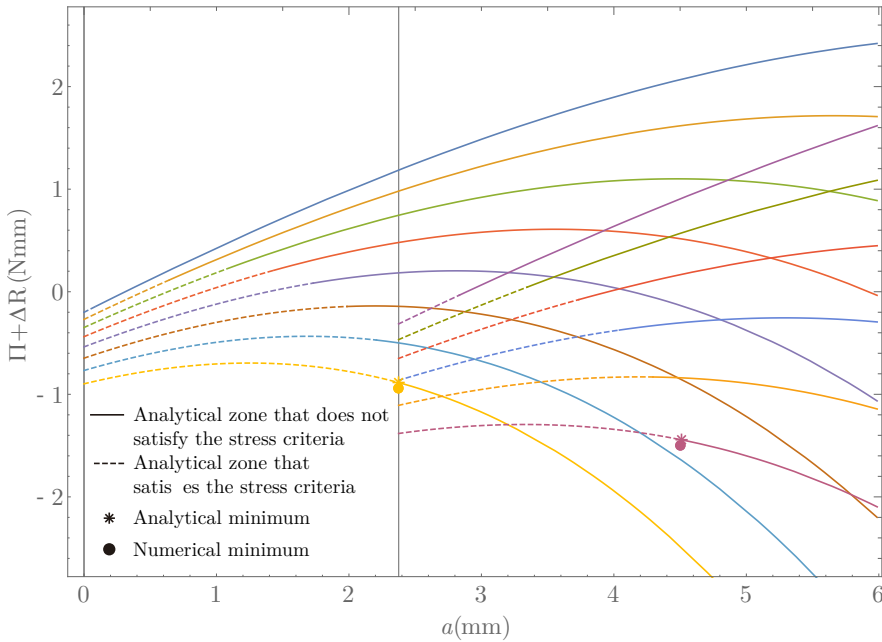
Figure 4.24: Functions $\Pi(a) + \Delta R(a)$ for a specific dimensionless boundary condition in load $\bar{P}$. Discontinuous lines are the region which satisfies the stress criteria. The dots are the minimum of a curve obtained by the numerical code. The asterisks are the minimum of a curve obtained by Eq. (4.67).

Fig. 4.24 includes the $\Pi(a) + \Delta R(a)$ curves of the first fourteen steps. As in the curves of the previous section, the discontinuous zone of the lines corresponds to the interface length that satisfies the stress criterion and the continuous line correspond to the interface zone that does not. These curves are calculated by the Eq. (4.66) and (4.55). As in the previous test, the curves are plotted using the analytical solution provided by Eqs. (4.66) and (4.67). The dots and asterisks represent the interface failure (if exists) at each step, calculated numerically and analytically, respectively. It should be noted, that the total potential energy of the system Π for each crack

length a has been chosen to be represented in the curves. This choice do not affect the solution and is used for an easier interpretation of the analytical solution. Morever, Fig. 4.24 shows that for the first seven load steps the imposed load is not high enough to cause that the stress field along the interface allows tunneling. However, in the eighth step the tunnelling does take place allowing the crack growth until a crack length a, indicated by the yellow dot. Starting from this yellow point, the system is loaded again, step by step, until the next failure, indicated by the purple dot, is obtained.

Finally, Fig. 4.24 shows the load-displacement curve the DCB test under load control. This figure presents the results of both codes used. Both curves are present a horizontal sawtooth wave behaviour due to the system is under load control. It is interesting to note that there are smaller differences between both methods in the present load control test than in the previous displacement control test. This is because it is more difficult to numerically adjust the applied load in systems where there are less damaged elements in each load step. As reference, in the load control test, the first steps damage seventeen to nineteen elements at each step, but as the curve progresses the damage stabilizes leading to a failure of fourteen elements.
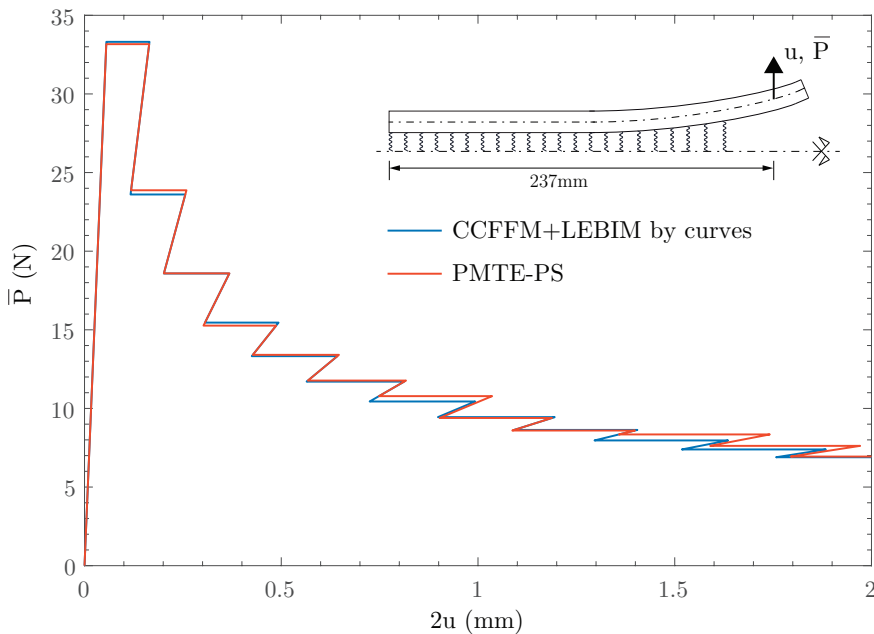
Figure 4.25: Load-displacement curves for the DCB test under load control.

The double pull-push shear test

5.1 Introduction

Adhesive joints between adherents were intensively studied in the last decades. Investigations were mainly focused on the used materials (for both adherents and adhesives) and the models used to get the stress field in the joints that were used to apply a failure criterion. Thus, the models that analyse the failure of adhesive joints can be divided into two groups: (i) analytical (closed-form), and (ii) numerical models. The choice of the model is not an easy task and it depends on the final objective (attempting to optimize the used resources), see da Silva et al. (2009) and Budhe et al. (2017) for an extensive review of existing models.

The evaluation of shear strength in adhesive joints has proven to be important issue, that is why several types of tests, aiming to characterize it, were proposed, e.g. Single Lap Joint (SLP) and Double Lap Joint (DLJ) tests (Hart-Smith, 1973a,b). Among the different types of adhesive joints, it is remarkable the bonding of Fibre-reinforced polymer (FRP) sheets as one of the most common ways to repair and strengthen civil engineering structures (Hollaway, 2010). Specifically the use of carbon fiber reinforced polymer (CFRP) laminates are one the most popular choice for concrete strengthening.

An adequate interface characterization of this kind of joints is quite relevant because the system failure usually occurs due to loss of adhesion between the adherents (J.G.Teng, 2001; Mazzotti et al., 2016). For this reason, a large number of publications have studied the behaviour of these kind of joints by different experimental set-ups. A review of different methods used to characterize the bond-slip behaviour can be found in Mazzotti et al. (2016) and Vaculik et al. (2018).

The Pull-Push Shear Test (PPST) is an experimental test configuration used to characterize the failure of the joint between a FRP laminate and a concrete surface. Specifically, this configuration is one of the most popular test methods for determining

(a)

(b)

l_a = bonded length
l_u = unbonded region length
l_r = reinforcement length
l_b = concrete block length
t_r = reinforcement thickness
t_b = concrete thickness
h_r = reinforcement height
h_b = concrete block height
$\sigma_x^r = P/h_r$

(c)
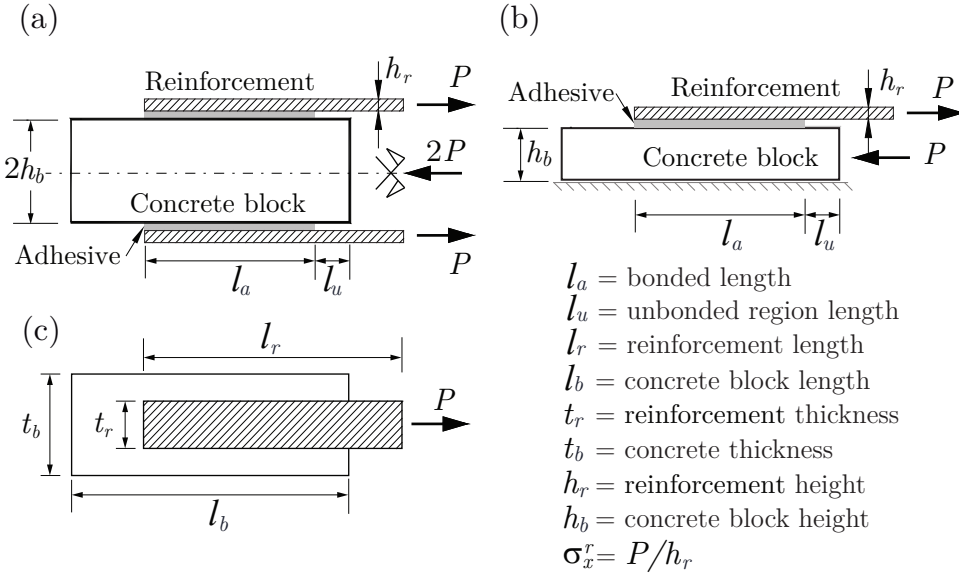
Figure 5.1: Side view of (a) double and (b) single pull-push shear tests. (c) Top view of both PSST set-ups.

the shear load transfer in the bond between two solids due to its simplicity (J.Yao et al., 2005). Two different PPST set-ups can be used: double and single PPST, see Figure 5.1 (a) and (b), respectively. The single PPST is the most common, due to from an experimental point of view it is the easiest to perform, since keeping a symmetrical configuration regarding the debond growth is difficult to control. However, as the bending moment produced in the single PPST is very small, the results obtained for both set-ups are approximately the same (Cornetti and Carpinteri, 2011; L.H.Sneed et al., 2015; T.D'Antino et al., 2016). For this reason and also because the double PPST is simpler to model, it is commonly used for analytical studies and their results compared with those from the single PPST. Figure 5.1 shows both PPST schemes, where the external load is applied to the reinforcement sheets at the same time that a pushing load is applied to the concrete block.

One of the aims of the present investigation is to determine the load that originates a debond along a weak interface in a Double Pull Push Shear (DPPS) specimen including a reinforcement adhesively bonded to a concrete block. Furhermore, the study includes the effect of different parameters acting on the debond.

Since Hillerborg et al. (1976) proposed the Cohesive Zone Model(CZM) to model fracture in concrete structures, it has been used by numerous authors (e.g. Wu et al. (2002); Yuan et al. (2004); Cornetti and Carpinteri (2011); Carrara and Ferretti (2013)). CZMs often provide accurate predictions of damage propagation in concrete thanks to suitably fitted cohesive softening functions. However, there are still some difficulties in fitting these softening functions with the behaviour of the material, specially under mixed mode conditions of fracture to achieve an adequate energy interpretation of the fracture path (Park and Paulino, 2011), and also in achieving a satisfactory computational efficiency and to guarantee the convergence of FEM

computations using CZMs (Cornetti et al., 2019). For these reasons, the CCFFM applied to LEBIM could open an alternative way to CZMs for predicting the onset and propagation of debonds along interfaces including concrete as an adherent, whereas CZMs remain as a reference model in this field. In fact, recently several comparisons of the CCFFM vs. CZM for different problems were published (e.g. Henninger et al. (2007); García et al. (2014); Távara et al. (2016); Cornetti et al. (2016); Martin et al. (2016); Cornetti et al. (2019)), as was indicated in the Section 2.

In Cornetti et al. (2012) the debond onset in the DPPS was studied using the CCFFM but considering only shear stresses along the interface. Thus, in the present investigation, DPPS is analysed by means of the CCFFM but taking into account both normal and shear stresses along the interface, in a similar way as done in Bigwood and Crocombe (1989); Bennati et al. (2009); Goglio and Rossetto (2011) and Dimitri et al. (2018) for other test configurations.

This chapter is organized into four parts. In Section 5.2, an analytical solution for the normal and shear stress fields along the interface between two solids in the DPPS test is developed, using the Winkler's beam on elastic foundation solution. In Section 5.3, the analytical solution described in Section 5.2 is compared to the solution for a shear lag model which are not able to transfer normal stresses. The Section 5.4 develops the analytical approach of the CCFFM+LEBIM for the DPPS test with the solution obtained in Section 5.2. In Section 5.5 some numerical models of the DPPS test used in the BEM code exposed in Section 3.2.1 are described and their convergences are studied. Finally, the Section 5.6 compares the experimental data from two different test campaigns found in the bibliography with the analytical and numerical results of the CCFFM+LEBIM developed in this chapter.

5.2 Analytical models for the interfacial normal and shear stress fields in the Double Pull-Push Shear test

The DPPS test, see Figure 5.2, can be considered as a modified version of the DLJ test including different boundary conditions. As mentioned above, the DPPS test is widely used to investigate the adhesion between a CFRP laminate and a concrete block or clay brick (Vaculik et al., 2018).

Although normal (peeling) stresses are neglected in several models, some investigations have shown that normal stresses along the interface may play an important role in the debond onset and propagation (Martinelli et al., 2011; Carrara et al., 2011; Carrara and Ferretti, 2013), especially for small overlap lengths. Moreover, some experimental results of Czaderski et al. (2010) showed that the assumption that the stress field in bonded joints include shear stresses only is not correct as the normal stresses are also involved and their contribution may not be neglected.

Also, the stress field in the interface is sensitive to the position of the reinforcement along the specimen, see Mazzotti et al. (2008). Is is noticeable that if the reinforcement is bonded until reaching the loaded end as shown in Figure 5.2(a), very high tensile stresses occur along this portion of the interface, and consequently an early fracture typically occurs in the concrete block in the form of triangular section.
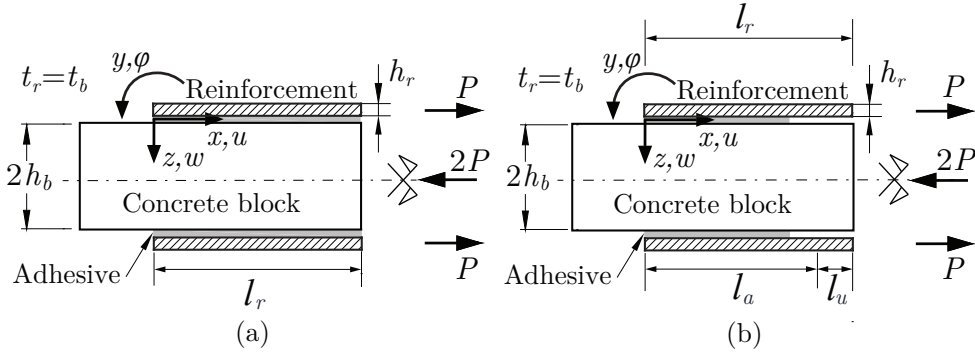
Figure 5.2: Double Pull-Push Shear (DPPS) test (a) with the CFRP laminate bonded starting from the right (loaded) side of the concrete block, and (b) with the CFRP laminate bonded relatively far from the right (loaded) side of the concrete block.

For this reason, in most test, the reinforcement is bonded starting from a certain distance from the loaded edge of the concrete block, as shown in Figure 5.2(b). This zone is normally called "unbonded zone" or "free zone".

In this study, the normal stress distribution has been taken into account and the both described scenarios have been studied:

- The reinforcement is joined until reaching the loaded end, Figure 5.2(a), i.e. without unbonded zone.

- The reinforcement is joined without reaching the loaded end, Figure 5.2(b), i.e. including an unbonded zone.

5.2.1   Stress distribution when the joint reaches the loaded end

The model developed in this section (Figure 5.3) uses a simplified geometry that includes symmetry boundary conditions along the midplane of the concrete block and it is studied under the following main assumptions:

- The adherents are modelled as Timoshenko beams. Due to symmetry conditions, the concrete block is subjected to normal stresses and is able to deform along the longitudinal axis, while the outer CFRP laminates are subjected to tension, bending and shear (and are able deform accordingly).

- The adhesive is modelled as an elastic interface of negligible thickness, i.e. a continuum spring distribution able to transfer normal and shear stresses. These values are assumed to be representative of the stress field in the mid-thickness plane of the adhesive layer, the remaining stress components in the adhesive are neglected.

- Plane strain hypothesis and a linear-elastic behaviour of the adherents are considered, the reinforcement being orthotropic and the block isotropic.

- The width of the adherents and the adhesive are equal, i.e. $t_r = t_b$.
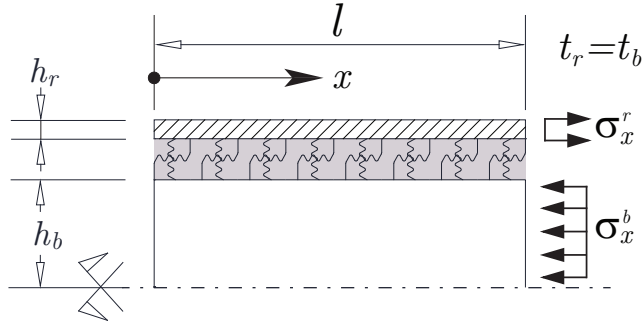
Figure 5.3: Boundary conditions of the DPPS test when the joint reaches the loaded end.

5.2.1.1 Governing equations

Referring to the free-body diagram of an element of length $\mathrm{d}x$ represented in Figure 5.4, the following equilibrium equations can be written for the CFRP laminate:
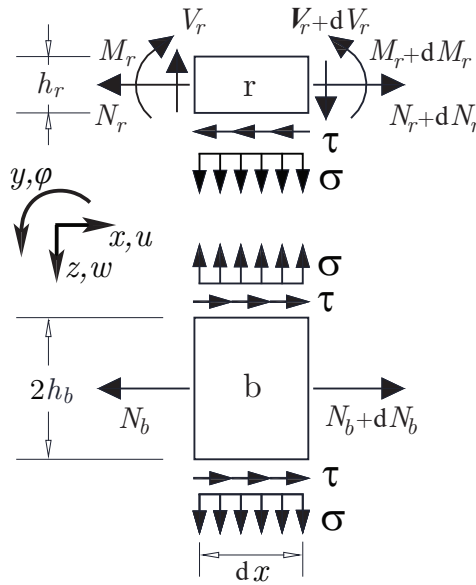
Figure 5.4: Equilibrium of an infinitesimal element of the beams system.

$$\frac{\mathrm{d}N_r}{\mathrm{d}x} - \tau = 0 \tag{5.1}$$

$$\frac{\mathrm{d}V_r}{\mathrm{d}x} + \sigma = 0 \tag{5.2}$$

$$\frac{\mathrm{d}M_r}{\mathrm{d}x} - V_r - \frac{h_r}{2}\tau = 0 \tag{5.3}$$

where, N_r, V_r and M_r are the axial force, the shear force and the bending moment per unit width, respectively; τ and σ are the shear and normal stresses along the adhesive; and h_r is the thickness of the CFRP laminate.

Regarding the concrete block, due to the symmetry conditions, the only non-trivial equilibrium equation is

$$\frac{\mathrm{d}N_b}{\mathrm{d}x} + 2\tau = 0, \tag{5.4}$$

Then, the kinematic equations for the CFRP laminate are

$$\varepsilon_r = \frac{\mathrm{d}u_r}{\mathrm{d}x} \tag{5.5}$$

$$\chi_r = \frac{\mathrm{d}\varphi_r}{\mathrm{d}x} \tag{5.6}$$

$$\gamma_r = \frac{\mathrm{d}w_r}{\mathrm{d}x} + \varphi_r \tag{5.7}$$

where u_r, ε_r, φ_r, χ_r, w_r, and γ_r are the longitudinal displacement, longitudinal membrane strain, rotation, curvature, transverse displacement and shear strain, respectively. Due to the symmetry condition, the only significant kinematic equation for the concrete block is

$$\varepsilon_b = \frac{\mathrm{d}u_b}{\mathrm{d}x} \tag{5.8}$$

where u_b and ε_b are the longitudinal displacement and axial strain, respectively.

Assuming an orthotropic CFRP laminate whose material symmetry axis 1 coincides with the reinforcement direction, the material plane 23 becomes a material symmetry plane. Then, constitutive equations can be deduced, in a similar way as in Távara et al. (2010), from the strain-stress law for a generalized plane strain state (Lekhnitskii, 1981; Ting, 1996)

$$\begin{pmatrix} \varepsilon_1 \\ \varepsilon_2 \\ \varepsilon_6 \end{pmatrix} = \begin{pmatrix} s'_{11} & s'_{12} & 0 \\ s'_{12} & s'_{22} & 0 \\ 0 & 0 & s'_{66} \end{pmatrix} \cdot \begin{pmatrix} \sigma_1 \\ \sigma_2 \\ \sigma_6 \end{pmatrix}, \quad s'_{IJ} = s_{IJ} - \frac{s_{I3}s_{3J}}{s_{33}} \tag{5.9}$$

where s'_{IJ} are the reduced elastic compliances, in this case material axis 3 is the direction where plane strain conditions apply. Hence, the reduced elastic compliances used in this work are:

$$s'_{11} = \frac{1 - \nu_{13}\nu_{31}}{E_1} = \frac{1}{E'_r} \quad \text{and} \quad s'_{66} = \frac{1}{G_{12}} = \frac{1}{G_r} \tag{5.10}$$

where, E'_r is the elastic modulus for plane strain conditions and G_r is the in-plane shear modulus. Let the material axes 1, 2 and 3 correspond to the (geometric) beam axes x, z and y, respectively. Then, the constitutive equations for the CFRP laminate become

$$\varepsilon_r = \frac{N_r}{E'_r h_r} \tag{5.11}$$

$$\chi_r = \frac{12M_r}{E'_r h_1^3} \tag{5.12}$$

$$\gamma_r = K_z \frac{V_r}{G_r h_r} \tag{5.13}$$

K_z being the shear factor of a Timoshenko beam (6/5, for a rectangular section).

Additionally, the only constitutive equation for the concrete block is

$$\varepsilon_b = \frac{N_b}{2E_b' h_b} \tag{5.14}$$

where, $E_b' = \frac{E_b}{(1-\nu_b^2)}$ is the elastic modulus for plane strain conditions for an isotropic material.

As the model developed is one-dimensional, the quantities do not vary along the thickness direction. Therefore, it is assumed the adherent and adhesive thicknesses are large enough to achieve plane strain conditions, see (5.10) and (5.14). Additionaly, due to the thinness of the considered reinforcement in the DPPS test, its shear deformability could be neglected. However, as stated above, the analytical model is expected to be applied also to thick outer adherents and, therefore, (5.13) is considered for the sake of generality.

As the adhesive layer is modelled by a spring distribution, then the normal and shear stresses are directly related to their respective relative displacements, δ_n and δ_t, between the adherents. Then, the Timoshenko beam kinematical assumption yields

$$\tau = k_t \delta_t = k_t \left(u_r + \varphi_r \frac{h_r}{2} - u_b \right) \tag{5.15}$$

$$\sigma = k_n \delta_n = -k_n w_r \tag{5.16}$$

where k_n and k_t represent, the normal and tangential stiffness of the adhesive layer or in a broader view the stiffness of the bonded joint.

5.2.1.2 Stress distribution along the interface and boundary conditions

Differentiating Eq. (5.15) and accounting for the constitutive Eqs. (5.11), (5.12) and (5.14) we obtain

$$\frac{d\tau}{dx} = k_t \left(\varepsilon_r + \chi_r \frac{h_r}{2} - \varepsilon_b \right) = k_t \left(\frac{N_r}{E_r' h_r} + \frac{6M_r}{E_r' h_r^2} - \frac{N_b}{2E_b' h_b} \right) \tag{5.17}$$

By differentiating again and accounting for the axial and rotational equilibrium Eqs. (5.1), (5.3) and (5.4) we get

$$\frac{d^2\tau}{dx^2} = k_t \left[\left(\frac{1}{E_b' h_b} + \frac{4}{E_r' h_r} \right) \tau + \frac{6V_r}{E_r' h_r^2} \right] \tag{5.18}$$

A third differentiation, accounting for the transverse equilibrium (5.2), that relates shear stresses to the normal stress distribution as follows

$$\frac{d^3\tau}{dx^3} = k_t \left[\left(\frac{1}{E_b' h_b} + \frac{4}{E_r' h_r} \right) \frac{d\tau}{dx} - \frac{6}{E_r' h_r^2} \sigma \right] \tag{5.19}$$

Considering now Eq. (5.16), differentiating and accounting for the kinematics in Eq. (5.7) and the constitutive relation in Eq. (5.13), gives

$$\frac{d\sigma}{dx} = -k_n \frac{dw_r}{dx} = k_n (\varphi_r - \gamma_r) = k_n \left(\varphi_r - K_z \frac{V_r}{G_r h_r} \right) \tag{5.20}$$

Further differentiations up to the third order and the use of the kinematics Eq. (5.6), the constitutive relation Eq. (5.12), the transverse equilibrium Eq. (5.2), and the rotational equilibrium Eq. (5.3) lead to

$$\frac{\mathrm{d}^2\sigma}{\mathrm{d}x^2} = k_n \left(\chi_r + \frac{K_z}{G_r h_r} \sigma \right) = k_n \left(\frac{12 M_r}{E'_r h_r^3} + \frac{K_z}{G_r h_r} \sigma \right) \tag{5.21}$$

$$\frac{\mathrm{d}^3\sigma}{\mathrm{d}x^3} = k_n \left(\frac{12 V_r}{E'_r h_r^3} + \frac{6}{E'_r h_r^2} \tau + \frac{K_z}{G_r h_r} \frac{\mathrm{d}\sigma}{\mathrm{d}x} \right) \tag{5.22}$$

By extracting V_r from Eq. (5.18) and σ from Eq. (5.19), and replacing each of them into Eq. (5.22), the following sixth order differential equation in τ is obtained after some algebraic manipulations:

$$\frac{\mathrm{d}^6\tau}{\mathrm{d}x^6} - \frac{k_n}{E'_r h_r} \left[\frac{k_t}{k_n} \left(\frac{E'_r h_r}{E'_b h_b} + 4 \right) + K_z \frac{E'_r}{G_r} \right] \frac{\mathrm{d}^4\tau}{\mathrm{d}x^4}$$

$$+ \frac{k_n}{E'_r h_r^2} \left[\frac{12}{h_r} + \frac{k_t K_z}{G_r} \left(\frac{E'_r h_r}{E'_b h_b} + 4 \right) \right] \frac{\mathrm{d}^2\tau}{\mathrm{d}x^2} - \frac{12 k_n k_t}{E'^2_r h_r^4} \left(\frac{E'_r h_r}{E'_b h_b} + 1 \right) \tau = 0 \quad (5.23)$$

Using similar hypotheses, other authors developed a similar solution but obtaining a seventh order differential equation for the shear stress field evaluation (Bigwood and Crocombe, 1990; Dimitri et al., 2018; Goglio and Rossetto, 2011). It is worth to mention that in Martinelli et al. (2011) a sixth order differential was also obtained but using a Bernoulli beam model and assuming that the concrete block is a rigid solid.

Table 5.1: Dimensionless variables and parameters.

$\xi = \frac{x}{l_{ch}}$	$\hat{\tau} = \frac{\tau}{P/l_{ch}}$	$\hat{\sigma} = \frac{\sigma}{P/l_{ch}}$		
$\lambda = \frac{l}{l_{ch}}$	$\eta = \frac{h_r}{l_{ch}}$	$\zeta = \frac{E'_r}{G_r}$	$\rho = \frac{E'_r h_r}{E'_b h_b}$	$\kappa = \frac{k_t}{k_n}$

In order to get a dimensionless expression, the characteristic length parameter l_{ch} is defined as $l_{ch} = \frac{E'_r}{k_n}$. It relates the stiffness of the laminate (reinforcement) to that of the interface. The applied axial force in the reinforcement P is defined in Figure 5.2. Then, Eq. (5.23) can be rewritten in terms of the dimensionless parameters defined in Table 5.1 as

$$\hat{\tau}^{\mathrm{vi}} - \frac{1}{\eta} \left[\kappa \left(4 + \rho \right) + K_z \zeta \right] \hat{\tau}^{\mathrm{iv}}$$

$$+ \frac{12}{\eta^3} \left[1 + \left(4 + \rho \right) \frac{\kappa \eta \zeta K_z}{12} \right] \hat{\tau}'' - \frac{12 \kappa}{\eta^4} \left(1 + \rho \right) \hat{\tau} = 0 \quad (5.24)$$

where the derivatives are now taken with respect to ξ. To solve (5.24), first its characteristic (sixth-order) equation is written as

$$q^6 - D_4 q^4 + D_2 q^2 - D_0 = 0 \tag{5.25}$$

where D_4, D_2 and D_0 are the absolute values of the multipliers of the fourth, second and zero order derivatives, respectively, in Eq. (5.24). Rewriting the sixth-order

polynomial in Eq. (5.25) considering q^2 as an independent variable, we get a cubic equation in terms of q^2. Thus, it is possible to obtain all the roots of Eq. (5.25) in a closed form because all of the roots of the cubic equation can be found algebraically. For the specific case of DPPS test, the obtained cubic equation has, in general, one real positive and two complex conjugate roots. Hence, the sixth-order equation has two opposite real roots and two pairs of complex conjugate roots. Especially, the six roots of Eq. (5.25) can be expressed as

$$q_{1,2} = \pm m, \quad q_{3,4} = n_1 \pm in_2, \quad q_{5,6} = -n_1 \pm in_2, \tag{5.26}$$

where m, n_1 and n_2 are positive real numbers as defined in Bigwood and Crocombe (1989) and Goglio and Rossetto (2011) and given in terms of the coefficients D_0, D_2 and D_4 of the characteristic equation:

$$m = \sqrt{\frac{\sqrt[3]{C}}{3\sqrt[3]{2}} + \frac{D_4}{3} - \frac{\sqrt[3]{2}(3D_2 - D_4^2)}{3\sqrt[3]{C}}} \tag{5.27}$$

$$n_1 = \sqrt[4]{X^2 + Y^2} \cos\left(\frac{1}{2}\arccos\left(\frac{X}{\sqrt{X^2 + Y^2}}\right)\right) \tag{5.28}$$

$$n_2 = \sqrt[4]{X^2 + Y^2} \sin\left(\frac{1}{2}\arccos\left(\frac{X}{\sqrt{X^2 + Y^2}}\right)\right) \tag{5.29}$$

where C, X and Y are:

$$C = 2D_4^3 - 9D_4D_2 + 27D_0 +$$
$$\sqrt{-4\left(D_4^2 - 3D_2\right)^3 + \left(2D_4^3 - 9D_4D_2 + 27D_0\right)^2} \tag{5.30}$$

$$X = \frac{-\sqrt[3]{(2C)^2} + 4\sqrt[3]{C}D_4 - \sqrt[3]{2^4}D_4^2 + 6\sqrt[3]{2}D_2}{12\sqrt[3]{C}} \tag{5.31}$$

$$Y = \frac{\sqrt[3]{2C^2} - 2D_4^2 + 6D_2}{\sqrt{3}\sqrt[3]{2^5C}} \tag{5.32}$$

Finally, the dimensionless shear stress $\hat{\tau}$ can be expressed as

$$\hat{\tau} = C_1 e^{m\xi} + C_2 e^{-m\xi} + C_3 e^{n_1\xi}\cos(n_2\xi) + C_4 e^{n_1\xi}\sin(n_2\xi)$$
$$+ C_5 e^{-n_1\xi}\cos(n_2\xi) + C_6 e^{-n_1\xi}\sin(n_2\xi) \tag{5.33}$$

where $C_1, \ldots, C_6$ are integration constants to be determined from the boundary conditions.

Then, from Eqs. (5.19) and (5.33) the following expression of the dimensionless normal stress $\hat{\sigma}$ is obtained:

$$\hat{\sigma} = -\frac{\eta}{6}\left[\frac{\eta}{\kappa}\hat{\tau}''' - (4+\rho)\hat{\tau}'\right] =$$

$$- C_1 \frac{\eta m e^{m\xi}}{6\kappa}\left[\eta m_1^2 - \kappa(\rho+4)\right] + C_2 \frac{\eta m e^{-m\xi}}{6\kappa}\left[\eta m_1^2 - \kappa(\rho+4)\right]$$

$$- C_3 \frac{\eta e^{n_1\xi}}{6\kappa}\left[n_2\sin(\xi n_2)\left[\kappa(\rho+4)-3\eta n_1^2 + \eta n_2^2\right] - n_1\cos(\xi n_2)\left[\kappa(\rho+4)-\eta n_1^2 + 3\eta n_2^2\right]\right]$$

$$+ C_4 \frac{\eta e^{n_1\xi}}{6\kappa}\left[n_2\cos(\xi n_2)\left[\kappa(\rho+4)-3\eta n_1^2 + \eta n_2^2\right] + n_1\sin(\xi n_2)\left[\kappa(\rho+4)-\eta n_1^2 + 3\eta n_2^2\right]\right]$$

$$- C_5 \frac{\eta e^{-n_1\xi}}{6\kappa}\left[n_2\sin(\xi n_2)\left[\kappa(\rho+4)-3\eta n_1^2 + \eta n_2^2\right] + n_1\cos(\xi n_2)\left[\kappa(\rho+4)-\eta n_1^2 + 3\eta n_2^2\right]\right]$$

$$+ C_6 \frac{\eta e^{-n_1\xi}}{6\kappa}\left[n_2\cos(\xi n_2)\left[\kappa(\rho+4)-3\eta n_1^2 + \eta n_2^2\right] - n_1\sin(\xi n_2)\left[\kappa(\rho+4)-\eta n_1^2 + 3\eta n_2^2\right]\right]$$

$$\tag{5.34}$$
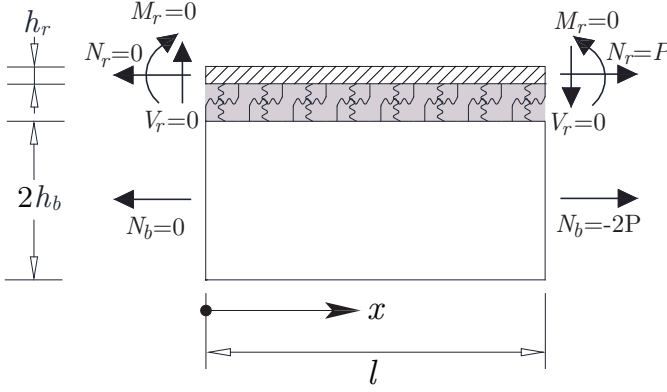
Figure 5.5: Boundary conditions used to model the DPPS test.

The six boundary conditions are obtained by substituting the values of the axial force, shear force and bending moment into the expressions of the lower order derivatives of the adhesive shear and normal stresses in Eqs. (5.17), (5.18) and (5.21), evaluated at the extremes (see Figure 5.5). To write these boundary conditions in dimensionless form, suitable dimensionless forces and bending moment are defined as follows: $\hat{N}_r = \frac{N_r}{P}, \hat{N}_b = \frac{N_b}{P}, \hat{V}_r = \frac{V_r}{P}, \hat{M}_r = \frac{M_r}{Pl_{ch}}$.

Thus, the first two boundary conditions are given by evaluating Eq. (5.17) at the extremes

$$\hat{\tau}'(0) = \frac{\kappa}{\eta}\left(\hat{N}_r(0) + \frac{6}{\eta}\hat{M}_r(0) - \frac{\rho}{2}\hat{N}_b(0)\right) \tag{5.35}$$

$$\hat{\tau}'(\lambda) = \frac{\kappa}{\eta}\left(\hat{N}_r(\lambda) + \frac{6}{\eta}\hat{M}_r(\lambda) - \frac{\rho}{2}\hat{N}_b(\lambda)\right) \tag{5.36}$$

The third and fourth boundary conditions are obtained from Eq. (5.18)

$$\hat{\tau}''(0) - \frac{\kappa}{\eta}(4+\rho)\hat{\tau}(0) = \frac{6\kappa}{\eta^2}\hat{V}_r(0) \tag{5.37}$$

$$\hat{\tau}''(\lambda) - \frac{\kappa}{\eta}(4+\rho)\hat{\tau}(\lambda) = \frac{6\kappa}{\eta^2}\hat{V}_r(\lambda) \tag{5.38}$$

Finally, Eq. (5.21) provides the fifth and sixth boundary conditions

$$\hat{\sigma}''(0) - \frac{\zeta K_z}{\eta}\hat{\sigma}(0) = \frac{12}{\eta^3}\hat{M}_r(0) \tag{5.39}$$

$$\hat{\sigma}''(\lambda) - \frac{\zeta K_z}{\eta}\hat{\sigma}(\lambda) = \frac{12}{\eta^3}\hat{M}_r(\lambda) \tag{5.40}$$

This group of the six static boundary conditions forms a system of six linear equations for (dimensionless) unknown constants $C_1, \ldots, C_6$, which can be solved in a closed form, although very lengthy expressions obtained are omitted here, for the sake of brevity. Then, the values of these constants suitably substituted into Eqs. (5.33) and (5.34) allow to obtain the interface shear and normal stresses, correspondingly.

Noteworthy, this method to obtain the stress distribution at a interface is valid for double lap joints under any loading type. Just the edge loads applied at the ends should be properly set. For the present case this loads are: $N_r = V_r = M_r = 0$ and $N_b = 0$ at $x = 0$; and $V_r = M_r = 0$, $N_r = P$ and $N_b = -2P$ at $x = l$. Therefore, in the present case this linear system is reduced to

$$\hat{\tau}'(0) = 0 \tag{5.41}$$

$$\hat{\tau}'(\lambda) = \frac{\kappa}{\eta}(1 + \rho)$$

$$\hat{\tau}''(0) - \frac{\kappa}{\eta}(4 + \rho)\hat{\tau}(0) = 0$$

$$\hat{\tau}''(\lambda) - \frac{\kappa}{\eta}(4 + \rho)\hat{\tau}(\lambda) = 0$$

$$\hat{\sigma}''(0) - \frac{\zeta K_z}{\eta}\hat{\sigma}(0) = 0$$

$$\hat{\sigma}''(\lambda) - \frac{\zeta K_z}{\eta}\hat{\sigma}(\lambda) = 0$$

5.2.2 Interfacial stress distribution with an unbonded zone at the loaded end including receding contact

The model developed in this section uses the same simplified geometry and the same main assumptions as those described in section 5.2.1. Figure 5.6 represents a scheme of the studied model. An important variation with respect to the model included in the previous section is that the present model includes two different zones:

- S1, undamaged interface zone.

- S2, adhesive-free zone, including contact conditions if necessary.

The free-body diagram of an element of length dx is different for each studied zone, represented in Figure 5.4 (a) for S1 zone and in Figure 5.4 (b) for S2 zone. Note that the S1 zone has exactly the same free-body diagram and governing equations than those included in the previous section model, where the interface is able to transfer shear and normal stresses. Therefore, the stress fields for S1 zone are defined above in Eqs. (5.33) and (5.34), and in this section they are renamed as $\hat{\sigma}_{S1}$ and $\hat{\tau}_{S1}$, correspondingly. However, the S2 zone is only able to transfer compressive normal
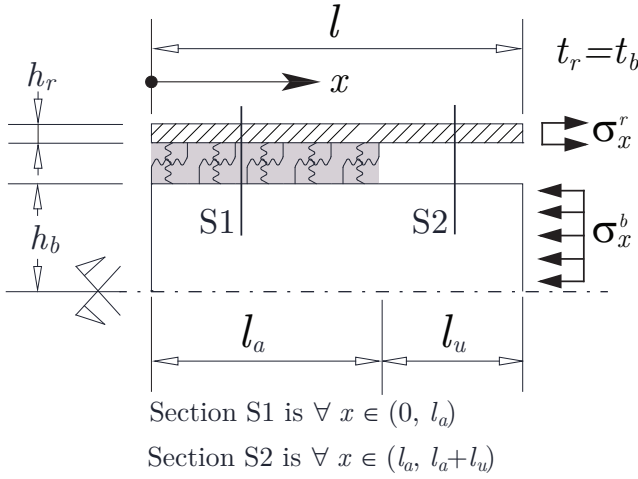
Figure 5.6: Boundary conditions of the PPST test with an unbonded zone at the loaded end including receding contact.

stresses($\hat{\sigma}_{S2}$), and they are obtained in this section. Moreover, the continuity of displacements on the reinforcement at the intersection point between the two zones is imposed using adequate boundary conditions.
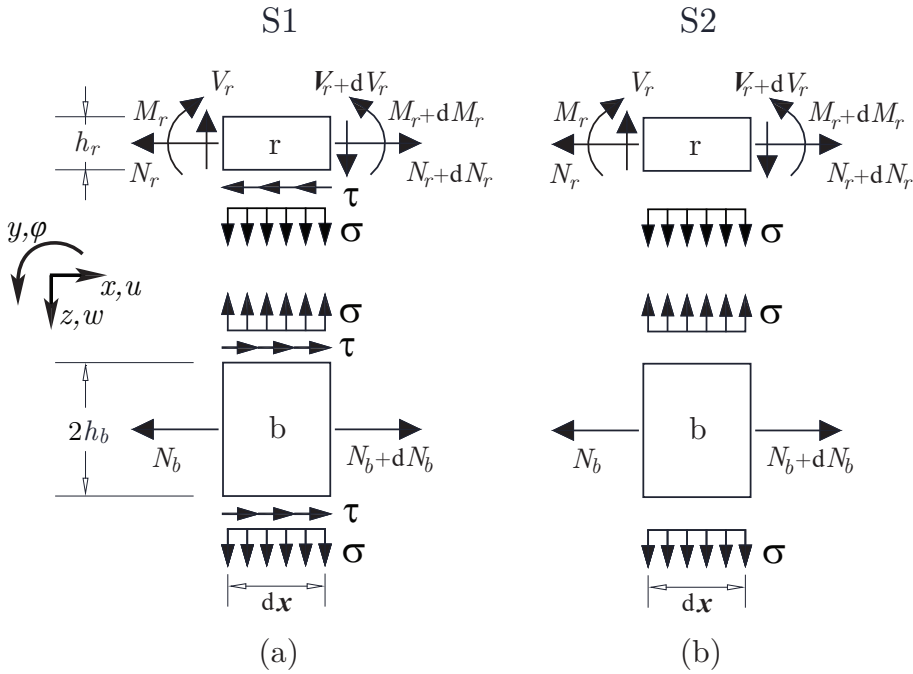
Figure 5.7: Equilibrium of an infinitesimal element of the beams system for (a) S1 zone and (b) S2 zone.

5.2.2.1 Governing equations for zone where there is not adhesive but could have contact

The equilibrium equations which govern the reinforcement in S2 zone are very similar to those in zone S1, with the difference that in this zone there are not tangential stress. Therefore, the equilibrium equations are written following the same nomenclature than section 5.2.1.1:

$$\frac{\mathrm{d}N_r}{\mathrm{d}x} = 0 \tag{5.42}$$

$$\frac{\mathrm{d}V_r}{\mathrm{d}x} + \sigma = 0 \tag{5.43}$$

$$\frac{\mathrm{d}M_r}{\mathrm{d}x} - V_r = 0 \tag{5.44}$$

and the only equilibrium equation in the concrete block is:

$$\frac{\mathrm{d}N_b}{\mathrm{d}x} = 0, \tag{5.45}$$

The kinematic and constitutive equations for this S2 zone are exactly the same that for the S1 zone, both for reinforcement and for concrete block: from the Eq. (5.5) to the Eq. (5.14). However, since there are only normal stresses at the interface in S2 zone, the behaviour is:

$$\tau_{S2} = 0 \tag{5.46}$$

$$\sigma_{S2} = k_n \delta_n = -k_n w_r \tag{5.47}$$

5.2.2.2 Stress distributions along the interface and boundary conditions

Similarly to the development of the Section 5.2.1.2, the expression (5.48) is obtained differentiating the Eq. (5.47) and taking into account the kinematic behaviour of the Eq.(5.7) kinematic behaviour of the Eq. (5.13):

$$\frac{\mathrm{d}\sigma_{S2}}{\mathrm{d}x} = -k_n \frac{\mathrm{d}w_r}{\mathrm{d}x} = k_n \left(\varphi_r - \gamma_r \right) = k_n \left(\varphi_r - K_z \frac{V_r}{G_r h_r} \right) \tag{5.48}$$

By differentiating two more times and accounting constitutive Eq. (5.12) and equilibrium Eq. (5.44):

$$\frac{\mathrm{d}^2\sigma_{S2}}{\mathrm{d}x^2} = k_n \left(\chi_r + \frac{K_z}{G_r h_r} \sigma_{S2} \right) = k_n \left(\frac{12M_r}{E'_r h_r^3} + \frac{K_z}{G_r h_r} \sigma_{S2} \right) \tag{5.49}$$

$$\frac{\mathrm{d}^3\sigma_{S2}}{\mathrm{d}x^3} = k_n \left(\frac{12V_r}{E'_r h_r^3} + \frac{K_z}{G_r h_r} \frac{\mathrm{d}\sigma_{S2}}{\mathrm{d}x} \right) \tag{5.50}$$

And differentiating one last time and replacing the Eq. (5.43):

$$\frac{\mathrm{d}^4\sigma_{S2}}{\mathrm{d}x^3} = k_n \left(\frac{-12\sigma_{S2}}{E'_r h_r^3} + \frac{K_z}{G_r h_r} \frac{\mathrm{d}^2\sigma_{S2}}{\mathrm{d}x^2} \right) \tag{5.51}$$

Then, Eq. (5.51) can be rewritten in terms of the dimensionless parameters defined in Table 5.1 as:

$$\hat{\sigma}_{S2}^{\text{iv}} - \frac{K_z \zeta}{\eta} \hat{\sigma}_{S2}'' + \frac{12}{\eta^3} \hat{\sigma}_{S2} = 0, \qquad (5.52)$$

And, as in the previous section, the derivatives are taken with respect to ξ. The characteristic fourth-order equation is written as:

$$q^4 - F_2 q^2 + F_0 = 0, \qquad (5.53)$$

where F_2 and F_0 are the absolute values of the multipliers of the second and zero order derivatives, respectively, in Eq. (5.52). Rewriting the fourth-order polynomial in Eq. (5.53) considering q^2 as an independent variable, we get a quadratic equation in terms of q^2. For the specific case of DPPS test, the discriminant of this quadratic equation is normally negative. Hence, the fourth-order equation has a pair of complex conjugate roots:

$$q_{1,2} = p_1 \pm ip_2, \quad q_{3,4} = -p_1 \pm ip_2 \qquad (5.54)$$

p_1 and p_2 are positive real numbers given in terms of the dimensionless parameters of problem defined in 5.1:

$$p_1 = \sqrt{\frac{F_2}{4} + \sqrt{\frac{F_0}{4}}} = \sqrt{\frac{\zeta K_z}{4\eta} + \sqrt{\frac{3}{\eta^3}}} \qquad (5.55)$$

$$p_2 = \sqrt{-\frac{F_2}{4} + \sqrt{\frac{F_0}{4}}} = \sqrt{-\frac{\zeta K_z}{4\eta} + \sqrt{\frac{3}{\eta^3}}} \qquad (5.56)$$

Finally, the dimensionless normal stress $\hat{\sigma}_{S2}$ can be expressed as:

$$\hat{\sigma}_{S2} = C_7 e^{q_1 \xi} \cos(q_2 \xi) + C_8 e^{q_1 \xi} \sin(q_2 \xi)$$
$$+ C_9 e^{-q_1 \xi} \cos(q_2 \xi) + C_{10} e^{-q_1 \xi} \sin(q_2 \xi), \quad (5.57)$$

where $C_7, \ldots, C_{10}$ are integration constants appertaining to zone S2 and these must be added to the integration constant of zone S1 ($C_1, \ldots, C_6$), which are part of $\hat{\sigma}_{S1}$ and $\hat{\tau}_{S1}$ (Eqs. (5.34) and (5.33) respectively). The boundary conditions must be able to determinate all of them and to define the stresses field in the whole interface.

The ten boundary conditions are obtained by substituting the values of the axial force, shear force and bending moment into the expressions of the lower order derivatives of the shear and normal stresses at S1 and S2 zones. And as in the previous section, suitable dimensionless forces and bending moment ($\hat{N}_r = \frac{N_r}{P}, \hat{N}_b = \frac{N_b}{P}, \hat{V}_r = \frac{V_r}{P}, \hat{M}_r = \frac{M_r}{Pl_{ch}}$) are used to write these boundary conditions in dimensionless form.

Thus, the first three boundary conditions are evaluated at $\xi = 0$, i.e. at unloaded end of the reinforcement, for this raison they are evaluated at the S1 zone by Eqs. (5.17), (5.18) and (5.21):

$$\hat{\tau}'_{S1}(0) = \frac{\kappa}{\eta} \left(\hat{N}_r(0) + \frac{6}{\eta}\hat{M}_r(0) - \frac{\rho}{2}\hat{N}_b(0) \right) \tag{5.58}$$

$$\hat{\tau}''_{S1}(0) - \frac{\kappa}{\eta}(4+\rho)\hat{\tau}_{S1}(0) = \frac{6\kappa}{\eta^2}\hat{V}_r(0) \tag{5.59}$$

$$\hat{\sigma}''_{S1}(0) - \frac{\zeta K_z}{\eta}\hat{\sigma}_{S1}(0) = \frac{12}{\eta^3}\hat{M}_r(0) \tag{5.60}$$

$$\tag{5.61}$$

The two next boundary condition are evaluated at $\xi = \lambda$, i.e. at loaded end of the reinforcement, thus they are evaluated at the S2 zone by Eqs. (5.49) and (5.50):

$$\hat{\sigma}''_{S2}(\lambda) - \frac{\zeta K_z}{\eta}\hat{\sigma}_{S2}(\lambda) = \frac{12}{\eta^3}\hat{M}_r(\lambda) \tag{5.62}$$

$$\hat{\sigma}'''_{S2}(\lambda) - \frac{\zeta K_z}{\eta}\hat{\sigma}'_{S2}(\lambda) = \frac{12}{\eta^3}\hat{V}_r(\lambda) \tag{5.63}$$

$$\tag{5.64}$$

The rest of the five boundary conditions are evaluated at the intersection between the two zones S1 and S2, at $\xi = \lambda_{1-2}$. The first one evaluates the transverse displacement by the equations of the zone S1 and the equations of the zone S2, since $w_{r(S1)}(\lambda_{1-2}) = w_{r(S2)}(\lambda_{1-2})$. Thus, if the Eq. (5.16) is equal to Eq. (5.47) the sixth boundary condition is expressed as:

$$\hat{\sigma}_{S1}(\lambda_{1-2}) - \hat{\sigma}_{S2}(\lambda_{1-2}) = 0 \tag{5.65}$$

Additionally, at intersection of the two zones, $\varphi_{r(S1)}(\lambda_{1-2}) = \varphi_{r(S2)}(\lambda_{1-2})$ and $\hat{V}_{r(S1)}(\lambda_{1-2}) = \hat{V}_{r(S2)}(\lambda_{1-2})$ must be fulfilled. Therefore, the seventh boundary condition is obtained by the Eqs. (5.20) and (5.48).

$$\hat{\sigma}'_{S1}(\lambda_{1-2}) - \hat{\sigma}'_{S2}(\lambda_{1-2}) = 0 \tag{5.66}$$

By extracting $\hat{V}_{r(S1)}(\lambda_{1-2})$ from Eq. (5.18) and replacing into Eqs. (5.50), the next boundary condition is written:

$$\hat{\tau}''_{S1}(\lambda_{1-2}) - \frac{\kappa}{\eta}(4+\rho)\hat{\tau}_{S1}(\lambda_{1-2}) - \frac{\eta\kappa}{2}\hat{\sigma}'''_{S2}(\lambda_{1-2}) + \frac{\zeta\kappa K_z}{2}\hat{\sigma}'_{S2}(\lambda_{1-2}) = 0 \tag{5.67}$$

As $\hat{M}_{r(S1)}(\lambda_{1-2}) = \hat{M}_{r(S2)}(\lambda_{1-2})$ is imposed. If $\hat{M}_{r(S2)}(\lambda_{1-2})$ is extracted from Eq. (5.49) and replaced into Eqs. (5.17), the next boundary conditions is:

$$\hat{\tau}'_{S1}(\lambda_{1-2}) - \frac{\eta\kappa}{2}\hat{\sigma}''_{S2}(\lambda_{1-2}) + \frac{\zeta\kappa K_z}{2}\hat{\sigma}_{S2}(\lambda_{1-2}) = \frac{\kappa}{\eta}\left(\hat{N}_r(\lambda_{1-2}) - \frac{\rho}{2}\hat{N}_b(\lambda_{1-2}) \right) \tag{5.68}$$

Finally, since $\hat{M}_{r(S1)}(\lambda_{1-2}) = \hat{M}_{r(S2)}(\lambda_{1-2})$ and $\hat{\sigma}_{S1}(\lambda_{1-2}) = \hat{\sigma}_{S2}(\lambda_{1-2})$ at the intersection of the two zone, the last boundary conditions is defined by Eqs. (5.21) and (5.49):

$$\hat{\sigma}''_{S1}(\lambda_{1-2}) - \hat{\sigma}''_{S2}(\lambda_{1-2}) = 0 \tag{5.69}$$

This group of the ten static boundary conditions forms a system of ten linear equations for (dimensionless) unknown constants $C_1, \ldots, C_{10}$, which can be solved in closed form, as the previous section. Then, the values of these constants suitably substituted into Eqs. (5.33), (5.34) and (5.57) allow to define the interface shear and normal stresses for S1 zone and normal stresses for S2 zone.

The system proposed is a general system for double lap joints under any loading type. If the loads applied at the ends and at the intersection between two zones are the same which in the Figure 5.8, this system solves the specific problem of the DPP test.
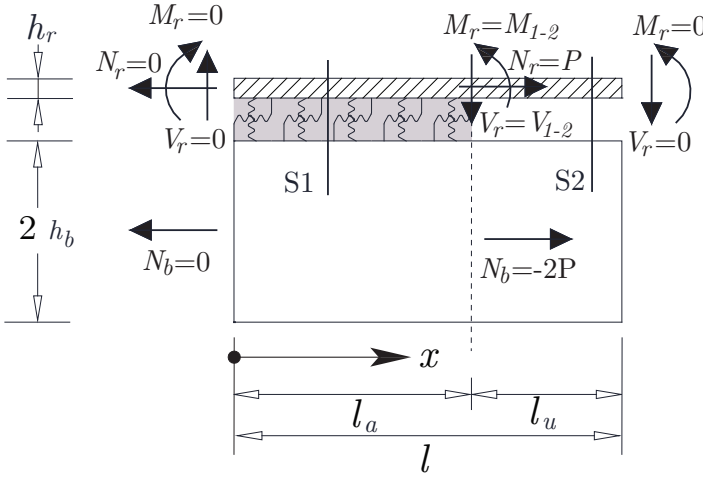
Figure 5.8: Boundary conditions used to model the DPPS test.

Therefore, in the present case this linear system is reduced to

$$\hat{\tau}'_{S1}(0) = 0 \tag{5.70}$$

$$\hat{\tau}''_{S1}(0) - \frac{\kappa}{\eta}(4+\rho)\hat{\tau}_{S1}(0) = 0$$

$$\hat{\sigma}''_{S1}(0) - \frac{\zeta K_z}{\eta}\hat{\sigma}_{S1}(0) = 0$$

$$\hat{\sigma}''_{S2}(\lambda) - \frac{\zeta K_z}{\eta}\hat{\sigma}_{S2}(\lambda) = 0$$

$$\hat{\sigma}'''_{S2}(\lambda) - \frac{\zeta K_z}{\eta}\hat{\sigma}'_{S2}(\lambda) = 0$$

$$\hat{\sigma}_{S1}(\lambda_{1-2}) - \hat{\sigma}_{S2}(\lambda_{1-2}) = 0$$

$$\hat{\sigma}'_{S1}(\lambda_{1-2}) - \hat{\sigma}'_{S2}(\lambda_{1-2}) = 0$$

$$\hat{\tau}''_{S1}(\lambda_{1-2}) - \frac{\kappa}{\eta}(4+\rho)\hat{\tau}_{S1}(\lambda_{1-2}) - \frac{\eta\kappa}{2}\hat{\sigma}'''_{S2}(\lambda_{1-2}) + \frac{\zeta\kappa K_z}{2}\hat{\sigma}'_{S2}(\lambda_{1-2}) = 0$$

$$\hat{\tau}'_{S1}(\lambda_{1-2}) - \frac{\eta\kappa}{2}\hat{\sigma}''_{S2}(\lambda_{1-2}) + \frac{\zeta\kappa K_z}{2}\hat{\sigma}_{S2}(\lambda_{1-2}) = \frac{\kappa}{\eta}(1+\rho)$$

$$\hat{\sigma}''_{S1}(\lambda_{1-2}) - \hat{\sigma}''_{S2}(\lambda_{1-2}) = 0$$

5.2.3 Stresses distribution with different bonded and unbonded lengths including receding contact

In order to know the behaviour of the solutions of the stress field obtained in the previous sections, the data in Table 5.2 are taken to represent graphically the normal and shear stresses in a specific interface. Mazzotti et al. (2016) provide ranges for all geometrical and mechanical characteristics of the DPPS test taken in the available bibliography. Thus, all the chosen parameters are within these ranges. The obtained values of the dimensionless parameters defined in Table 5.1 are also presented in Table 5.2.

Table 5.2: Default mechanical and geometrical characteristics used for the debond analysis in the DPPS test.

	l_b(mm)	h_b(mm)	E_b(GPa)	ν_b	G_b
Concrete block	100	50	30.0	0.20	12.5
	l_r(mm)	h_r(mm)	E_1(GPa)	ν_{13}	G_{12}
Reinforcement	100	1.5	135.0	0.30	5
	k_n(MPa/μm)	k_t(MPa/μm)			
Adhesive	0.72	0.18			
Characteristic length and reinforcement stiffness:					
	l_{ch}=206.04mm	E_r'=148.35GPa			
Dimensionless parameters	λ=0.485	$\eta = 0.00728$	$\rho = 0.142$	$\kappa = 0.25$	$\zeta = 29.67$

Figure 5.9 depicts the solution of stresses field obtained in Section 5.2.1.2 where the reinforcement is bonded to whole interface, from unloaded end to loaded end. Note that, the distributions of stresses represented in mentioned figure show that the largest normal and shear stress values are obtained at the right end of the interface (loaded end), coinciding with the zone where loads are applied over the concrete block and laminate, see Figure 5.5. Regarding the normal stress distribution, it is interesting to notice that a large increase of compressions appear at the right end but also tensions appear in a neighbour small zone. Moreover, tensions also occur at the opposite (left) end, free end in Figure 5.5.

Also, the data in Table 5.2 are taken to represent graphically the solution of the stresses field obtained in Section 5.2.2.2. In this occasion, the reinforcement is positioned at a certain distance from the edge of the concrete block (l_u), and therefore the bonded region is $l_a = l - l_u$, as Figure 5.8 represents. Figure 5.10 depicts the normal and shear stresses for two different cases which present different unbonded zone lengths. The continuous lines represent an unbonded region smaller than the case represented by the dashed line. Regarding the normal stress distribution, it is important to highlight that at the unbonded zone occurs a contact zone, where the normal stress peak decreases with increasing contact area. Be that as it may, Figure 5.10 shows that the contact zone does not change from the unloaded system to the loaded system. This type of contact is called conforming (Garrido et al., 1988, 1997).
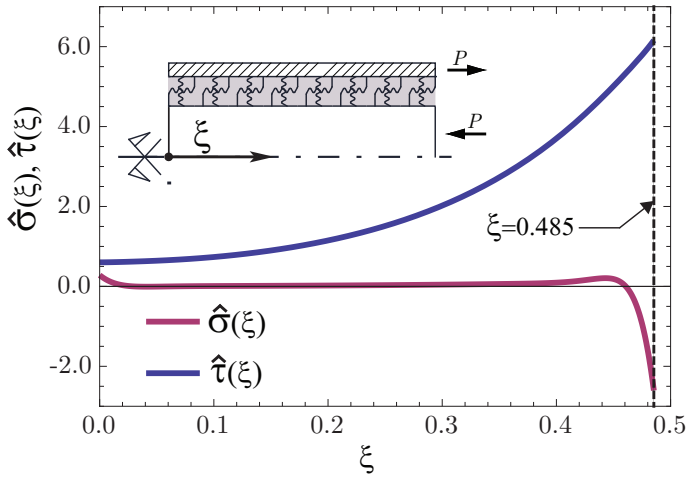
Figure 5.9: Dimensionless normal and shear stress distributions along the interface in the DPPS test.
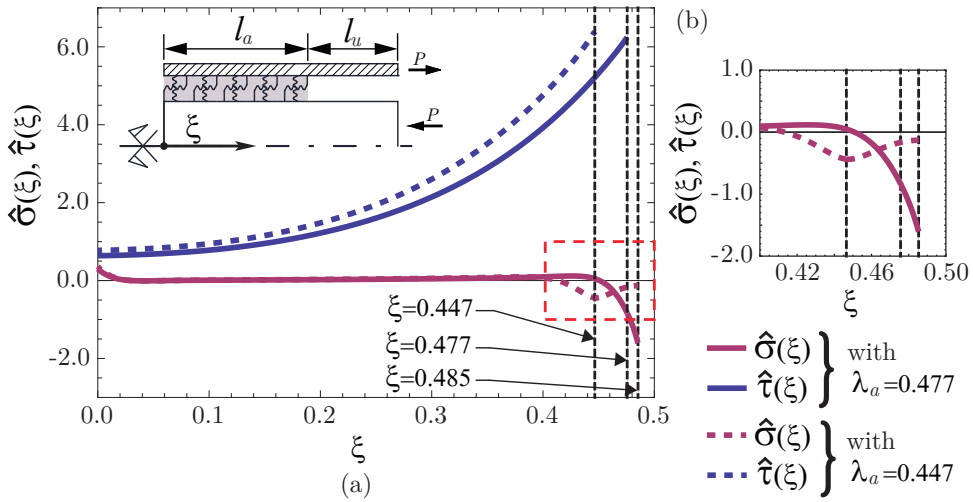
Figure 5.10: Dimensionless normal and shear stress distributions along the interface in the DPPS test with $\lambda=0.485$ and two different adhesive zones lengths: $\lambda_a=0.477(l_a=98mm)$ and $\lambda_a=0.447(l_a=92mm)$.

However, a lifting of the loaded end is produced if the unbonded zone increases. An example of this case is presented in Figure 5.11, where the bonded zone is shorter than the previous cases. Figure 5.11 (b) shows a small tension zone which does not warrant properly the equilibrium in the whole interface. Actually, it is produced because of a positive relative displacement between reinforcement and concrete is not taken into account. These cases where the contact zone diminishes after the application of the load are called receding contact, which leads to the need to use numerical iterations to predict the exact size of the contact zone(Garrido et al., 1988, 1997).
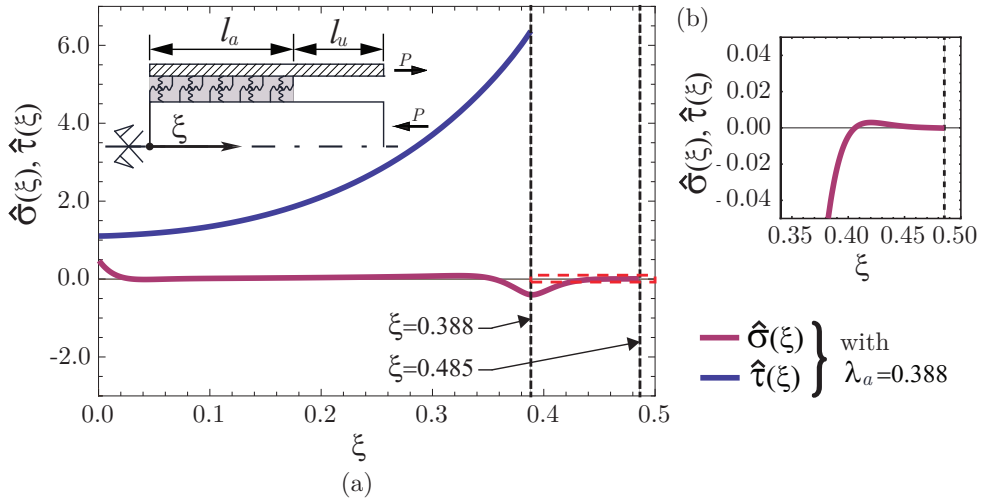
Figure 5.11: Dimensionless normal and shear stress distributions along the interface in the DPPS test with λ=0.485 and λ_a=0.388 (l_a=80mm).

Note that the linear system obtained in 5.2.2.2 evaluates two boundary condition at loaded end of the reinforcement, $\xi = \lambda$. Nevertheless, in the receding contact cases, these boundary conditions should be evaluated at the point where positive relative displacement between reinforcement and concrete starts. To obtain this point a simple loop has been used, and the Algorithm 5.1 show its pseudocode. The problem is initiated assuming the contact zone as the initial unbonded region $\lambda_{uc} = \lambda_u$, where λ_{uc} is updated at each step of the loop and it is always within the unbonded region. Therefore, in each step, the point $\xi = \lambda$ where the boundary conditions mentioned above are evaluated can be defined as $\lambda = \lambda_a + \lambda_{uc}$. This point is where the lifting of the reinforcement stars. In each step, the linear system is solved for these variables and the zone where tension appear are considered for the next step free of contact.

Once the correct size of contact zone has been determined the the right stresses field can be defined. Figure 5.12 shows five different case with different λ_a and solve with the algorithm 5.1.

Algorithm 5.1: Loop to define the receding contact size.

---

   data   : Define geometry and material properties in terms of the dimensionless
              parameters defined in Table5.1
   input : Initialize $\lambda = \lambda_r$ and $\lambda_{uc} = \lambda_u$
   output: Final λ and λ_{uc}

   for every step **do**

        Solve the system of of ten linear equations for unknown constants $C_1 - C10$;

        Find root ξ_r of $\hat{\sigma}_{S2}(\xi) = 0$ for $\lambda_a \geq \xi \geq \lambda_a + \lambda_{uc}$;

        if $\xi_r \neq \emptyset$ **then**
         | $\lambda = \xi_r$ and $\lambda_{uc} = \lambda - \lambda_a$;
        else
            λ and λ_{uc} remain unchanged;
            Break;
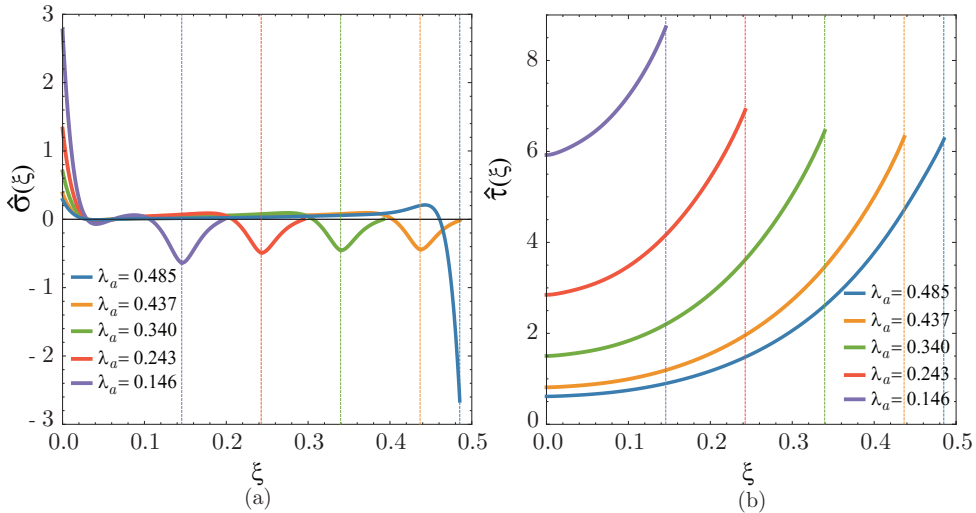
Figure 5.12: Dimensionless normal and shear stress distributions along the interface in the DPPS test with $\lambda = 0.485$ and five different adhesive zones lengths: $\lambda_a = \lambda = 0.485$ ($l_a = 100$mm), $\lambda_a = 0.437$ ($l_a = 90$mm), $\lambda_a = 0.340$ ($l_a = 70$mm), $\lambda_a = 0.243$ ($l_a = 50$mm) and $\lambda_a = 0.146$ ($l_a = 30$mm).

5.3 Comparison of the solutions of models with and without normal interfacial stresses

It is worth recalling the solution provided by the simpler shear lag (SL) model introduced in Cornetti et al. (2012). Accordingly, the adhesive is modelled as a bed of tangential springs, which are not able to transfer normal stresses ($k_n = 0$); thus, neither peeling stresses nor compressions in the adhesive layer are present in the SL model. Moreover, the adherents are assumed to withstand only axial forces. Regarding the shear stresses at the interface, the SL solution (Cornetti et al., 2012) , using the dimensionless quantities defined above, yields

$$\hat{\tau}_{SL} = \sqrt{\frac{\kappa(1+\rho)}{\eta}} \frac{\cosh\left(\xi\sqrt{\frac{\kappa(1+\rho)}{\eta}}\right)}{\sinh\left(\lambda\sqrt{\frac{\kappa(1+\rho)}{\eta}}\right)} \tag{5.71}$$

Note that the SL model is not a particular case of the present one, i.e. it cannot be achieved by setting $k_n = 0$ into the present developed model (for instance, the rotational equilibrium given by Eq. (5.3) would never be satisfied). Nevertheless, the shear stress field provided by the SL model, Eq. (5.71), agrees very well with the one provided by Eq. (5.33).

The differences obtained between both models will be analysed in detail in this section for several characteristic parameters of the DPPS test. Specifically, the influence of the parameters on the stress distributions and the dimensionless parameters defined in Table 5.1 are analysed using Eqs. (5.33) and (5.34). Additionally, the SL solution given by Eq. (5.71) will also be depicted for comparison purposes. In the following analyses, the values presented in Table 5.2 will be used except for the parameter to be analysed in each case, which will vary in the range defined in each figure. Specifically, the influence of the parameters on the stress distributions and the dimensionless parameters defined in Table 5.1 are analysed using Eqs. (5.33) and (5.34). Additionally, the SL solution given by Eq. (5.71) will also be depicted for comparison purposes. In the following analyses, the values presented in Table 5.2 will be used except for the parameter to be analysed in each case, which will vary in the range defined in each figure.

The first analysed parameter is λ, representing the length of the bonded joint (overlap length), Figures 5.13 and 5.14, show shear and normal stress distributions for several overlap lengths λ. Small differences are shown for $\hat{\tau}$ values obtained using the present model and using the SL model in Cornetti et al. (2012) for all analysed values of λ. It is noticeable that the highest differences occur at the right (loaded) end of the interface, which is the zone where the debond onset is expected to take place.

It is interesting to recall the importance of the normal stress distribution, see Figure 5.14, especially for small overlap lengths, where large tension values appear in the left end with traction free boundary conditions. Interestingly, the size of the zone under traction is independent of the overlap lenght, as highlighted in Figure 5.14(b). These results are in accordance with previous investigations (Martinelli et al., 2011; Carrara et al., 2011; Carrara and Ferretti, 2013; Czaderski et al., 2010).
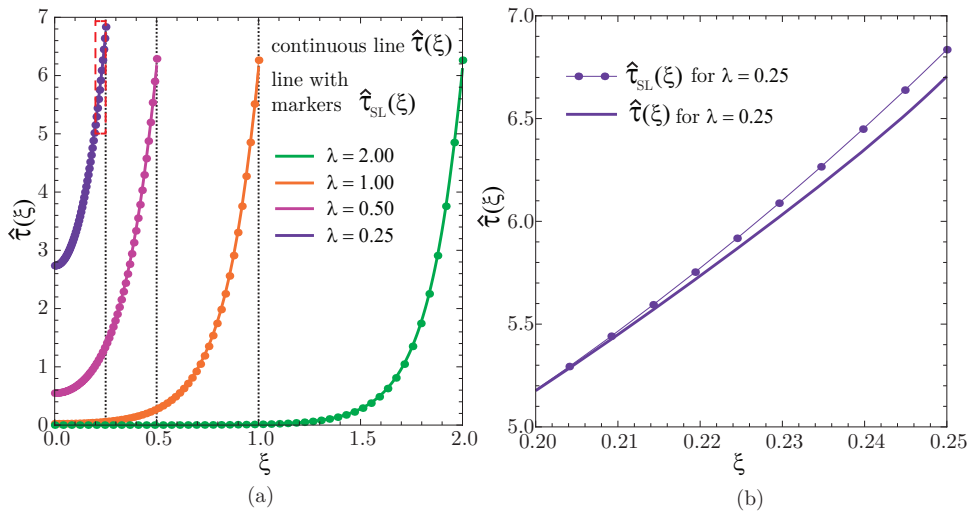
Figure 5.13: (a) Dimensionless shear stress distribution along the interface for different λ values, with $\eta = 0.00728$, $\rho = 0.142$, $\kappa = 0.25$ and $\zeta = 29.67$ (b) Zoom at the right (loaded) end of the interface for $\lambda=0.25$.
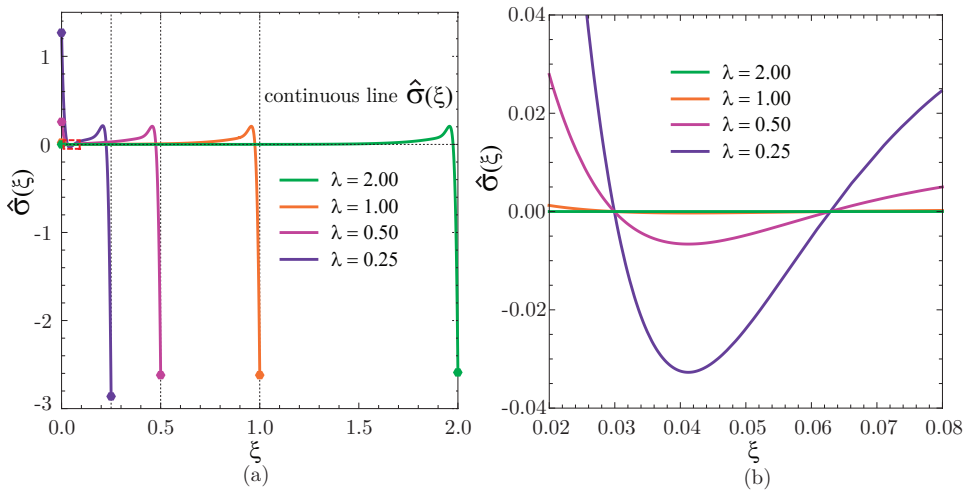
Figure 5.14: (a) Dimensionless normal stress distribution along the interface for different λ values, with $\eta = 0.00728$, $\rho = 0.142$, $\kappa = 0.25$ and $\zeta = 29.67$. (b) Zoom at the left (free) end of the interface.

The second parameter to be analysed is $\eta = \frac{h_r}{l_{ch}}$ which is directly related to the laminate (reinforcement) thickness. Also here shear stress distributions obtained by the present model and by the SL model present small differences, see Figure 5.15. The larger differences are obtained at the loaded end, where these differences slightly increase for larger values of the laminate thickness.
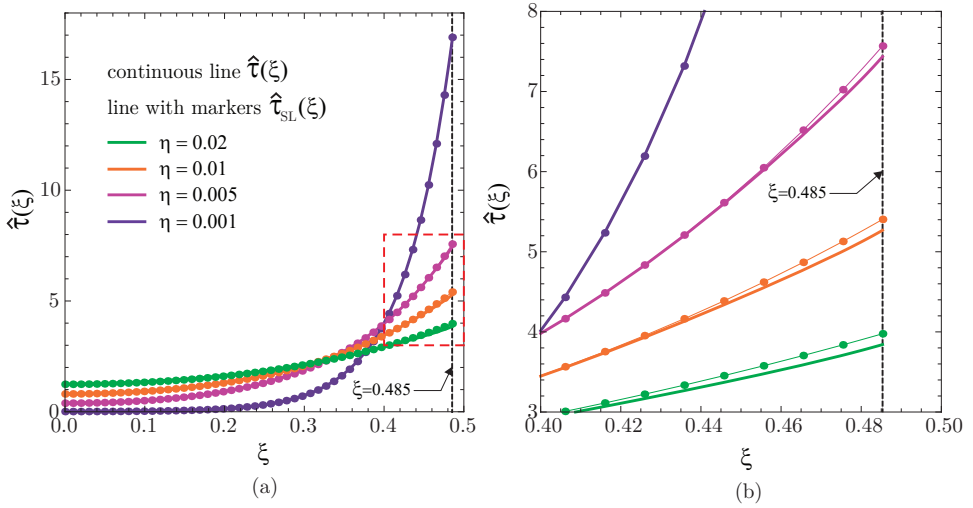
Figure 5.15: (a) Dimensionless shear stress distribution along the interface for different η values, with $\lambda = 0.485$, $\rho = 0.142$, $\kappa = 0.25$ and $\zeta = 29.67$. (b) Zoom at the loaded end.
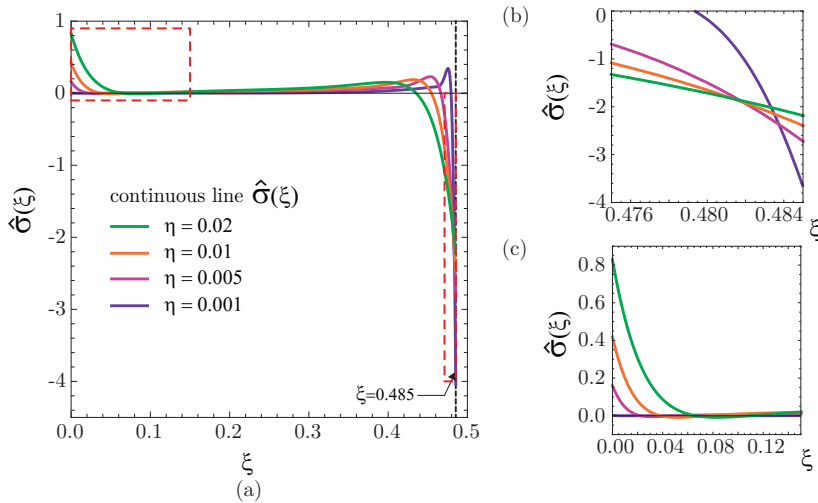
Figure 5.16: (a) Dimensionless normal stress distribution along the interface for different η values, with $\lambda = 0.485$, $\rho = 0.142$, $\kappa = 0.25$ and $\zeta = 29.67$. (b) Zoom at the loaded end. (c) Zoom at the traction free end.

Figure 5.16 presents the influence of η on the normal stress distribution. Results show that the zone of tensions and the maximum tension value at the left (free) end increase with increasing values of laminate thickness, whereas, at the opposite (loaded) end, a decrease of the maximum compression value occurs for larger laminate thickness although the zone of compressions is larger. The behaviour associated with η shows that, for larger laminate thickness, shear stresses are more uniformly distributed, while compressions at the loaded end are balanced (at least partially, in view of another intermediate zone of moderate tensions) by tensions at the free end. This fact may cause, for some geometries, debond onset at the free end.

It should be noted that although several η values are used in Figures 5.15 and 5.16. The comparison is made at constant relative axial stiffness between block and reinforcement, i.e. at constant $\rho = \frac{E'_r h_r}{E'_b h_b}$.

Then, the influence of the parameter ρ is analysed in Figures 5.17 and 5.18. Results show that a decrease of the block axial stiffness raises the shear stress peak in the loaded end as depicted in Figure 5.17.

Additionally, compressions in the loaded end increase while tensions decrease in the traction free end, as shown in Figure 5.18. It is noteworthy that this behaviour is the opposite as the one observed when η increases.
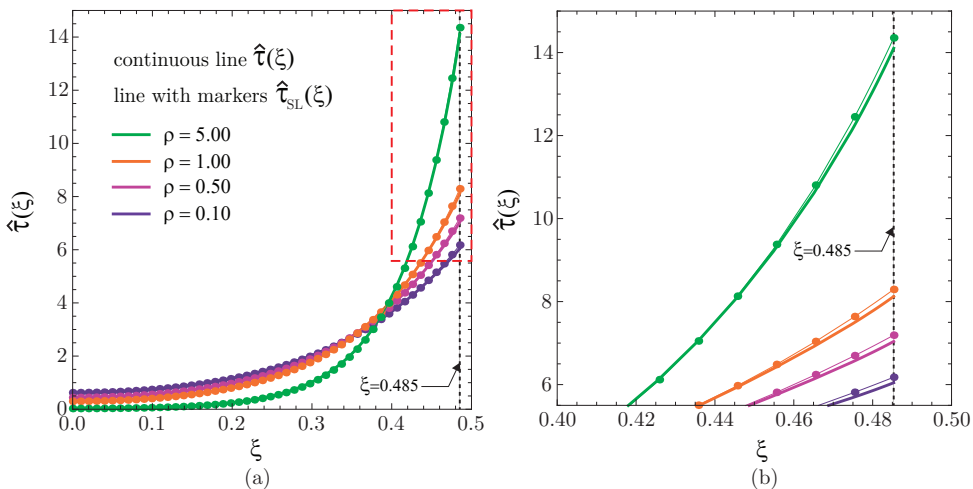
Figure 5.17: (a) Dimensionless shear stress distribution along the interface for different ρ values, with $\lambda = 0.485$, $\eta = 0.00728$, $\kappa = 0.25$ and $\zeta = 29.67$. (b) Zoom at the loaded end.

Finally, Figures 5.19 and 5.20 show stress distribution for different $\kappa = \frac{k_t}{k_n}$ values. It is interesting to notice, as indicated Mantič et al. (2015) and Távara et al. (2011), that $\kappa < 0.50$ for isotropic adhesive layers while $\kappa > 0.50$ values may be associated to orthotropic adhesive layers.

In the DPPS test, stresses along the interface are mainly dominated by shear stresses. Thus, for smaller κ values, the stress distribution along the interface is more uniform. As can be expected, this effect is more pronounced for shear stresses.
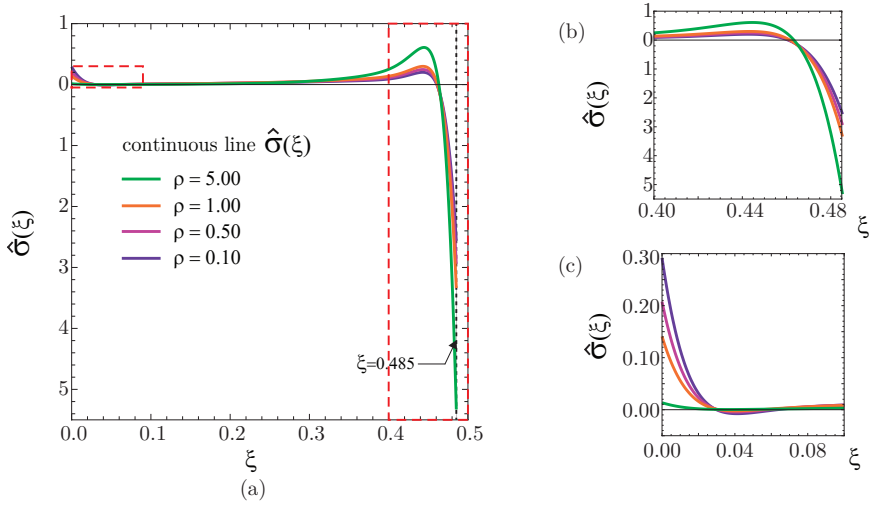
Figure 5.18: Dimensionless normal stress distribution along the interface for different ρ values, with $\lambda = 0.485$, $\eta = 0.00728$, $\kappa = 0.25$ and $\zeta = 29.67$. (b) Zoom at the loaded end. (c) Zoom at the traction free end.

Nevertheless, it is noticeable that compressions almost disappear in the traction free end for larger κ values. This behaviour is very similar to the one obtained for η.
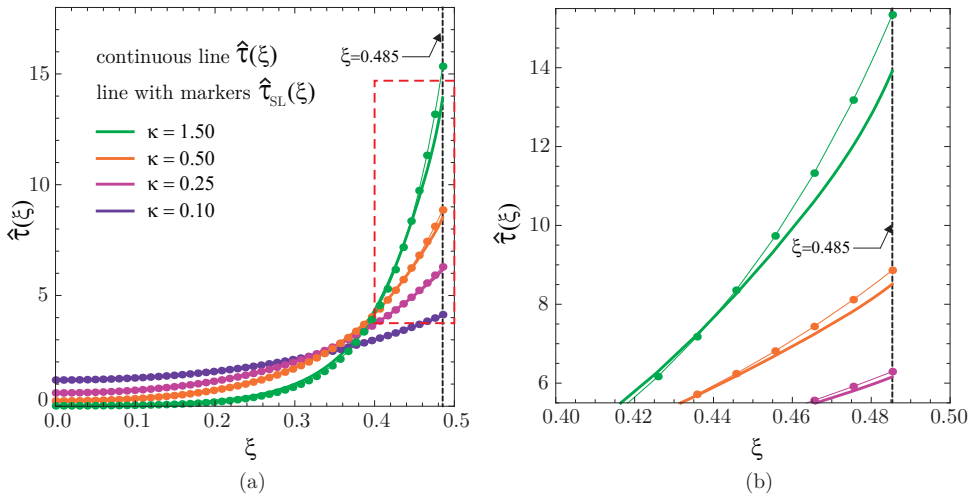
Figure 5.19: (a) Dimensionless shear stress distribution along the interface for different κ values, with $\lambda = 0.485$, $\eta = 0.00728$, $\rho = 0.142$ and $\zeta = 29.67$. (b) Zoom at the loaded end.
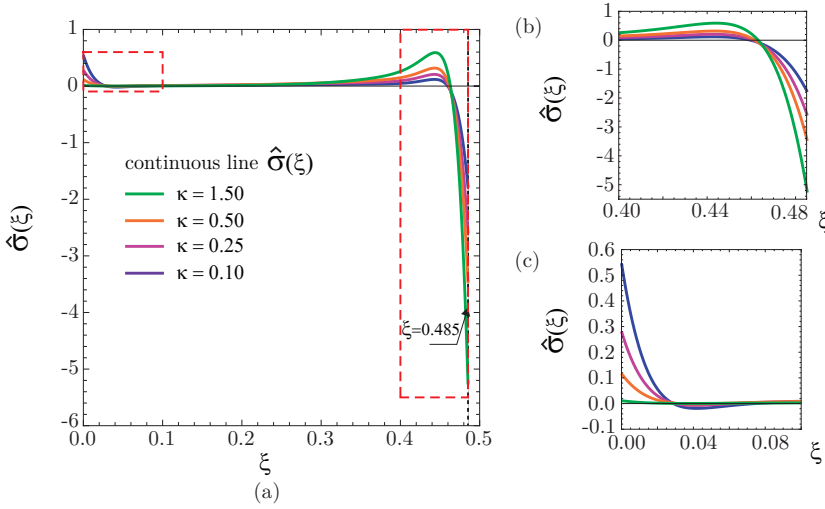
Figure 5.20: (a) Dimensionless normal stress distribution along the interface for different κ values, with $\lambda = 0.485$, $\eta = 0.00728$, $\rho = 0.142$ and $\zeta = 29.67$. (b) Zoom at the loaded end. (c) Zoom at the traction free end.

5.4 Analytical study about the Coupled Criterion of Finite Fracture Mechanics (CCFFM) applied to linear-elastic interfaces in the DPPS test

In this section, the CCFFM applied to LEBIM based on stress and energy criteria curve is used to predict the critical load which generates the crack onset in the interface in the DPPS test. This analytical application will follow the development presented in Section 3.2 but with nomenclature and dimensionless parameter adapted to this problem. As discussed in Section 3.2, the CCFFM uses both the stress and incremental energy criteria, predicting the onset of a crack with a finite (dimensionless) length $\Delta\lambda$ when both criteria are simultaneously fulfilled.

As explained in the previous section, the linear elastic behaviour of an undamaged spring, located at an interface point x, is given by relations $\sigma(x) = k_n\delta_n(x)$ and $\tau(x) = k_t\delta_t(x)$, defined for this problem in Eqs. (5.15) and (5.16). Following the development of the LEBIM of Section 2.4, the Energy Release Rate (ERR) due to an interface fracture is actually given by the energy stored in the spring (per unit area) before fracture. Thus, the ERR at an interface point can be expressed by the interface tension and shear stresses acting there, as define in (2.16), (2.17a) and (2.17b) Consequently, the ERR at an interface part under compression is associated to pure mode II, i.e. $G(x) = G_{II}(x)$.

If the dimensionless variables and parameters defined in Table 5.1 are used, also a suitable dimensionless ERR can be defined in terms of the dimensionless stresses, $\hat{\tau}(\xi)$ and $\hat{\sigma}(\xi)$, obtained in the previous section, (cf. Mantič (2009); Mantič and García

(2012)),

$$\hat{G}(\xi) = \frac{2k_t l_{ch}^2}{P^2} G(\xi) = \hat{G}_I(\xi) + \hat{G}_{II}(\xi) = \kappa \langle \hat{\sigma}(\xi) \rangle_+^2 + \hat{\tau}^2(\xi) \tag{5.72}$$

Then, the definition of the energy based fracture-mode-mixity angle $\psi(\xi)$, originally given in terms of the ERR components as $\tan^2 \psi = \frac{\hat{G}_{II}(\xi)}{\hat{G}_I(\xi)}$ for a positive $G_I(\xi) > 0$, can be extended to cover the whole angle range as follows Mantič et al. (2015)

$$\tan \psi(\xi) = \sqrt{\kappa^{-1}} \left(\frac{\hat{\tau}(\xi)}{\hat{\sigma}(\xi)} \right), \quad \text{for} \quad -\pi \leq \psi(\xi) \leq \pi \tag{5.73}$$

The plot of the fracture-mode-mixity angle $\psi(\xi)$ at undamaged points ξ, for the DPPS test model with the parameters given in Table 5.2, is shown in Figure 5.21. As can be observed, significant compressions appear in the loaded end while significant tensions occur in the free end.
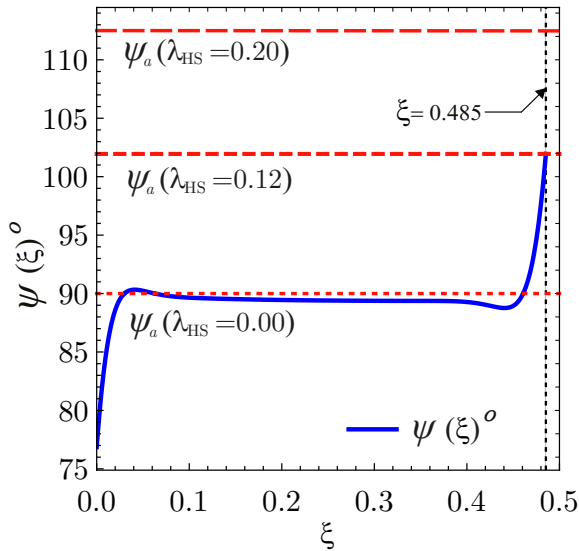
Figure 5.21: Fracture-mode-mixity angle $\psi(\xi)$ in degrees computed along the undamaged interface, for the parameters shown in Table 5.2. Additionally, ψ_a defined in (5.4.1) is indicated for several values of λ_{HS}.

In the following, the CCFFM will be applied to the DPPS test considering the parameter values defined in Table 5.2.

5.4.1 Energy based criterion

Similarly as in Mantič (2009); Mantič and García (2012), the incremental energy criterion under mixed mode is satisfied when

$$\int_{\lambda - \Delta \lambda}^{\lambda} G(\lambda') \, d\lambda' \geq \int_{\lambda - \Delta \lambda}^{\lambda} G_c(\psi(\xi)) \, d\xi, \tag{5.74}$$

where, according to Figure 5.22, $\Delta\lambda$ is a finite crack advance and $G(\lambda')$ is the ERR at the tip of a virtual interface crack of length $\Delta\lambda'$ computed by (5.72). $G_c(\psi(\xi))$ is the fracture energy associated to an undamaged interface point ξ before the debonding propagation. It is given as a function of the fracture-mode-mixity angle $\psi(\xi)$ defined in Eq. (5.73), which is coherent with the main hypothesis of FFM assuming an abrupt onset of a crack of a finite size, see García and Leguillon (2012) for a discussion. Figure 5.22 shows the way how λ' is associated to a virtual-interface-crack tip, and ξ to a point in an initially undamaged segment $\Delta\lambda$ of the interface.
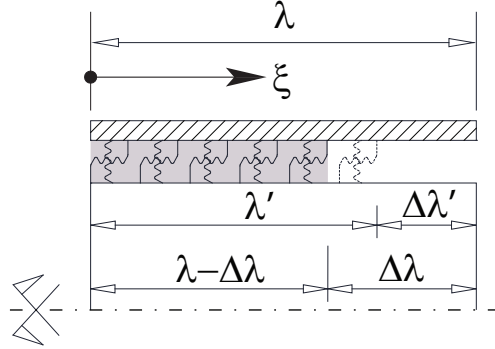
Figure 5.22: Finite crack advance description and coordinates for the incremental energy criterion.

Figs. 5.23 and 5.24, respectively, show the plots of dimensionless stresses $\hat{\tau}(\lambda')$ and $\hat{\sigma}(\lambda')$ at the tip of the virtual interface crack of length $\Delta\lambda'$ and overlap length λ', with $\lambda - \Delta\lambda \leq \lambda' \leq \lambda$. These stresses are referred to the crack tip, assuming that the debond onset will occur at the loaded end. These stress values will be used to compute the ERR associated with the debond onset.

It can be observed that both shear and normal stresses, $\hat{\tau}(\lambda')$ and $\hat{\sigma}(\lambda')$, tend to infinity when the overlap length λ' is small. Moreover, the shear stresses computed using the present model and the SL model have very similar behaviour.

Regarding the normal stress evolution, depicted in Figure 5.24, compressions appear in a small zone ahead of the interface crack tip, thus, $\hat{G}(\lambda') = \hat{G}_{II}(\lambda')$. Thus, ERR will be a function of $\hat{\tau}(\lambda')$ only, similarly as in the solution obtained by the SL model (Cornetti et al., 2012). Nevertheless, there are only small differences between both shear stress evolutions, see Figure 5.23(b). Consequently, there are also small differences between $\hat{G}(\lambda')$ values obtained from both solutions, see Figure 5.25.

For this particular study of the DPPS test, it is convenient expressing the ERR in terms of the dimensionless ERR function $\hat{G}(\lambda')$ defined previously in Eq. (5.72), but in this occasion it is associated to the virtual interface crack tip,

$$G(\lambda') = \frac{(\sigma_x^r)^2 \eta^2}{2k_t} \hat{G}(\lambda'), \tag{5.75}$$

where σ_x^r is the tension per unit width applied in the laminate (reinforcement). Note that, σ_x^r and k_t fulfill the function of σ_{nom} and k_{ch} defined in Section 3.1.
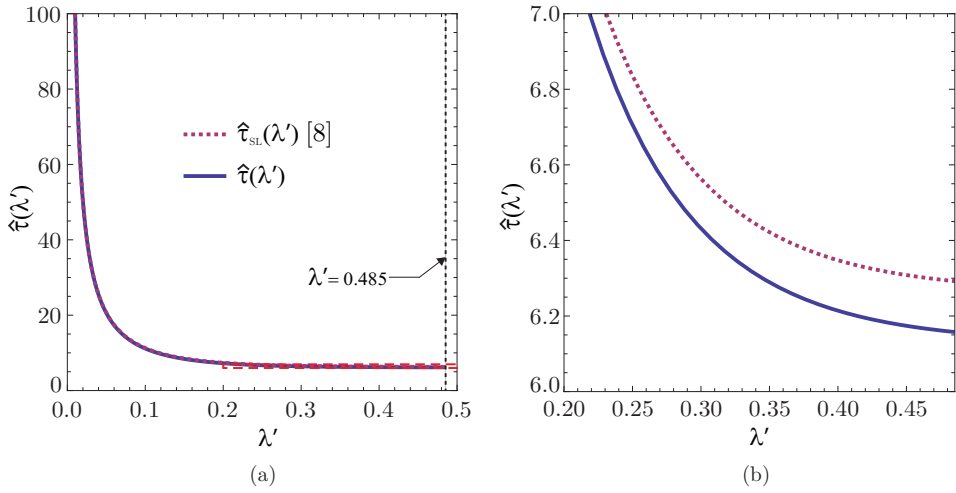
Figure 5.23: Shear stress values computed at an interface crack tip at a position λ', for the parameter values given in Table 5.2.
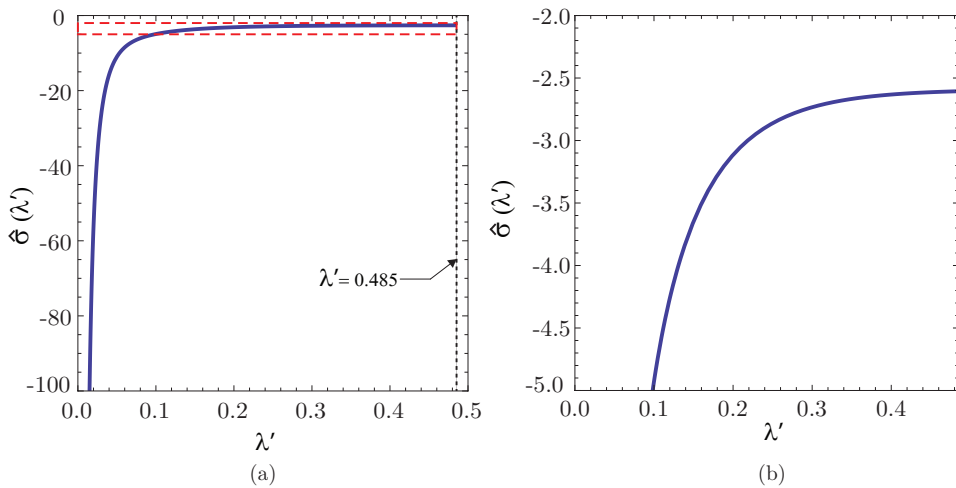
Figure 5.24: Normal stress values computed at an interface crack tip at a position λ', for the parameter values given in Table 5.2.
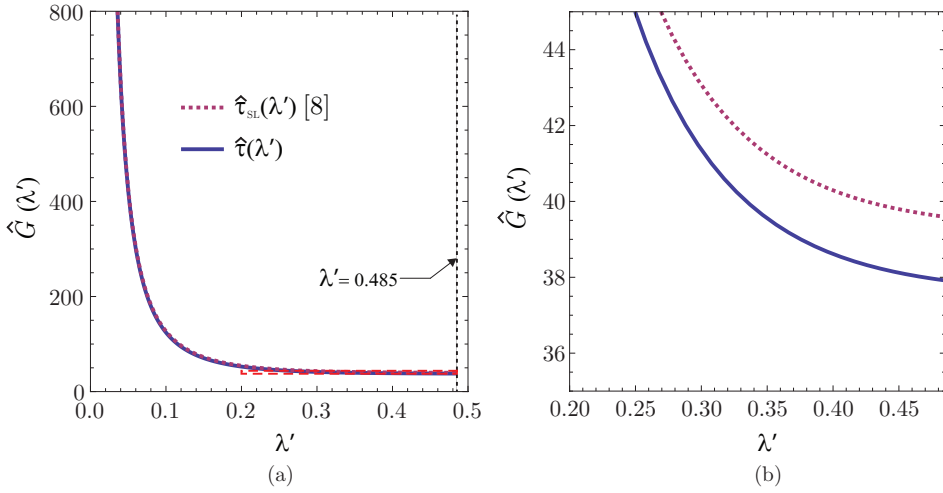
Figure 5.25: Dimensionless ERR function $\hat{G}(\lambda')$, for the parameter values shown in the Table 5.2.

Similarly, $G_c(\psi(\xi))$ can be defined in terms of a dimensionless fracture energy function

$$G_c(\psi(\xi)) = \bar{G}_{\text{IIc}} \hat{G}_c(\psi(\xi)), \tag{5.76}$$

where the $\bar{G}_{\text{IIc}} = \frac{\bar{\tau}_{\max}^2}{2k_t}$ is the fracture energy for pure mode II, with $\bar{\tau}_{\max}$ denoting the maximum shear stress associated to the energy criterion (Cornetti et al., 2012).

The dimensionless function $\hat{G}_c(\psi(\xi))$, used in this study, is similar to that proposed by Hutchinson and Suo (1992) and defined in (2.26), but using the fracture energy in mode II because the present problem has a predominant fracture behaviour in this mode,

$$\hat{G}_c(\psi(\xi)) = \sin^2\left(\lambda_{\text{HS}} \frac{\pi}{2}\right) \left(1 + \tan^2(1 - \lambda_{\text{HS}})\psi(\xi)\right), \tag{5.77}$$

$$\text{with} \quad |\psi| < \bar{\psi}_a(\lambda_{\text{HS}}), \quad 0 \le \lambda_{\text{HS}} \le 1,$$

$$\text{where} \quad \bar{\psi}_a(\lambda_{\text{HS}}) = \min\{\psi_a(\lambda_{\text{HS}}), \pi\} \quad \text{and} \quad \psi_a(\lambda_{\text{HS}}) = \frac{\pi}{2(1 - \lambda_{\text{HS}})}.$$

For the specific case of the DPPS test, a large λ_{HS} value seems to be adequate considering that fracture mode II is dominant in this test. The asymptotic values $\psi_a(\lambda_{\text{HS}})$ for several λ_{HS} are shown in Figure 5.21. Notice that interface damage cannot be produced at those points ξ where $\psi_a(\lambda_{\text{HS}}) < |\psi(\xi)|$, see Mantič et al. (2015). This is especially evident in the limit case of $\lambda_{\text{HS}} = 0$, where an interface failure under compressions is not possible. Therefore, a $\lambda_{\text{HS}} \ge 0.12$ must be selected in the present case to allow interface fracture at any position.

In Figure 5.26, $\hat{G}_c(\psi(\xi))$ in the DPPS test is plotted for several values of λ_{HS}. As can be observed, the fracture energy strongly increases at the loaded end of the interface as λ_{HS} decreases. In order to take into account the dominant fracture mode II $\lambda_{\text{HS}} = 0.5$ is used in some of the following calculations.
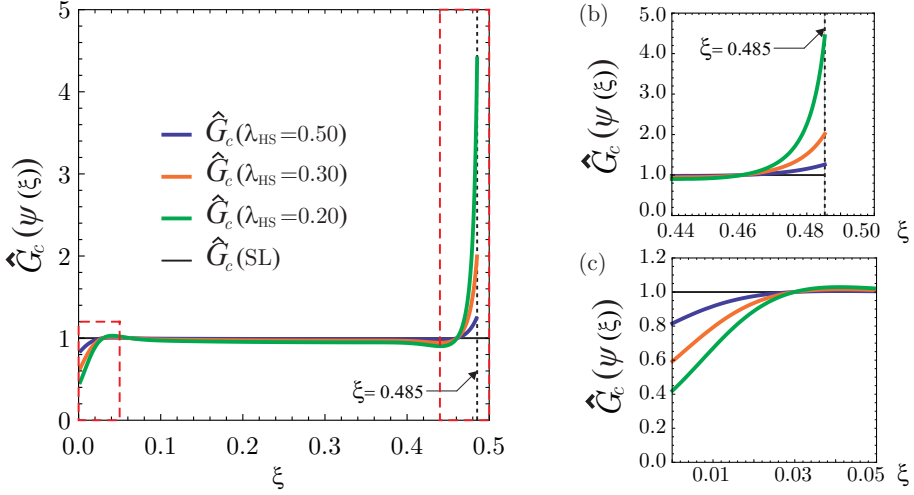
Figure 5.26: Dimensionless fracture energy function $\hat{G}_c(\psi(\xi))$ using the parameters included in Table 5.2 and for different λ_{HS} values.

Following the procedure introduced in Section 3.2 (see (3.22)) and in view of (5.75) and (5.76), the dimensionless function characterizing the ratio of the dissipated and released energies due to the debond onset

$$g(\lambda - \Delta\lambda) = \frac{\int_{\lambda-\Delta\lambda}^{\lambda} \hat{G}_c(\psi(\xi))\,\mathrm{d}\xi}{\int_{\lambda-\Delta\lambda}^{\lambda} \hat{G}(\lambda')\,\mathrm{d}\lambda'} \tag{5.78}$$

allows us to rewrite the incremental energy criterion (5.74) as

$$\frac{(\sigma_x^r)^2 \eta^2}{2k_t \bar{G}_{\text{IIc}}} \geq g(\lambda - \Delta\lambda) \tag{5.79}$$

Energy criterion curves obtained for several values of λ_{HS} are plotted in Figure 5.27. The curve obtained by the SL model introduced in Cornetti et al. (2012) is also plotted for comparison purposes. g is represented as a function of $(\lambda - \Delta\lambda)$ to relate it easily with the specimen geometry and especially the interface crack configuration. As can be observed, the energy criterion is strongly sensitive to λ_{HS} values close to the loaded end due to high compressions acting there.

5.4.2 Stress based criterion

To predict debond onset and propagation, in addition to the energy criterion (5.74), also a stress criterion must be fulfilled along an undamaged finite segment from $\xi = \lambda$ to $\xi = \lambda - \Delta\lambda$, making possible a finite crack advance $\Delta\lambda > 0$, see Figure 5.28.

The pointwise stress criterion, originally proposed in Leguillon (2002) for mode I crack onset, can be generalized to mixed mode fracture using the modulus of the interface traction vector $t(\xi)$ and its critical value $t_c(\psi(\xi))$, as indicate in (3.1),
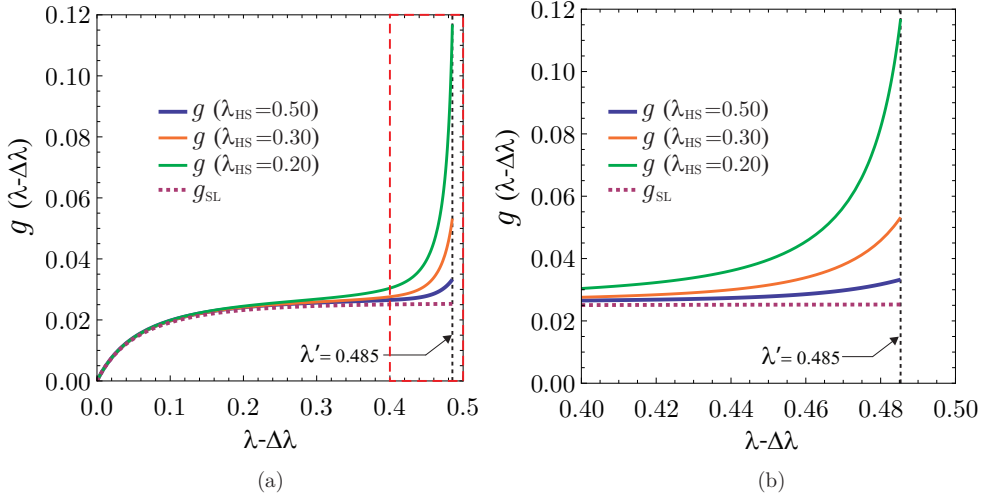
Figure 5.27: Dimensionless function of the incremental energy criterion $g(\lambda - \Delta\lambda)$, for the parameter values given in Table 5.2.
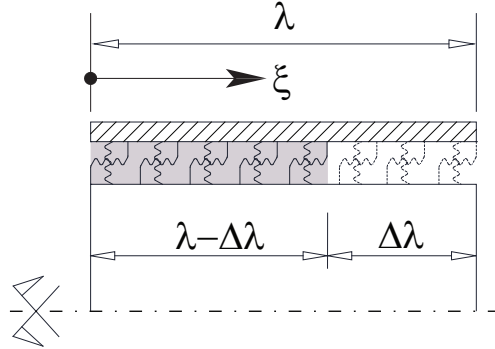
Figure 5.28: Finite crack advance in the stress based criterion.

$$\frac{t(\xi)}{t_c(\psi(\xi))} \geq 1, \quad \text{for all } \xi, \quad \lambda - \Delta\lambda \leq \xi \leq \lambda \tag{5.80}$$

where

$$t(\xi) = \sqrt{\sigma^2(\xi) + \tau^2(\xi)} \quad \text{and} \quad t_c(\psi(\xi)) = \sqrt{\sigma_c^2(\psi(\xi)) + \tau_c^2(\psi(\xi))} \tag{5.81}$$

The normal and shear critical tractions, $\sigma_c(\psi)$ and $\tau_c(\psi)$, respectively, used in the last equation can be expressed in terms of the critical shear traction for pure mode II $\bar{\tau}_c$ and a dimensionless function (Mantič et al., 2015; Távara et al., 2011). Similarly as in (2.25), the mixed mode stress criterion is chosen coherently with the energy

criterion, leading to the following expressions, cf. Mantič et al. (2015):

$$\sigma_c(\psi(\xi)) = \bar{\tau}_c\sqrt{\kappa^{-1}}\sqrt{\hat{G}_c(\psi(\xi))} \cdot \begin{cases} \cos\psi(\xi), & |\psi| \leq \frac{\pi}{2}, \\ -|\cot\psi(\xi)|, & |\psi| \geq \frac{\pi}{2}, \end{cases} \tag{5.82}$$

$$\tau_c(\psi(\xi)) = \bar{\tau}_c\sqrt{\hat{G}_c(\psi(\xi))} \cdot \begin{cases} \sin\psi(\xi), & |\psi| \leq \frac{\pi}{2}, \\ \operatorname{sign}\psi(\xi), & |\psi| \geq \frac{\pi}{2}. \end{cases} \tag{5.83}$$

As in the energy criterion, the stress criterion can also be written in terms of a dimensionless function by expressing the modulus of the traction vector $t(\xi)$ and its critical value $t_c(\psi(\xi))$ in terms of two dimensionless functions

$$t(\xi) = \sigma_x^r\eta\sqrt{\hat{\sigma}^2(\xi) + \hat{\tau}^2(\xi)} = \sigma_x^r\eta\hat{t}(\xi), \tag{5.84}$$

$$t_c(\psi(\xi)) = \bar{\tau}_c\hat{t}_c(\psi(\xi)). \tag{5.85}$$

Notice that both the modulus of the critical traction vector $t_c(\psi(\xi))$ as well as the previously defined fracture energy $G_c(\psi(\xi))$ depend on the same fracture-mode-mixity angle $\psi(\xi)$ evaluated at a considered undamaged point ξ before the debond onset, see Figure 5.21. If the Hutchinson-Suo empirical law (5.4.1) is assumed for $\hat{G}_c(\psi)$, then, similarly as in the energy criterion, interface fracture at a point ξ is allowed only if $|\psi(\xi)| < \bar{\psi}_a(\lambda_{\mathrm{HS}})$.
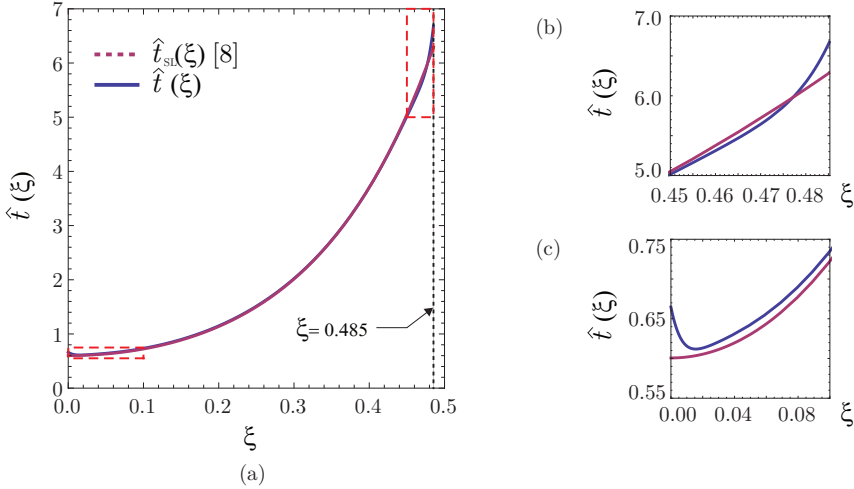
Figure 5.29: Dimensionless modulus of tractions $\hat{t}(\xi)$, for the parameter values given in Table 5.2.

Figure 5.29 shows distributions of $\hat{t}(\xi)$ for the present model and the SL model. Noteworthy, the behavior of $\hat{t}(\xi)$ is very similar for both models except for the end zones of the interface, as could be expected from the plots of tractions shown in Section 5.3.

Distributions of $\hat{t}_c(\xi)$ for several values of λ_{HS} are presented in Figure 5.30. As could be expected, smaller values of λ_{HS} lead to higher differences in the very end zones of the interface.
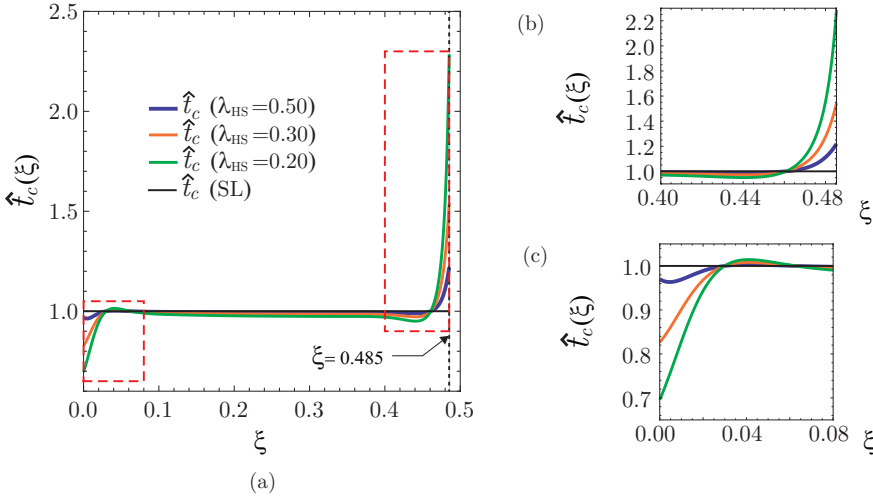
Figure 5.30: Dimensionless critical modulus of traction $\hat{t}_c(\xi)$, for the parameter values given in Table 5.2.

Then, the stress criterion in Eq. (5.80) for a finite crack advance $\Delta\lambda$ from the loaded end of the interface can be expressed in terms of the dimensionless function

$$s(\xi) = \frac{\hat{t}_c(\psi(\xi))}{\hat{t}(\xi)} \tag{5.86}$$

as

$$\frac{\sigma_x^r}{\bar{\tau}_c} \geq \frac{s(\xi)}{\eta} \quad \text{for all } \xi, \quad \lambda - \Delta\lambda \leq \xi \leq \lambda \tag{5.87}$$

or as

$$\frac{\sigma_x^r}{\bar{\tau}_c} \geq \frac{\bar{s}(\lambda - \Delta\lambda)}{\eta}, \quad \text{where} \quad \bar{s}(\lambda - \Delta\lambda) = \max_{\lambda - \Delta\lambda \leq \xi \leq \lambda} s(\xi) \tag{5.88}$$

is a monotonous function.

Function $s(\xi)$ is shown in Figure 5.31 for several λ_{HS} values. This function characterizes the load factor (LF) required to produce the debond onset according to the stress criterion. Noteworthy, a local minimum of the function $s(\xi)$ in the neighbourhood of the loaded end indicates a highly stressed region there. This observation agrees with the experimental data in Czaderski et al. (2010), where small cracks are observed in this zone prior to the failure.

5.4.3 Coupled criterion

A way to characterize the predictions of the coupled criterion of FFM + LEBIM, applied in the present study, is to use the dimensionless characteristic parameter μ, defined in (3.12), using parameters for pure fracture mode II, as

$$\mu = \frac{2k_t \bar{G}_{\mathrm{IIc}}}{\bar{\tau}_c^2} = \frac{\tau_{\max}^2}{\bar{\tau}_c^2}, \tag{5.89}$$
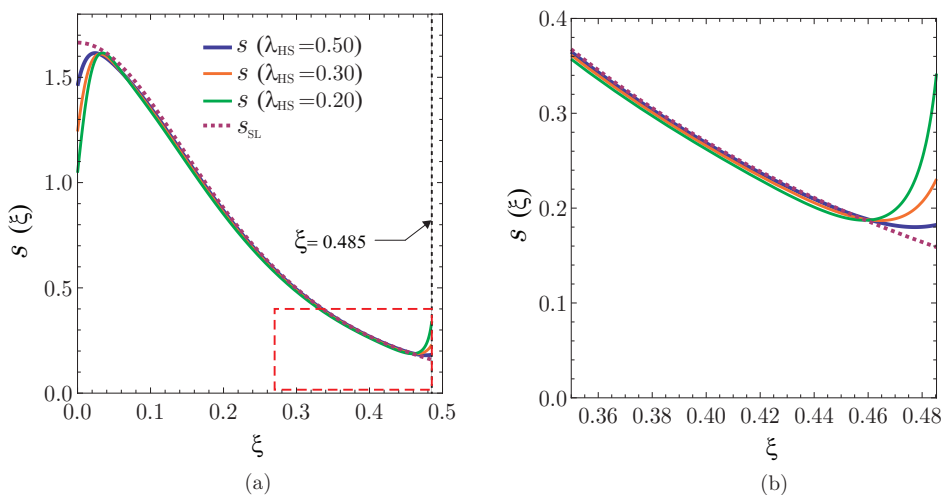
Figure 5.31: Dimensionless function of the stress criterion $s(\xi)$, for the parameter values shown in Table 5.2.

where $\tau_{\max}$ and $\bar{\tau}_c$ are the maximum and critical shear stresses associated to the energy and stress criteria, respectively. As can be seen from the previous sections, the fracture energy and the strength of the interface are independent data in the present FFM+LEBIM approach. Recall that in the original LEBIM these variables were directly related by an equality including the interface stiffness (Mantič et al., 2015; Távara et al., 2011).

To combine both criteria in Eq. (5.79) and Eq. (5.88), the energy criterion is rewritten in a form similar to that of the stress criterion

$$\frac{\sigma_x^r}{\bar{\tau}_c} \geq \frac{\sqrt{\mu}}{\eta} \sqrt{g(\lambda - \Delta\lambda)}. \tag{5.90}$$

Then, by combining Eqs. (5.88) and (5.90), the CCFFM+LEBIM, can be expressed in the present case as

$$\frac{\sigma_x^r}{\bar{\tau}_c} \geq \frac{\sigma_{\mathrm{crit}}^r}{\bar{\tau}_c} = \min_{\Delta\lambda} \max \left\{ \frac{\bar{s}(\lambda - \Delta\lambda)}{\eta}, \frac{\sqrt{\mu}}{\eta} \sqrt{g(\lambda - \Delta\lambda)} \right\}, \tag{5.91}$$

where the minimum is achieved at $\Delta\lambda = \lambda_{\mathrm{crit}}$ and σ_{crit}^r is the critical values of σ_x^r.

Figure 5.32 shows failure curves for the energy and stress criteria obtained with the present model and the SL model, using the parameters given in Table 5.2 and $\lambda_{\mathrm{HS}} = 0.5$. The figure includes the solutions for several values of μ. It can be observed that both criteria coincide for $\mu = 1$, predicting an infinitesimal crack initiation with $\lambda_{\mathrm{crit}} = 0$, but for increasing μ values, λ_{crit} and the failure load increase as well. For the chosen value λ_{HS} the differences between the developed model and the SL model are quite small, however, for smaller values of λ_{HS} they can become quite large.

Finally, debond growth (crack propagation) is presented in Figure 5.33 for $\mu = 8$ and $\mu = 4$. The intersection of both (energy and stress based) criteria allows to obtain the load factor (f_{FFM}) required to produce a debond onset or growth with a finite
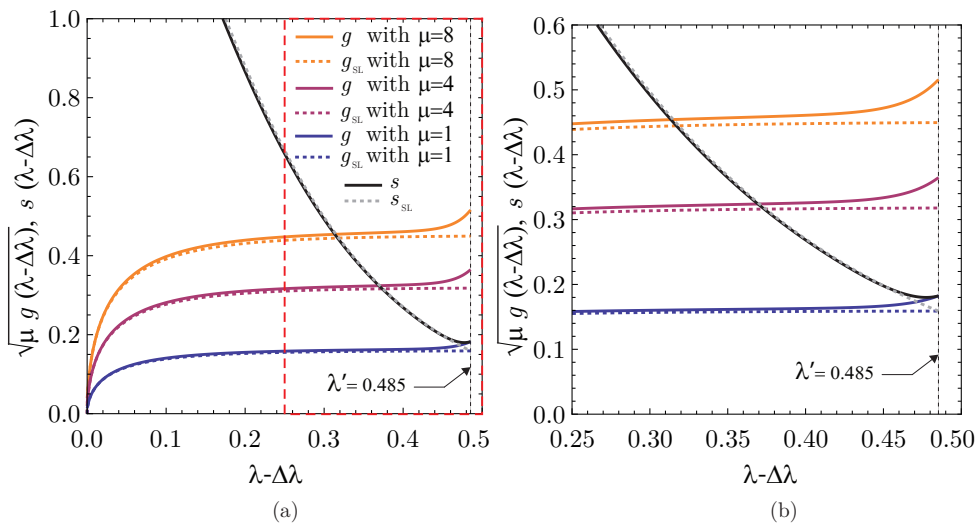
Figure 5.32: Intersection of the curves $\sqrt{\mu g(\lambda - \Delta\lambda)}$ and $s(\lambda - \Delta\lambda)$ for the present model and the SL model, for several values of μ and for the parameter values shown in Table 5.2.
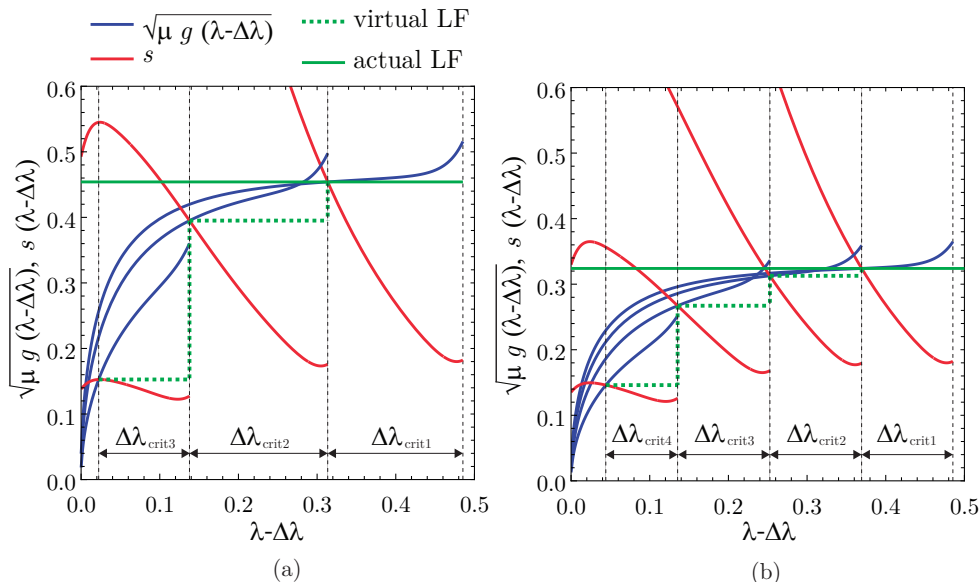
Figure 5.33: Prediction of the stepwise debond growth (propagation) in the DPPS test, for the parameter values shown in Table 5.2, with $\lambda_{\mathrm{HS}} = 0.5$ and for (a) $\mu = 8$ and (b) $\mu = 4$.

length λ_{crit}. Then, for each debond a "new" overlap length, $\lambda' = \lambda - \lambda_{\text{crit}}$, is used in the coupled criterion. To be consistent with the non-local method used, horizontal lines are represented for each f_{FFM} with its corresponding λ_{crit}, thus a stepped graph representing a series of finite crack advances is obtained. From a physical point of view, these results show that fracture is actually unstable under load-control and the first f_{FFM} will produce a complete debond of the interface. Hence, the jumps included in the stepped graph are associated to a kind of hypothetical f_{FFM}.

It should be mentioned that for small overlap lengths also another debond might occur in the opposite (free) end. This alternative failure mechanism is not studied in the present investigation, assuming that the unstable character of the crack growth will produce a one-way debond advancing.

5.5 Convergence study in BEM for DPPS test

In order to check the adequacy of the implementation of the criterion proposed above, in the next sections, two different experimental tests of the bibliography will be compared with the numerical and analytical solutions presented in previous sections. However, caution should be exercised in some configurations studied by numerical LEBIM.

As mentioned above, the CCFFM approach has been incorporated into LEBIM in order to characterize adequately thin adhesive layers with a high stiffness. Nevertheless, because of the CCFFM requires the evaluation of the energy released at the crack tip, in a numerical model of an adhesive joint, the high stiffness of a thin adhesive layer may cause difficulties in convergence of the traction solution in the crack tip, which may lead to large errors in crack onset and propagation predictions. Since, Lenci (2001) showed that there is a singularity of the stress gradient at the crack tip in the interface modelled by a spring distribution (LEBIM), leading to a steep peak of tractions there, which is particularly sharp for stiff interfaces. Notice that although stresses along the interface are bonded in LEBIM, they locally follow an asymptotic law in the zone close to the crack tip. Thus, stresses tend to the Griffith solution (for perfect interface) as the weak interface becomes stiffer.

To overcome this issue, i.e. the singularity of stress gradients close to the crack tip, very refined meshes are needed to obtain the maximum stress values with an acceptable discretization error. Therefore, a mesh convergence analysis should be done in every problem under study. The simplified numerical model used for this convergence study is presented in Figure 5.34. Note that the interface mesh is more refined than the rest of model because is in the interface where the singularity of the stress gradient is appear. Also, a finer mesh is needed for thin reinforcement layer to adequately model its bending and to allow an accurate computation of the stresses along the interface.

It should be noted that, as shown in Figure 5.43, the interface is modelled by a continuous spring distribution (zero thickness interface). Actually, the LEBIM constitutive law is established considering the equilibrium and compatibility conditions along the interface between both the solids. A detailed explanation of the LEBIM implementation in the 2D BEM code is presented in Mantič et al. (2015) and Távara et al. (2010, 2011, 2019).

Five different meshes are used, where the only difference is the size of boundary elements along the interface: m1–0.0667mm, m2– 0.10mm, m3–0.20mm, m4–0.40mm and m5–1.00 mm.
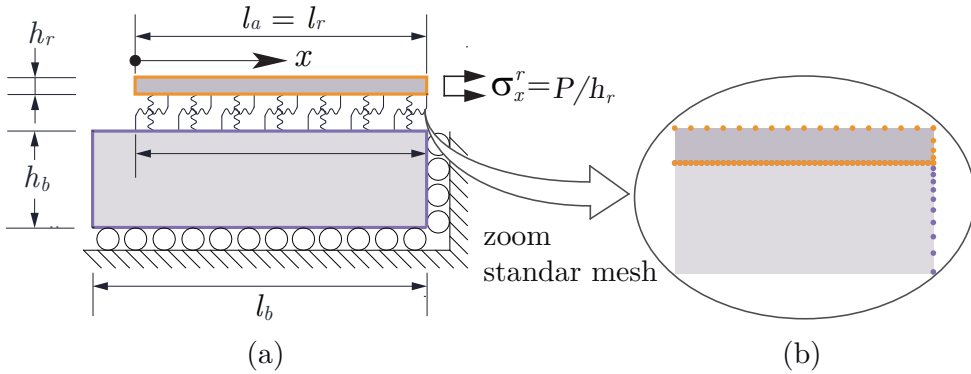
Figure 5.34: (a) Shear stresses along the interface. (b) Normal stresses along the interface.

The mechanical and geometrical characteristics used for the concrete block are: E_b=30GPa, ν_b=0.20 and h_b=50mm; and for the reinforcement: E_r=160GPa, ν_r=0.30 and h_r=2mm. The bonded zone length between the solids is l=190mm. Finally, to study the influence of the adhesive stiffness on the mesh convergence, the following values are used: k_t=4GPa/m, k_t=180GPa/m and k_t=720GPa/m, using a ratio k_n/k_t=4 for every case.
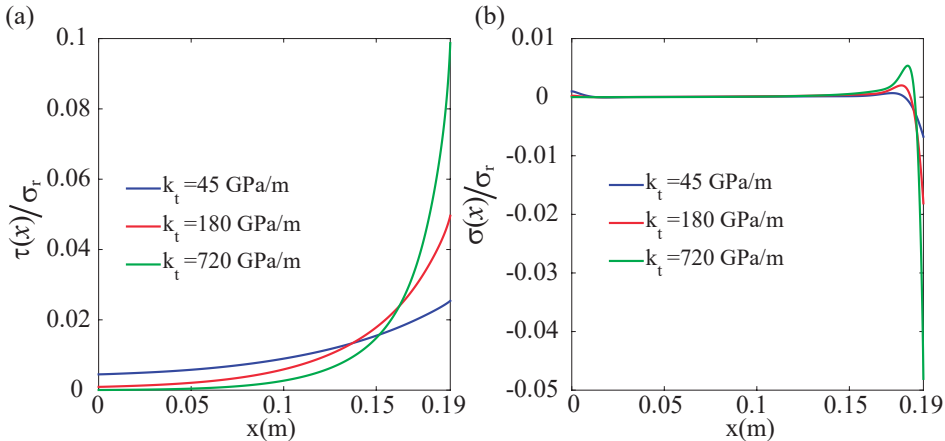
Figure 5.35: (a) Shear stresses along the interface. (b) Normal stresses along the interface.

Figures 5.35 (a) and (b) show the shear and normal stress distribution for the different stiffness values used and for the model m1 (finest mesh). It should also be remarked that the differences between the different meshes are negligible except in a zone close to the crack tip. It can also be noticed that both normal and shear stresses

have an asymptotic behaviour close to the crack tip (right part of the curves). That is why, a mesh refinement is needed when stiff interfaces are intended to be modelled.
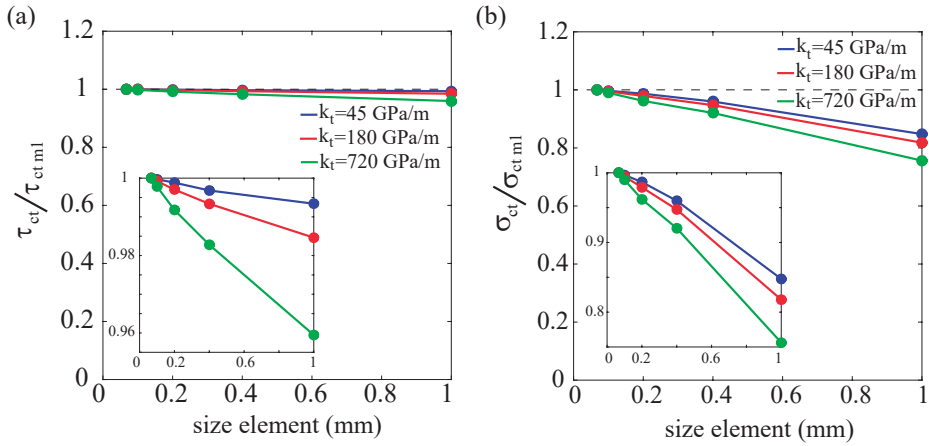
Figure 5.36: (a) Dimensionless shear stresses at the crack tip. (b) Dimensionless normal stresses at the crack tip

The convergence analysis of the 5 used meshes as function of the interface stiffness is presented in Figures 5.36 (c) and (d). These curves show the dimensionless normal and shear stress values at the crack tip versus the element size along the interface. Dimensionless values are obtained dividing the stress values in the different models by their corresponding value in the model m1 (finest mesh).

Once the convergence study is done, the model with the finest mesh (m1) is chosen to apply the coupled criterion using different stiffness along the interface, while the other parameters remain constant. With this, the influence of the interface stiffness on the results predicted by the present procedure can be analysed for the conclusions of this study. Thus, chosen fracture parameters are: G_{Ic}=8.62J/m^2, G_{IIc}=41.80J/m^2, $\bar{\sigma}_{\mathrm{c}}$=1.76MPa, $\bar{\tau}_{\mathrm{c}}$=1.94MPa and k_n/k_t. Thus, for k_t=180GPa/m and k_t=720GPa/m values, μ=4 and μ=16 are obtained respectively.

Figure 5.37 shows the critical applied load in the reinforcement, σ_{crit}, needed to produce the debond onset. As defined above, the curves representing the energy criterion ($g(\Delta a)$) and stress criterion ($s(\Delta a)$) are depicted in the figure. As is explained in Section 3.2, the intersection of both curves represents the first point where both criteria are fulfilled, i.e. a debond onset with size a_{crit} is caused by a critical load σ_{crit}. Results indicate that stiffer interfaces need a slightly higher critical loads (σ_{crit}) while the initial crack advance (a_{crit}) is smaller.

In Figures 5.38 (a) and (b) the first two increment of the crack are very similar for each interface stiffness value. This debond length can be defined as a characteristic overlap length in the DPPS test, this length depends on the characteristics of the materials (Cornetti et al., 2012).

It can be concluded that in the DPPS test the new tool is able to accurately predict debond onset and growth even for stiff interfaces, but a mesh refinement is
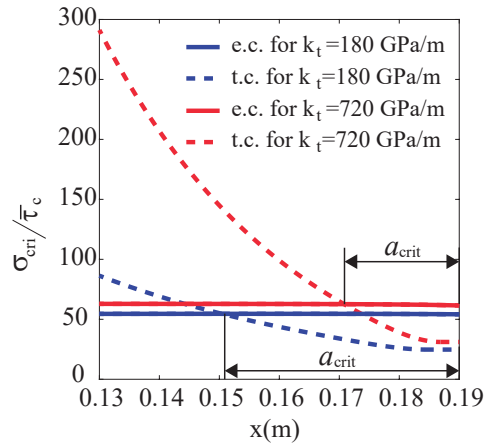
Figure 5.37: a_{cri} and σ_{cri} values predicted by the CCFFM criterion in the pull push shear test.
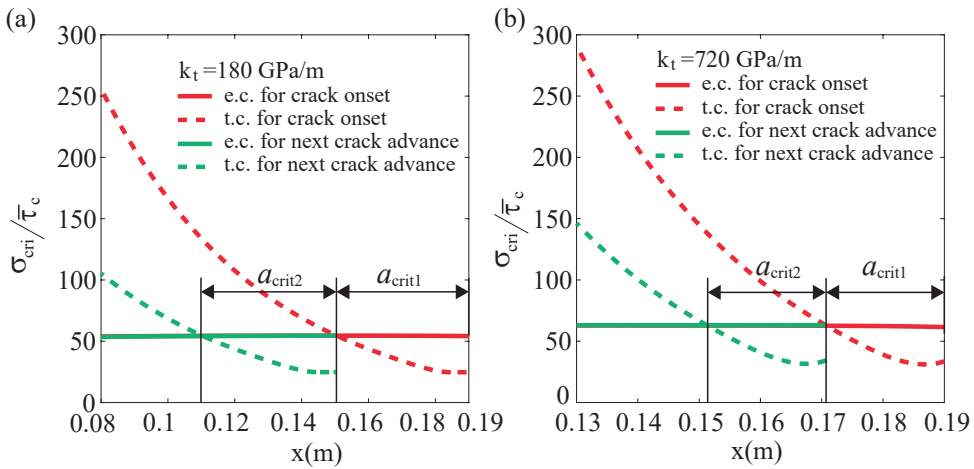
Figure 5.38: Crack onset and propagation for two different stiffness

needed at least in the zone close to the crack tip when this kind of the interfaces are modelled.

5.6 Comparison with experimental results

This section aims to compare the predictions obtained by the presented procedure and some experimental data available in literature, where numerous types of shear test can be found, see Mazzotti et al. (2016) and Zhang et al. (2018) for a review. In this chapter two different tests will be compared whit the analytical and numerical results for the CCFFM + LEBIM.

The first comparative study will show the results by Carrara et al. (2011) and the solutions of the analytical procedure developed in Section 5.4. The second study will compare the experimental data by Yuan et al. (2019a) with a numerical study made with the algorithm 3.1 and implemented in the BEM code mentioned above.

In every case, the results obtained depend on the laboratory test setup, the mechanical properties of materials and the type of control during the tests. Thus, for an adequate comparison, the mechanical and geometrical characteristics of the concrete block and reinforcement are necessary. Moreover, it is well known that the failure of the joint between the reinforcement and the concrete block is normally produced in a zone within the concrete close to the adhesive layer. This zone can be considered as part of the joint. However, the mechanical and geometrical properties of this zone oscillate for each type of joint. Therefore the joint quality depends on several factors including the mechanical properties of the reinforcement and the concrete surface (Mazzotti et al., 2016; Yuan et al., 2019; I.Iovinella et al., 2013). This is the reason why it is difficult to determine the parameters k_t, k_n, $\bar{G}_{\mathrm{IIc}}$, $\bar{\tau}_{\mathrm{c}}$ and λ_{HS}. Therefore an inverse analysis is an attractive option to obtain these parameters, cf. Martin et al. (2018) and Távara et al. (2019b); however a large number of test is required. As the objective of this investigation is not a complete interface characterization, a simplified inverse analysis, providing only the fracture toughness and the critical shear stress, is applied.

5.6.1 Comparison with the tests of Carrara et al. (2011)

The experimental results by Carrara et al. (2011), studying a shear test for different reinforcement lengths shorter than the effective anchorage length, are used to compare with the present theoretical predictions. Note that for the reinforcement lengths longer than the effective anchorage length, the values of λ_{crit} and σ^r_{crit} (the critical values of σ^r_x) are always the same. For this reason, these tests are a good option for an inverse analysis, since the only parameter which significantly varies is the length of the joint.

Four different tests in Carrara et al. (2011) are used for this comparison, namely 30B, 60C, 90B and 120B. In Table 5.3, the mechanical and geometrical characteristics of the concrete block and reinforcement used in Carrara et al. (2011) are indicated. As no further information was found, the reinforcements are considered homogeneous and isotropic.

In Table 5.4, the interface properties used in the present procedure are shown. Additionally, $\lambda_{\mathrm{HS}} = 0.5$ (Hutchinson and Suo, 1992) is assumed since the shear test was carried out in a predominant fracture mode II. The k_t value is calibrated in order to fit the slopes of the load-displacement curves for every test. The relation

Table 5.3: Geometrical and elastic properties of the different tests obtained from Carrara et al. (2011).

Concrete block	l_b(mm)	h_b(mm)	t_b(mm)	E_b(GPa)	ν_b
	300	90	150	28.7	0.20
Reinforcements	l_r(mm)	h_r(mm)	t_r(mm)	E_1(GPa)	ν_{13}
30B	31	1.32	30.5	168.5	0.248
60C	61	1.33	30.3	168.5	0.248
90B	91	1.31	29.3	168.5	0.248
120B	121	1.22	29.8	168.5	0.248

$\kappa = \frac{k_t}{k_n} = 0.25$ is taken assuming an isotropic behaviour of the interface. Finally, to determine $\bar{G}_{\mathrm{IIc}}$ and $\bar{\tau}_c$ a simplified inverse analysis with the four tests is performed.

Table 5.4: Interface properties of the different tests used in the procedure presents in Section 5.4.

Specimens	k_t(MPa/mm)	$\kappa = \frac{k_t}{k_n}$	$\bar{G}_{\mathrm{IIc}}$(N/mm)	$\bar{\tau}_c$(MPa)	λ_{HS}
30B	280	0.25	0.42	5.8	0.5
60C	90	0.25	0.42	5.8	0.5
90B	340	0.25	0.42	5.8	0.5
120B	65	0.25	0.42	5.8	0.5

In Figure 5.39, the load-displacement predictions are presented. P is the load applied on the reinforcement and the "slip" is the relative tangential displacement (δ_t) produced between the loaded edge of the reinforcement and the concrete block. The thick lines represent the solutions obtained by the procedure presents in Section 5.4 and the thin lines are the experimental results in Carrara et al. (2011) for the different configurations. Recall that in the present model, only the debond onset is predicted since the boundary conditions include a load control. In this sense, the arrow size is associated to the first finite debond-size produced in the debond onset, whereas the subsequent unstable debond propagation is indicated by the dashed line. However, the tests are driven under displacement control and are able to capture even a snap-back behaviour, which was one of the aims in Carrara et al. (2011). Except for this difference, an good agreement between the experimental response and the model predictions is observed.

Noteworthy, the debonds are not always produced at the loaded edge of the reinforcement. For the shorter joints, the debonds are produced at the free edge, as described in Carrara et al. (2011). The procedure presented is this work is also able to predict the variation of the debonding onset location, since the load necessary to produce the debond at the free end for specimens 30B and 60C is smaller than load necessary to originate the failure at the loaded edge. For the prediction of the load at the free edge one simply has to change the reference system for finite crack advance description or to switch the boundary conditions between the free and loaded edges. Although the difference between these two loads is not large in specimen 60C, this difference is sufficient for the present procedure to predict the debond at the free edge using the interface properties in Table 5.4.
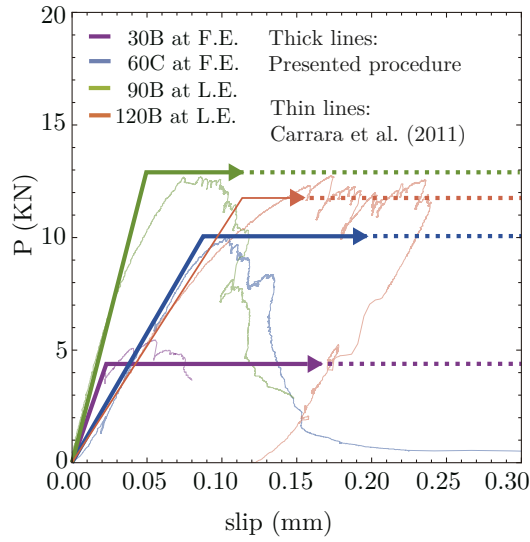
Figure 5.39: Experimental load vs. displacement plots obtained from Carrara et al. (2011) compared with the failure load predictions by the procedure presents in Section 5.4. F.E. and L.E. mean the free end and loaded end, respectively.

Table 5.5: Comparison of the maximum load for every specimen.

Specimens	Experimental tests Carrara et al.(2011)	Analytical Procedure	CZM Carrara and Ferretti(2013)
30B	5.5kN at F.E.	4.5kN at F.E.	5.8kN at F.E.
60C	10.0kN at F.E.	10.1kN at F.E.	10.6kN at F.E.
90B	12.6kN at L.E.	12.9kN at L.E.	13.8kN at L.E.
120B	12.8kN at L.E.	11.8kN at L.E.	15.3kN at L.E.

It should be noted that only a few CZMs are able to model adequately the tests by Carrara et al. (2011). This is because a mixed mode fracture model, similar to that proposed by Carrara and Ferretti (2013), is necessary to predict the phenomenon of the free edge failure. In Table 5.5, the results in Carrara and Ferretti (2013) are compared with the predictions obtained by the present procedure. This table shows an excellent agreement between the maximum load achieved in the tests and the predictions by the present procedure and by Carrara and Ferretti (2013). Note that in Carrara and Ferretti (2013) the stiffnesses of the interface (k_t and k_n) are taken from the Italian standards. A discussion about a quite wide range of admissible values for these parameters can be found in that work.

5.6.2 Comparison with the tests of Yuan et al. (2019a)

Recently, Yuan et al. (2019a,b) carried out several test campaigns to study the effects of some characteristics on this type of joints. Three experimental tests described

in Yuan et al. (2019a) are used in this investigation for comparison with the present numerical results. In the mentioned study, the interfacial behaviour between hybrid FRP (carbon and basalt) and concrete blocks are evaluated. Yuan's results show the effects of FRP stacking sequence and the mechanical properties of FRP on the joint behaviour.

The three types of specimens used keep the same geometry and mechanical properties, except for the reinforcements, which differ in the composition of their laminates. The reinforcement laminates of the chosen specimens from Yuan et al. (2019a) are (keeping their names):

- 2C with two Carbon FRP layers (named 2C).

- 1C4B with one Carbon FRP layer (named 1C) bonded to the concrete block and four layers of Basalt FRP (named 4B) attached to the top of 1C.

- 4B1C with four Basalt FRP layers (named 4B) bonded to the concrete block and one Carbon FRP layer (named 1C) attached to the top of 4B.

The geometrical and mechanical characteristics of the solids used in the experimental tests are shown in Table 5.6. All the characteristics were obtained from Yuan et al. (2019a), with the exception of E_b, ν_b and ν_r, which have been estimated within the usual range of properties (fib special activity group et al., 2013; Mazzotti et al., 2016).

Table 5.6: Geometrical and mechanical characteristics of the solids used in the PPST (Yuan et al., 2019a).

Concrete block		l_b(mm)	t_b(mm)	h_b(mm)	E_b(GPa)	ν_b
		350	350	150	30	0.2
Reinforcements	l_u(mm)	l_a(mm)	t_r(mm)	h_r(mm)	E_r(GPa)	ν_r
2C	50	200	40	0.334	191	0.30
1C4B	50	200	40	0.647	85	0.30
4B1C	50	200	40	0.647	85	0.30

Moreover, as mentioned above, the mechanical behaviour of the interface depends not only on the adhesive but also on the concrete block characteristics and the bonding process. This is due to the experimentally observed fact that the debond surface is typically produced in a thin layer of concrete close to the reinforcement laminate. For this reason, a simplified inverse analysis is proposed in this investigation with the aim to characterize the interface of the experimental tests of Yuan et al. (2019a). This analysis is described in the following subsection.

5.6.2.1   Inverse analysis applied to the PPST

Several authors used inverse analyses to calibrate the FRP–Concrete behaviour by means of interface laws, e.g. M.Savoia et al. (2009); Woo and Lee (2010) and Y.Li et al. (2018). Some authors obtained fracture mechanics parameters within the framework of CCFFM (Martin et al., 2018) or LEBIM (Távara et al., 2019) using an inverse

analysis. Using analytical solutions for PPST obtained in Section 5.4, an inverse analysis will be developed to determine two parameters needed for the present procedure: $\bar{G}_{\text{IIc}}$ and $\bar{\tau}_c$.

It should be recalled that the failure along the interface using the CCFFM applied to LEBIM is characterised by three independent parameters: $G_{\text{c,ch}}$, $\sigma_{\text{c,ch}}$ and k_{ch}. In the problem under study, these parameters are: $\bar{G}_{\text{IIc}}$, $\bar{\tau}_c$ and k_t, respectively. In the experimental tests studied (Yuan et al., 2019a), k_t can be obtained from the load-displacement curves in a straightforward way. This is possible because the first part of these curves shows that the displacements are proportional to the load, therefore, this part will depend only on the elastic parameters of the system (Cornetti and Carpinteri, 2011; Cottone and Giambanco, 2009; Carrara and Ferretti, 2013). As, in this case, the elastic parameters of the concrete and the reinforcement are set through specific experimental tests defined in Yuan et al. (2019a), the stiffness of the interface in the numerical model can be fitted by comparison with the slope of the corresponding experimental load-displacement curve before debond occurs. Values of k_t used for each type of specimen are shown in Table 5.7.

In order to obtain the other two parameters mentioned above by means of the inverse analysis, at least two different tests with the same geometrical and mechanical properties (except for different values of a governing parameter relevant for the failure load of the interface) are required.

Thus, a failure surface $\sigma^r_{\text{crit}}(\bar{G}_{\text{IIc}}, \bar{\tau}_c)$ can be obtained for each test configuration, and it can be compared with the $\sigma^r_{\text{crit,exp}}$ value taken directly from the experimental tests. In this study, three different tests have been used to obtain a pair of adequate values of $\bar{G}_{\text{IIc}}$ and $\bar{\tau}_c$, and the considered governing parameter is the stiffness of different reinforcements described in Table 5.6.

In Yuan et al. (2019a) three specimens were tested for each configuration. Thus, they obtained three debond loads for each type of reinforcement (2C, 1C4B and 4B1C), which are also shown in Table 5.7. This loads correspond to the first peak in the load-displacement curves. In the present investigation, $\sigma^r_{\text{cri,exp}}$ was established for each reinforcement using the arithmetic mean of the three loads provided by Yuan et al. (2019a).

Table 5.7: Debonding loads and the used interface stiffnesses extracted from the experimental data in Yuan et al. (2019a).

	2C	1C4B	4B1C
Debond load 1 (kN)	12.50	12.50	16.09
Debond load 2 (kN)	13.13	14.38	17.97
Debond load 3 (kN)	13.43	11.88	17.40
$\sigma^r_{\text{crit,exp}}$ (MPa) (mean value)	974.55	499.23	662.80
k_t (MPa/mm)	3.6	4.7	7.0

Although the failure surfaces $\sigma^r_{\text{crit}}(\bar{G}_{\text{IIc}}, \bar{\tau}_c)$ can be obtained from the numerical solutions of the problem for several pairs of $\bar{G}_{\text{IIc}}$ and $\bar{\tau}_c$ values, the analytical solution for the double pull push shear test presented in Section 5.4 has been used for the sake of simplicity. The points that generate the failure surface for each configuration are

obtained applying (2.3). Then, the load applied at the end of the reinforcement that produces the debond along the interface, σ_{crit}^r, can be written in terms of a_{crit}:

$$\sigma_{\text{crit}}^r = \bar{\tau}_c \; s\left(a_{\text{crit}}\left(\mu\right)\right) = \bar{\tau}_c \; s\left(a_{\text{crit}}\left(\frac{2\bar{G}_{\text{IIc}}k_t}{\bar{\tau}_c^2}\right)\right) \tag{5.92}$$
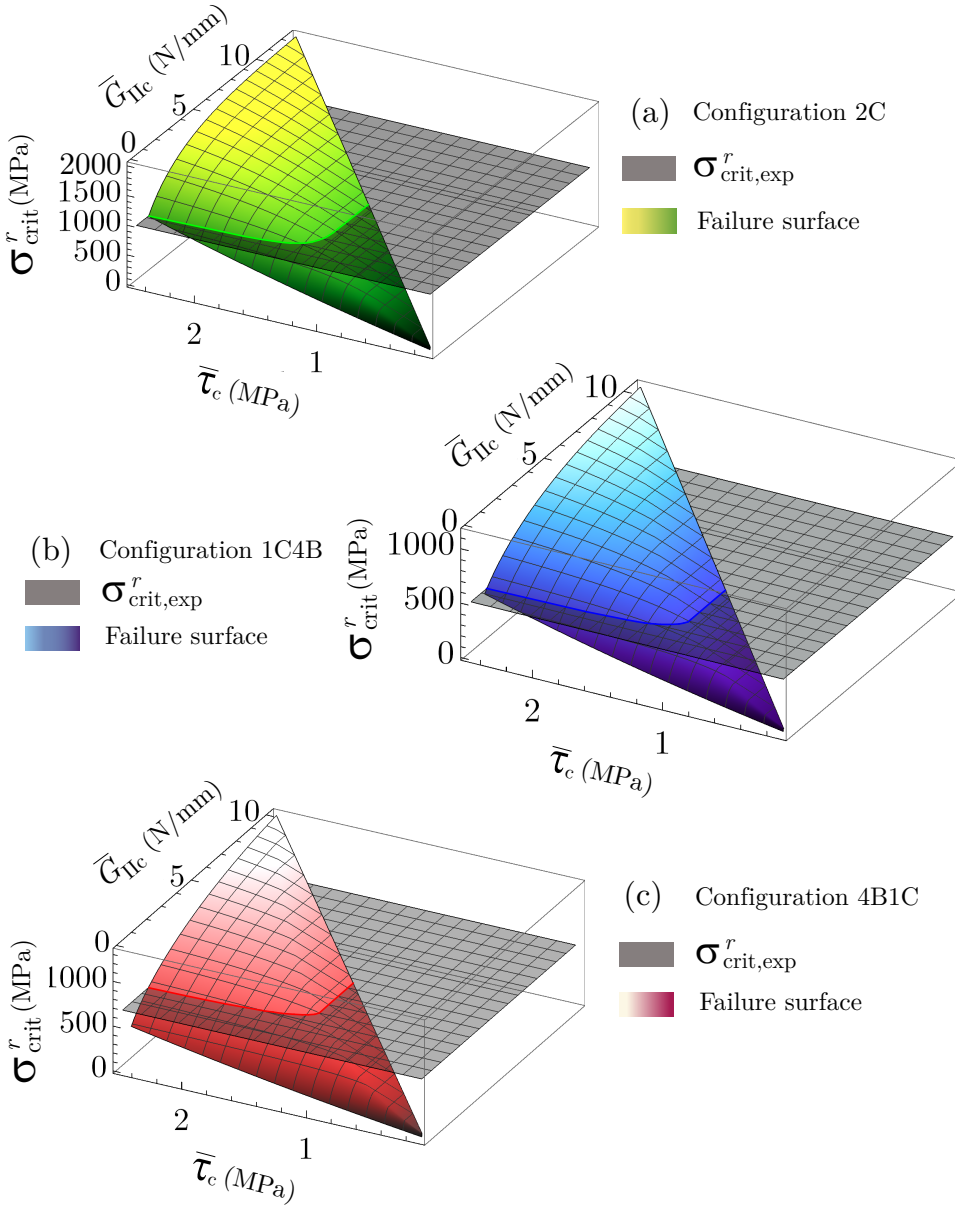
Figure 5.40: Intersections between the failure surfaces and the planes $\sigma_{\text{crit,exp}}^r$ for the configurations: (a)2C, (b) 1C4B and (c)4B1C.

To create the failure surface 5000 points of $\sigma_{\text{crit}}^r(\bar{G}_{\text{IIc}}, \bar{\tau}_c)$ were computed for each test. The ranges of values used for $\bar{G}_{\text{IIc}}$ and $\bar{\tau}_c$ are 0.0015-11.5 N/mm and 0.1-2.5 MPa, respectively.

In Figure 5.40, the intersections between the failure surface and the plane defined by $\sigma_{\text{crit,exp}}^r$ for each of the three studied configurations are presented. These intersections provide isolines that represent every pairs of values, $\bar{G}_{\text{IIc}}$ and $\bar{\tau}_c$, leading to predicted $\sigma_{\text{crit}}^r(\bar{G}_{\text{IIc}}, \bar{\tau}_c) = \sigma_{\text{crit,exp}}^r$. Although Figure 5.40 focuses on the intersection curves with the plane given by the mean value $\sigma_{\text{crit,exp}}^r$, a range of values is actually taken. This range goes from the minimum to the maximum load obtained experimentally for each test, these values being indicated in Table 5.7. In Figure 5.41, the isolines given by the intersections of surfaces and planes plotted in Figure 5.40 are presented by dashed lines, and continuous lines represent the isolines obtained using the minimum and the maximum experimental load for each test.
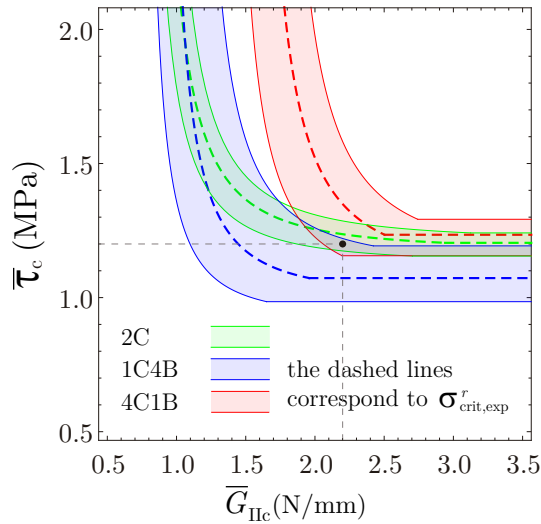
Figure 5.41: Experimental failure zone for each test configuration. The line that limits each zone represents the isolines obtained with the minimum and maximum debond load values and the dashed lines are obtained using $\sigma_{\text{crit,exp}}^r$ for each test configuration.

The selected pair of values are estimated in a zone close to the three failure zones. Specifically, the chosen values for the following numerical and analytical calculations for the fracture toughness and critical shear stress are G_{IIc}=2.2 N/mm and τ_c=1.20 MPa. They are represented with a dot in Fig. 5.41,

5.6.2.2   Details of models

The geometry and boundary conditions considered in the numerical model used to simulate the experimental tests presented in Yuan et al. (2019a), are shown in Figure 5.42. The model includes two isotropic solids, representing as accurate as possible the properties provided by Yuan et al. (2019a), although the code able to model orthotropic materials. The properties of these two solids are indicated in Table 5.6.

The algorithm described in 3.2.1 and implemented in the BEM code mentioned above has been used in this work; hence, only the boundary of both solids are meshed.
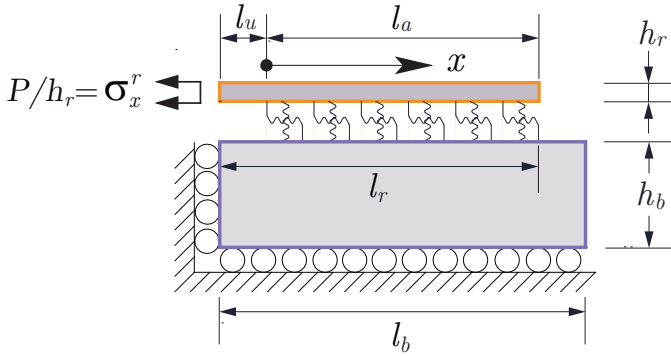
Figure 5.42: Geometry and boundary conditions in the numerical model of the double pull-push shear test.

The concrete block includes 2587 linear boundary elements, with 2500 elements used in a uniform mesh discretizing the interface boundary (bonded or unbonded with possible contact conditions with the reinforcement(i.e. the zone indicated by l_r). Thus, the element size along the interface is 0.1 mm. The remaining 87 elements are distributed over the other boundaries of the concrete block with variable element size and using a spacing ratio lower than 1.2.

The high mesh density along the interface is due to the need to adequately model the stress distributions ahead the virtual-crack tip when it moves along the interface. Because, as shown in Section 5.5 a, fine mesh is also needed due to the presence of a stress peak with a logarithmic singularity in the stress gradient at the crack tip.

On the other hand, the mesh for the reinforcement includes 3343 linear boundary elements. As mentioned above, a finer mesh was needed for this thin reinforcement layer to adequately model its bending behaviour and to allow an accurate computation of the stresses along the interface. The interface boundary of the reinforcement is also discretized with 2500 elements. Thus, a conforming mesh along the interface is used for this study.

The mesh used for some configurations is shown in Figure 5.43, specifically this mesh is used for 1C4B and 4B1C. For the case of the 2C configuration, the used mesh is the same; but the thickness of the reinforcement is different.

The obtained characteristics described in the previous section (k_t, $\bar{G}_{\text{IIc}}$ and $\bar{\tau}_c$) are used to model the interface. In the zone close to the loaded end, there are large compressive stresses due to the bending strain of the reinforcement as is described in Section 5.3. Therefore, it is important to study the effect that the adhesive-zone free (or already debonded), l_u, existing in this test may have. Previous investigations (Martinelli et al., 2011) showed that compressive stresses close to the loaded end appear at part or the whole adhesive-free zone (depending on the value of l_u). Since the debond propagation increases this zone, this effect may be significant and that is why two numerical calculations are performed in this study:
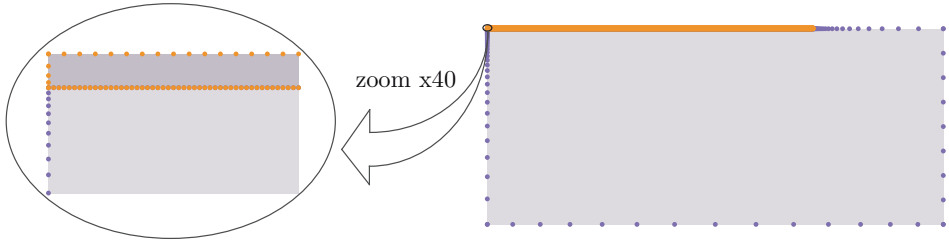
Figure 5.43: Boundary element mesh used for the double pull-push shear test model.

- In the first model, penetrations between solids are allowed in every element of the adhesive-free zone once the interface failure occurred. This option is referred to as "non-contact" (NC) in the following figures.

- In the second numerical model, compressions in the adhesive-free zone are taken into account as the debond zone increases. The results of this calculation are referred to as frictionless contact (C) in all figures. A penalty contact condition is considered in this case.
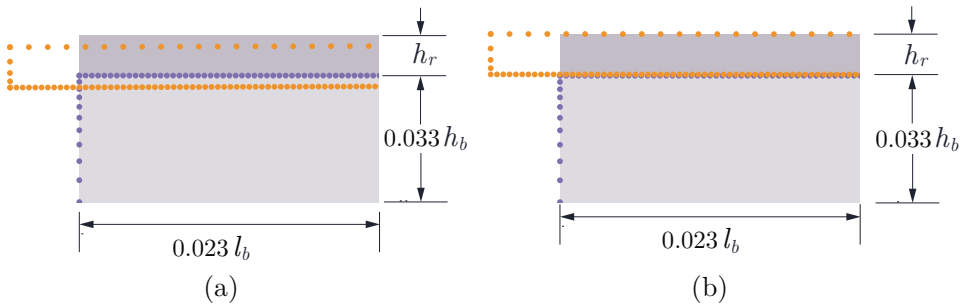
Figure 5.44: Deformed mesh (actual scale) of the 1C4B configuration for (a) the non-contact and (b) the penalty contact numerical models.

As an example, the deformed meshes (in actual scale) of the configuration 1C4B obtained at the beginning of the first step are shown in Figure 5.44, for the non-contact and the contact models. Only the loaded end zone is represented in order to visualize the difference between both numerical results.

Even though the aim of this section is the comparison of the numerical results with the experimental data, by these two calculations, a comparison between the analytical and numerical results is also possible in order to check the solutions of the code described in Section 3.2.1. In addition, the influence of compressions on the solution in the adhesive-free zone is studied for these specific configurations. The fracture mode mixity computed using both formulations described in Section 3.2 is also plotted to observe their influence on the predictions for the present test.

5.6.2.3   Comparison between the numerical and analytical results

In this section the analytical results obtained using the solution proposed in Section 5.4 and the numerical result obtained by the code presented in Section 3.2.1 are shown. The penetration between solids is allowed in the adhesive-free zone, as in the analytical model in Section 5.4, thus a possible effect of compressions in the adhesive-free zone is not considered. For the sake of brevity, only one of the three studied in this investigation is considered in this section, specifically the 1C4B. It should be recalled that the target of this section is only to assess the accuracy of the numerical code.

In Figure 5.45 (a) the dimensionless stresses obtained by the numerical (NP) and the analytical (AP) procedures are shown. Both curves present a very good agreement.
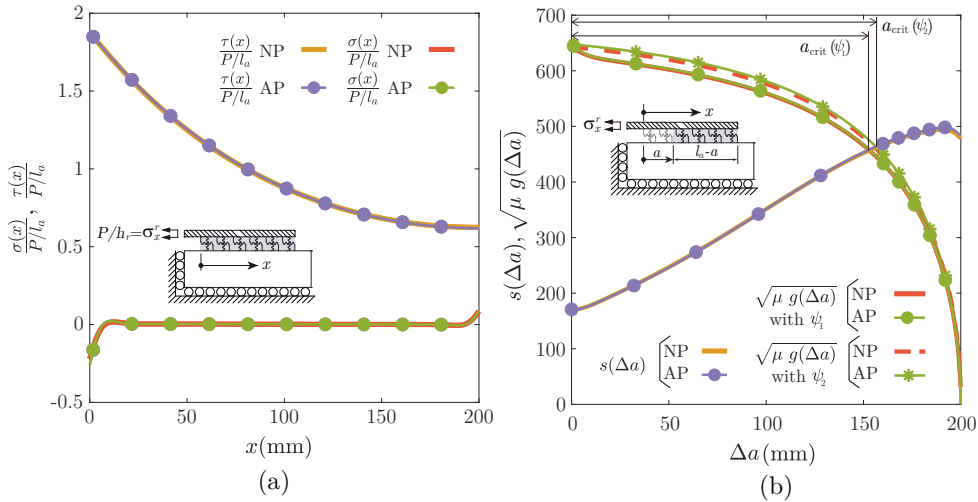
Figure 5.45: (a) Dimensionless stresses along the interface obtained by the numerical (NP) and analytical (AP) procedures. (b) $s(\Delta a)$ and $\sqrt{\mu\, g(\Delta a)}$ curves and their intersections for the two different fracture mode mixity definitions and NP and AP.

In Figure 5.45(b) the intersection between $s(\Delta a)$ and $\sqrt{\mu\, g(\Delta a)}$ is also presented for both definitions of the fracture mode mixity, ψ_1 and ψ_2, as provided in Section 3.2. No relevant differences between the curves obtained by the energy criterion using ψ_1 and ψ_2 are observed (see Table 5.8, where the results associated to the growth of the first finite segment of the crack for each model and the two mode mixity angles are presented).

5.6.2.4   Comparison between the numerical models

The principal target of this section is the comparison between the numerical model with compressions in the adhesive-free zone (denoted as C - contact) and the numerical model that allows penetrations between solids in that zone (denoted as NC - non contact). When penetrations into the adhesion-free zone behind the crack tip are

allowed, the solution can be affected by an error. By this comparison, the magnitude of this error is assessed for PSST tests.

As in the previous figure, the stress distributions along the interface and the energetic and stress criteria curves are represented in Figure 5.46 for the 1C4B test. Note that in Figure 5.46 (b) only small differences between the two energy criterion curves are observed again.
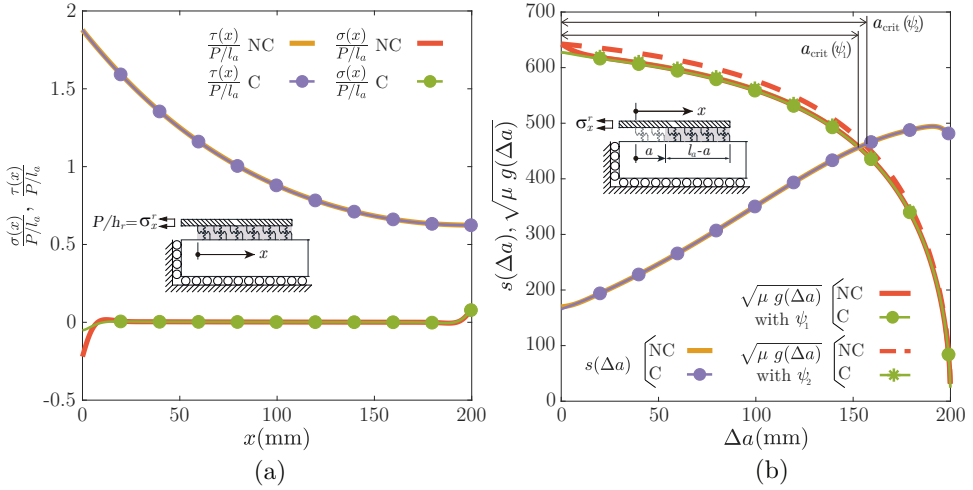
Figure 5.46: (a) Dimensionless stresses along the interface obtained by the numerical procedure including contact in the adhesive-free zone (C) and non-contact condition in the same zone (NC). (b) $s(\Delta a)$ and $\sqrt{\mu\,g(\Delta a)}$ curves for the two different fracture mode mixity formulations and intersections of these curves for C and NC models.

Although these small differences continue in the debond propagation, the differences between $g(\Delta a)$ curves in Figure 5.46 (b) are small. In this case, the energy criterion curves evaluated by ψ_1 are almost coincident for the models C and NC, however, there is a perceptible difference between the energy criterion curves evaluated by ψ_2 for the models C and NC. This is due to the fact that ψ_2 is evaluated at the virtual advancing crack tip, while ψ_1 is taken from the stresses at the undamaged interface, and the difference between C and NC models is especially notable at the crack tip. It should be noticed that the error obtained by not considering the contact in the adhesive-free zone for these tests is small.

As mentioned previously, Table 5.8 shows the results of the first finite advance of the crack at the interface for each specimen, calculated for several models including contact or not and also different fracture mode mixity angles ψ_1 and ψ_2. No significant differences are observed between the different models.

5.6.2.5 Comparison between the numerical and experimental results

This section compares the numerical results obtained by the developed code and the experimental data by Yuan et al. (2019a). Results for the three chosen configurations to check the CCFFM + LEBIM procedure are represented in Fig. 5.47. As described in Section 5.6.2, three specimens have been tested for each configuration. The data

Table 5.8: Critical stress that produces a crack onset and the first finite advance of the debond for each specimen, using the numerical and analytical models and for ψ_1 and ψ_2.

		$a_{\mathrm{cri}}(\psi_1)$ (mm)	$a_{\mathrm{cri}}(\psi_2)$ (mm)	$\sigma^r_{\mathrm{crit}}(\psi_1)$ (MPa)	$\sigma^r_{\mathrm{crit}}(\psi_2)$ (MPa)
Analytical model no contact	2C	158.25	160.26	951.89	955.85
	1C4B	152.90	156.31	549.81	556.29
	4B1C	147.65	151.46	632.37	645.50
Numerical model no contact	2C	158.14	159.50	950.30	952.94
	1C4B	152.89	155.87	548.30	553.74
	4B1C	147.90	151.24	629.57	640.65
Numerical model with contact	2C	157.93	158.20	951.07	951.60
	1C4B	152.68	153.48	547.94	549.43
	4B1C	147.65	148.54	628.77	631.80

of these tests are represented in grayscale lines. Together with experimental data, the numerical results of the two described models and for the two possible energy criteria evaluated with different fracture mode mixities are shown. These figures represent, for each test, the applied load versus the relative displacement between the reinforcement loaded edge and the concrete edge. Therefore, the displacement includes both the shear slip of the bonded part and the elongation of the unbonded part of FRP laminates.

Note that, under load control, when the critical load is reached the whole interface fails. Although the finite crack growth takes place under a constant load, the CCFFM provides a snap-back as occurs in experiments under displacement control (Yuan et al., 2004; Carrara et al., 2011) or in cohesive zone model simulations (Cornetti and Carpinteri, 2011). Fig. 5.47 shows that the relative displacement presents a snap-back behaviour predicted by the CCFFM. Figs. 5.45 and 5.46 show that the first finite segment of the crack is produced in large part of the interface. After this step, the stress distribution increases in the zone close to the free end, therefore in the next steps the interface close to the free end, close to the loaded end (Muñoz Reja et al., 2020b; Carrara et al., 2011) or simultaneously at both zones (l'Armée and Becker, 2019; Risso, 2018)) could be damaged.
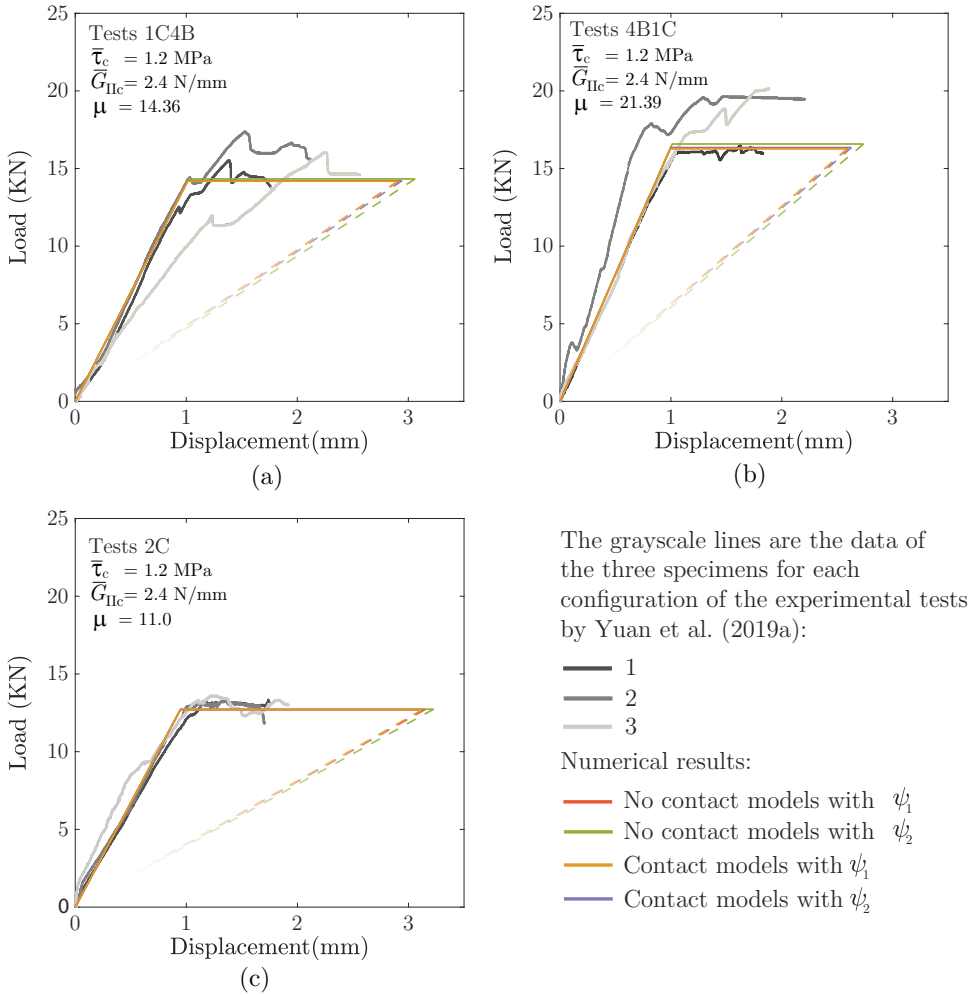
Figure 5.47: Comparison between experimental results and numerical predictions for the double PPST.

5.7 Concluding remarks

One of the goals of this study was the development of an analytical model able to characterize the crack onset and propagation along the interface between two adherents of any thickness/stiffness in double joints. Therefore, the present model is based on the Timoshenko beam theory and the linear elastic interface model.

As an application, the crack onset and propagation along the interface in the Double Pull-Push Shear (DPPS) test is studied using this original analytical solution.

The peeling stresses in the the shear tests keep the discussion about the fracture energy still open (Carrara and Ferretti, 2013; Mazzotti et al., 2016; Martinelli et al., 2011). The fracture energy in Mode I in the interface is significantly lower than the fracture energy in Mode II for these tests, therefore, even a small increase in the peel-

ing stress could reduce the bearing capacity of the interface (Mazzotti et al., 2016). For this reason, the expressions for the normal and shear stresses in the adhesive layer are deduced for the DPPS test in a suitable dimensionless form, pointing out the role of the main characteristic variables and parameters of this test. Several parametric studies are carried out to analyse the influence of the geometry and material (adherents and adhesive) characteristics on the stress distributions. The obtained results show that:

- Normal stresses at the loaded end are important for reinforcement stiffness larger than the block stiffness (i.e., large values of ρ), relatively small values of the reinforcement thickness (i.e., small values of η), and for adhesives whose shear stiffness is larger than the normal stiffness (i.e., for large values of κ).

- The normal stresses become more important for small overlap lengths because these stresses increase their presence throughout the interface.

- Tensions at the free end can increase achieving relevant values although compressions at loaded end decrease, e.g. when the laminate (reinforcement) thickness increases (i.e., for large values of η or for small overlap lengths).

- When tensions become relevant at the free end, the shear stresses present a quasi-uniform distribution Carrara and Ferretti (2013) (i.e., for large values of η and small values of ρ).

In general, these results are in agreement with some experimental data in the literature Carrara and Ferretti (2013); Czaderski et al. (2010); Martinelli et al. (2011). Specially, the present procedure is compared with the experimental data by Carrara et al. (2011), a satisfactory agreement being obtained. Thus, we can conclude that in general the interface normal stresses can not be neglected a priori in a DPPS test analysis, as assumed in the simple Shear Lag (SL) model.

Using the computed interface stress distributions, the Coupled Criterion of Finite Fracture Mechanics (CCFFM) covering mixed mode fracture is applied to predict failure loads for debond onset and propagation in this test. As expected, the results obtained by the present analytical model and by the SL model show some differences which could become significant for some parameter values, for example, for small overlap lengths, for which the damage could even start by the free end. Thus, the present work allows assessing the accuracy and range of validity of the predictions obtained by the SL model.

Moreover, the results of two numerical models have been compared with the results of experimental tests, showing a good agreement. For the characterization of the interface failure, a simple inverse analysis has been used to fit $\bar{G}_{\mathrm{IIc}}$ and $\bar{\tau}_{\mathrm{c}}$ by exploiting the results from three different test configurations.

A discussion about two possible ways of defining the fracture mode mixity to be used in the energy criterion within the CCFFM was also provided. Numerical and analytical predictions have been calculated accordingly. However, specifically for the PPST (where mode II is dominant), the choice of the mode mixity definition does not affect significantly the results.

The proposed numerical tool is therefore suitable for predicting the failure of an interface with a relatively short computational time. As a future task, we remark that, in order to increase the efficiency of computations using LEBIM, a complete knowledge about the singular stress field near the crack tip growing along the elastic interface is necessary; its proper inclusion in the discretization procedure will avoid the use of highly refined meshes close to the crack tip.

Failure initiation in long-fiber reinfonced composites under transverse loads

A frequent failure mechanism in composites is associated to the presence of debonds along the interfaces between fibres and matrix in a unidirectional composite lamina under transverse loads. For this reason, an adequate modelling of the interface behavior is required. This problem has been widely studied, for quite extensive reviews of works studying this problem see París et al. (2007); Mantič (2009) and Távara et al. (2011).

LEBIM has proven that can be used to model the fracture process at a weak interface between two solids. It has been shown, see Távara et al. (2010, 2011); Mantič et al. (2015) and numerous references therein, that LEBIM can adequately describe the interface crack onset and growth in this kind of interfaces. Lenci (2001) compared the weak and perfect (strong) interface models, showing that the latter may provide (possibly non-conservative) predictions of higher failure load values. Nevertheless, when the actual interface becomes stiffer the LEBIM may produce inaccurate predictions.

This drawback of the original LEBIM formulation motivated Cornetti et al. (2012) and Weißgraeber and Becker (2013), among others, to apply the Couple Criterion of Finite Fracture Mechanics (CCFFM) (Leguillon, 2002; Cornetti et al., 2006) to linear elastic interfaces in a pure mode II and mixed mode of fracture, respectively.

In the present chapter the original mixed mode LEBIM proposal is coupled with the CCFFM criterion, following the previously Chapter 3. The CCFFM+LEBIM code based in curves (Section 3.2.1) is used. Fist, the micromechanical problem under study, i.e. a single-fibre subjected to biaxial remote transverse loads, is presented in Section 6.1, defining the geometry, materials and loads for all studied cases.

Subsequently, in Section 6.2, the CCFFM approach applied to the LEBIM in its specific form for the present problem is presented and also the parameters and equa-

tions used in the computational code are briefly described. Two different interface failure criteria are employed: the interface fracture criterion proposed by Hutchinson and Suo (1992), and the well-known quadratic stress criterion as expressed in Brewer and Lagace (1988), cf. Hashin (1980). Each criterion is adopted to be used in both the stress and energy conditions of CCFFM in separate way, as presented in Section 2.4.1.

In view of the logarithmic stress singularity at a linear-elastic-interface crack tip (Erdogan, 1997; Lenci, 2001; Távara et al., 2010) the (local) maximum of tractions therein, which in particular determines the Energy Release Rate (ERR), may be highly ill-defined. Thus, the convergence of the ERR and also of interface stress distributions (both used in the coupled criterion of CCFFM) with h-refinement of the BEM mesh is studied Section 6.3.

In Section 6.4, the numerical results of the parametric study carried out are analyzed and compared to some previous results using other procedures.

The Section 6.5 studies the appearance of one debond (non-symmetrical configuration) or two debonds (symmetrical configuration) in the fibre-matrix interface, and the results are compared with the results obtained by García et al. (2015) for perfect interfaces.

Finally, in Section 6.6 the capacity of CCFFM+LEBIM to study a multifibre geometry, specifically two fibres is checked.

6.1 Single cylindrical inclusion under biaxial transverse loads

A plane strain problem of a fibre embedded in a very large matrix cell is considered, which represents an approximation of a dilute fibre packing where fibre interactions can be neglected. The fibre-matrix interface is initially considered as undamaged. The fibre-matrix system is subjected to a biaxial remote loading. Fibre radius $a = 7.5 \ 10^{-6}$m and a $2H$ side square matrix with $H/a = 200/3$ are used, see Fig. 6.1.

Both inclusion and matrix are considered to be isotropic linear elastic materials, whose characteristics are presented in Table 6.1. LEBIM is used to model the interface as a continuum spring distribution, with k_n and k_t given in Table 6.2, which corresponds to $\mu = 1$. For larger values of μ, k_n increases proportionally.

Table 6.1: Properties of the constituents used for the bimaterial systems (f, fiber; m, matrix).

	$E_m(\text{GPa})$	ν_m	$E_f(\text{GPa})$	ν_f	$r_f(\mu\text{m})$
glass-epoxy	2.79	0.33	70.8	0.22	7.5
carbon-epoxy	2.79	0.33	13.0	0.20	7.5

θ_d is defined as the debond angle which defines the crack size in each step. When a crack propagation occurs springs placed within the angle θ_d lose the capability of transmit the load between solids (stiffness becomes zero). Then, the springs located at the ends of the interface part determined by θ_d represent the crack tips.
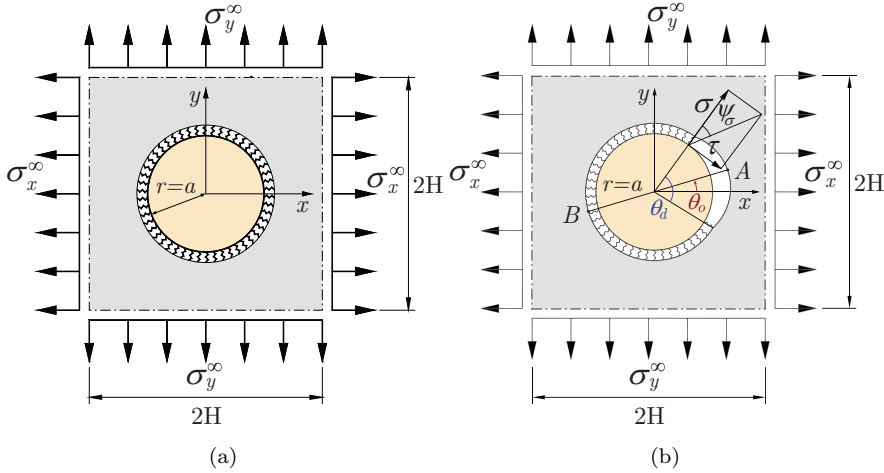
Figure 6.1: Inclusion problem configuration under biaxial remote transverse loads (a) without and (b) with a partial debond.

Table 6.2: Interface properties (k_n value is for $\mu = 1$ case)

	$\bar{G}_{Ic}$ (Jm^{-2})	$\bar{\sigma}_c(MPa)$	k_n (MPa/μm)	k_t/k_n
interface	2	90	2025	0.25

The applied remote loads, σ_x^∞ and σ_y^∞ with $\sigma_x^\infty \geq \sigma_y^\infty$, are shown in Fig. 6.1. The following general load-biaxiality parameter, introduced by Mantič et al. (2015), is used to represent the biaxiality relation between the applied remote loads:

$$\chi = \frac{\sigma_x^\infty + \sigma_y^\infty}{2\max\{|\sigma_x^\infty|, |\sigma_y^\infty|\}}, \quad -1 \leq \chi \leq 1, \tag{6.1}$$

Although, the problem has a symmetrical configuration, the properties chosen for the interface may lead to produce crack onset in a position different from the symmetry axes x or y, see Mantič et al. (2015). The position where the crack onset occurs is denoted by the polar angle θ_o, defining the diameter AB, see Fig. 6.1(b).

6.2 CCFFM applied to LEBIM formulation for a fibre-matrix system

In the present investigation, the couple criterion must be fulfilled following the formulation developed in Section 3.1.2. However, here a suitable formulation is proposed for the problem to be studied.

For this particular problem, $G(a)$ and $G_c(\psi(a))$ can be written in terms of two dimensionless functions (Mantič, 2009; Mantič and García, 2012), $\hat{G}(\theta_d)$ and $\hat{G}_c(\psi(\theta_d))$, correspondingly.

$$G(a) = \frac{(\sigma_x^\infty)^2 r}{E^*} \hat{G}(\theta_d), \tag{6.2}$$

$$G_c(\psi(a)) = \bar{G}_{Ic} \hat{G}_c(\psi(\theta_d)), \tag{6.3}$$

where, in (6.2), $E^\star$ is defined as the harmonic mean of the effective elastic moduli of fibre and matrix, and r is the fibre radius (see Mantič (2009)). In (6.3), $\bar{G}_{Ic} = \frac{\sigma_{max}^2}{2k_n}$ is the fracture toughness for the pure mode I and σ_{max} is the maximum normal tension associated to the energy based criterion (Cornetti et al., 2012).

Two dimensionless functions $\hat{G}_c(\psi(\theta_d))$ are used herein, the first one is similar to that proposed by Hutchinson and Suo (1992), defined in Section 2.4.1.1 with $\lambda = 0.3$ and the second one is related to well-known quadratic criterion, defined in Section 2.4.1.2.

Hence, the energy criterion can be written in terms of the dimensionless function $g(\Delta\theta)$:

$$g(\Delta\theta) = \frac{\int_0^{\Delta\theta} \hat{G}_c(\psi(\theta_d)) \, d\theta_d}{\int_0^{\Delta\theta} \hat{G}(\theta_d) \, d\theta_d} \tag{6.4}$$

in the following form:

$$\frac{(\sigma_x^\infty)^2 r}{\bar{G}_{Ic} E^*} \geq g(\Delta\theta) \tag{6.5}$$

Besides the energy based criterion defined in (6.5), the stress based criterion must be fulfilled along an undamaged finite (circular arc) segment from $x = 0$ to $x = \Delta a$, thus the crack growth is produced by a finite advance $\Delta a > 0$.

Like the energy criterion, the stress condition can also be written in terms of a dimensionless function by expressing the modulus of the traction vector $t(x)$ and of the critical traction vector $t_c(\psi(x))$ in terms of two dimensionless functions:

$$t(x) = \sigma_x^\infty \hat{t}(\theta_d), \tag{6.6}$$

$$t_c(\psi(x)) = \bar{\sigma}_c \hat{t}_c(\psi(\theta_d)). \tag{6.7}$$

So that, the stress criterion for a finite crack advance given by $\Delta\theta$ can be expressed as

$$\frac{\sigma_x^\infty}{\bar{\sigma}_c} \geq s(\Delta\theta) = \frac{\hat{t}_c(\psi(\Delta\theta))}{\hat{t}(\Delta\theta)}, \tag{6.8}$$

where the fact that, in the present case, the function $s(\Delta\theta)$ is an increasing function was taken into account.

6.2.1 The coupled criterion

A way to characterize the coupled CCFFM+LEBIM criterion applied in the present study is to use a suitably defined dimensionless characteristic parameter μ defined in Section 3.1.3. Remember that, this parameter for pure fracture mode I is defined as

$$\mu = \frac{2k_n \bar{G}_{Ic}}{\bar{\sigma}_c^2} = \frac{\sigma_{\max}^2}{\bar{\sigma}_c^2}, \tag{6.9}$$

where $\sigma_{\max}$ and $\bar{\sigma}_c$ are the maximum and critical tensions associated to the energy and stress criteria, respectively.

As can be seen from Section 3.1.3 the fracture toughness, strength and stiffness of the interface are independent in the present CCFFM + LEBIM approach.

In order to rewrite the energy criterion (6.5) in a form similar to the stress criterion (6.8), a suitable structural parameter referred to as brittleness number(Mantič, 2009) is defined as

$$\gamma = \frac{1}{\bar{\sigma}_c}\sqrt{\frac{\bar{G}_{Ic}E^*}{r}}.$$ (6.10)

Then, the energy criterion (6.5) takes the form

$$\frac{\sigma_x^\infty}{\bar{\sigma}_c} \geq \gamma\sqrt{g(\Delta\theta)}.$$ (6.11)

By combining (6.8) and (6.11), the coupled criterion of FFM can be expressed, in the present case, as

$$\frac{\sigma_x^\infty}{\bar{\sigma}_c} \geq \frac{\sigma_c^\infty}{\bar{\sigma}_c} = \min_{\Delta\theta}\max\left\{s(\Delta\theta),\gamma\sqrt{g(\Delta\theta)}\right\},$$ (6.12)

where the minimum is achieved at $\Delta\theta = \theta_c$.

It is interesting to introduce the relation between μ and γ when CCFFM+LEBIM is applied. From equations (6.9) and (6.10) the subsequent relation can be obtained:

$$\mu = \frac{2k_n r}{E^*}\gamma^2.$$ (6.13)

Thus, for a fixed value of the dimensionless ratio of the interface and bulk stiffness including also a characteristic geometric size, $k_n r/E^*$, considered, μ is directly proportional to γ^2.

6.3   CCFFM result by a 2D BEM code

The formulation of CCFFM+LEBIM under fracture mixed mode introduced above has been implemented in a computational code based on 2D BEM, which has been applied to analyse the onset and propagation of a debond in the single fibre problem described in the previous section. The computational procedure propagates the interface crack in a discrete way, depending on the boundary element discretization of the interface. In each step, to define the finite crack advance a limited number of linear solutions is carried out for possible lengths of the next crack extension at one of its ends, defined by $\Delta\theta_d$.

On one hand, the energy and fracture toughness at critical points (position where the crack initiates or crack tips when the crack already exists) are computed and the minimum remote loads necessary to produce a crack onset or growth according to the energy based criterion, for a given $\Delta\theta_d$, are predicted. On the other hand, the computational procedure also computes the minimum remote load necessary to produce a crack onset or growth in the same zone defined by $\Delta\theta_d$ but considering an undamaged interface and the stress based criterion.

Finally, the load necessary to produce or propagate a crack by a $\Delta\theta_d$ advance is defined by the intersection of both criteria, which defines the new crack size to be considered in the next step. This procedure is illustrated in Fig. 6.2(a).
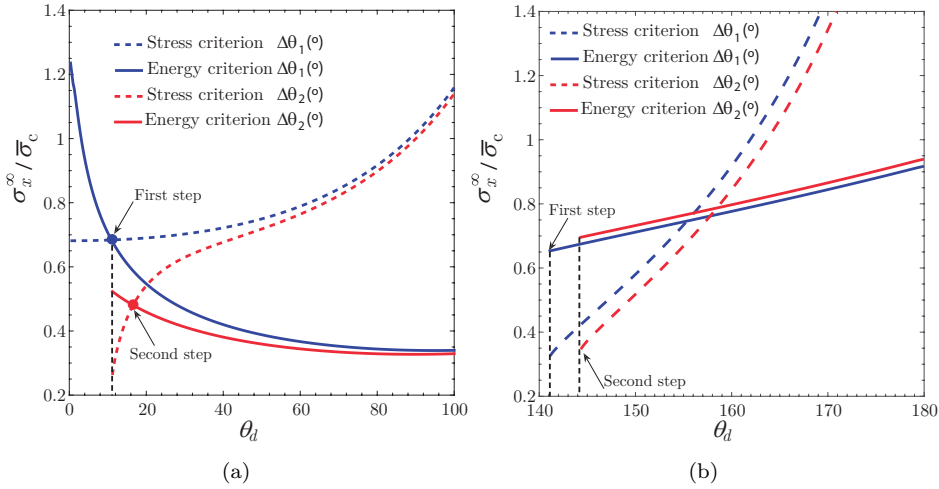
Figure 6.2: Two steps of the present crack-advancing-procedure for a cylindrical inclusion embedded in a matrix under a transverse tension for $\mu = 4$ and $\chi = 0.5$ (uniaxial case). The crack advance is defined by the minimum load fulfilling both criteria which is given by (a) the intersection of the two criteria curves or (b) the minimum of the energy criterion curve (actually plot (b) is computed for a different and much coarser mesh, making in this way the crack advances visible in the two steps shown).

Typically, once the crack has a certain size, it may occur that the minimum load necessary to produce a crack propagation is not defined by the intersection of both criteria but it is defined by the minimum load given by just one of these criteria, usually the energetic one, because the stress criterion is then automatically fulfilled. This situation can be observed in Fig. 6.2(b), where the energy based criterion for the first step defines the minimum necessary load to cause a crack propagation.

For the sake of implementation simplicity and computational efficiency, the procedure implemented herein allows a crack propagation only in one direction starting from one critical point, i.e. a traction concentration point or crack tip. A more general approach would require a suitable optimization procedure to be implemented in order to avoid a huge number of BEM analyses for every possible crack advance without differentiating between them.

6.3.1 Convergence study of the BEM mesh in the problem under study

The proposed procedure in the present work requires the evaluation of the energy at a crack tip in each step during the crack propagation analysis. This fact may lead to numerical errors if the mesh used is not sufficiently refined. Although interface tractions in LEBIM are bounded at the crack tip, the gradient of local tractions in the zone close to the interface crack tip is singular (Távara et al., 2010; Lenci, 2001), leading to a traction peak whose accurate value is difficult to be computed. Therefore, some errors may arise in crack propagation prediction in particular when the fibre-matrix interface becomes stiffer because stresses at such an interface crack tip converge to the perfect interface solution with singular stresses at the crack tip.
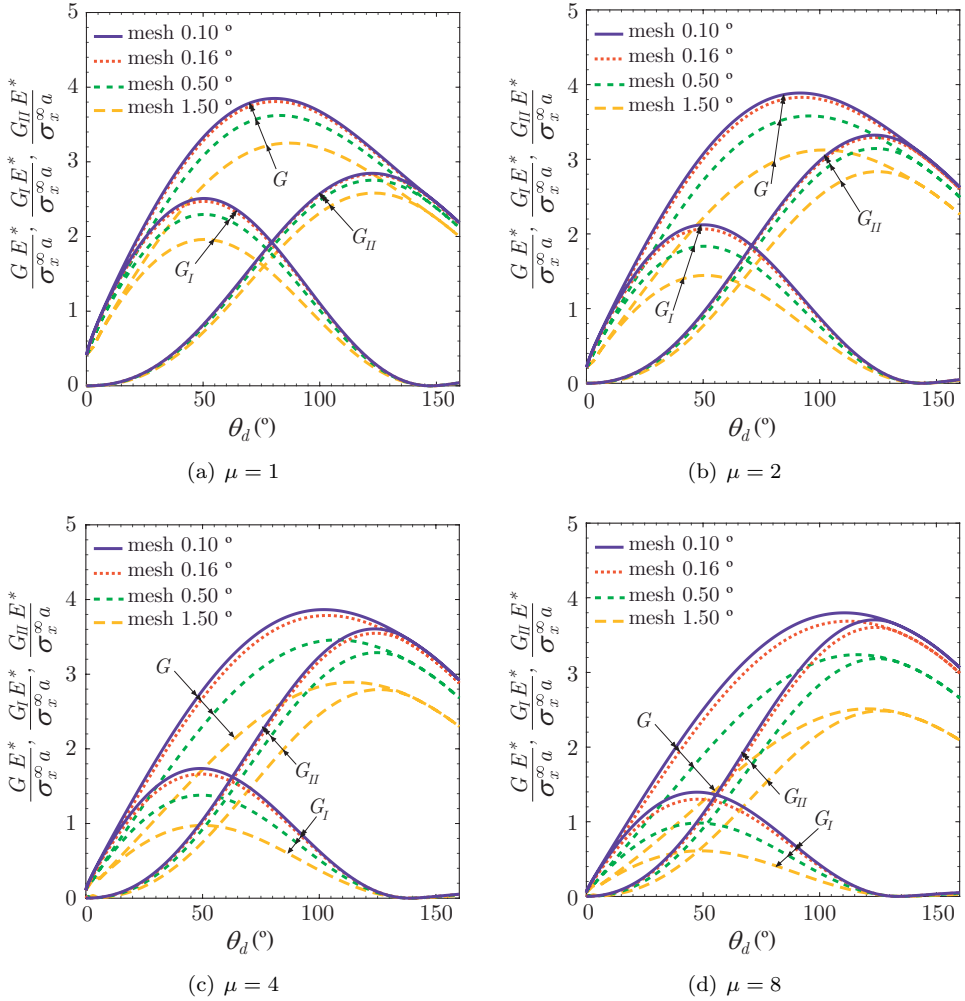
Figure 6.3: ERRs for different crack sizes (different θ_d values) with $\chi =0.5$ (uniaxial case) for different mesh sizes and (a) $\mu =1$, (b) $\mu =2$, (c) $\mu =4$ and (d) $\mu =8$.

The solved numerical examples of the single fibre problem, see Fig. 6.1, model the interface by a distribution of springs between the nodes along the fibre and matrix. Linear and continuous boundary elements are used. Thus, each element has two geometrical nodes (one at each extreme). Then, when a spring fails, forming a new portion of an interface crack, the minimum $\Delta\theta_d$ size is restricted by the boundary element size.

Due to the facts mentioned above, before studying closely the considered problem, a convergence study for the used mesh is necessary. Several single fibre problems for a glass-epoxy system with $\chi = 0.5$ (uniaxial tension with $\sigma_y^\infty = 0$), for different values of μ (1, 2, 4 and 8) are solved. As the solution of this problem is symmetric, for this convergence study a symmetry plane coincident with the x-axis is considered. Thus, a strong mesh refinement is feasible keeping the computational time reduced.

The total ERR and mode I and II contributions are depicted in Fig. 6.3 for different

(a) $\mu = 1$ and $\theta_d = 36°$

(b) $\mu = 2$ and $\theta_d = 36°$

(c) $\mu = 4$ and $\theta_d = 48°$

(d) $\mu = 8$ and $\theta_d = 48°$
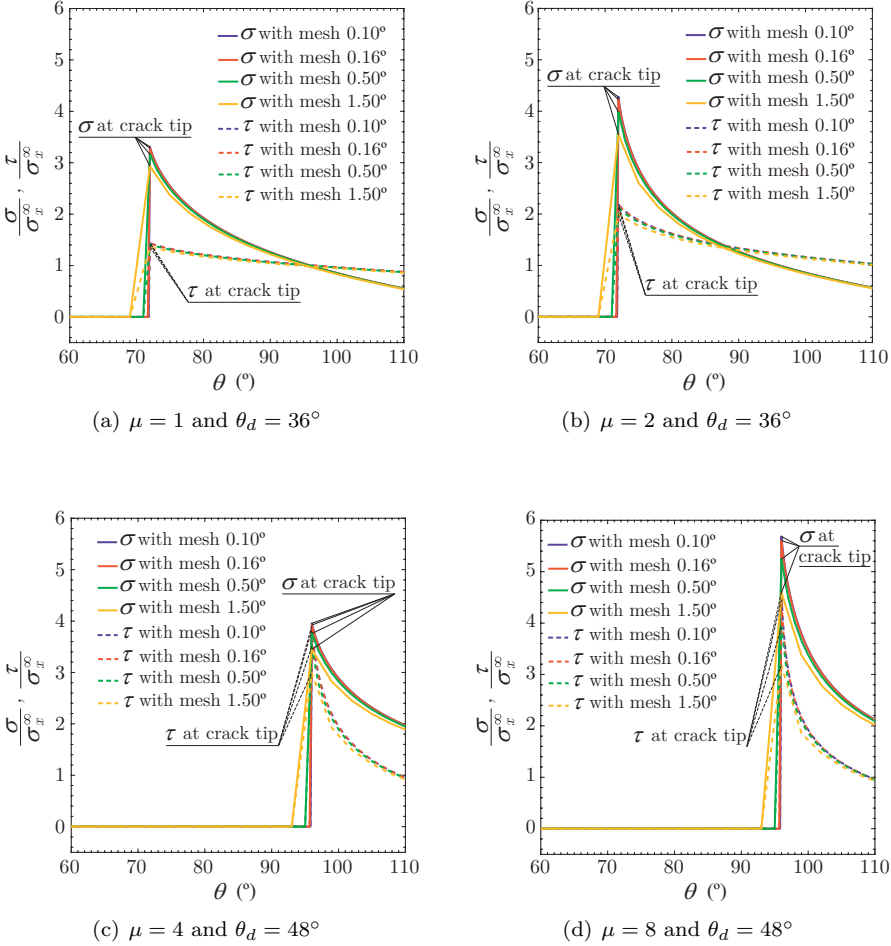
Figure 6.4: Normal and shear stress along the interface for a specific crack size (θ_d value) with $\chi = 0.5$ (uniaxial case) for different mesh sizes and (a) $\mu =1$ (b) $\mu =2$, (c) $\mu =4$ and (d) $\mu =8$.

crack sizes (θ_d). Four mesh refinements are considered for the fibre-matrix interface with element sizes defined by the polar angles $0.10°$, $0.16°$, $0.50°$ and $1.50°$. It can be seen that when the interface becomes stiffer, i.e. μ is increasing, the solution convergence is slower. Thus, in order to get an accurate value of the ERR for a stiff interface a very fine mesh is required.

This fact is a consequence of the difficulty in the approximation of tractions at a crack tip when using linear elements in the BEM code, due to the traction gradient singularity therein. The distribution of normal and shear stresses for a specific crack size (θ_d) is represented in Fig. 6.4. The crack size chosen for each value of μ, is the one with the largest differences in the plots of ERR in Fig. 6.3. In Fig. 6.4, different slopes of the solution are observed for different μ values. A large μ value (stiff interface) has a steep slope in the zone close to the crack tip. Then, in order to obtain an accurate approximation of tractions in that zone, a fine mesh is necessary.

From the results obtained in this convergence study a slight mesh dependence is

observed. Thus, in order to get reliable results for the model under study, a mesh size with a polar angle of $0.15°$ and $\mu = 4$ is used in the following.

6.4 CCFFM+LEBIM numerical results for a single inclusion under biaxial transverse loads

In this section the results obtained for the single fibre problem, introduced in Section 3, for different interface stiffnesses and different biaxial loading configurations are presented and discussed.

6.4.1 Effect of the interface criterion used and interface stiffness

Using as reference the steps depicted in Fig. 6.2(a), and analysing also the subsequent steps, the interface crack propagation is shown in Fig. 6.5, where the crack angle θ_d is plotted versus the necessary remote applied load in the x-direction that causes the onset or propagation of the interface crack. Specifically, the plots in Fig. 6.5 represent the solutions for the single fibre problem in a glass-epoxy system, under a biaxial tension with $\chi = 0.75$. The Hutchinson and Suo based criterion (HS-criterion) is used for these plots in its point-wise form in Fig. 6.5(a) and in its average form in Fig. 6.5 (b), see (2.4.1.1).

According to these plots, after the onset of a crack of polar angle θ_c, referred to as critical angle, and assuming load control, the crack is expected to continue growing along the interface in an unstable manner up to a certain arrest angle denoted as θ_a.

As follows from Fig. 6.5(a), the solution for the coupled criterion introduced in this paper for $\mu = 1$ is similar to the solution obtained with the original LEBIM formulation. In Fig. 6.5(b), the solution for $\mu = 1$ does not coincide exactly with the LEBIM solution, since the crack increment does not vanish (as it theoretically should) but it is equal to the mesh size (boundary element length), although the differences are negligible.

A slight decrease of the critical loads obtained as the interface becomes stiffer is noteworthy. This effect may be caused by the influence of the increase of stiffness on the mode mixity angle; actually a detailed study showed that when μ increases the mode mixity angle changes in all undamaged fibre-matrix interface points.

In general, only a quite small influence of the interface stiffness in the present single fibre problem solution is observed in Fig. 6.5. In particular, this can be shown in very close predicted values of the arrest angle θ_a. Thus, very similar results for interface stiffness larger than $4k_n$ (i.e. $\mu > 4$ and $G_{Ic}=2\text{Jm}^{-2}$ and $\bar{\sigma}_c=90\text{MPa}$) are expected. To prove this hypothesis, the results obtained for the critical remote load in the x-direction (σ_c^∞, load necessary to produce crack onset) and the critical angle (θ_c, initial crack size produced in the crack onset) for the interface stiffness $8k_n$ are compared in Table 3 with the results obtained for the perfect interface case, corresponding to $\mu = \infty$, by Mantič (2009). Two well-known composite systems glass-epoxy and carbon-epoxy are studied. In both cases two different values of the interface fracture toughness and critical stress found in literature are used. Notice that different *lambda*
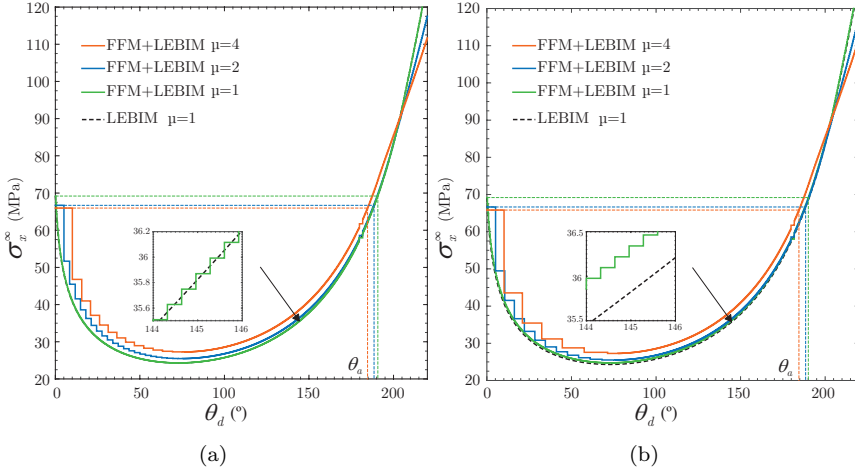
Figure 6.5: The remote applied load σ_x^∞ with respect to the debond angle θ_d, for $\chi=0.75$ and different μ values using the HS-criterion and (a) the point-wise and (b) the average form.

are used for the energetic and the stress criteria only for comparison purposes. Due to HS-criterion with $lambda = 0$ leads to a similar criterion as the normal tension criterion, as Mantič (2009) used. It is noticeable that, although the results were obtained by different procedures the differences observed are very small.

Table 6.3: Comparison of the results obtained in the present work (CCFFM+LEBIM using the HS-criterion with $\lambda = 0.3$ and 0, respectively for the energetic and stress criterion) for $\chi = 0.5$, and results obtained by CCFFM (using the HS-criterion with $\lambda = 0.3$ and normal tension criterion) applied to the perfect interface case in Mantič (2009).

	$\bar{\sigma}_c$ (MPa)	$\tilde{G}_{Ic}$ (Jm^{-2})	γ	$\theta_c(°)$	$\sigma_c^\infty/\bar{\sigma}_c$	
glass/ epoxy	60	10	1.49	78	1.2	Mantič (2009)
				79.46	1.259	CCFFM+LEBIM with $\mu = 8$
	90	2	0.44	14.8	0.7	Mantič (2009)
				13.04	0.696	CCFFM+LEBIM with $\mu = 8$
carbon/ epoxy	60	10	1.37	71.4	1.2	Mantič (2009)
				75.22	1.285	CCFFM+LEBIM with $\mu = 8$
	90	2	0.41	12.2	0.8	Mantič (2009)
				11.26	0.763	CCFFM+LEBIM with $\mu = 8$

Fig. 6.6 show plots analogous to those in Fig. 6.5 but obtained using the quadratic interface failure criterion. It is noticeable that the results obtained by HS and quadratic criteria are quite similar. A small influence of the interface stiffness is observed in Fig. 6.6 again. In both figures, the slope tendency of the solution for stiffer interfaces changes at the end of the curves, when θ_d exceeds 180°, this fact being more pronounced for the quadratic criterion. This effect is due to the contact between crack faces at the crack tip when the interface crack achieves a certain size. Recall here that in the present model the crack is able to propagate even in presence of compressions at the closed crack tip.
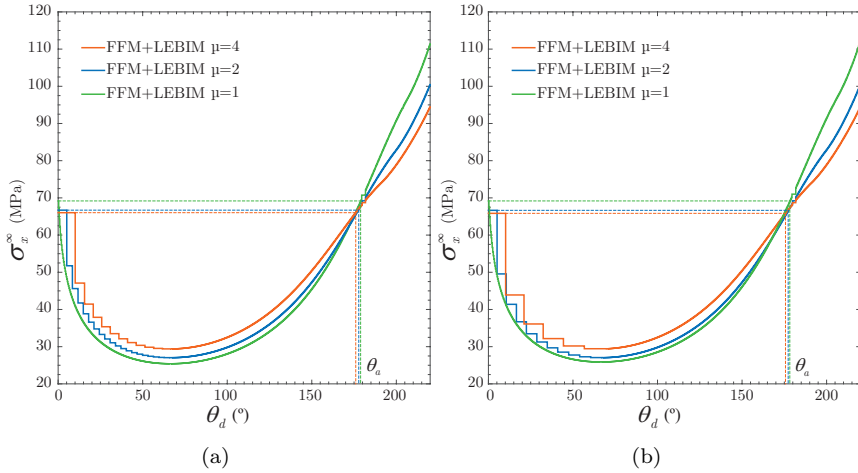
Figure 6.6: The remote applied load σ_x^∞ with respect to the debond angle θ_d, for χ=0.75 and different μ values using the quadratic criterion and (a) the point-wise and (b) the average stress based criterion.

6.4.2 Effect of the load biaxiality

In Fig. 6.7 the crack size θ_d is plotted versus the remote applied load σ_x^∞, for $\mu = 4$, and for different configurations of the biaxial loading defined by χ (6.1): $\chi = 0.75$ stands for a biaxial tension, $\chi = 0.50$ for the uniaxial tension, and $\chi = 0$ and $\chi = -0.25$ for two biaxial tension-compression cases. From the predictions by both interface failure criteria, it can be seen that a compressive remote load acting as a secondary load makes easier crack onset (i.e. a lower critical load is necessary to produce crack onset). Moreover, the arrest angle θ_a in these cases is smaller than when a tension is acting as a secondary load. This can be explained on one hand by the lower critical load originating the crack onset, and on the other hand by the presence of compressions at the crack tip which may lead to the closure of the interface crack tip once the crack reaches a certain size.

Table 6.4: The arrest angle θ_a for different biaxial loading configurations defined by χ and the HS-criterion and quadratic criterion.

	$\chi = 0.75$	$\chi = 0.50$	$\chi = 0$	$\chi = -0.25$	$\chi = -0.50$
HS-C.	186.30°	143.99°	118.94°	112.98°	104.25°
Q. C.	183.06°	156.42°	139.09°	132.65°	102.6°

In Table 6.4, the arrest angles θ_a for different biaxial loading configurations and both criteria used are presented. In most of the cases, the quadratic criterion leads to slightly larger angles than the HS-criterion.

A different way to study the global behaviour of the fibre-matrix system is represented in Fig. 6.8, where the applied remote load is plotted against the averaged longitudinal strain, ε_{AB}, along the segment defined by the matrix points A and B, (see Fig. 6.1). This strain is formed by the strain due to the purely elastic behaviour of the system (with no interface damage) and the strain due to the interface debond
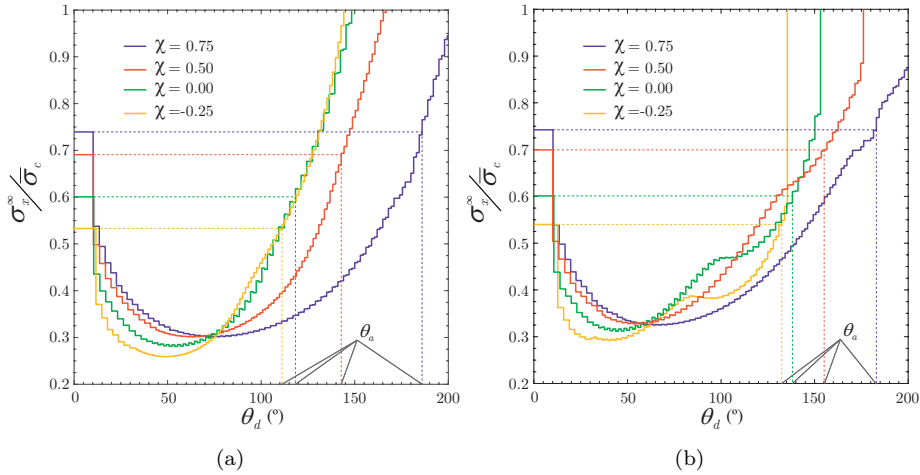
Figure 6.7: The normalized remote applied load in the x-direction with respect to the debond angle θ_d, for different biaxial load combinations using (a) the HS-criterion and (b) the quadratic criterion.
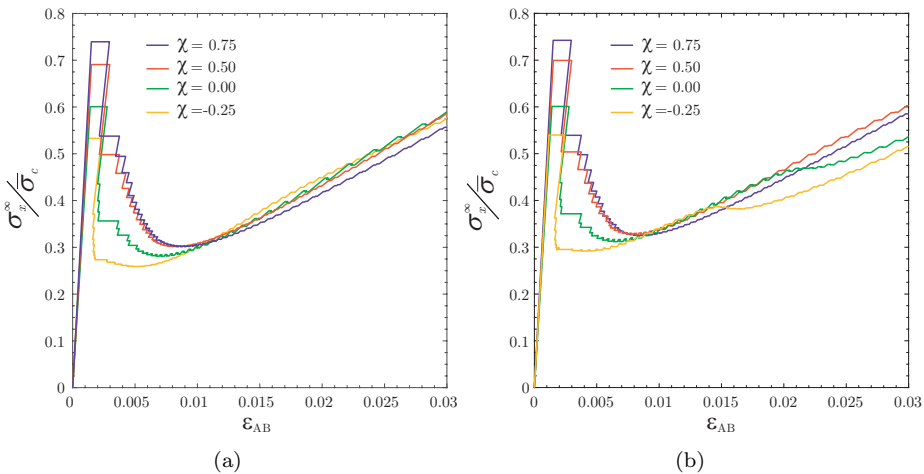
Figure 6.8: The normalized remote applied load in the x-direction with respect to the longitudinal strain ε_{AB} (see Fig. 6.1 for A and B locations), for different biaxial load combinations using (a) the HS-criterion and (b) the quadratic criterion.

propagation, thus $\varepsilon_{AB} = \varepsilon_{AB}^e + \varepsilon_{AB}^d$. It is noteworthy that some of the curves shown in Fig. 6.8 present an unstable behaviour known as snap-back.

In Figs. 6.7 (b) and 6.8(b) corresponding to the quadratic criterion, an abrupt change in the slope of some curves, including inflexion points and a kind of plateau, is observed, this effect being more pronounced in the tension-compression cases with $\chi = 0$ and $\chi = -0.25$. This is essentially due to form of the curve of the quadratic criterion shown in Fig. 3.2(b) which has an inflexion point and a kind of plateau in the region where tensions switch to compressions. Notice that the curve of the HS-criterion in Fig. 3.2(a) is convex.

6.4.3 Position of the crack onset

In Mantič et al. (2015) it is shown that the position where crack onset takes place (defined by the angle θ_o) depends on the dimensionless parameters: χ, λ (for the HS-criterion), ξ, and a structural parameter γ (see Eq. 6.10).

Table 6.5: The onset angle θ_o for different values of μ and biaxial loading configurations.

	$\chi = 0.75$	$\chi = 0.50$	$\chi = 0$	$\chi = -0.25$	$\chi = -0.50$
$\mu = 1$	$0.00°$	$0.00°$	$0.00°$	$0.00°$	$13.20°$
$\mu = 2$	$0.00°$	$0.00°$	$0.00°$	$6.00°$	$17.85°$
$\mu = 4$	$0.00°$	$0.00°$	$9.15°$	$16.05°$	$20.55°$

In the present approach, another independent parameter which governs the interface stiffness is defined: μ. Thus, in the present approach if the interface stiffness increases the position where the crack onset is produced may change too, in agreement with the previous results presented in Mantič et al. (2015).

According to Table 6.5, increasing secondary compressive load as well as the interface stiffness lead to nonzero values of the onset angle θ_o. In these cases, after a first step which produces a non-symmetric crack, the subsequent steps make the interface crack to growth tending to form a symmetric crack. This behaviour is observed for both the HS-criterion and quadratic criterion.

6.4.4 Failure curves

Fig. 6.9 shows the failure curve representing the normalized biaxial remote loads which cause a debond at an initially undamaged fibre-matrix interface with $\mu = 4$. The curve is compared with the analytical curve obtained by LEBIM with $\mu = 1$ in Mantič et al. (2015) using Gao's elastic solution (Gao, 1995). Surprisingly only small differences are observed in the results when the interface stiffness is increased, while the tendencies in both curves are the same.

The relatively small difference between CCFFM+LEBIM and LEBIM predictions is somewhat analogous to that observed in Cohesive Crack Modelling, where the effect of the cohesive law shape is relatively weak once we fix the fracture energy and tensile strength, provided that the process zone is sufficiently smaller than the other geometrical lengths, see Wang (2013). In the same way, CCFFM+LEBIM models with different stiffness are expected to provide similar failure stresses if the crack extension is sufficiently small.

The failure curves show that a secondary compressive load makes easier the debond onset originated by a primary tensional load. Both HS and quadratic criterion lead to very similar results for tension-tension biaxial states, whereas for compression-tension biaxial states little differences appear.
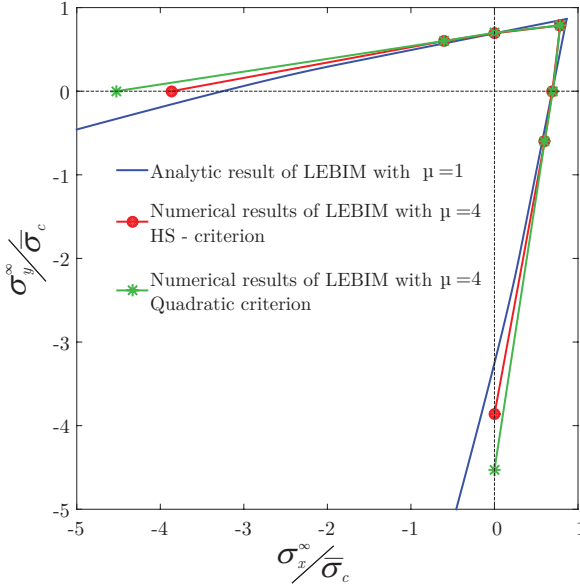
Figure 6.9: Failure curves for a glass fibre embedded in a large epoxy matrix under biaxial transverse loads.

6.5 CCFFM+LEBIM predictions regarding the symmetrical or non-symmetrical debonds onset along a fibre-matrix interface

García et al. (2015) studied the appearance of one debond (non-symmetrical configuration) or two debonds (symmetrical configuration) along fibre-matrix interfaces. A failure criterion based on the CCFFM hypothesis and a coupling of the (incremental) energy and stress criteria considering a perfect fibre-matrix interface was applied to study this problem (Mantič, 2009; Mantič and García, 2012). In this Section, the same problem is studied using CCFFM + LEBIM and the results are compared with the results obtained by García et al. (2015) for perfect interfaces.

A single fibre configuration under uniaxial transverse loads is considered in the present investigation, see Fig. 6.10. A plane strain state is assumed. In the initial state, a fully undamaged interface is considered. Then, the matrix is loaded by a uniaxial remote tension, σ_x^∞, in the x-direction. Typically one of two following possibilities may occur: either one debond or two debonds appear, as showed in Fig. 6.10.

As all configurations are symmetric with respect to the x-axis, only the upper-half of the geometry is considered for the one debond configuration whereas one quarter of the geometry is considered for the two debond configuration. Hence, the polar angle θ_d (debond semiangle) and also other angles are defined as $\theta \geq 0$.

A glass fibre-epoxy matrix system is used with the isotropic linear elastic properties for the fibre and matrix shown in Table 6.1, exactly the same than those used in García et al. (2015).
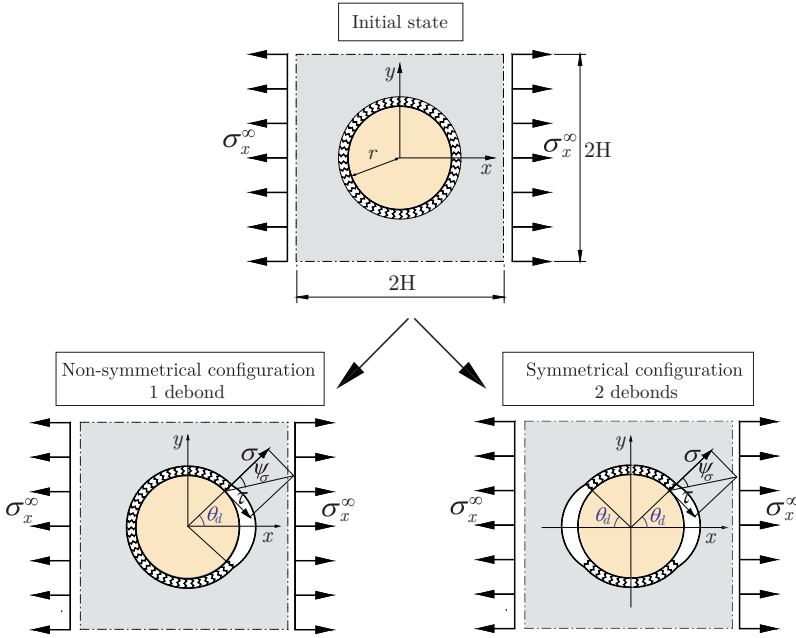
Figure 6.10: Description of debonds that may be produced in a single fibre problem.

Several stiffness interface configurations were used in the present study. Recalling that, for $\mu = 1$ the present model reverts to the original LEBIM, and when μ value increases, for a fixed $\bar{G}_{Ic}$ and $\bar{\sigma}_c$, the interface becomes stiffer, and for $\mu \to \infty$ a perfect (rigid) interface is obtained. The interface properties needed for the CCFFM+LEBIM model are shown in Table 6.6. Notice that the above defined dimensionless numbers μ and γ are also included in this table. According to (6.12), γ modulates the influence of the stress and energy criteria governing the transition from brittle configurations (for small values of γ) to tough configurations (for large values of γ).

Table 6.6: Interface properties.

$\bar{\sigma}_c$ (MPa)	$\bar{G}_{Ic}$ (J/m^2)	k_n (MPa/μm)	k_t/k_n	μ	γ
25	10	16200	0.25	518.4	3.58
30	10	16200	0.25	360	2.98
35	10	16200	0.25	264.5	2.56
60	10	16200	0.25	90	1.49
200	10	16200	0.25	8.1	0.45

6.5.1 Numerical results

The model is defined by a fibre radius $r = 7.5\mu$m and a rectangular matrix of vertical side length 2H with H/r=200/3. Then, taking into account the symmetries used in

the numerical model, 230 (or 220) elements are used to model the matrix boundary, 200 uniform elements for the fibre boundary where the symmetry is applied, and 1800 (or 900) uniform elements are used for each fibre-matrix interface side, for the one debond (or two debonds) configuration, respectively. The element size at the interface is defined by the polar angle $0.1°$.

Initially, the energy and stress criteria are studied in an independent way in Figs. 6.11 and 6.12.
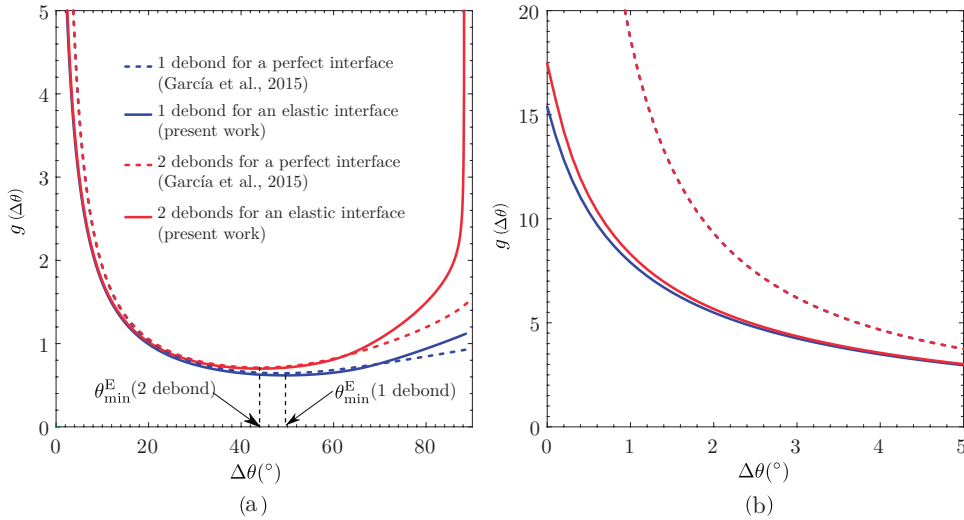
Figure 6.11: (a) Dimensionless function g (6.4) of resistance against the debond onset due to the energy criterion as a function of debond advance $\Delta\theta$, and (b) is a detail view of the plot in (a).

First, the energy criterion is considered through the dimensionless function $g(\Delta\theta, n)$ defined in (6.4), which can be interpreted as the resistance against the debond onset when this criterion is applied. In the present problem, $g(\Delta\theta, n)$ is the function of the crack advance in terms of the debond semiangle $\Delta\theta$ and the number of debonds ($n = 1, 2$). $g(\Delta\theta, n)$ functions are plotted in Fig. 6.11, which shows that $g(\Delta\theta, 1)$ is smaller than $g(\Delta\theta, 2)$. The differences between their values increases with $\Delta\theta$, which can be explained by the increasing shielding effect in the case of two debonds for larger debonds. This figure also includes previous results considering perfect interfaces (dashed lines), as in García et al. (2015). Blue lines are associated to one debond configuration while red lines are associated to the two debond configuration. For both configurations, $g(\Delta\theta, n)$ is decreasing with $\Delta\theta$ up to minimum values at $\theta_{\min}^{E}$, which are very similar to those obtained for a perfect interface in García et al. (2015).

It should be noticed that the results obtained using elastic interfaces are very similar to those using perfect interfaces for intermediate values of $\Delta\theta$, but differ for small and large values of $\Delta\theta$. These differences may be explained, for small values of $\Delta\theta$, due to the fact that elastic interfaces allow openings and slidings in the zone ahead of the crack tip, however this behaviour is not allowed for perfect interfaces. Moreover, $g(\Delta\theta) \to \infty$ for $\Delta\theta \to 0$, in the case of perfect interfaces, whereas it
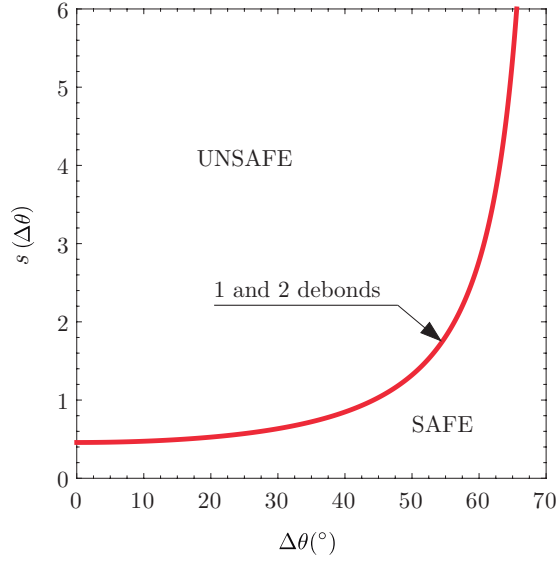
Figure 6.12: Graphical representation of the stress criterion.

approaches a finite value for elastic interfaces, see Fig. 6.11 (b). On the other hand, for large values of $\Delta\theta$, the matrix and the fibre are in contact. Then, differences arise due to the fact that contact conditions are modelled in a different way for each case. Signorini (perfect) contact condition is used for the perfect interface case while a penalty contact condition is used for the elastic interface case.

Second, the function $s(\Delta\theta)$ which gives a minimum remote tension necessary to originate the debond according to the stress criterion is plotted in Fig. 6.12. As the stress criterion is based on the initial elastic state, both configurations, with one and two debonds, are equivalent when this criterion is only used. As mentioned before, for both failure configurations, the function $s(\Delta\theta)$ is increasing with $\Delta\theta$.

Then, when the fulfillment of both criteria is required, a critical remote tension σ_c^∞ originating a finite debond onset/growth and the size of this debond given by θ_c are predicted, as shown in (6.12). The critical value σ_c^∞ is the minimum remote tension σ^∞ for which both criteria are fulfilled which is achieved for the value of $\Delta\theta = \theta_c$.

In the plane $(\Delta\theta, \sigma^\infty/\sigma_c)$ for $\Delta\theta < \theta_{\min}^E$, the two curves given by these criteria have either one or none at all intersection point, $s(\Delta\theta) = \gamma\sqrt{g(\Delta\theta, n)}$. Then, the following two scenarios may occur as in García et al. (2015); Mantič (2009); Mantič and García (2012):

- Scenario C (coupled): If the two curves have one intersection point for $\Delta\theta < \theta_{\min}^E$, the minimum remote tension fulfilling both criteria for the debond onset σ_c^∞ is given by this intersection point $(\theta_c, s(\theta_c) = \gamma\sqrt{g(\theta_c, n)})$, see Fig. 6.13.

- Scenario E (energetic): If the two curves have none intersection point for $\Delta\theta < \theta_{\min}^E$, the remote tension fulfilling both criteria for the debond onset σ_c^∞ is given
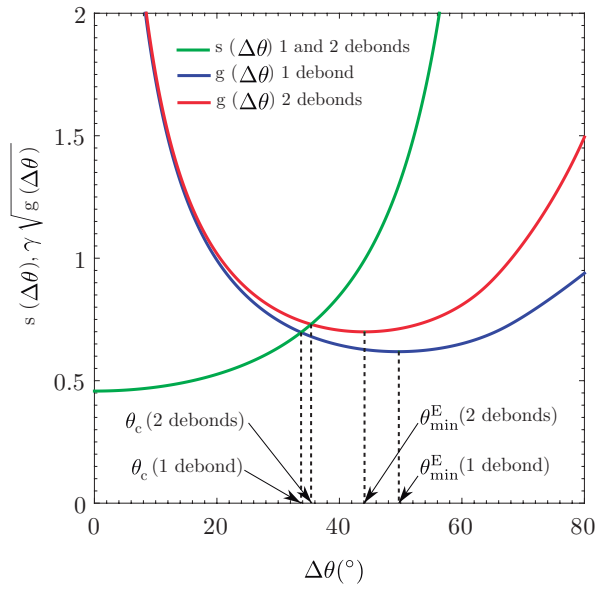
Figure 6.13: Scenario C for $\bar{\sigma}_c =$60(MPa), $\bar{G}_{Ic} =$10(J/m^2), $\mu =$90 and $\gamma =$1.49.

by the minimum value of $g(\Delta\theta)$, see Fig. 6.14.
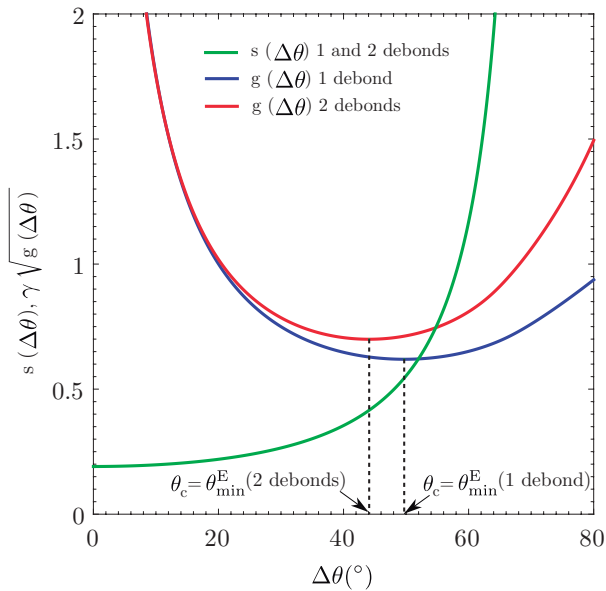
Figure 6.14: Scenario E for $\bar{\sigma}_c =$25(MPa), $\bar{G}_{Ic} =$10(J/m^2), $\mu =$518.4 and $\gamma =$3.58.

The critical semiangle θ_c is defined as the semiangle of the debond produced in its instantaneous onset, while the arrest semiangle θ_a is the semiangle of the debond after its subsequent unstable growth (Mantič and García, 2012). Actually, θ_a defines the end of this unstable debond growth. If after a debond onset, such an unstable debond growth does not exist, then $\theta_a = \theta_c$.

The critical and arrest semiangles, θ_c and θ_a, respectively, for perfect and elastic interfaces are plotted in Fig. 6.15 as functions of γ and the failure configuration. In this figure, the lines (both continuous and dashed), represent results for perfect interfaces (Mantič et al., 2015), while dots represent results for linear elastic interfaces, see Table 6.6. The continuous lines are associated to critical semiangles, while dashed lines represent arrest semiangles. The blue lines and dots correspond to the one-debond configuration, while the red ones correspond to the two-debond configuration.

It is interesting to notice that the results for the critical angles using linear elastic
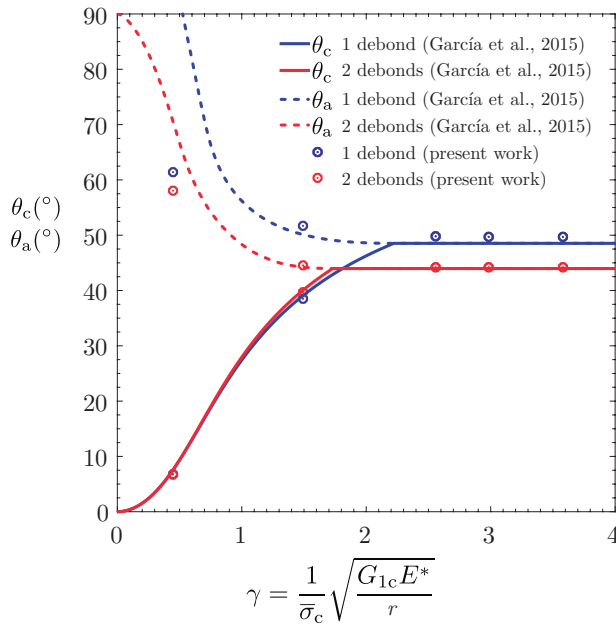
Figure 6.15: Critical and arrest semiangles, θ_c and θ_a.

interfaces are very similar to those for perfect interfaces. Regarding the arrest angle, results for linear elastic interfaces differ from those for perfect interfaces when γ values are small, while they are very similar for increasing γ values. Moreover, if we increase the interface stiffness we observe the results become closer to those obtained for the perfect interface. Therefore with this method we can adjust the stiffness of the interface to the real one.

Fig. 6.16 shows $\sigma_c^\infty / \bar{\sigma}_c$ as a function of γ for the two failure configurations. σ_c^∞ is quite constant for small γ values (scenario C), but it increases strongly for $\gamma \geq 1$, for both perfect and elastic interfaces (García et al., 2015); actually it is a linear function of γ for sufficiently large values of γ (scenario E). As in the previous figures,
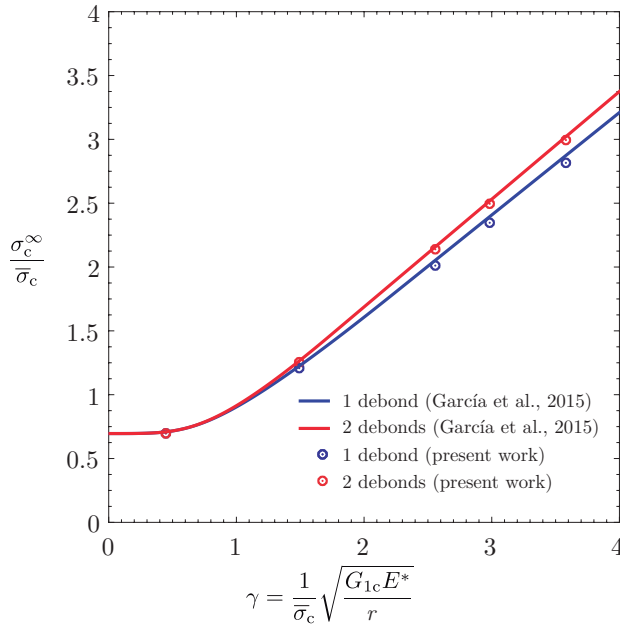
Figure 6.16: Critical remote tension σ_c^∞ for the two post-failure configurations.

the present results are very similar to those obtained for a perfect interface.

Thus, in view of Figs. 6.15 and 6.16, the non-symmetrical configuration is preferential for a glass/epoxy system. The percentage difference between the critical tensions predicted for the two configurations defined by

$$\triangle\sigma_c^\infty(\%) = 100 \cdot \frac{\sigma_c^\infty(n = 2) - \sigma_c^\infty(n = 1)}{\sigma_c^\infty(n = 1)}, \tag{6.14}$$

is shown in Fig. 6.17. In this figure, it can be clearly seen that $\sigma_c^\infty(n = 2) > \sigma_c^\infty(n = 1)$ for $\gamma > 0$. Due to the scale of this figure the differences between the results, for perfect and elastic interfaces, are more remarkable. Finally, we can conclude that the non-symmetrical configuration is preferential independently of γ, however, the difference between the two post-failure configurations is very small for brittle fibre-matrix system characterized by small values of $\gamma < 1$. Nevertheless, for tough fibre-matrix systems, characterized by high values of $\gamma \gtrsim 2$, the percentage difference between the predicted critical tensions can achieve values more than 6%, for the cases studied in the present work.
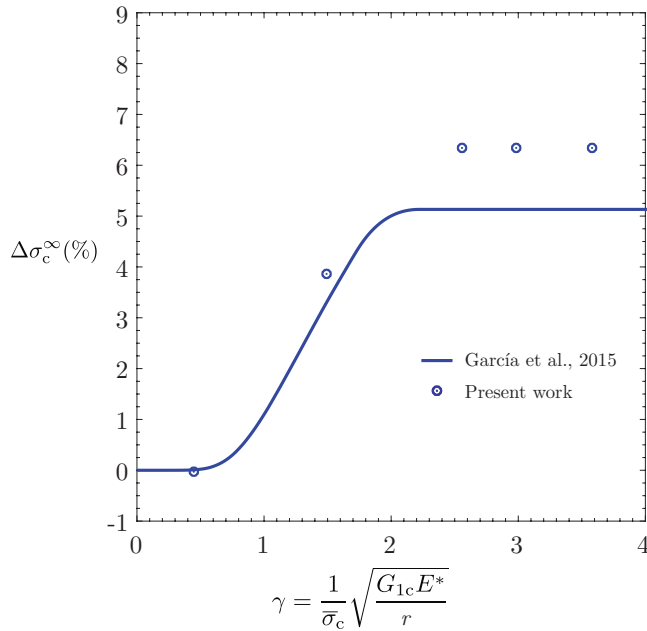
Figure 6.17: Percentage difference between the critical remote tensions for the symmetrical and non-symmetrical post-failure configurations.

6.6 CCFFM+LEBIM predictions under the presence of a secondary fibre

The purpose of this section is to check the capacity of the new approach to study a multifibre geometry, specifically two fibres.

For this reason, a two-fibre configuration represented in Fig. 6.18 is briefly studied. It includes two glass fibres embedded in a infinity epoxy matrix and subjected to a remote loading transverse to the fibres. In order to analyze the fibre interaction, the distance between the fibres d is varied, see Fig. 6.18. As in previous sections, inclusions and matrix are considered isotropic linear elastic materials, whose characteristics are presented in Table 6.1. The mechanical characteristics of the interfaces were also previously described in Table. 6.2. The mesh used includes 1440 linear elements for each interface face (matrix and fibre sides) with boundary elements whose polar angle is $0.25°$.

The applied remote loads, σ_x^∞ and σ_y^∞ are shown in Figure 6.18. The position where the crack onset occurs is denoted by the polar angle θ_o, measured from a diameter parallel to the y-axis. The critical angle, θ_c, is the initial crack size produced in the crack onset.

In the following subsections the influence of a second fibre will be analyzed and also compared with the single fibre case, for four different loading conditions. The crack onset position given by θ_o and the critical load (load necessary to produce the debond onset) σ^∞ will be determined for several distances between fibres and different
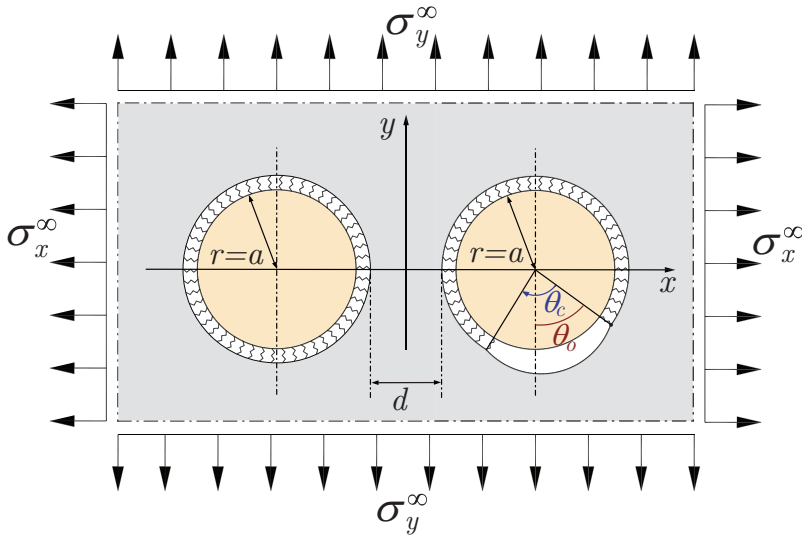
Figure 6.18: Two-fibre configuration under biaxial remote transverse loads.

interface stiffnesses (obtained by varying μ).

6.6.1   Loading Case 1: $\sigma_x^\infty = 0$ and $\sigma_y^\infty = \sigma^\infty$

This case represents a uniaxial loading condition with the far field loads applied parallel to the y-axis. σ^∞ is defined as the load necessary to produce the fibre-matrix debond. The influence of the distance d on the crack onset angle values θ_o and the critical applied remote stress σ^∞ are depicted in Figures 6.19(a) y (b), respectively. Notice that this distance d increases up to the limit of the single fibre case, described in the plots as $d/a = \infty$.
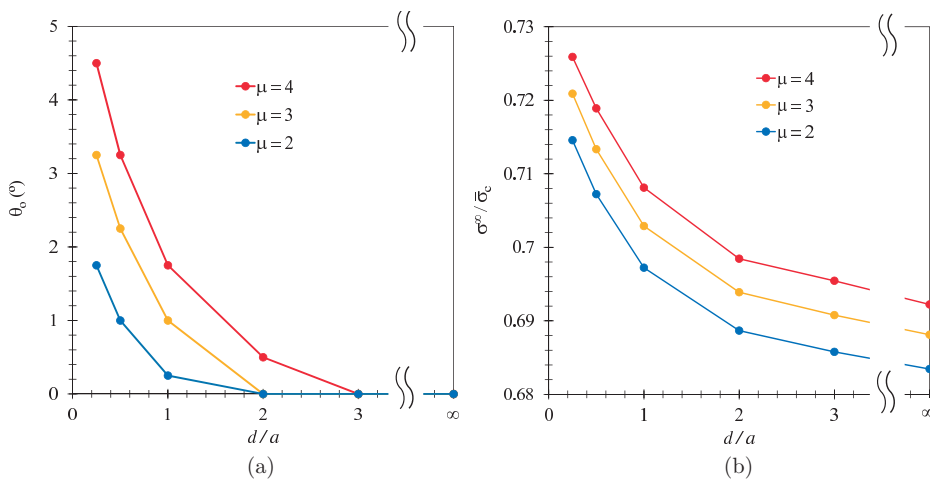
Figure 6.19: (a) The crack onset angle θ_o and (b) the critical remote applied load σ^∞/σ_c versus the distance between two fibers for $\sigma_x^\infty = 0$ and $\sigma_y^\infty = \sigma^\infty$.

It can be seen in Figure 6.19(a) that the crack onset angle increases when the fibres become closer and also when the interface stiffness increases. The deviation of the onset position is produced in a similar manner for all the solved cases (as shown in Figure 6.18). Results show that the crack onset is produced at the fibre-matrix interface part distant from the other fibre (similarly as shown in Figure 6.18). Then, the debond (interface crack) grows towards the interface part closer to the other fibre.

The initial crack size defined by the angle θ_c is the same for each μ value, independently of the fibre distance d. The obtained θ_c values are: 5.75^o for $\mu = 2$, 8.75^o for $\mu = 3$ and 11.00^o for $\mu = 4$. As it may be expected, the critical remote load increases with increasing values of the interface stiffness. This critical load also increases with decreasing the distance between fibres. Thus, higher loads are required to produce a debond in the case of two neighbour fibres than in the single fibre case. However, all these differences are quite small.

6.6.2   Loading Case 2: $\sigma_x^\infty = \sigma^\infty$ and $\sigma_y^\infty = 0$

This case represents a uniaxial loading condition with the remote loads applied parallel to the x-axis. As in the previous case σ^∞ is the critical load value.

Figure 6.20: The critical remote applied load σ^∞/σ_c versus the distance between two fibers for $\sigma_x^\infty = \sigma^\infty$ and $\sigma_y^\infty = 0$.

In Figure 6.20, the influence of the distance between fibres on the critical applied remote stress σ^∞ is shown. It is noticeable that for this case the crack onset position is always the same. In all the cases $\theta_o = 90°$, i.e. the crack onset takes place at the interface point closest to the other fibre. Thus, no influence of the fibre proximity nor the interface stiffness on θ_o is observed.

Regarding the critical crack size, θ_c is independent of the distance d, being 5.75^o for $\mu = 2$, 8.75^o for $\mu = 3$ and 11.00^o for $\mu = 4$. Notice that these angles are equal to those obtained in the loading case 1.

The single fibre case is again represented by $d/a = \infty$. It can also be observed that a higher critical load is necessary when the fibres move away from each other,

this effect is very significant. On the other hand the increase of the stiffness seems to have only a very little influence.

6.6.3   Loading Case 3: $\sigma_x^\infty = -\sigma^\infty$ and $\sigma_y^\infty = \sigma^\infty$

A tension-compression biaxial state is considered herein because according to Távara et al. (2016) it may be the most dangerous biaxial situation. Remote load σ^∞ is applied in both directions, as tensile stress parallel to the y-axis and as compressive stress parallel to the x-axis.
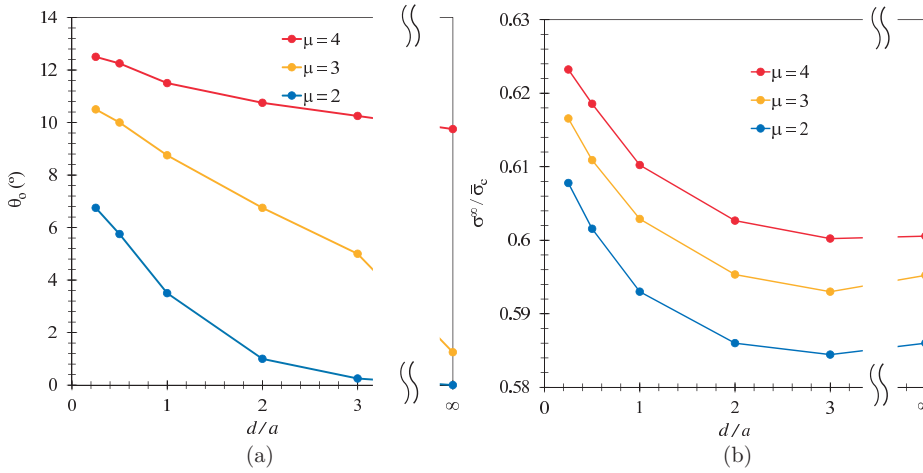
Figure 6.21: (a) The crack onset angle θ_o and (b) the critical remote applied load σ^∞/σ_c versus the distance between two fibers for $\sigma_x^\infty = -\sigma^\infty$ and $\sigma_y^\infty = \sigma^\infty$.

In Figure 6.21, the influence of d on θ_o and σ^∞ is depicted. The tendencies shown are similar to the loading case 1. Nevertheless, θ_o values are much higher for the present loading case. Notice that θ_o may be different from 0° even for the single fibre case. σ^∞ values are considerably lower than for the loading case 1. Results confirm that a transverse compression acting as secondary load makes the crack onset easier. Finally, θ_c values are the same as for the previous loading cases.

6.6.4   Loading Case 4: $\sigma_x^\infty = \sigma^\infty$ and $\sigma_y^\infty = -\sigma^\infty$

A tension-compression biaxial state is considered herein. Remote load σ^∞ is applied in both directions, as tensile stress parallel to the x-axis and as compressive stress parallel to the y-axis.

The results for the present loading case are shown in Figure 6.22. The critical load evolution has a similar tendency as in the loading case 2, but with lower values (due to the secondary compression effect). While the crack onset position for the single fibre case changes, for the present two-fibre cases it keeps on 90°. These results show that the position of the crack onset is more influenced by the presence of a secondary fibre rather than by a change of the interface stiffness. Once again the values obtained for θ_c are the same as in the previous loading cases.

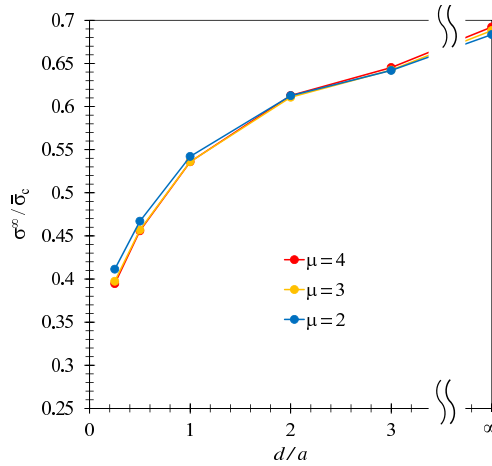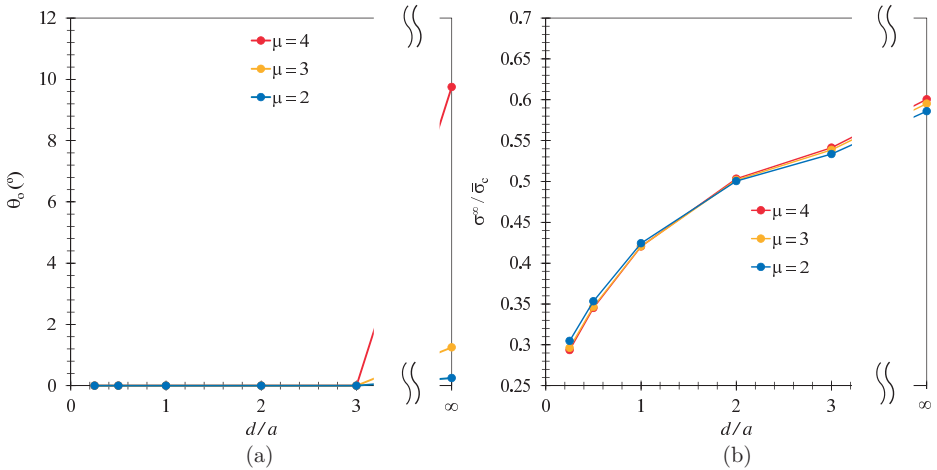Figure 6.22: (a) The crack onset angle θ_o and (b) the critical remote applied load σ^∞/σ_c versus the distance between two fibers for $\sigma_x^\infty = \sigma^\infty$ and $\sigma_y^\infty = -\sigma^\infty$.

6.7 Concluding remarks

The CCFFM+LEBIM code described in Section 3.2.1 can be used together with different interface failure criteria. In the present chapter the quadratic and Hutchinson and Suo criteria have been considered, although the formulation is prepared to be used with any other interface failure criterion.

It is interesting to observe that for the present fibre-matrix system the predictions of the crack onset and propagation obtained by CCFFM and LEBIM differ only slightly from those obtained by the original LEBIM, which indicates only a moderate dependence of these predictions on the interface stiffness.

It is noticeable that although the single-fibre problem is symmetric, the position where the onset of the interface crack occurs may be quite away from the symmetry plane. This effect is emphasized in the cases with a stiffer interface and where a compressive remote load appears. A biaxiality effect is observed in the failure curves obtained showing that the presence of a secondary compressive remote load makes easier the debond onset.

Also, the same CCFFM+LEBIM code has been applied to model two aligned fibres within a large matrix under four different loading cases varying the distance between the fibres. The aim was to study the effect of a secondary fibre on the position where the debond (interface crack) initiates, θ_o, the initial debond size, θ_c, and the critical load (the load necessary to produce the debond), σ_x^∞.

Loading cases includes two uniaxial tensile loading cases and two biaxial tensile-compressive loading cases. The obtained results show that θ_c is only influenced by the interface stiffness used, being larger for larger values of the dimensionless parameter μ (6.9).

Regarding the position where the debond initiates, it seems that θ_o values increase when the distance between fibres decreases for loading cases where the maximum principal remote stress is perpendicular to the line joining fibre centres (tension applied

parallel to the y-axis in the present configuration). Nevertheless when the maximum principal remote stress is parallel to the line joining fibre centres (tension applied parallel to the x-axis) this position does not change, it being always placed in the closest point between fibres.

The critical remote load increases for smaller distances between the fibres and for higher values of μ when the maximum principal remote stress is perpendicular to the line joining fibre centres. However, this critical remote load decreases for smaller distances between the fibres when the maximum principal remote stress is parallel to the line joining fibre centres. Thus, there is some shielding effect between fibres, retarding the debond onset, in the former configurations, while in the latter configurations, the second fibre makes easier the debond onset.

In general, the presence of a second fibre may have a great influence on the debond onset and growth, specially regarding the critical remote load in the cases of the maximum principal remote stress parallel to the line joining fibre centres.

Conclusions and future developments

7.1 Conclusions

The work carried out in this thesis has been focused on the two research lines, corresponding to Part 2 and Part 3 of this thesis as defined in the Introduction, respectively:

(i) The development and implementation of the Coupled Criterion of the Finite Fracture Mechanics (CCFFM) applied to LEBIM (CCFFM + LEBIM). The implementations developed are based on two different approaches: the definition of the curves generated by the energy and stress criteria, and the principle of Minimum Total Energy subject to a Stress Condition (PMTE-SC).

(ii) The numerical study of different damage mechanisms in fibre reinforced composites and their joints at macro and micro scales, that may provide support in the knowledge of the behaviour of the numerical and analytical tools developed, while allowing to deepen the knowledge of damage mechanisms in composites.

In the following the main contributions of the present thesis grouped in the above mentioned two research lines are detailed. In this sense, first, the contributions to the developments of the models and numerical tools, and, then, to the analysis of some damage mechanisms at composites are described.

7.1.1 Development of the coupled criteria applied to LEBIM and numerical tools

Two computational procedures described in this thesis, which combine the CCFFM and LEBIM formulations, have been developed and implemented in a 2D BEM code and in code based in FEM. These procedures open new possibilities to study the onset

and propagation of cracks along interfaces and adhesive layers. This is due to the use of realistic values of strength, fracture toughness and in particular interface stiffness, which can be significantly higher than in the original LEBIM, and are decoupled in the present procedure. It is noticeable that when $\mu = 1$ the present procedure essentially reverts to the original LEBIM. Furthermore, this method predicts an instantaneous crack generation without the need of an infinitesimal failure growth. This allows the appearance of several fractures at the same time in the same problem.

The numerical codes have been successfully applied to several specific problems, in part 3 of this thesis. It has been shown that the implementation of the procedures leads to a very good agreement with analytical models and experimental tests.

A discussion about two possible ways of defining the fracture mode mixity needed the energy criterion within the CCFFM was also provided. However, the choice of the mode mixity definition is still an open debate.

The proposed numerical tools are therefore suitable for predicting the failure of an interface with a relatively short computational time. As a future task, we remark that, in order to increase the efficiency of computations using LEBIM, a complete knowledge about the singular stress field near the crack tip growing along the elastic interface is necessary; its proper inclusion in the discretization procedure will avoid the use of highly refined meshes close to the crack tip or the convergence study for each problem.

7.1.2 Studied cases of damage and failure in composite materials and their joints at macro and micro scale

Double cantilever beam:
The isotropic DCB test is studied under load and displacement control separately. The aim of this study is to analyse the differences between the two approaches outlined in the CCFFM + LEBIM. Four analytical solutions based on Bernoulli's beam are developed and compared with the numerical solution for each test.

The test under displacement control shows an infinitesimal crack growth along the interface, so the numerical and analytical solution of the method based on the curves leads to the solution of the original LEBIM. The analytical and numerical results of the method based on the PMTE-SC also coincide with this infinitesimal propagation of the interface failure. However, the increase in the load on the algorithm must be adjusted so that this infinitesimal propagation is done correctly.

The behaviour of this test under load control is very different from the previous one, since when the delamination load is reached the interface failure happen in an unstable way. In this case, the two methods of CCFFM + LEBIM, either analytically or numerically, predict the same failure load and the same interface damage. In the code based on the PMTE-SC, the definition of the load at each step should be readjusted, so that it is not always increasing, otherwise, it would not be able to capture the snap-through instability of the problem.

The double pull-push shear test:

The crack onset and propagation along the interface in the Double Pull-Push Shear (DPPS) test is studied using an original analytical solution based on the Timoshenko beam theory. This solution takes into account the normal stresses (peeling) that appear in this test.

Although the normal stresses in the shear tests keep the discussion about the fracture energy still open (Carrara and Ferretti, 2013; Mazzotti et al., 2016; Martinelli et al., 2011), the solution provided can be used for any test between two adherents of any thickness/stiffness in double joints. Also, in the shear tests, the fracture energy in Mode I along the interface is significantly lower than the fracture energy in Mode II, therefore, even a small increase in the normal stresses could reduce the bearing capacity of the interface (Mazzotti et al., 2016). Therefore, a parametric study is made to analyse the influence of geometry and material characteristics (adhesives and adherents) on the stress distributions.

Using this analytical solution the Coupled Criterion of Finite Fracture Mechanics (CCFFM) including fracture mixed mode is applied to predict failure loads for debond onset and propagation in this test. The results obtained show some discrepancies for some parameter values with previous studies that do not take into account normal stresses. For example, for small overlap lengths, for which the damage could even start by the free end. The results with small overlap lengths have been compared with the experimental tests, showing a good agreement.

Moreover, the analytical solution is also compared with the numerical results and with experimental tests found in literature, showing a good agreement between all of them. For the characterization of the interface failure, a simple inverse analysis has been used to fit $\bar{G}_{\mathrm{IIc}}$ and $\bar{\tau}_{\mathrm{c}}$ by exploiting the results from three different test configurations.

Failure initiation in long-fiber reinforced composites under transverse loads:

The micro-mechanical behavior of cracks between matrix and fibre under transversal loads is studied in detail in Chapter 6. The CCFFM + LEBIM code described in Section 3.2.1 can be used together with different interface failure criteria. Specifically, the quadratic and Hutchinson and Suo criteria have been considered.

It is interesting to observe that for the present fiber-matrix study the predictions of the crack onset and propagation obtained by CCFFM + LEBIM by curve method differ only slightly from those obtained by the original LEBIM, which indicates only a moderate dependence of these predictions on the interface stiffness. However, it would be interesting to study this case with the PMTE-SC, in order to know the predisposition of failure growth in several areas of the interface.

The same question arises about the approach of the CCFFM+LEBIM used, when testing the fiber-matrix system to biaxial loads. Because, although the studied problem is symmetric, the position where the onset of the interface crack occurs may be quite away from the symmetry plane. And, this effect is emphasized in the cases with a stiffer interface and where a compressive remote load appears.

The results obtained on the interaction between two fibres positioned at a certain distance are interesting. The critical remote load increases for smaller distances between the fibres and for higher values of μ when the maximum principal remote

stress is perpendicular to the line joining fibre centres. However, this critical remote load decreases for smaller distances between the fibres when the maximum principal remote stress is parallel to the line joining fibre centres. Thus, there is some shielding effect between fibres, retarding the debond onset, in the former configurations, while in the latter configurations, the second fibre makes easier the debond onset.

It is also remarkable the study about the appearance of symmetrical or non-symmetrical debond along a fibre-matrix interface which shows that a non-symmetrical debond is preferential. Results shown that this effect is caused by the energy criterion, which captures the shielding effect of the second debond for relatively large debond angles. Furthermore, the code used showed good agreement with the results of the study of the same problem carried out with a failure criterion based on the CCFFM hypothesis and a coupling of the (incremental) energy and stress criteria considering a perfect fibre-matrix interface.

7.2 Future developments.

The work carried out in the present thesis will further continue as a more extensive study exploring the possibilities of the presented method based in the CCFFM applied to LEBIM. The research developed in this thesis has answered many questions but has opened up other interesting ones.

The efficiency of the method described in this work, which combines the finite fracture mechanics criterion with the LEBIM, has been successfully demonstrated. However, the codes developed need to be adjusted to increase their efficiency and a better definition of the input parameters.

Except for the DCB test, the rest of the composite problems in the present thesis have been solved using CCFFM+LEBIM by the curve method. All of them could be solved with code based on PMTE-SC for comparison purposes. Such a comparison will be very interesting to judge the adequacy of each method, and it will require also some experimental results. The code based on curves provides the exact load for the initiation of the interface failure and the finite segment damage that occurs instantaneously. However, it is not able to explore the creation of several separate damages at the same time, and location of damage initiation is still defined by the original LEBIM. Therefore, for problems where the onset and behaviour of the damage is known, this code can predict quite reliably the applied load that produces the fracture and the size of that fracture.

However, it seems that the code based on the PMTE-SC is more versatile in predicting the failure of complex interface damage problems. The location of the interface failure initiation is not always defined by the maximum stress point, and several separate areas of the problem may fail at the same time. This opens up an important field in predicting the onset of interface failure. Therefore, it would be interesting to explore the different configurations of damage initiation N for some problems with known results. Driving to a global minimum from any N configuration may not always be possible. An heuristic, e.g., based on the level sets given by the stress criterion and/or the components of Γ_C with nodes in A_σ, can be used to define D_n leading to an approximation of the minimum of the total energy computed at acceptable computational costs.

The coupled criterion has given the LEBIM more versatility, but this model still has a difficult problem to solve: the solution of the asymptotic stress field at the crack tip. These are relevant for achieving a high accuracy in the computational modeling of crack growth with a maximum algorithmic efficiency, minimizing the necessary computing resources. For this, special finite elements could be developed, located at the crack tip, whose special singular shape functions reproduce these asymptotic elastic solutions. These special elements implemented in FEM and in BEM codes could allow us to discretize solids with cracks without the need to use very refined meshes or to do a convergence study.

The inclusion of the friction effect in the CCFFM + LEBIM could be also very useful for some applications in composites. In particular, in tests where friction between the solids in contact is important, such as the shear test to characterize the interface in composite concrete reinforcements. Since, the bond capacity between the FRP system and the concrete depends on the surface preparation methods, and therefore, the anchorage length and the critical failure load also depends on this preparation.

There is currently a UMAT subroutine developed by the GERM group, which allows the 3D LEBIM in ABAQUS. So a future line of direct application of this thesis would be to apply the PMTE-SC to LEBIM 3D. This could solve problems where 3D effects should not be neglected.

By the definition of LEBIM this model is only used in the interfaces between two solids, but recently a similar model has been used to reproduce the kink out of the interface. It would be interesting to study the behaviour of this model and the possibilities of applying the CCFFM by the PMTE-SC in order to obtain a numerical tool capable of covering more applications.

Bibliography

Bank-Sills, L. and D. Ashkenazi (2000). A note on fracture criteria for interface fracture. *International Journal of Fracture 103*, 177–188.

Barenblatt, G. (1959). The formation of equilibrium cracks during brittle fracture. General ideas and hypotheses. Axially-symmetric cracks. *Journal of Applied Mathematics and Mechanics 23*, 622–636.

Bennati, S., M. Colleluori, D. Corigliano, and P. S. Valvo (2009). An enhanced beam-theory model of the asymmetric double cantilever beam (ADCB) test for composite laminates. *Composites Science and Technology 69*(11), 1735 – 1745.

Bennati, S., P. Fisicaro, L. Taglialegne, and P. S. Valvo (2019). An Elastic Interface Model for the Delamination of Bending-Extension Coupled Laminates. *Applied Sciences 9*(17).

Benveniste, Y. and T. Miloh (2001). Imperfect soft and stiff interfaces in two-dimensional elasticity. *Mech Mater 33*, 309–323.

Benzeggagh, M. and M. Kenane (1996). Measurement of mixed-mode delamination fracture toughness of unidirectional glass/epoxy composites with mixed-mode bending apparatus. *Composites Science and Technology 56*(4), 439–449.

Bialas, M. and Z. Mróz (2005). Modelling of progressive interface failure under combined normal compression and shear stress. *International Journal of Solids and Structures 42*(15), 4436–4467.

Bigwood, D. and A. Crocombe (1989). Elastic analysis and engineering design formulae for bonded joints. *International Journal of Adhesion and Adhesives 9*(4), 229 – 242.

Bigwood, D. and A. Crocombe (1990). Non-linear adhesive bonded joint design analyses. *International Journal of Adhesion and Adhesives 10*(1), 31 – 41.

Brewer, J. C. and . A. Lagace (1988). Quadratic stress criterion for initiation of delamination. *Journal of Composite Materials : 1141 22*, 1141–1155.

Budhe, S., M. Banea, S. de Barros, and L. da Silva (2017). An updated review of adhesively bonded joints in composite materials. *International Journal of Adhesion and Adhesives 72*, 30 – 42.

Camacho, G. and M. Ortiz (1996). Computational modelling of impact damage in brittle materials. *International Journal of Solid and Structures 33*, 2899–2938.

Camanho, G., C. Dávila, and M. de Moura (2003). Numerical simulation of mixed-mode progressive delamination in composite materials. *Journal of Composite Materials 37*, 1415–1438.

Camanho, P. P., C. G. Davila, and M. F. de Moura (2012). A finite fracture mechanics model for the prediction of the open-hole strength of composite laminates. *Composites Part A: Applied Science and Manufacturing 43*(8), 1219–1225.

Carpinteri, A. (1989a). Cusp catastrophe interpretation of fracture instability. *Journal of the Mechanics and Physics of Solids 37*, 567–582.

Carpinteri, A. (1989b). Post-peak and post-bifurcation analysis on cohesive crack propagation. *Engineering Fracture Mechanics 32*, 265–278.

Carpinteri, A., P. Cornetti, and N. Pugno (2009). Edge debonding in FRP strengthened beams: Stress versus energy failure criteria. *Engineering Structures 31*, 2436–2447.

Carpinteri, A., P. Cornetti, N. Pugno, A. Sapora, and D. Taylor (2008). A finite fracture mechanics approach to structures with sharp V-notches. *Engineering Fracture Mechanics 75*(7), 1736–1752.

Carrara, P. and D. Ferretti (2013). A finite-difference model with mixed interface laws for shear tests of frp plates bonded to concrete. *Composites Part B: Engineering 54*, 329 – 342.

Carrara, P., D. Ferretti, F. Freddi, and G. Rosati (2011). Shear tests of carbon fiber plates bonded to concrete with control of snap-back. *Engineering Fracture Mechanics 78*(15), 2663 – 2678.

Carraro, P. and M. Quaresimin (2014). Modelling fibre-matrix debonding under biaxial loading . *Composites Part A: Applied Science and Manufacturing 61*, 33–42.

Carrere, N., E. Martin, and D. Leguillon (2015). Comparison between models based on a coupled criterion for the prediction of the failure of adhesively bonded joints. *Engineering Fracture Mechanics 138*, 185–201.

Charalambides, M. and Y. W. . J. W. A.J.Kinloch (1992). On the analysis of mixed-mode failure. *International Journal of Fracture 54*, 269–291.

Comninou, M. (1977). The Interface Crack. *Journal of Applied Mechanics 44*(4), 631–636.

Cornetti, P. and A. Carpinteri (2011). Modelling the FRP-concrete delamination by means of an exponential softening law. *Engineering Structures 33*(6), 1988–2001.

Cornetti, P., V. Mantič, and A. Carpinteri (2012). Finite Fracture Mechanics at elastic interfaces. *International Journal of Solids and Structures 49*, 1022–1032.

Cornetti, P., M. Muñoz Reja, A. Sapora, and A. Carpinteri (2019). Finite fracture mechanics and cohesive crack model: Weight functions vs. cohesive laws. *International Journal of Solids and Structures 156-157*, 126–136.

Cornetti, P., N. Pugno, A. Carpinteri, and D. Taylor (2006). Finite fracture mechanics: a coupled stress and energy failure criterion. *Engineering Fracture Mechanics 73*, 2021–2033.

Cornetti, P., A. Sapora, and A. Carpinteri (2016). Short cracks and V-notches: Finite Fracture Mechanics vs. Cohesive Crack Model. *Engineering Fracture Mechanics 168*, 2–12.

Cottone, A. and G. Giambanco (2009). Minimum bond length and size effects in FRP–substrate bonded joints. *Engineering Fracture Mechanics 76*(13), 1957–1976.

Czaderski, C., K. Soudki, and M. Motavalli (2010). Front and side view image correlation measurements on FRP to concrete pull-off bond tests. *Journal of Composites for Construction 14*(4), 451–463.

da Silva, L. F., P. J. das Neves, R. Adams, and J. Spelt (2009). Analytical models of adhesively bonded joints - Part I: Literature survey. *International Journal of Adhesion and Adhesives 29*(3), 319 – 330.

Davila, C. G., P. P. Camanho, and C. A. Rose (2005). Failure Criteria for FRP Laminates. *Journal of Composite Materials 39*(4), 323–345.

Dimitri, R., P. Cornetti, V. Mantič, M. Trullo, and L. D. Lorenzis (2017). Mode-i debonding of a double cantilever beam: A comparison between cohesive crack modeling and finite fracture mechanics. *International Journal of Solids and Structures 124*, 57 – 72.

Dimitri, R., F. Tornabene, and G. Zavarise (2018). Analytical and numerical modeling of the mixed-mode delamination process for composite moment-loaded double cantilever beams. *Composite Structures 187*, 535 – 553.

Doitrand, A., E. Martin, and D. Leguillon (2020). Numerical implementation of the coupled criterion: Matched asymptotic and full finite element approaches. *Finite Elements in Analysis and Design 168*, 103344.

Doitrand, A. and A. Sapora (2020). Nonlinear implementation of Finite Fracture Mechanics: A case study on notched Brazilian disk samples. *International Journal of Non-Linear Mechanics 119*, 103245.

England, A. (1965). A crack between dissimilar media. *Journal of Applied Mechanics 32*, 400–402.

Entov, V. and R. Salganik (1968). On the Prandtl brittle fracture model. *Mechanics of Solids 3*, 79–89. (translated from Russian).

Erdogan, F. . (1965). Stress distribution in bonded dissimilar materials with cracks. *Journal of Applied Mechanics 32*, 403–410.

Erdogan, F. (1997). *Fracture mechanics of interfaces, In: Damage and Failure of Interfaces.* Balkema Publishers: Rotterdam.

Erdogan, F. (2000). Fracture mechanics. *International Journal of Solids and Structures 37*(1-2), 171–183.

fib special activity group, N. M. C., L. Taerwe, and S. Matthys (2013). *fib model code for concrete structures 2010.* Ernst & Sohn, Wiley.

Fosdick, R. and L. Truskinovsky (2003). About Clapeyron's Theorem in Linear Elasticity. *Journal of Elasticity 72*, 145–172.

Gao, Z. (1995). A circular inclusion with imperfect interface: Eshelby's tensor and related problems. *Journal of Applied Mechanics 62*, 860–866.

García, I. (2014). *Crack initiation in composites at micro and meso scales. Development and applications of nite fracture mechanics.* Ph. D. thesis, Universidad de Sevilla.

García, I. and D. Leguillon (2012). Mixed-mode crack initiation at a v-notch in presence of an adhesive joint. *International Journal of Solids and Structures 49*, 2138–2149.

García, I., V. Mantič, and E. Graciani (2015). A model for the prediction of debond onset in spherical-particle-reinforced composites under tension. Application of a coupled stress and energy criterion. *Composites Science and Technology 106*, 60–67.

García, I., M. Paggi, and V. Mantič (2014). Fiber-size effects on the onset of fiber-matrix debonding under transverse tension: A comparison between cohesive zone and finite fracture mechanics models. *Engineering Fracture Mechanics 115*, 96–110.

Garg, A. (1988). Delamination - A damage mode in composite structures. *Engineering Fracture Mechanics 29*, 557–584.

Garrido, J., A. Foces, and F. París (1988). Sobre Problemas de Contacto con Retroceso Usando el Método de los Elementos de Contorno. In *Anales de Ingeniería Mecánica VI*, Volume 3, pp. 115–122.

Garrido, J., A. Foces, and F. París (1997). B.E.M. applied to receding contact problems with friction. *Mathematical and Computer Modelling 15*(3–5), 143–153.

Geubelle, P. and W. Knauss (1995). Crack propagation in homogeneous and bimaterial sheets under general in-plane loading: nonlinear analysis. *Journal of Applied Mechanics 62*, 601–606.

Geymonat, G., F. Krasucki, and S. Lenci (1999). Mathematical analysis of a bonded joint with a soft thin adhesive. *Mathematics and Mechanics of Solids 4*, 201–225.

Goglio, L. and M. Rossetto (2011). Precision of the one-dimensional solutions for bonded double lap joints. *International Journal of Adhesion and Adhesives 31*(5), 301 – 314.

Goland, M. and E. Reissner (1944). The stresses in cemented joints. *Journal of Applied Mechanics 11*, A17–A27.

Graciani, E., V. Mantič, F. París, and A. Blázquez (2005). Weak formulation of axi-symmetric frictionless contact problems with boundary elements: Application to interface cracks. *Computer and Structures 83*, 836–855.

Griffith, A. A. (1921). The phenomena of rupture and flow in solids. *Philosophical transaction of the royal society of London. Sieres A. Containing papers of a Mathematical or physical character 221*, 163–198.

Griffith, A. A. (1924). The theory of rupture. In *First International Congress of Applied Mechanics*, pp. 55–63.

Hart-Smith, L. (1973a). Adhesive-bonded double-lap joints. Technical report, NASA Contract Report 112235.

Hart-Smith, L. (1973b). Adhesive-bonded single-lap joints. Technical report, NASA Contract Report 112236.

Hashin, Z. (1980). Failure Criteria for Unidirectional Fiber Composites. *Journal of Applied Mechanics 47*, 329–334.

Hashin, Z. (1996). Finite thermoelastic fracture criterion with application to laminate cracking analysis. *Journal of the Mechanics and Physics of Solids 44*(7), 1129 – 1145.

He, M.-Y. and J. Hutchinson (1989). Kinking of a crack out of an interface. *Journal of Applied Mechanics 55*, 270–278.

Henninger, C., D. Leguillon, and E. Martin (2007). Crack initiation at a V-notch-comparison between a brittle fracture criterion and the Dugdale cohesive model. *Comptes Rendus MÃ©canique 335*(7), 388–393.

Hilleborg, A., M. Modeer, and P. Petersson (1976). Analysis of a crack formation and crack growth in concrete by fracture mechanics and finite elements. *Cement and Concrete Research 6*, 773–782.

Hillerborg, A., M. ModÃ©er, and P.-E. Petersson (1976). Analysis of crack formation and crack growth in concrete by means of fracture mechanics and finite elements. *Cement and Concrete Research 6*(6), 773 – 781.

Hills, D. and J. Barber (1993). Interface cracks. *International Journal of Mechanical Sciencies 35*, 25–37.

Hills, D., P. Kelly, D. Dai, and A. Korsunsky (1996). Solutions of Crack Problems. The Distributed Dislocation Technique. *Kluwer Academic Publishers: Dordrecht*.

Hollaway, L. C. (2010). A review of the present and future utilisation of FRP composites in the civil infrastructure with reference to their important in-service properties. *Construction and Building Materials 24*(12), 2419–2445.

Hutchinson, J. W. and Z. Suo (1992). Mixed mode cracking in layered materials. *Advances in Applied Mechanics 29*, 63–191.

I.Iovinella, A.Prota, and C.Mazzotti (2013). Influence of surface roughness on the bond of FRP laminates to concrete. *Construction and Building Materials 40*, 533–542.

Inglis, C. (1913). Stress in a plate due to the presence of cracks and shap corners. *Transactions on the Institute of Naval Architects 55*, 219–241.

Irwin, G. R. (1948). Fracture dynamics. *Fracturing of metals. American Society for metals*, 147–166.

Irwin, G. R. (1957). Analysis of stresses and strains near the end of a crack transversing a plate. *Journal of applied mechanics 24*, 361–364.

J.G.Teng (2001). *FRP Composites in Civil Engineering: proceedings of the International Conference on FRP Composites in Civil Engineering*. Elsevier.

Jiménez, M., J. Cañas, V. Mantič, and J. Ortiz (2007). Numerical and experimental study of the interlaminar fracture test of composite-composite adhesively bonded joints. (in Spanish). *Materiales Compuestos 07, Asociación Española de Materiales Compuestos, Universidad de Valladolid*, 499–506.

J.Yao, J.G.Teng, and J.F.Chen (2005). Experimental study on FRP-to-concrete bonded joints. *Composites Part B: Engineering 36*(2), 99–113.

Kanninen, M. F. (1973). An augmented double cantilever beam model for studying crack propagation and arrest. *International Journal of Fracture 9*, 83–92.

Klarbring, A. (1991). Derivation of a model of adhesively bonded joints by the asymptotic expansion method. *International Journal of Engineering Science 29*, 493–512.

Knowles, J. and E. Sternberg (1983). Large deformations near the tip of an interface crackbetween two Neo-Hookean sheets. *Journal of Elasticity 13*, 257–293.

Lamé, G. (1852). *Leçons sur la Théorie Mathématique de l˜Élasticité des Corps Solides.* Paris, Bachelier.

l'Armée, A. T. and W. Becker (2019). Coupled stress and energy criterion for composite failure: Pointwise versus averaged evaluation of the stress criterion. *Mechanics of Advanced Materials and Structures*, 1–12.

Leguillon, D. (2002). Strength or toughness? a criterion for crack onset at a notch. *European Journal of Mechanics A/Solids 21*, 61–72.

Leguillon, D. and S. Murer (2012). Fatigue crack nucleation at a stress concentration point. In *4th International Conference on "Crack Paths", CP 2012*.

Lekhnitskii, S. G. (1981). *Theory of Elasticity of an Anisotropic Body*. Mir Publishers: Moscow.

Lenci, S. (2001). Analysis of a crack at a weak interface. *International Journal of Fracture 108*, 275–290.

L.H.Sneed, T.D'Antino, C.Carloni, and C.Pellegrino (2015). A comparison of the bond behavior of PBO-FRCM composites determined by double-lap and single-lap shear tests. *Cement and Concrete Composites 64*, 37–48.

Li, J., D. Leguillon, E. Martin, and X.-B. Zhang (2019). Numerical implementation of the coupled criterion for damaged materials. *International Journal of Solids and Structures 165*, 93–103.

Liechti, K. M. and Y. S. Chai (1992, 06). Asymmetric Shielding in Interfacial Fracture Under In-Plane Shear. *Journal of Applied Mechanics 59*(2), 295–304.

Liu, C. and I. Feng-Chen (1996). Interface cracks in a layered solid subjected to contact stresses. *Journal of Applied Mechanics 63*, 271–277.

Maier, G. and A. Frangi (1998). Symmetric boundary element method for 'discrete' crack modelling of fracture processes. *Computer Assisted Mechanics and Engineering Sciences 5*, 201–226.

Malyshev, B. and R. Salganik (1965). The strength of adhesive joints using the theory of cracks. *International Journal of Fracture and Mechanics* (1), 114–128.

Mantič, V. (2008). Discussion: "On the reference length and mode mixity for a bimaterial interface". *Journal of Engineering Materials and Technology 130*, 045501:1–2.

Mantič, V. (2009). Interface crack onset at a circular cylindrical inclusion under a remote transverse tension. Application of a coupled stress and energy criterion. *International Journal of Solids and Structures 46*, 1287–1304.

Mantič, V. (2014). Prediction of initiation and growth of cracks in composites. Coupled stress and energy criterion of the finite fracture mechanics. In *16th European Conference on Composite Materials, ECCM 2014*.

Mantič, V., A. Blázquez, E. Correa, and F. París (2006). *Analysis of interface cracks with contact in composites by 2D BEM, In: Fracture and Damage of Composites, M. Guagliano and M. H. Aliabadi (Eds.)*, Volume 8, Chapter 8, pp. 189–248. WIT Press: Southampton.

Mantič, V. and I. García (2012). Crack onset and growth at the fibre–matrix interface under a remote biaxial transverse load. Application of a coupled stress and energy criterion. *International Journal of Solids and Structures 49*, 2273–2290.

Mantič, V., L. Távara, A. Blázquez, E. Graciani, and F. París (2015). A linear elastic - brittle interface model: Application for the onset and propagation of a fibre-matrix interface crack under biaxial transverse loads. *International Journal of Fracture 195*, 15–38.

Martin, E., D. Leguillon, O. Sevecek, and R. Bermejo (2018). Understanding the tensile strength of ceramics in the presence of small critical flaws. *Engineering Fracture Mechanics 201*, 167 – 175.

Martin, E., T. Vandellos, D. Leguillon, and N. Carrère (2016). Initiation of edge debonding: coupled criterion versus cohesive zone model. *International Journal of Fracture 199*(2), 157–168.

Martinelli, E., C. Czaderski, and M. Motavalli (2011). Modeling in-plane and out-of-plane displacement fields in pull-off tests on FRP strips. *Engineering Structures 33*(12), 3715 – 3725.

Mazzotti, C., A. Bilotta, C. Carloni, F. Ceroni, T. D'Antino, E. Nigro, and C. Pellegrino (2016). *Bond Between EBR FRP and Concrete*, Chapter 3, pp. 39–96. Dordrecht: Springer Netherlands.

Mazzotti, C., M. Savoia, and B. Ferracuti (2008). An experimental study on delamination of FRP plates bonded to concrete. *Construction and Building Materials 22*(7), 1409–1421.

Melro, A., P. Camanho, F. Andrade Pires, and S. Pinho (2013a). Micromechanical analysis of polymer composites reinforced by unidirectional fibres: Part I - Constitutive modelling. *International Journal of Solids and Structures 50*(11), 1897–1905.

Melro, A., P. Camanho, F. Andrade Pires, and S. Pinho (2013b). Micromechanical analysis of polymer composites reinforced by unidirectional fibres: Part II - Micromechanical analyses. *International Journal of Solids and Structures 50*(11), 1906–1915.

M.Savoia, B.Ferracuti, and L.Vincenzi (2009). Inverse Analysis for the Calibration of FRP-Concrete Interface Law. *Advances in Structural Engineering 12*(5), 613–625.

Muñoz Reja, M., P. Cornetti, L. Távara, and V. Mantič (2020a). A numerical implementation of the Coupled Criterion of Finite Fracture Mechanics for elastic interfaces. *Theoretical and Applied Fracture Mechanics 108*.

Muñoz Reja, M., P. Cornetti, L. Távara, and V. Mantič (2020b). Interface crack model using finite fracture mechanics applied to the double pull-push shear test. *International Journal of Solids and Structures 188–189*, 56–73.

Muñoz Reja, M., L. Távara, and V. Mantič (2018). Convergence of the BEM Solution Applied to the CCFFM for LEBIM. *Key Engineering Materials 774*, 355–360.

Muñoz Reja, M., L. Távara, V. Mantič, and P. Cornetti (2016). Crack onset and propagation at fibre-matrix elastic interfaces under biaxial loading using finite fracture mechanics. *Composites Part A 82*, 267–278.

Needleman, A. (1987). A continuum model for void nucleation by inclusion debonding. *Journal of Applied Mechanics 54*, 525–532.

Neuber, H. (1958). *Theory of notch stresses: Principles for exact calculation of strength with reference to structural form and material*. Springer.

Orowan, E. (1949). Fracture and strength of solids. *Reports on Progress in Physics 12*(1), 185–232.

Ortiz, M. and A. Pandolfi (1999). Finite-Deformation irreversible cohesive elements for three dimensional crack propagation analysis. *International Journal for Numerical Methods in Engineering 44*, 1267–1283.

París, F. (2001). A Study of Failure Criteria of Fibrous Composite Materials. Technical report, NASA CR-2001-210661.

París, F. and J. Cañas (1997). *Boundary Element Method, Fundamentals and Applications.* Oxford University Press: Oxford.

París, F., E. Correa, and V. M. c (2007). Kinking of transverse interface cracks between fiber and matrix. *Journal of Applied Mechanics 74*, 703–716.

Park, K. and G. Paulino (2011). Cohesive zone models: A critical review of traction-separation relationships across fracture surfaces. *Applied Mechanics Reviews 64*(6), 1–20.

Prandtl, L. (1933). A thought model for the fracture of brittle solids. *Zeitschrift für Physikr Angenwandte Mathematik und Mechanik 13(2)*, 129–133.

Rice, J. R. (1988). Elastic fracture mechanics concepts for interfacial cracks. *Journal of Applied Mechanics 55*(1), 98–103.

Rice, J. R. and G. Sih (1965). Plane problems of cracks in dissimilar media. *Journal of Applied Mechanics 32*, 418–423.

Risso, G. (2018, July). A finite fracture mechanics approach to brittle failure of adhesive lap joints. Master's thesis, Politecnico di Torino.

Rosendahl, P. L. and P. Weißgraeber (2019). Modeling snow slab avalanches caused by weak layer failure – Part I: Slabs on compliant and collapsible weak layers. *The Cryosphere Discussions 2019*, 1–28.

Roubíček, T. (2015). Maximally-dissipative local solutions to rate-independent systems and application to damage and delamination problems. *Nonlinear Analysis: Theory, Methods & Applications 113*, 33–50.

Roubíček, T., V. Mantič, and C. Panagiotopoulos (2013). A quasistatic mixed-mode delamination model. *Discrete & Continuous Dynamical Systems 6*, 591—-610.

Sapora, A., P. Cornetti, and A. Carpinteri (2013). A Finite Fracture Mechanics approach to V-notched elements subjected to mixed-mode loading. *Engineering Fracture Mechanics 97*(1), 216–226.

Sapora, A., P. Cornetti, and A. Carpinteri (2014). V-notched elements under mode II loading conditions. *Structural Engineering and Mechanics 49*(4), 499–508.

Sapora, A., P. Cornetti, A. Carpinteri, and D. Firrao (2015). An improved Finite Fracture Mechanics approach to blunt V-notch brittle fracture mechanics: Experimental verification on ceramic, metallic, and plastic materials. *Theoretical and Applied Fracture Mechanics 78*, 20–24.

Shih, C. and R. Asaro (1988). Elastic-plastic analysis of cracks on bimaterial interfaces: Part I-Small scale yielding. *Journal of Applied Mechanics 55*, 299–316.

Shih, C. and R. Asaro (1989). Elastic-plastic analysis of cracks on bimaterial interfaces: Part II-Structure of small scale yielding fields. *Journal of Applied Mechanics 56*, 763–779.

Sneddon, I. N. (1946). The distribution of stress in the neighbourhood of a crack in an elastic solid. *Proceedings of the Royal Society of London A: Mathematical, Physical and Engineering Sciences 187(1009)*, 229–260.

Távara, L., I. García, R. Vodička, C. Panagiotopoulos, and V. Mantič (2016). Revisiting the problem of debond initiation at fibre-matrix interface under transversal biaxial loads - A comparison of several non-classical fracture mechanics approaches. *Key Engineering Materials 713*, 232–235.

Távara, L., V. Mantič, E. Graciani, J. Cañas, and F. París (2008). BEM model of mode I crack propagation along a weak interface applied to the interlaminar fracture test of composites. *Advances in Boundary Element Techniques IX, EC Ltd, Eastleight*, 461–466.

Távara, L., V. Mantič, E. Graciani, J. Cañas, and F. París (2010). Analysis of a crack in a thin adhesive layer between orthotropic materials. an application to composite interlaminar fracture toughness test. *CMES-Computer Modeling in Engineering and Sciences **58***(3), 247–270.

Távara, L., V. Mantič, E. Graciani, and F. París (2011). BEM analysis of crack onset and propagation along fiber-matrix interface under transverse tension using a linear elastic-brittle interface model. *Engineering Analysis with Boundary Elements 35*, 207–222.

Távara, L., V. Mantič, E. Graciani, and F. París (2016). Modelling interfacial debonds in unidirectional fibre reinforced composites under biaxial transverse loads. *Composite Structures **136***, 305–312.

Távara, L., L. Moreno, E. Paloma, and V. Mantič (2019). Accurate modelling of instabilities caused by multi-site interface-crack onset and propagation in composites using the sequentially linear analysis and Abaqus. *Composite Structures 225*, 110993.

Távara, L., J. Reinoso, A. Blázquez, and V. Mantič (2019a). On the 3D extension of failure models for adhesive joints under mixed-mode fracture conditions: LEBIM and CZM. *Theoretical and Applied Fracture Mechanics 100*, 362–376.

Távara, L., J. Reinoso, A. Blázquez, and V. Mantič (2019b). On the 3D extension of failure models for adhesive joints under mixed-mode fracture conditions: LEBIM and CZM. *Theoretical and Applied Fracture Mechanics 100*, 362–376.

Távara, L., J. Reinoso, D. Castillo, and V. Mantič (2018). Mixed-mode failure of interfaces studied by the 2Dlinear elastic–brittle interface model: Macro and micromechanical finite-element applications incomposites. *The Journal of Adhesion 94*, 627–656.

Tay, T. (2003). Characterization and analysis of delamination fracture in composites: An overview of developments from 1990 to 2001. *Applied Mechanics Reviews 56*, 1–31.

Taylor, D., P. Cornetti, and N. Pugno (2005). The fracture mechanics of finite crack extension. *Engineering fracture mechanics 72*, 1021–1038.

T.D'Antino, L.H.Sneed, C.Carloni, and C.Pellegrino (2016). Effect of the inherent eccentricity in single-lap direct-shear tests of PBO FRCM-concrete joints. *Composite Structures 142*, 117–129.

Ting, T. (1996). *Anisotropic Elasticity Theory and Applications*. Oxford University Press: Oxford.

Tszeng, T. (1993). A model of void nucleation from ellipsoidal inclusions in ductile fracture. *Scripta Metallurgica et Materialia 28*(9), 1065–1070.

Vaculik, J., P. Visintin, N. Burton, M. Griffith, and R. Seracino (2018). State-of-the-art review and future research directions for FRP-to-masonry bond research: Test methods and techniques for extraction of bond-slip behaviour. *Construction and Building Materials 183*, 325 – 345.

Valoroso, N. and L. Champaney (2006). A damage-mechanics-based approach for modelling decohesion in adhesively bonded assemblies. *Engineering Fracture Mechanics 73*(18), 2774–2801.

Vodička, R. (2016). A quasi-static interface damage model with cohesive cracks: SQP–SGBEM implementation. *Engineering Analysis with Boundary Elements 62*, 123–140.

Vodička, R., V. Mantič, and T. Roubíček (2014). Energetic versus maximally-dissipative local solutions of a quasi-static rate-independent mixed-mode delamination model. *Meccanica 49*, 2933–2963.

Volkersen, O. (1938). Die Nietkraftverteilung in Zugbeanspruchten Nietverbindungen mit Konstanten Laschen-querschnitten. *Luftfahrtforschung 15*, 4–47.

Wang, C. (1997). Elastic fields produced by a point source in solids of general anisotropy. *Journal of Engineering Mathematics 32*, 41–52.

Wang, J. (2013). Investigating Some Technical Issues on Cohesive Zone Modeling of Fracture. *Journal of engineering materials and technology-transactions of the asme 135*.

Wang, J.-S. and Z. Suo (1990). Experimental determination of interfacial toughness curves using Brazil-nut-sandwiches. *Acta Metallurgica et Materialia 38*(7), 1279–1290.

Weißgraeber, P. and W. Becker (2013). Finite Fracture Mechanics model for mixed mode fracture in adhesive joints. *International Journal of Solids and Structures 50*, 2383–2394.

Weißgraeber, P., D. Leguillon, and W. Becker (2016). A review of Finite Fracture Mechanics: crack initiation at singular and non-singular stress raisers. *Archive of Applied Mechanics 50*, 2383–2394.

Westergaard, H. M. (1939). Bearing pressures and cracks. *Journal of Applied Mechanics 49*, 49–53.

Wieghardt, K. (1907). Über das Spalten und Zerreissen elastischer Körper (On splitting and cracking of elastic bodies). *Zeitschrift für Mathematik und Physik 55* (1-2), 60–103. Translation: Rossmanith H.P. Fatigue Fract Engng Mater Struct 1995, 12: 1371-1405.

Williams, M. (1959). The stress around a fault of crack in dissimilar media. *Bull. Seismol. Soc. Am. 49*, 199–204.

Woo, S.-K. and Y. Lee (2010, May). Experimental study on interfacial behavior of CFRP-bonded concrete. *KSCE Journal of Civil Engineering 14* (3), 385–393.

Wu, Z., H. Yuan, and H. Niu (2002). Stress transfer and fracture propagation in different kinds of adhesive joints. *Journal of Engineering Mechanics 128* (5), 562–573.

Y.Li, J.Bielak, J.Hegger, and R.Chudoba (2018). An incremental inverse analysis procedure for identification of bond-slip laws in composites applied to textile reinforced concrete. *Composites Part B: Engineering 137*, 111–122.

Yuan, C., W. Chen, T. M. Pham, and H. Hao (2019a). Bond behaviour between hybrid fiber reinforced polymer sheets and concrete. *Construction and Building Materials 210*, 93–110.

Yuan, C., W. Chen, T. M. Pham, and H. Hao (2019b). Effect of aggregate size on bond behaviour between basalt fibre reinforced polymer sheets and concrete. *Composites Part B: Engineering 158*, 459–474.

Yuan, C., W. Chen, T. M. Pham, H. Hao, J. Cui, and Y. Shi (2019). Strain rate effect on interfacial bond behaviour between bfrp sheets and steel fibre reinforced concrete. *Composites Part B: Engineering 174*, 107032.

Yuan, H., J. Teng, R. Seracino, Z. Wu, and J. Yao (2004). Full-range behavior of frp-to-concrete bonded joints. *Engineering Structures 26* (5), 553 – 565.

Zhang, D., X.-L. Gu, Q.-Q. Yu, H. Huang, B. Wan, and C. Jiang (2018). Fully probabilistic analysis of FRP-to-concrete bonded joints considering model uncertainty. *Composite Structures 185*, 786–806.

Zienkiewicz, O. C., R. L. Taylor, and J. Z. Zhu (2005). *The Finite Element Method: Its Basis and Fundamentals, Sixth Edition*. Butterworth-Heinemann.

List of contributions

The following international and national publications have been originated during the work in the present Thesis

International Peer-Review Publications

1. Muñoz-Reja, M. Távara, L. Mantič, V. and Cornetti, P. Crack onset and propagation at fibre-matrix elastic interfaces under biaxial loading using finite fracture mechanics. *Composites Part A*, **82**:267-278, 2016. doi: https://doi.org/f8b9jb

2. Muñoz-Reja, M. Távara, L. and Mantič, V. Symmetrical or Non-Symmetrical Debonds at Fiber-Matrix Interfaces: A Study by BEM and Finite Fracture Mechanics on Elastic Interfaces. *Journal of Multiscale Modeling*, **8(3-4)**:740008-1–740008-14, 2017. doi: https://doi.org/ftjp

3. Muñoz-Reja, M. Távara, L. and Mantič, V. Convergence of the BEM solution applied to the CCFFM for LEBIM. *Key Engineering Materials*, **774**:355-360, 2018. doi: https://doi.org/ftjq

4. Cornetti, P. Muñoz-Reja, M. Sapora, A. and Carpinteri, A. Finite fracture mechanics and cohesive crack model: Weight functions vs. cohesive laws. *International Journal of Solids and Structures*, **156-157**:126-136, 2019. doi: https://doi.org/ftjr

5. Muñoz-Reja, M. Távara, L. Mantič, V. and Cornetti, P. Interface crack model using finite fracture mechanics applied to the double pull-push shear test. *International Journal of Solids and Structures*, **188-189**:56-73, 2020. doi: https://doi.org/ftjt

6. Muñoz-Reja, M. Távara, L. Mantič, V. and Cornetti, P. A numerical implementation of the Coupled Criterion of Finite Fracture Mechanics for elastic interfaces. *Theoretical and Applied Fracture Mechanics*, **108**:102607-1–102607-11, 2020. doi: https://doi.org/ftjv

International Conference

1. Muñoz-Reja, M. Távara, L. Mantič, V. and Cornetti, P. Crack onset and propagation in composite materials using Finite Fracture Mechanics on elastic interfaces. *Procedia Materials Science*, **3**:1365-1370, 2014. In 20th European Conference on Fracture. June 30th- July 4th 2014, Trondheim (Norway).

2. Muñoz-Reja, M. Távara, L. Mantič, V. and Cornetti, P. Crack onset and propagation along fibre-matrix elastic interfaces under biaxial loading using finite fracture mechanics. *16th European Conference on Composite Materials* June, 22nd-26th 2014, Seville (Spain).

3. Muñoz-Reja, M. Távara, L. Mantič, V. and Cornetti, P. Analysis of crack onset and propagation at elastic interfaces by using Finite Fracture Mechanics. *15th International Conference on Boundary Element Techniques* July 15th-17th 2014, Florence (Italy).

4. Muñoz-Reja, M. Távara, L. Mantič, V. and Cornetti, P. BEM analysis of fibre-matrix interface crack onset and propagation under biaxial transverse loads using Finite Fracture Mechanics on elastic interfaces. *16th International Conference on Boundary Element Techniques* July 6th-8th 2015, Valencia (Spain).

5. Muñoz-Reja, M. Távara, L. Mantič, V. and Cornetti, P. Influence of a neighbour fibre on the onset and growth of a fibre-matrix debond under biaxial loading. A study by Finite Fracture Mechanics at linear elastic interfaces. *Procedia Structural Integrity*, **2**:2022-2029, 2016. In 21st European Conference on Fracture. June, 20th-24th 2016, Catania (Italy).

6. Muñoz-Reja, M. Távara, L. Mantič, V. and Cornetti, P. Double pull-push shear test by finite fracture mechanics and linear elastic interfaces. *ICF 2017 - 14th International Conference on Fracture*, **2**:924-925, 2017. June, 18th-20th 2017, Rhodes (Greece).

7. Muñoz-Reja, M. Távara, L. Mantič, V. and Cornetti, P. Double pull-push shear test by finite fracture mechanics and linear elastic interfaces. *ICF 2017 - 14th International Conference on Fracture*, **2**:924-925, 2017. June, 18th-20th 2017, Rhodes (Greece).

8. Cornetti, P. Muñoz-Reja, M. Sapora, A. and Carpinteri, A. Extending finite fracture mechanics by means of stress weight functions. *ICF 2017 - 14th International Conference on Fracture*, **2**:681-682, 2017. June, 18th-20th 2017, Rhodes (Greece).

9. Távara, L. Muñoz-Reja, M. and Mantič. Implementation of the finite fracture mechanics criterion at elastic interfaces in the FEM package abaqus. *ICF 2017 - 14th International Conference on Fracture*, **2**:932-933, 2017. June, 18th-20th 2017, Rhodes (Greece).

10. Muñoz-Reja, M. Távara, L. Mantič, V. and Cornetti, P. Interface crack growth in composite materials by finite fracture mechanics at elastic interfaces for displacement and load control. *ICF 2017 - 14th International Conference on Fracture*, **2**:944-945, 2017. June, 18th-20th 2017, Rhodes (Greece).

11. Muñoz-Reja, M. Távara, L. and Mantič, V. Debond predictions using Finite Fracture Mechanics along Elastic Interfaces by a FEM code. *22nd European Conference on Fracture.* August, 26th-31st 2018, Belgrade (Serbia).

12. Cornetti, P. Muñoz-Reja, M. Mantič, V. and Sapora, A. A finite fracture mechanics approach to debonding accounting for residual friction. *22nd European Conference on Fracture.* August, 26th-31st 2018, Belgrade (Serbia).

13. Muñoz-Reja, M. Távara, L. and Mantič, V. Convergence of the BEM Solution Applied to the CCFFM for LEBIM. *17th International Conference on Fracture and Damage Mechanics.* September, 4th-6th 2018, Seville (Spain).

National Conference

1. Muñoz-Reja, M. Távara, L. Mantič, V. and Cornetti, P.. Nuevo modelo de inicio y propagación de grietas en la interfase de materiales compuestos fibrosos. *XXXI Encuentro del GEF* April, 2th-3th 2014, Madrid (Spain).

2. Muñoz-Reja, M. Távara, L. Mantič, V. and Cornetti, P.. Modelo del comportamiento de grietas de interfase en el ensayo a cortante pull-push usando la mecánica de la fractura finita. *XXXII Encuentro del GEF* April, 27th-29th 2015, Zamora (Spain).

3. Muñoz-Reja, M. Távara and L. Mantič, V. Simetría o no simetría en el fallo de la interfase fibra-matriz. Estudio de interfases elásticas en el marco de la mecánica de la fractura finita. *XXXV Encuentro del GEF* March, 14th-16th 2018, Málaga (Spain).

4. Muñoz-Reja, M. Távara and L. Mantič, V. Convergencia de la solución numérica obtenida usando el método de elementos de contorno. Aplicado al criterio acoplado de fractura finita en interfases débiles. *XXXVI Encuentro del GEF* April, 3th-5th 2019, Sevilla (Spain).

5. Muñoz-Reja, M. Távara, L. Panagiotopoulos, C. and Mantič, V. Analysis of onset and growth of multiple debonds by means of an ABAQUS implementation of the CCFFM+LEBIM. *Congresso de Métodos Numéricos em Engenharia.* July, 1st-3rd 2019, Guimarães (Portugal).